

ULTRAFAST TWO-PHOTON ABSORPTION IN ORGANIC MOLECULES:  
QUANTITATIVE SPECTROSCOPY AND APPLICATIONS

by

Nikolay Sergeevich Makarov

A dissertation submitted in partial fulfillment  
of the requirements for the degree

of

Doctor of Philosophy

in

Physics

MONTANA STATE UNIVERSITY  
Bozeman, Montana

April 2010

© COPYRIGHT

by

Nikolay Sergeevich Makarov

2010

All Rights Reserved


APPROVAL

of a dissertation submitted by

Nikolay Sergeevich Makarov

This dissertation has been read by each member of the dissertation committee and has been found to be satisfactory regarding content, English usage, format, citation, bibliographic style, and consistency, and is ready for submission to the Division of Graduate Education.

Dr. Aleksander Rebane



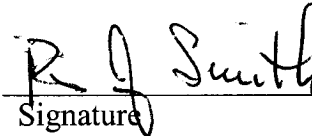
Signature



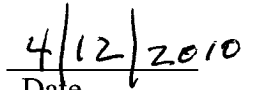
Date

Approved for the Department of Physics

Dr. Richard J. Smith



Signature



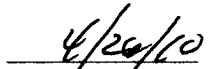
Date

Approved for the Division of Graduate Education

Dr. Carl A. Fox



Signature



Date

## STATEMENT OF PERMISSION TO USE

In presenting this dissertation in partial fulfillment of the requirements for a doctoral degree at Montana State University, I agree that the Library shall make it available to borrowers under the rules of the Library. I further agree that copying of this dissertation is allowable only for scholarly purposes, consistent with “fair use” as described in the U.S. Copyright Law. Requests for extensive copying or reproduction of this dissertation should be referred to ProQuest Information and Learning, 300 North Zeeb Road, Ann Arbor, Michigan 48106, to whom I have granted “the non-exclusive right to reproduce and distribute my dissertation in and microfilm along with the non-exclusive right to reproduce and distribute my abstract in any format in whole or in part”.

Nikolay Sergeevich Makarov

April 2010

## ACKNOWLEDGEMENTS

This dissertation is the result of almost six years of work during which I was interacting with many people who I would like to thank.

First, I would like to thank my advisor, Prof. Aleksander Rebane, for the opportunity to work in one of the strongest, and probably the best nonlinear spectroscopy group. Aleks' enthusiasm, leadership and devotion to his work are the best components needed for success.

I would like to thank Dr. Mikhail Drobizhev, the Research Assistant Professor in our group. His help with many experiments is invaluable. His ability to make a theory explaining almost everything is amazing.

I would like to thank many of our collaborators for providing interesting compounds for our research and for useful conversations. My thanks to Thomas Hughes, Jean Starkey, Charles and Brenda Spangler, Shane Tillo, Heinz Wolleb, Heinz Spahni, Thomas Cooper, Joy Haley, Kirk Schanze, Harry Anderson, Tomas Torres, Daniel Gryko, Yuriy Stepanenko, Erich Beuerman, Desiree Peone, and Bret Davis.

I would like to thank our current and previous department staff for the help with many things: Sarah, Jeremy, Bo, Sherry, Margaret, Brian, Rose, Glenda, Jeannie, and Norm.

Finally, thanks to my friends for hanging out with me sometimes, and, especially, to Greg Merchant for being with me in the parks and many other places.

## TABLE OF CONTENTS

1. INTRODUCTION .....	1
Introduction to Research Topic.....	1
Overview of Dissertation .....	4
2. THE MAIN CONCEPTS OF TWO-PHOTON ABSORPTION.....	8
One-Photon Absorption: Introduction of Dipole Moments .....	8
Introduction of Two-Photon Absorption .....	10
Quantitative Description of Two-Photon Absorption with a Few- Essential-Levels Model.....	12
3. DESCRIPTION OF EXPERIMENTAL TECHNIQUES: MEASUREMENTS OF TWO-PHOTON ABSORPTION AND TRANSIENT ABSORPTION SPECTRA ..	17
Experimental Setup for Measuring of Absolute Two-Photon Absorption Spectra.....	17
Experimental Setup for Measuring of Femtosecond Excited State Absorption.....	21
4. MEASUREMENTS OF TWO-PHOTON ABSORPTION SPECTRA AND CROSS SECTIONS: REFERENCE STANDARDS IN 550–1600 NM EXCITATION RANGE.....	26
Correction Curve for Measurements of Two-Photon Absorption Spectra and Cross Sections in Wide Range of Excitation Wavelengths .....	28
Two-Photon Absorption Spectra of the Reference Standards and their Comparison with the Literature Data.....	31
5. APPLICATION OF THE FEW-ESSENTIAL ENERGY LEVELS MODEL FOR QUANTITATIVE DESCRIPTION OF THE TWO-PHOTON ABSORPTION SPECTRA AND CROSS SECTIONS.....	38
Two-Level Model .....	39
Three-Level Model .....	50
6. APPLICATION OF TWO-PHOTON ABSORPTION: 3D OPTICAL MEMORY...64	
Basic Principles of Two-Photon Volumetric Recording and Readout .....	65
Fast Bit Access Rate and Single Femtosecond Pulse Recording.....	67
Using Resonance Enhancement of Two-Photon Absorption to Increase Signal-to-Noise .....	69

## TABLE OF CONTENTS – CONTINUED

Numerical Simulations: Tradeoff between Signal-to-Noise and Signal-to-Background Ratios.....	71
Experimental Characterization of a Model Compound for 3D Optical Memory.....	76
Simulation of Signal-to-Background and Signal-to-Noise Ratios Using Experimentally Obtained Molecular Parameters.....	79
Non-Centrosymmetrical Phthalocyanines for Volumetric Optical Memory .....	81
Spectra of the Non-Centrosymmetrical Phthalocyanines .....	84
Photoinduced Tautomerization of the Non-Centrosymmetrical Phthalocyanines .....	91
Comparison of the Studied Phthalocyanines in Connection with Optimization of the Volumetric Memory .....	96
<b>7. APPLICATION OF TWO-PHOTON ABSORPTION SPECTROSCOPY FOR DETECTION OF CANCER CELLS.....</b>	<b>99</b>
Experimental Setup for Two-Photon Imaging of Cancer Cells in Tissue Phantoms.....	101
Spectroscopy of Styryl-9M in Tissue Phantoms.....	103
Analysis of the Two-Photon-Excited Fluorescence Images Helps to Identify Cancer Cells .....	107
Evaluation of Ultimate Sensitivity of Cancer Cell Detection.....	113
<b>8. SUMMARY AND CONCLUSIONS .....</b>	<b>120</b>
Measurements of Two-Photon Absorption Spectra and Cross Sections: Reference Standards in 550–1600 nm Excitation Range (Chapter 4) .....	120
Application of the Few-Essential Energy Levels Model for Quantitative Description of the Two-Photon Absorption Spectra and Cross Sections (Chapter 5) .....	121
Applications of Two-Photon Absorption for Volumetric Optical Memory (Chapter 6) .....	122
Applications of Two-Photon Absorption for Cancer Detection (Chapter 7).....	123
Quantitative Nonlinear Spectroscopy .....	123
<b>REFERENCES CITED.....</b>	<b>126</b>
<b>APPENDICES .....</b>	<b>145</b>
APPENDIX A Derivation of the Expression for Two-Photon Cross Section in Case of Two-Level Model .....	146

## TABLE OF CONTENTS – CONTINUED

APPENDIX B Description of the Standard Linear Measurements for Determination of the Values of the Dipole Moments Between the Ground and Excited States .....	154
APPENDIX C Measurements of the Two-Photon Cross Sections .....	162
APPENDIX D Data Tables .....	185
APPENDIX E Details on the Modeling of the Signal-To-Noise and Signal-To-Background Ratios for Volumetric Optical Memory .....	205
APPENDIX F Spectroscopic Characterization of Styryl-9M .....	217
APPENDIX G Some Documentation on the Pump-Probe Experimental Setup .....	236



## LIST OF TABLES

Table	Page
D.1. Extinction coefficients at maximum wavelength, fluorescence wavelength range and 2PA wavelength range for the dyes.....	186
D.2. Comparison of two-photon cross sections of the reference standards with the literature data.....	187
D.3. Two-photon cross sections (GM) of the dyes at selected wavelengths (nm). The relative error of numbers shown here is $\pm 15\%$ (First four compounds).....	189
D.4. Two-photon cross sections (GM) of the dyes at selected wavelengths (nm). The relative error of numbers shown here is $\pm 15\%$ (Second four compounds).....	190
D.5. Two-photon cross sections (GM) of the dyes at selected wavelengths (nm). The relative error of numbers shown here is $\pm 15\%$ (Third four compounds).....	192
D.6. Two-photon cross sections (GM) of the dyes at selected wavelengths (nm). The relative error of numbers shown here is $\pm 15\%$ (Last four compounds).....	194
D.7. Measured spectroscopic parameters .....	196
D.8. Cross sections, transition dipole moments and angle between them, and line shape function of <i>TBTAC</i> : $\sigma_2^{\text{exp}}$ and $\sigma_2^{\text{theor}}$ refer to experimental and theoretical 2PA cross sections in the peak of the <i>g-g</i> transition recalculated to remove resonance enhancement as $\sigma_2(\nu) \frac{(\nu_{01} - \nu)^2}{\nu^2}$ .....	197
D.9. Properties of photochromic materials suggested for two-photon absorption storage. The columns present 2PA cross section $\sigma_2$ (form A at laser wavelength $\lambda_{\text{ex}}$ ), quantum efficiency of fluorescence $\phi^B$ (form B), quantum efficiency of photo-transformation $\phi_{A \rightarrow B}$ , molecular figure of merit, $FOM = \sqrt{\sigma_2^A \sigma_2^B \phi^B \phi_{A \rightarrow B}}$ , and working temperature.....	198
D.10. Parameters used in model simulations of SNR and SBR .....	199
D.11. 1PA and 2PA cross sections of the studied phthalocyanines in $\text{CH}_2\text{Cl}_2$ .....	200

## LIST OF TABLES – CONTINUED

Table	Page
D.12. Quantum yields and temperature stability of the non-centrosymmetrical phthalocyanines.....	201
D.13. Comparison of the efficiency of the molecules as photochromes for 3D optical memory .....	202
D.14. Linear properties of Styryl-9M .....	203
D.15. Composition of some of the biological phantoms .....	204

## LIST OF FIGURES

Figure	Page
2.1.	Four versions of few-essential energy levels model: (a) Two-level model for non-centrosymmetric chromophore with non-zero permanent dipole moment difference, $\Delta\vec{\mu}_{01} = \vec{\mu}_{00} - \vec{\mu}_{11}$ ; (b) Three-level system, where the laser frequency $\nu$ is far detuned from the frequency of transition, $\nu_{01}$ , between the ground state $0$ and intermediate state $1$ , and $\Delta\vec{\mu}_{01} = 0$ and resonance enhancement has a relatively small effect on the 2PA; (c) Three-level system, where the transition frequency $\nu_{01}$ is only slightly higher than $\nu$ and $\Delta\vec{\mu}_{01} = 0$ and resonance enhancement has a large effect; (d) Three-level system with $\Delta\vec{\mu}_{01} \neq 0$ : Quantum interference may arise between the two pathways, (a) and (b) or (c), leading to further enhancement (constructive interference) or suppression (destructive interference) of the 2PA efficiency .....13
3.1.	Layout of the experimental setup for 2PA measurements .....19
3.2.	Schematic of the pump-probe experimental setup: Second harmonic of the amplified Ti:Sapphire beam is used as the pump to excite the sample, and the tunable output of the OPA is used as the probe beam. Both beams are automatically aligned using computer controlled motorized mirrors (M1-M3) and computer controlled motorized beam splitter (BS1). InGaAs photodiode quad detectors (QD1 and QD2) are used to monitor the beam overlap at the sample. Computer controlled flipping mirror (M4) directs beams either to QD2 or to the sample. SM1 – spherical mirror, NDFW – neutral density filter wheel, SH1, and SH2 – shutters .....23
4.1.	Correction function in 550–1600 nm range: green symbols correspond to second harmonic of the OPA signal, orange symbols correspond to second harmonic of the OPA idler, and red symbols correspond to the fundamental OPA signal .....30
4.2.	Normalized fluorescence spectra of the reference dyes.....32
4.3.	Two-photon absorption spectrum of the <i>Fluorescein</i> (dark blue symbols). Additional data points are shown based on the data available in literature .....33
4.4.	Two-photon absorption spectrum of the <i>Rhodamine 6G</i> (dark blue symbols). Additional data points are shown based on the data available in literature .....34

## LIST OF FIGURES – CONTINUED

Figure	Page
4.5. Two-photon absorption spectrum of the <i>Rhodamine B</i> (dark blue symbols). Additional data points are shown based on the data available in literature .....	36
5.1a. 2PA (symbols) and 1PA (lines) spectra of substituted diphenylaminostilbenes. In 2PA spectrum of the molecule 2 one can see the OPA tuning gap around the wavelengths $\lambda \approx 380$ -400 nm. Vertical arrow indicates the wavelength, where $\sigma_2^{ex}$ is evaluated (corresponding to the maximum of the lowest-energy 1PA transition) .....	42
5.1b. 2PA (symbols) and 1PA (lines) spectra of meso-DPAS and BDPAS-substituted porphyrins. Dashed lines show decomposition of the long-wavelength portion of the 2PA spectrum into two Gaussians. Vertical arrow indicates the wavelength, where $\sigma_2^{ex}$ is evaluated (corresponding to the maximum of the lowest-energy 1PA transition) .....	44
5.1c. 2PA (symbols) and 1PA (lines) spectra of substituted diphenylaminostilbenes (group (iii)). Dashed lines show decomposition of the long-wavelength portion of the 2PA spectrum into two Gaussians. Vertical arrow indicates the wavelength, where $\sigma_2^{ex}$ is evaluated (corresponding to the maximum of the lowest-energy 1PA transition) .....	47
5.2. Comparison between the cross sections predicted by the two-level model (horizontal axis) and that measured in experiment (vertical axis). Solid rectangles – group (i), empty rectangles – group (ii), empty circles – group (iii). Vertical 20% error bars are due to the experimental uncertainty in the direct measurement of $\sigma_2^{ex}$ . Horizontal 30% error bars are due to the uncertainty in the determination of the dipole moment values (see text for details) .....	49
5.3. One-photon absorption (solid black line, left scale), two-photon absorption (black squares, right scale), fluorescence anisotropy (solid black line on the upper panel), and decomposition of the one-photon absorption spectra into transitions parallel (red dash line) and perpendicular (blue dot line) to the $S_0 \rightarrow S_1$ transition of the free-base tribenzotetraazachlorin. Also shown is the chemical structure of the molecule. Level diagram shows possible energy transitions. Red arrows indicate a laser frequency needed to excite the $S_0 \rightarrow S_i$ 2PA transition .....	53

## LIST OF FIGURES – CONTINUED

Figure	Page
5.4.	Transient absorption spectrum of the free-base tribenzotetraazachlorin. Negative values of extinction correspond to a saturation of absorption, and positive values correspond to a singlet-singlet excited state absorption. Level diagram shows possible energy transitions. Blue arrow represents the pump laser pulse, red arrow represents the probe laser pulse, and black arrow represents fast population decay from the higher-energy excited states to the first excited state. Insert on the top shows the decay of the normalized $\Delta OD$ at two wavelengths: 1250 nm (black squares) and 1125 nm (red circles). Lines show exponential fits to the decays .....55
5.5.	Two-photon (black squares) and excited state (red circles) line shapes of the free-base tribenzotetraazachlorin. Excited state absorption spectrum is plotted in the full (pump+probe) transition frequencies for easier comparison of the transitions .....59
5.6.	Comparison of the experimentally measured two-photon absorption spectrum (from figure 5.3, black squares) with the prediction (red line) based on the excited state absorption measurements and three-level model .....61
6.1.	Basic principle of 2PA-based volumetric optical disk. $T$ , $d_h$ , $d_v$ are the thickness, horizontal and vertical sizes of the voxel, respectively, $h_h$ is the distance between two neighboring voxels in a layer, $h_v$ is the distance between layers. (a) Writing. Upon 2PA excitation, form A switches to form B, which is separated by energy barrier (insert). (b) Readout. 2PA of form B results in its fluorescence that is collected by the focusing lens. Dichroic mirror (DM) reflects the fluorescence to a photo detector (PD).....67
6.2.	SNR versus SBR diagrams obtained for an “ideal” molecule as a result of model simulations for a set of parameters described in appendix E and presented in table D.10. Each marked data point represents a particular integer value of detuning, $\nu_{0I}-\nu$ , with the corresponding value in $\text{cm}^{-1}$ shown on top of the curve. The desired parameter space, where $\text{SNR}>4$ and $\text{SBR}>4$ , is shown as non-shaded area. Figure 6.2a shows a family of curves with different peak 2PA cross section values, $\sigma_2(\nu_{0I})$ with fixed temperature (300 K) and peak laser intensity ( $3\times 10^{29} \text{ photons}\cdot\text{cm}^{-2}\cdot\text{s}^{-1}$ ). In figure 6.2b we vary laser intensity, while the temperature (300 K) and the peak 2PA cross section ( $10^4 \text{ GM}$ ) are fixed. Figure 6.2c presents the effect of temperature variation with constant cross section ( $10^4 \text{ GM}$ ) and intensity ( $I=10^{29} \text{ photons}\cdot\text{cm}^{-2}\cdot\text{s}^{-1}$ ) .....73

## LIST OF FIGURES – CONTINUED

Figure	Page
6.3. 1PA (solid line) and 2PA (symbols) spectra of $\text{Pc}_3\text{Nc}$ . 1PA spectrum is measured in methylene chloride at room temperature. The open squares present 2PA data obtained at room temperature in methylene chloride, open circles – at 77 K in polyethylene film, and the asterisk corresponds to the datum obtained at 77 K from the rate of photochemical transformation. Dashed line is the best fit of experimental 2PA spectrum to the Voigt function with central frequency fixed at $13330\text{ cm}^{-1}$ . Inset shows semi-logarithmic presentation of the spectra.....	77
6.4. Dependence of fluorescence signal intensity ( $I$ ) on excitation laser pulse energy ( $P$ ) at different laser wavelengths, presented in double logarithmic scale. Solid lines are the best fits of data to power dependence, $I = P^a$ . Inset shows the detuning values and the corresponding power exponent for each detuning.....	78
6.5. SNR versus SBR diagram, obtained as a result of numerical simulations for $\text{Pc}_3\text{Nc}$ at $T = 77\text{ K}$ . Each curve corresponds to a particular laser peak intensity, indicated on top of the curve. Different symbols on the curves label the particular values of frequency detuning from 1PA maximum. Shaded regions correspond to forbidden values of $\text{SNR} < 4$ or/and $\text{SBR} < 4$ . Other parameters used in simulation are summarized in table D.10, third column.....	81
6.6. Chemical structures of the molecules .....	82
6.7. Possible isomers of Pd-substituted version of molecule 4.....	83
6.8. 1PA (lines) and 2PA (symbols) spectra of phthalocyanines 1 ( $\text{Pc}_3\text{Nc}$ ) and 2 in carbon tetrachloride at room temperature. The two near-IR peaks in 1PA spectra correspond to the $Q_x$ and $Q_y$ bands.....	85
6.9. 1PA (lines) and 2PA (symbols) spectra of isomers of phthalocyanines 3 and 4 in carbon tetrachloride at room temperature. The two near-IR peaks in 1PA spectrum correspond to the $Q_x$ and $Q_y$ bands .....	86
6.10. 1PA (lines) and 2PA (symbols) spectra of isomers of phthalocyanines 5 and 6 in carbon tetrachloride at room temperature. The two near-IR peaks in 1PA spectrum correspond to the $Q_x$ and $Q_y$ bands .....	87

## LIST OF FIGURES – CONTINUED

Figure	Page
6.11. Transformation of tautomer $T_1$ into tautomer $T_2$ in phthalocyanines 1 and 3 in polyethylene film at 77K. Main figure – absorption spectra at different illumination times at constant laser intensity. Insert shows the increase of the $T_2$ peak absorption with irradiation dose.....	94
6.12. Transformation of tautomer $T_1$ into tautomer $T_2$ in phthalocyanines 4 and 5 in polyethylene film at 77K. Main figure – absorption spectra at different illumination times at constant laser intensity. Insert shows the increase of the $T_2$ peak absorption with irradiation dose.....	95
7.1. (a) Experimental setup for imaging of biological phantoms with Styryl-9M: (1) Laser beam entrance, (2) focusing lens, (3) sample cuvette (4) 75 mm f/1.4 objective lens, (5) variable wavelength filter, (6) – CCD camera, (7) He-Ne laser. (b) Sample cuvette with a phantom. (c) Field of view of the CCD camera with a 75-mm objective lens .....	102
7.2. 2PA spectra of Styryl-9M in tissue phantoms with no cells (black squares), with normal cells (red circles), and with cancer cells (green triangles), all in relative units.....	105
7.3. 2PA spectra of Styryl-9M in water, “blue” form (blue +), in ethanol, “red” form, (pink x), and their linear superpositions with different weights (described in the inset), corresponding to a phantom without cells (dark blue squares), a phantom with normal cells (purple circles) and a phantom with cancer cells (brown triangles) .....	106
7.4. First two steps of the optical imaging technique for cancer localization (black line – integral along horizontal direction of the CCD sensor, red line – integral along vertical direction of the CCD sensor) .....	109
7.5. Third step of the optical imaging technique used for detecting cancer cells: the curves show the integral fluorescence signal at two excitation wavelengths along the vertical direction of the CCD sensor with subtracted background .....	110

## LIST OF FIGURES – CONTINUED

Figure	Page
7.6.	Dependence of the $F(1100)/F(1200)$ fluorescence ratio on the laser propagation distance inside the phantom: black curve corresponds to the uniform phantom with normal cells; red curve corresponds to the uniform phantom with +SA cancer cells; green curve corresponds to the phantom with normal cells and introduced +SA cancer colony; blue curve corresponds to the phantom with normal cells and introduced 4T1 cancer colony; cyan curve corresponds to the phantom with normal cells and introduced MB231 cancer colony. Distance is measured from the middle point of the cuvette containing phantom. Vertical dashed lines show approximate location of the cancer colony introduced in the phantoms .....112
7.7.	Determination of the sensitivity of cancer cell localization based on the phantoms containing a known number of cancer cells: black squares – NIHOVCAR3 cancer line, and red circles – +SA cancer line .....115
7.8.	Determination of the binding energy of Styryl-9M to cancer cells of the +SA cancer line: Parameters obtained from the expression (7.4) are: $A = 1.05$ , $B = 1.85$ ; The best fit gives $C = 0.008$ (solid green line), and the corresponding fitting errors give: $C = 0.004$ (dashed blue line), and $C = 0.016$ (dashed pink line).....118
8.1.	Flowchart showing typical approach to independently justify the 2PA cross section of a new compound .....124
A.1.	Numerical simulations of 2PA in two-level system. Comparison of population of excited state for molecule with zero difference in dipole moments of ground and excited state $\Delta\vec{\mu}_{01}$ (dashed line) and for molecule with $\Delta\vec{\mu}_{01} = 10D$ difference (solid line). 2PA peak is well visible for the second case. On the inserts are: a) the comparison of the difference in excited state population due to 2PA ( $\Delta\rho_{11}$ ) vs. square of intensity, showing saturation effect; and b) the comparison of line shape of 1PA and 2PA peaks of excited state population and Lorentz function. The parameters were used as follow: $T_1=1600$ fs, $T_2=50$ fs, pulse duration=100 fs, $\nu_{01}=25000$ $\text{cm}^{-1}$ , $\mu_{01}=10$ D. The detuning frequency is a difference between transition frequencies of the laser and absorption resonance .....151
B.1.	Solvatochromic (Stokes) shifts in a series of solutions for compounds 1, 4, 5, and 10. The solvents are: n-octane, butyl ether, isobutyl isobutyrate, isobutyl acetate, 2-chlorobutane, and pentanal. Solid lines show linear fits ....157



## LIST OF FIGURES – CONTINUED

Figure	Page
B.2. Fluorescence decay curves for compounds 1, 4, 6, and 9: dashed lines show single exponential fits to extract fluorescence lifetimes.....	160
C.1. An example of autocorrelation function (black) and its Gaussian fit (red) for $\lambda=1160$ nm .....	167
C.2. OPA pulse duration in 550-1600 nm wavelength range (a) and comparison of OPA pulse duration of signal and its second harmonic (b) .....	168
C.3. CCD picture of the beam profile (a), integral of the beam intensity along horizontal axis (b), and integral of the beam intensity along vertical axis (c); pictures are shown for $\lambda=1160$ nm. Gaussian fits to beam profiles are also shown (red lines) .....	169
C.4. Horizontal (squares), vertical (circles) beam diameter in 550-1600 nm range, and a model of a wavelength dependence of the constant beam diameter due to its propagation divergence .....	170
C.5. Chemical structures of 16 standard reference compounds .....	175
C.6. Two-photon absorption (symbols) and one-photon absorption (solid lines) spectra of the <i>ClAnt</i> .....	176
C.7. Two-photon absorption (symbols) and one-photon absorption (solid lines) spectra of the <i>diClAnt</i> .....	176
C.8. Two-photon absorption (symbols) and one-photon absorption (solid lines) spectra of the <i>BDPAS</i> .....	177
C.9. Two-photon absorption (symbols) and one-photon absorption (solid lines) spectra of the <i>Perylene</i> .....	177
C.10. Two-photon absorption (symbols) and one-photon absorption (solid lines) spectra of the <i>Coum540</i> .....	178
C.11. Two-photon absorption (symbols) and one-photon absorption (solid lines) spectra of the <i>Coun485</i> .....	178
C.12. Two-photon absorption (symbols) and one-photon absorption (solid lines) spectra of the <i>LY</i> .....	179

## LIST OF FIGURES – CONTINUED

Figure	Page
C.13. Two-photon absorption (symbols) and one-photon absorption (solid lines) spectra of the <i>TPP</i> .....	179
C.14. Two-photon absorption (symbols) and one-photon absorption (solid lines) spectra of the <i>AlPc</i> .....	180
C.15. Two-photon absorption (symbols) and one-photon absorption (solid lines) spectra of the <i>tBuPcZn</i> .....	180
C.16. Two-photon absorption (symbols) and one-photon absorption (solid lines) spectra of the <i>tPhTPcZn</i> .....	181
C.17. Two-photon absorption (symbols) and one-photon absorption (solid lines) spectra of the <i>SiNc</i> .....	181
C.18. Two-photon absorption (symbols) and one-photon absorption (solid lines) spectra of the <i>Styryl9M</i> .....	182
E.1. Long-wavelength absorption of $\text{Pc}_3\text{Nc}$ in semi-logarithmic scale. Absorption spectrum in methylene chloride at room temperature is shown by bold solid black line and its best fit to expression (E.13) by dashed blue line. Green line shows normalized and corrected fluorescence spectrum, measured at 77 K. Dash-dotted color lines show fluorescence spectra weighted with Boltzmann factor, according to (E.15) at different temperatures .....	213
E.2. Spectral changes observed upon 2PA-induced transformation of tautomer form $\text{T}_1$ into form $\text{T}_2$ in $\text{Pc}_3\text{Nc}$ in polyethylene film at 77K. The sample was irradiated with 783-nm femtosecond laser pulses of constant intensity and different exposure times. Laser spectrum is indicated with dotted line. Laser intensity was $4 \times 10^{27} \text{ photons} \cdot \text{s}^{-1} \cdot \text{cm}^{-2}$ . Vertical arrows show the spectral changes during irradiation. Insert shows the structure of the two tautomers .....	215
E.3. Kinetics of 2PA-induced $\text{T}_1 \rightarrow \text{T}_2$ phototransformation at two different laser intensities. Filled circles correspond to peak intensity of $4 \times 10^{27} \text{ photons} \cdot \text{s}^{-1} \cdot \text{cm}^{-2}$ and open circles – to $8 \times 10^{27} \text{ photons} \cdot \text{s}^{-1} \cdot \text{cm}^{-2}$ . The continuous lines represent the best fits with exponential function .....	216
F.1. Two-photon absorption (symbols), one-photon absorption (solid line), and fluorescence (dashed line) of Styryl-9M in chloroform .....	218

## LIST OF FIGURES – CONTINUED

Figure	Page
F.2. Solvatochromic shifts of Styryl-9M in a series of solvents .....	221
F.3. Dependence of the absorption of Styryl-9M on the pH-level of the solvent .....	222
F.4. Dependence of the fluorescence of Styryl-9M on the pH-level of the solvent .....	223
F.5. Dependence of the ratio of the intensity of the fluorescence peaks of Styryl-9M on pH of DI water .....	223
F.6. Two-photon absorption (symbols), and one-photon absorption (lines) of Styryl-9M in a series of solvents with different polarity .....	225
F.7. (a) 1PA-induced fluorescence of Styryl-9M excited at several visible wavelengths in a set of solvents with different polarity (b) Position of the absorption maximum of Styryl-9M versus solvent polarity function. Linear fit is shown. The solvents used are: 1 – 2-chlorobutane; 2 – dichloromethane; 3 – pentanal; 4 – isopropanol; 5 – ethylene glycol; 6 – acetone; 7 – ethanol; 8 – mixture of 70% ethanol + 30% DI water; 9 – mixture of 50% ethanol + 50% DI water; 10 – acetonitrile; 11 – mixture of 30% ethanol + 70% DI water .....	227
F.8. (a) 2PA-induced fluorescence of Styryl-9M excited at two infrared wavelengths in a set of solvents with different polarity. (b) Ratio of the fluorescence intensity of Styryl-9M excited via 2PA at 900 nm and 1000 nm as a function of solvent polarity function .....	229
F.9. Dependence of the ratio of the fluorescence intensity of Styryl-9M excited via 2PA at 950 nm and 1100 nm on the content of biological phantom .....	231
F.10. Cancer cells detection using the ratio of fluorescence of Styryl-9M excited at 1100 and 1200 nm. Phantoms with cancer cells can be differentiated from the phantoms with normal cells and phantoms without any cells. Aggressive cancer cell line 4T1 shows an artifact due to collagen gel contraction several hours after sample preparation .....	233
G.1. Schematic of the amplifier for Si/InGaAs sandwich detector (ThorLabs DSD2) .....	237
G.2. Schematic of the variable voltage power supply for magnetic stirring of the sample .....	238

## LIST OF FIGURES – CONTINUED

Figure	Page
G.3a. First 8 outputs of the 16-motor controller.....	239
G.3b. Last 8 outputs of the 16-motor controller .....	240
G.3c. Power control and address demultiplexing of the 16-motor controller .....	240
G.4. Front panel of the VI for manual alignment of the computer-controlled mirrors.....	241
G.5. Block diagram of the VI for manual alignment of the computer-controlled mirrors.....	241
G.6. Front panel of the VI for the acquisition of the ESA spectra.....	242
G.7. Block diagram of the VI for the acquisition of the ESA spectra .....	243

## ABSTRACT

This dissertation explores quantitative two-photon absorption spectroscopy to relate molecular structure with optical properties of organic chromophores.

The dissertation describes an advanced fluorescence-based technique for reliable measurements of the two-photon spectra and cross sections. To facilitate the measurements it establishes a set of reference compounds measured with a 15% absolute accuracy covering a broad range of excitation and fluorescence wavelengths.

The dissertation shows that in many cases the few-essential-levels model can be successfully applied for the description and interpretation of two-photon absorption spectra and cross sections, at least for the low-energy transitions.

The dissertation presents examples of applications of two-photon absorption for volumetric optical storage and cancer tumor detection. It describes the basic principles of the two-photon absorption-based optical memory and limitations imposed on two-photon sensitivity of photochromic materials by a necessity of fast access to the data. It also proposes a novel technique for sensitive detection of cancer cells by using two-photon excitation of near-IR fluorescence of a commercial dye and discusses the mechanisms responsible for differentiation between the normal and the cancer cells.

The methods described in this dissertation can be applied to understanding the relations between structure and two-photon absorption strength of individual transitions of organic and biological chromophores, which can be used for design of new materials, maximally adapted for particular applications.

## 1. INTRODUCTION

### Introduction to Research Topic

Simultaneous absorption of two photons or two-photon absorption (2PA) was first predicted theoretically by Maria Göppert-Mayer [1] in 1931. This effect was observed experimentally in the early 1960's [2]. Since then 2PA has become a valuable practical tool especially in high resolution microscopy [3-12], and also in many other applications, such as ultrafast optical power limiting [13-26], deep tissue photodynamic therapy (PDT) [27-38], volumetric 3D optical memory [39-59], 3D microfabrication [60-69], and ultrafast pulse characterization [70-74]. Shortly after the first experimental observation, 2PA also was engaged as a spectroscopic tool, suitable to study transitions to states whose one-photon transitions are prohibited by parity selection rules [75-83].

Nowadays, about 50 years later, 2PA of organic chromophores continues to be a rapidly growing area of research, especially since tunable femtosecond lasers have become available providing a source of high intensity light ideally suited for the observation and study of 2PA.

This dissertation utilizes a modern tunable femtosecond laser for quantitative 2PA spectroscopy of organic chromophores and illustrates applications of 2PA in volumetric optical memory and biological imaging.

The efficiency of 2PA varies with the wavelength and is characteristic to a particular chromophore, in a similar way as for conventional linear absorption spectra. However, the rate of a 2PA transition increases as a square of the number of photons incident on the sample per unit area per unit time. This kind of nonlinear intensity

dependence, also known as a quadratic law, is crucial for most practical applications of 2PA. For example, when the light beam is tightly focused, then 2PA occurs mostly at the focal volume (voxel), i.e. where the intensity is the highest. This inherent 3D focusing property serves as a basis for greatly increased spatial resolution of 2PA-induced fluorescence microscopy as well as for high capacity volumetric data storage.

The same way conventional spectroscopy studies wavelength dependence of linear (one-photon) absorption, 2PA spectroscopy studies the wavelength dependence of 2PA. The efficiency of a 2PA process is characterized by the 2PA cross section,  $\sigma_2$ , which is usually expressed in terms of Göppert-Mayer units ( $1 \text{ GM} = 10^{-50} \text{ cm}^4 \cdot \text{s} \cdot \text{photon}^{-1}$ ). Because typical peak 2PA cross section values are rather small ( $\sigma_2 \sim 1\text{--}100 \text{ GM}$ ) and also because measuring the 2PA spectra requires high peak intensity laser pulses (typical peak intensity  $\sim \text{GW cm}^{-2}$  for 100 fs duration pulses) and very sensitive fluorescence photon detectors, measuring  $\sigma_2$  with sufficient accuracy has remained a challenging task. The situation is further aggravated by the fact that the 2PA spectra of many organic systems need to be measured over a broad range of wavelengths, usually from visible to near-IR. Due to these daunting technical complications, even though scientific literature is full of 2PA data, reliable measurements of 2PA spectra are hard to come by, and the scientific community has come to agreement that developing high accuracy two-photon absorption spectroscopy is not only desirable but urgently needed.

A tested approach to this problem, employed in the dissertation, is by establishing calibrated absolute reference standards for 2PA. Developing such standards, even though conceptually straightforward, is a tedious procedure since it implies, among other

requirements, very careful characterizations of the laser pulses and other experimental conditions, such as the spatial and temporal profiles of the excitation beam, efficiency of the fluorescence photon collection, etc. Once this work is accomplished, one can relatively easily correct for experimental uncertainty in the measurement of 2PA of new or previously uncharacterized chromophores. This dissertation describes experiments where we collect 2PA data for a set of reference dyes, measured with 15% absolute accuracy, whose spectra cover a broad range of excitation (550–1600 nm) and fluorescence (400–900 nm) wavelengths.

As in any kind of advanced spectroscopy, extracting useful information from the observed features requires correct interpretation of measured 2PA spectra. Quantitative 2PA spectroscopy is used for establishing structure-properties relations for various organic and inorganic chromophores and is a key for designing of new efficient 2PA materials. The dissertation explores avenues for quantitative interpretation of the 2PA spectra, based on the so-called few-essential-levels model. Even though higher-order perturbation theory involves summation of the transition amplitudes to all possible intermediate states, under certain conditions, the 2PA cross sections of the low-energy excited states may be well described to be due to transitions from the ground state directly to the final state without interaction with any intermediate energy states (two-level model) or with the interaction with only one or two intermediate states (three- and more level model). In this dissertation we investigate when such a simplified approach may be applied.



The dissertation also presents two examples of application of quantitative 2PA spectroscopy to practical problems in optical data storage and medical imaging. The first example presents a detailed study of the requirements imposed on 2PA chromophores for a fast access volumetric optical memory. In the second example we use 2PA spectroscopy for detection and precise localization of a few cancer cells surrounded by a large number of normal healthy cells in a tissue phantom, simulating optical properties of opaque tissues.

### Overview of Dissertation

The rest of the dissertation is organized as follows:

Chapter 2 introduces the main concepts of two-photon absorption. It shows how the strength of 2PA can be expressed in terms of molecular parameters, such as dipole moments and line shape functions.

Chapter 3 briefly describes experimental setups used through the entire dissertation for nonlinear measurements. It also introduces an idea of quantitative 2PA spectroscopy.

Chapter 4 presents a set of standard reference dyes whose 2PA spectra are measured with high resolution and low noise. The dyes are suitable for measurements of 2PA spectra and cross sections of unknown compounds using the relative fluorescence-based method. The results presented in this chapter are published (N.S. Makarov, M. Drobizhev, A. Rebane, "Two-photon absorption standards in the 550-1600 nm excitation wavelength range", *Opt. Expr.*, **16**, 4029-4047 (2008)).

Chapter 5 presents the systematic study of applicability of the few-essential-levels model for describing 2PA spectra and cross sections. The chapter shows that the two-

photon cross section of a dipolar molecule, i.e. molecule possessing a non-zero permanent dipole moment difference between the ground and excited states, at least in the peak of the lowest energy dipole-allowed transition, can be predicted with 20% accuracy solely based on its one-photon absorption (1PA) properties. For certain 1PA-forbidden transitions, the peak 2PA cross sections and the measured spectra can be predicted using a three-level model. The results presented in the first part of the chapter are published (A. Rebane, N.S. Makarov, M. Drobizhev, B. Spangler, E.S. Tarter, B.D. Reeves, C.W. Spangler, F. Meng, Z. Suo, “Quantitative prediction of two-photon absorption cross section based on linear spectroscopic properties”, *J. Phys. Chem. C*, **112**, 7997-8004 (2008)) and results from the second part of the chapter will be published shortly (to be submitted).

Chapter 6 addresses the question of what molecular parameters may limit the access speed of a proposed 2PA-based photochromic 3D optical disk. We formulate the minimum requirements on the 2PA cross section of the chromophores from the viewpoint of a tradeoff between the Signal-to-Noise Ratio (SNR) and Signal-to-Background Ratio (SBR). Experimental study of the efficient nonsymmetrical phthalocyanines shows that even though some existing chromophores may satisfy the key requirements, further substantial improvement of the two-photon properties of chromophores is required in order to make high-speed, high-capacity, rewritable, volumetric optical storage practical. The results presented in the chapter are published (N.S. Makarov, A. Rebane, M. Drobizhev, H. Wolleb, H. Spahni, “Optimizing two-photon absorption for volumetric optical data storage”, *J. Opt. Soc. Am. B*, **24**, 1874-1885 (2007)).

Chapter 7 shows how 2PA excitation can be used in biology for imaging and localization of malignant cancer cells. It presents a novel way of optical detection of malignant cancer cell colonies by using multi-wavelength 2PA-excited fluorescence of the commercial dye Styryl-9M. The experiments show that the 2PA-excited fluorescence from colonies embedded in a phantom simulating human and mouse mammary tissue provides information on the type of cancer cells as well as on the composition of the phantom. Using the ratio between the fluorescence excited at 1100 and 1200 nm, it is possible to distinguish between samples containing no cell colonies at all, samples with colonies of normal cells and samples with a few cancer cells surrounded by a large number of normal cells. The results from the chapter will be published shortly (to be submitted).

Chapter 8 presents a summary of the work done in the dissertation together with conclusions.

Because the dissertation touches upon numerous topics, a substantial amount of information, especially details of experiments and theory, are placed in attached Appendices.

Appendix A derives a quantum-mechanical expression for the 2PA cross section in the case of a two-level model.

Appendix B describes linear measurements of the molecular parameters, such as extinction coefficients, fluorescence quantum yields, and permanent dipole moments, used for quantitative prediction of 2PA cross sections in two- and three-level models.

Appendix C describes experimental details of the measurements of the 2PA reference standards and the proposed method for relative measurements using the standards as well as the 2PA spectra of the standard reference dyes.

Appendix D contains data tables with the measured and calculated parameters described in the main text.

Appendix E presents details of the modeling of Signal-to-Noise and Signal-to-Background ratios relevant for volumetric 2PA optical memory, discussed in chapter 6.

Appendix F presents details on linear and 2PA spectroscopy of Styryl-9M that is used in the cancer imaging experiments in chapter 7.

Appendix G contains further details on the transient absorption spectrometer, such as schematics and screenshots of the LabView Virtual Instruments.

## 2. THE MAIN CONCEPTS OF TWO-PHOTON ABSORPTION

This chapter introduces the main concepts of 2PA and shows how the strength of the 2PA can be expressed in terms of molecular parameters. It introduces expressions that are used later in the dissertation for the description of the 2PA in terms of few-essential-levels model. The chapter relies on the treatment of 2PA introduced previously in the dissertation of A. Karotki [34].

### One-Photon Absorption: Introduction of Dipole Moments

Let us consider a molecule illuminated by monochromatic light of frequency  $\nu$ . To the first order, the interaction of the molecule with the light results in linear absorption, where the differential one-photon absorption (1PA) cross section is described by the following expression [84]:

$$\sigma(\nu) = \frac{\pi e^2}{m_e c} \sum_j f_{0j} g_j(\nu), \quad (2.1)$$

where  $e$  is the charge of the electron,  $m_e$  is the mass of the electron,  $c$  is the speed of light, the  $g_j(\nu)$  are normalized line shape functions of the  $j$ -th electronic transition ( $\int_{\nu} g_j(\nu) d\nu = 1$ ), and the  $f_{0j}$  are oscillator strengths for the electronic transitions from the ground state  $0$  to the  $j$ -th excited state. In organic molecules it is usually possible to ascribe separate peaks of the 1PA spectrum to individual electronic transitions. In this case the oscillator strength can be defined similarly to one in atomic systems [84]:

$$f_{0j} = \frac{2m_e}{3\hbar^2} (E_j - E_0) \left| \langle 0 | \hat{r} | j \rangle \right|^2. \quad (2.2)$$

Here the  $\Delta E_j = E_j - E_0$  are the energies of electronic transitions from the ground state  $0$  to the  $j$ -th excited state,  $\hat{r}$  is the position operator,  $\langle 0|$  is the electronic wavefunction of the ground state,  $|j\rangle$  is the electronic wavefunction of the  $j$ -th excited state, and  $\hbar$  is the Planck constant. In the expression (2.1) the line shapes  $g_j(\nu)$  take into account line broadening due to various effects, such as vibronic interactions and thermal broadening due to dephasing. The oscillator strength,  $f_{0j}$ , represents integral strength of a particular electronic transition.

Another useful molecular parameter that relates to the experiments described in this dissertation is transition dipole moment,

$$\vec{\mu}_{ij} = \langle i | e\hat{r} | j \rangle, \quad (2.3)$$

which describes a transition between any possible energy states  $|i\rangle$  and  $|j\rangle$  of the molecule, including the ground state and the final state. One can distinguish between the transition dipole moments from the ground to the excited states and the transition dipole moments between the excited states. The first can be measured from the 1PA spectra, and the last can be measured from transient absorption spectra, provided that the initial excited state is populated more than the final excited state.

The 1PA can also be characterized in terms of an extinction coefficient,  $\varepsilon$ , where  $\varepsilon \ln 10 = \sigma N_A$ , and  $N_A$  is the Avogadro's number.

If the wavefunctions  $\langle i|$  and  $|j\rangle$  represent the same energy state, then the expression (2.3) defines permanent dipole moment. If the molecule lacks a center of symmetry, then the permanent dipole moments are generally not zero, and may have

different values in different states. The dipole moment in the excited state usually differs from that in the ground state. To describe this property one usually introduces the permanent dipole moment difference between the ground and excited states,  $\Delta\vec{\mu}_{0j} = \vec{\mu}_{00} - \vec{\mu}_{jj}$ . The permanent dipole moment difference is usually related to the Stark effect, where the transition frequencies of the molecule shift proportional to applied external electric field.

The transition and permanent dipole moments are essential molecular parameters that describe properties of 1PA and 2PA.

### Introduction of Two-Photon Absorption

If the photon energy is less than the energy difference between the ground state and the first excited state, then the probability of 1PA drops significantly, if the difference in the energies is larger than several times the width of the line shape,  $g_1(\nu)$ . Simultaneous absorption of two photons can excite the molecule even when 1PA vanishes, provided that the sum of the energies of the absorbed photons falls within the width of a two-photon transition. The absorption of two-photons is simultaneous in the sense that there is no population created in intermediate energy levels.

In the dissertation we consider the simplest case of 2PA, when the frequencies of the two photons are equal,  $\nu_1 = \nu_2 = \nu$ . The approximate timescale for such 2PA is set by inverse of the frequency detuning with respect to the nearest energy level,  $\tau \sim 1/(\nu_{01} - \nu)$ , where  $\nu_{01}$  is the 1PA transition frequency. The probability of 2PA follows quadratic power law,

$$P \propto I^2, \quad (2.4)$$

where  $I$  is the flux density of the photons.

The strength of 2PA is described in terms of 2PA cross sections,  $\sigma_2$ , which are often presented in GM units ( $1 \text{ GM} = 10^{-50} \text{ cm}^4 \cdot \text{s} \cdot \text{photon}^{-1}$ ). Typical chromophores have cross section values  $\sigma_2 \sim 1-100 \text{ GM}$  and require photon flux,  $I \sim 10^{10} - 10^{12} \text{ W/cm}^2$  for excitation comparable in efficiency to 1PA excitation typical to linear spectroscopy. Such high intensities can be readily attainable with the help of femtosecond lasers.

If all the energy levels, transition dipole moments, permanent dipole moments, and line shape functions of the molecule are known, then one can calculate 2PA strength of each transition. Second-order perturbation theory gives the following expression for the 2PA cross section for a transition from the initial state  $|i\rangle$  to the final state  $|j\rangle$  [34]:

$$\sigma_2^{(i \rightarrow j)}(\nu) = 2 \frac{(2\pi f)^4 \nu^2}{(nhc)^2} \left\langle \left| \sum_m \frac{(\vec{\mu}_{im} \cdot \vec{e})(\vec{\mu}_{mj} \cdot \vec{e})}{(\nu_{im} - \nu)} \right|^2 \right\rangle_{\bar{\Omega}} g_j(2\nu), \quad (2.5)$$

where  $\nu_{ij}$  is the transition frequency,  $n$  is the solvent refractive index,  $h$  is the Planck

constant,  $\vec{e}$  is the unit vector parallel to the optical electric field ( $\vec{E} = \vec{e}E$ ),  $f$  is the local

field factor ( $f_L = \frac{n^2 + 2}{3}$  for the Lorentz field factor, and  $f_o = \frac{3n^2}{2n^2 + 1}$  for the Onsager

field factor). The summation is made over all states  $m$  of the molecule, including the

initial and the final states, and  $\langle \rangle_{\bar{\Omega}}$  represents isotropic averaging over all possible

orientations of the molecules relative to excitation optical electric field.



Note that the 2PA cross section for a transition from the initial state  $|i\rangle$  to the final state  $|j\rangle$  depends only on the line shape function of the final state, and does not depend on the line shapes of the initial or intermediate states.

### Quantitative Description of Two-Photon Absorption with a Few-Essential-Levels Model

The sum-over-states expression (2.5) includes values of transition dipole moments, permanent dipole moments, and transition frequencies for all excited electronic states. In practice, only a small fraction of this information is available from experiment; higher-energy states are particularly difficult to fully characterize. Nevertheless, in many practical situations (especially if the 2PA cross section is relatively large,  $\sigma_2 > 100$  GM) a useful quantitative description of the experimentally measured 2PA cross sections and 2PA spectra may be achieved by considering only a few lowest energy states. In this case, most if not all needed parameters can be determined or estimated from independent linear measurements and excited state pump-probe spectroscopy. Figure 2.1 illustrates the energy levels and associated molecular parameters for four versions of few-essential energy levels model.

The 2PA cross section of a two-level system can be obtained from a perturbation solution of the density matrix equations of motion, describing the interaction of the two-level molecule with the monochromatic electric field, using the following expression (for details of derivation see appendix A) [85]:

$$\sigma_2^{two-state} = C_1 (1 + 2 \cos^2 \beta) |\bar{\mu}_{01}|^2 |\Delta \bar{\mu}_{01}|^2 g(2\nu), \quad (2.6)$$

where  $\vec{\mu}_{01}$  is the transition dipole moment vector between the ground state  $0$  and the final excited state  $1$ ,  $\Delta\vec{\mu}_{01}$  is the difference between the permanent dipole moments in the excited and ground-state,  $\beta$  is the angle between the above two vectors,  $g(2\nu)$  is the normalized line shape function ( $\int_{\nu} g(2\nu)d\nu = 1$ ), and  $C_1$  is the proportionality constant:

$$C_1 = \frac{2}{15} \frac{(2\pi f)^4}{(nhc)^2}. \quad (2.7)$$

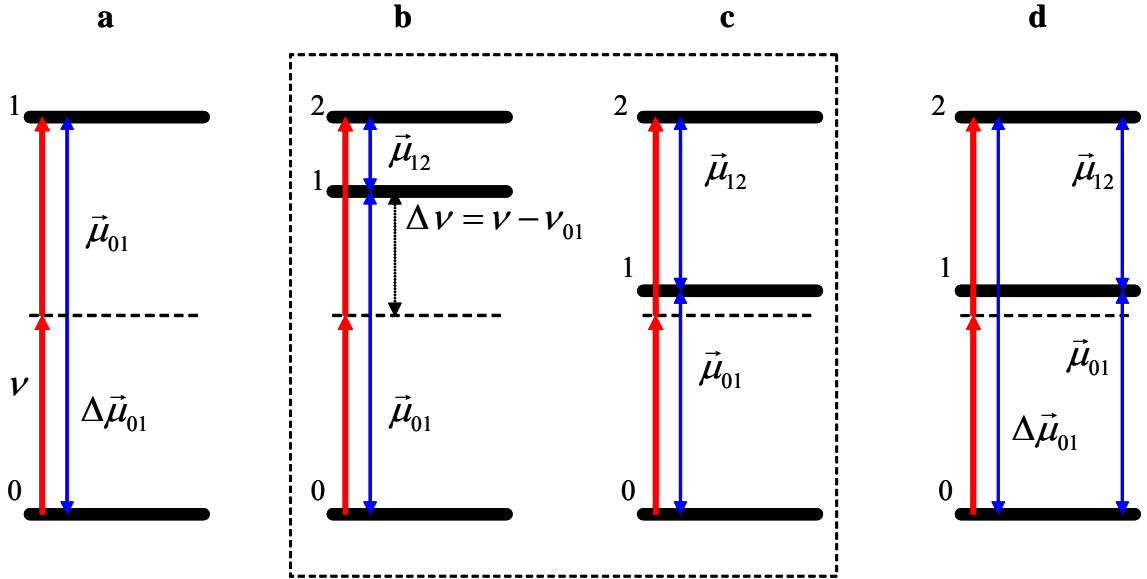


Figure 2.1. Four versions of few-essential energy levels model: (a) Two-level model for non-centrosymmetric chromophore with non-zero permanent dipole moment difference,  $\Delta\vec{\mu}_{01} = \vec{\mu}_{00} - \vec{\mu}_{11}$ ; (b) Three-level system, where the laser frequency  $\nu$  is far detuned from the frequency of transition,  $\nu_{01}$ , between the ground state  $0$  and intermediate state  $1$ , and  $\Delta\vec{\mu}_{01} = 0$  and resonance enhancement has a relatively small effect on the 2PA; (c) Three-level system, where the transition frequency  $\nu_{01}$  is only slightly higher than  $\nu$  and  $\Delta\vec{\mu}_{01} = 0$  and resonance enhancement has a large effect; (d) Three-level system with  $\Delta\vec{\mu}_{01} \neq 0$ : Quantum interference may arise between the two pathways, (a) and (b) or (c), leading to further enhancement (constructive interference) or suppression (destructive interference) of the 2PA efficiency

In order to compare measured 2PA cross sections with the predictions by expression (2.6) one needs to know the transition dipole moment and the permanent dipole moment difference between the ground state and the final excited state, the angle between them, and the line shape of the transition. The dipole moments and the line shape can be measured using linear techniques. The angle between the dipole moments can be determined by comparing 2PA-induced fluorescence excited by linearly and circularly polarized light or guessed based on the chemical structure of the molecule.

In the case of a three-level system with a zero permanent dipole moment difference, the corresponding relation reads [59]:

$$\sigma_2^{three-state} = C_1(1 + 2\cos^2 \alpha) \frac{|\vec{\mu}_{01}|^2 |\vec{\mu}_{12}|^2}{(1 - \nu_{01}/\nu)^2} g(2\nu), \quad (2.8)$$

where  $\vec{\mu}_{12}$  is the transition dipole moment between the intermediate state 1 and the final state, 2, and  $\alpha$  is the angle between the two transition dipole moment vectors. The proportionality constant is again given by (2.7).

Comparison of the measured 2PA cross sections with the predictions by expression (2.8) relies on knowledge of the transition dipole moments, the angle between them, the line shape of the transition, and the detuning factor,  $1 - \nu_{01}/\nu$ . The transition dipole moment between the excited states can be obtained from the transient absorption spectrum.

Here it is often useful to distinguish between two cases: If the laser frequency is far from the intermediate transition frequency  $\nu_{01}$  (figure 2.1b) but still larger than  $\nu_{01}/2$ , then the resonance denominator in expression (2.8) tends to  $1/4$ , and we say that

resonance enhancement is not a significant factor. Alternatively, if the detuning is small (figure 2.1c), then the denominator in (2.8) becomes much smaller than unity, and we say that the 2PA cross section is enhanced by the intermediate resonance. This effect, is called resonance enhancement and is well-known for multiphoton processes in atomic systems, where the transitions are relatively narrow [86]. In organic molecules with broad transitions the resonance enhancement effect was shown only recently [87].

In case of the three-level system with  $\Delta\vec{\mu}_{01} \neq 0$ , a quantum interference may arise between the two pathways, (a) and (b) or (c), leading to further enhancement (constructive interference) or suppression (destructive interference) of the 2PA efficiency. The character of the interference depends on the relative phase between the dipole moments. This topic requires further study and is out of scope of the dissertation.

Below we will study in detail under which conditions we can use the expressions (2.6)–(2.8) for quantitative description of 2PA. Here let us make some order-of-magnitude estimations by supposing that all molecular dipoles,  $\Delta\vec{\mu}_{01}$ ,  $\vec{\mu}_{01}$ ,  $\vec{\mu}_{12}$  are parallel and amount to a reasonably large value, 15 Debye, and that the 2PA linewidth is  $\sim 1000 \text{ cm}^{-1}$ . If there is no intermediate state, then the maximum two-level 2PA cross section is,  $\sigma_2 \sim 2000 \text{ GM}$ . If an intermediate state is present, but the detuning factor is large, then the maximum 2PA cross section is  $\sigma_2 \sim 6000 \text{ GM}$ . Much higher values,  $10^4$ – $10^5 \text{ GM}$ , can be achieved with the help of resonance enhancement; however, the effect is restricted to a narrow frequency interval, which typically varies from  $\sim 500 \text{ cm}^{-1}$  for some tetrapyrroles [88] up to  $\sim 2000 \text{ cm}^{-1}$  for molecules with pronounced charge-transfer character, such as substituted diphenylaminostilbenes [85].

As an alternative to the perturbation approach, one can calculate the 2PA probability by solving density matrix equations of motion (e.g. by numerical methods). Such an approach, although more complicated, offers a possibility of accounting for the saturation, pulse propagation, non-Lorentzian line shape, and other effects not included in the current perturbation approach [89]. An example of this approach is shown in appendix A.

### 3. DESCRIPTION OF EXPERIMENTAL TECHNIQUES: MEASUREMENTS OF TWO-PHOTON ABSORPTION AND TRANSIENT ABSORPTION SPECTRA

In this dissertation we use a combination of one-photon (linear) spectroscopy and nonlinear spectroscopy. The linear measurements of absorption and fluorescence spectra use standard techniques and are described in appendix B. The nonlinear experiments are measurements of two-photon absorption and excited state absorption. In this chapter we present a brief description of the setups and the corresponding procedures. Appendix C provides further details about 2PA measurements.

#### Experimental Setup for Measuring of Absolute Two-Photon Absorption Spectra

The nonlinear transmission (NLT) technique and the fluorescence-based technique are the two main methods of the measurements of the 2PA spectra and cross sections. The NLT technique allows for direct measurements of the total absorption in the sample, comparing the laser power transmitted through the cuvette containing the unknown sample and the pure solvent. Since the 2PA absorption is weak, NLT relies on tight focusing of the laser beam in the highly concentrated sample. The absorption measured by NLT in addition to 2PA usually includes contributions from several other linear and nonlinear effects, such as stimulated emission, amplified spontaneous emission, Raman scattering, self-phase modulation, and continuum and plasma generation. These side effects cannot be separated from 2PA and usually result in underestimation of  $\sigma_2$ . The fluorescence-based technique evaluates  $\sigma_2$  by comparing the 2PA-excited fluorescence with the fluorescence and detection efficiency and the excitation pulse parameters. The

method offers high sensitivity for the 2PA detection but relies on careful characterization of the excitation laser pulse properties and total efficiency of the detection of the fluorescence.

We use a modified fluorescent method for measurements of the 2PA spectra [34]. The measurements of the spectra are done by monitoring of the wavelength-dependent two-photon-excited fluorescence and normalizing it by the square of the excitation laser power. The intensity of two-photon excited fluorescence is compared to the intensity of one-photon excited fluorescence of the same sample under the same detection conditions. The one-photon excitation is used to calibrate the unknown efficiency of the detection channel and fluorescence quantum yield. It allows for direct measurement of 2PA in a broad variety of compounds with the fluorescence (or phosphorescence) quantum yield,  $\phi > 0.005$ . A detailed description of the method is given in appendix C.

Figure 3.1 shows the experimental setup. The laser system comprises a Ti:Sapphire femtosecond oscillator (Coherent Mira 900) pumped with a 4.5W output from a continuous-wave (CW) frequency-doubled Nd:YAG laser (Coherent Verdi). The oscillator is used to seed a 1-kHz repetition rate Ti:Sapphire femtosecond regenerative amplifier (Coherent Legend-HE). The output pulses from the amplifier have an energy of  $\sim 1.3$  mJ and duration of  $\sim 100$  fs at wavelength  $\sim 795$  nm, and are down-converted with an optical parametric amplifier (OPA) (Quantronix TOPAS-C). The output of the OPA (signal and idler) can be continuously tuned from 1100 to 2200 nm. The corresponding pulse energy is 100–300  $\mu$ J (5–30  $\mu$ J after frequency doubling). For two-photon excitation we use either the fundamental of the signal (1100–1600 nm) or second

harmonic of either idler (790–1100 nm) or signal (550–790 nm) beam. We use a Glan-prism polarizer placed before the second harmonic generation (SHG) crystal to select either vertical (signal) or horizontal (idler) polarization. If second-harmonic excitation is used, then the residual fundamental beam (signal or idler) is cut with color filters, placed after the SHG crystal. For one-photon excitation, the second harmonic of either the Ti:Sapphire amplifier output (397 nm) or 1100 nm OPA signal output (550 nm) is used. The polarization of the excitation laser beam is vertical for both 1PA and 2PA. With the second harmonic of the signal, a  $\lambda/2$  plate is used after the reference detector to rotate polarization by  $90^\circ$ .

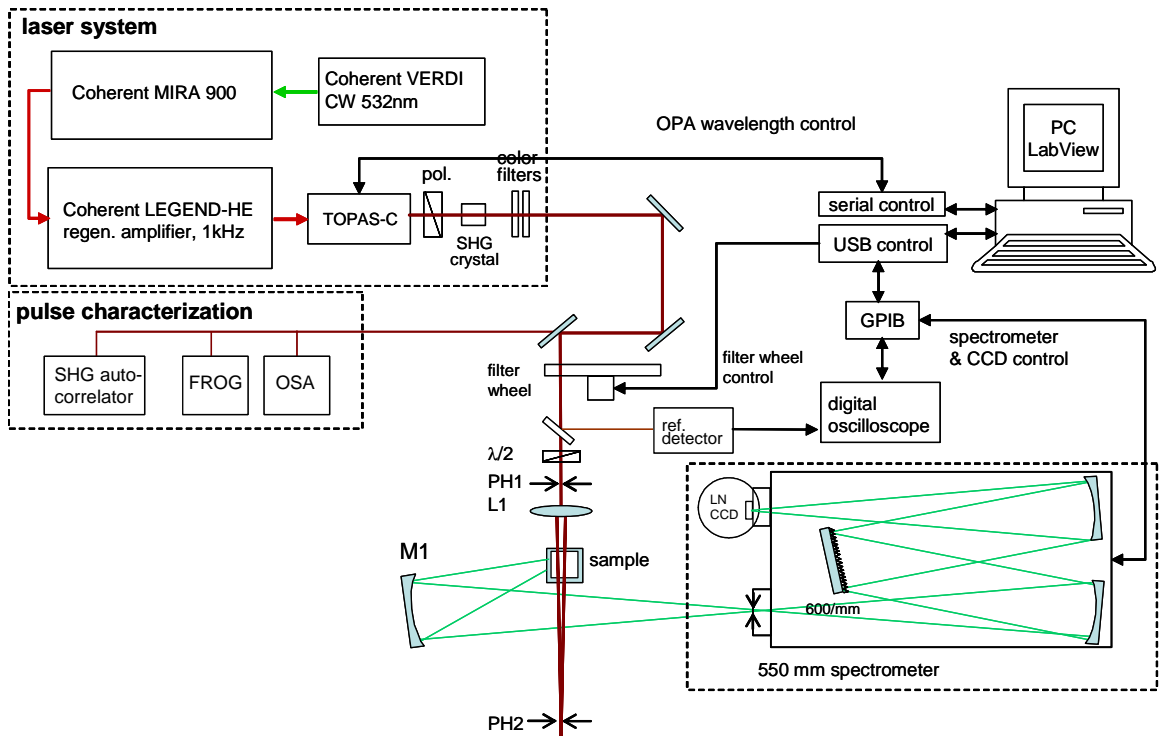


Figure 3.1. Layout of the experimental setup for 2PA measurements

The laser beam (either for one- or two-photon excitation) passes through two pinholes, which are placed before and after the sample, 35 cm apart from each other. The



pinholes insure that the beam always passes at 1 mm distance from the side wall of the sample cell. During the measurements, we keep the first pinhole completely open (much wider than the beam diameter). In both modes of excitation, the laser beam is slightly focused by an  $f = 25$  cm lens, which is placed after the first pinhole and 14 cm before the sample. This provides a virtually constant beam cross section on its way along the 1-cm long cell.

The fluorescence is collected at  $90^\circ$  to the laser beam direction with a spherical mirror ( $f = 50$  cm, diameter  $d = 10$  cm), which focuses the horizontally-elongated image of fluorescence track with a magnification ratio  $\sim 1:1$  on the entrance plane of the fluorescence grating spectrometer (Jobin Yvon Triax 550). The height of the vertical spectrometer slit is much larger than the height of the fluorescence image. The spectral dispersion on a two-dimensional CCD detector (Jobin Yvon Spectrum One) occurs in the horizontal direction, while the signal in the vertical direction is integrated over the whole slit height. The slit width is much smaller than the horizontal dimension of the fluorescence image and is kept the same in both 1PA and 2PA signal measurements. While recording the fluorescence spectrum, special care is taken to eliminate any spurious signals, such as scattered laser light, fluorescence of impurities, etc. The fluorescence spectra of the sample excited via 1PA and 2PA always had the same shape and maximum. The fluorescence intensity is measured by integrating the CCD output over 0.5–5 seconds and over 40–60 nm spectral region around the emission peak wavelength. Each data point is obtained by averaging of 2–5 acquisitions.

The average laser power at the sample is measured with a calibrated power meter (OPHIR, Nova II). In the case of one-photon excitation, the laser intensity is attenuated with a neutral density filter(s), such that the sample fluorescence signal is of the same order as upon two-photon excitation.

The laser spectrum and the corresponding central wavelength are measured by placing a piece of paper at the location of the sample cell and recording the scattered laser light. The spectrometer wavelength is calibrated with a He-Ne laser.

The raw spectra are obtained by measuring 2PA-excited fluorescence normalized to a square of the excitation laser power in a range of interest of excitation wavelengths. The absolute spectra are obtained by calibrating the unknown efficiency of fluorescence detection and fluorescence quantum yield and by correcting the raw spectra for the wavelength-dependent spatial and temporal laser pulse profile. The details are presented in appendix C.

#### Experimental Setup for Measuring of Femtosecond Excited State Absorption

The excited state absorption (ESA) experimental setup is shown in figure 3.2. It utilizes the same 1 KHz repetition rate femtosecond laser system as the 2PA setup. A small portion (~4%) of the Ti:Sapphire amplifier output is split-off before the beam enters the OPA. The split-off portion is frequency doubled in a BBO crystal to produce ~10 mW at 400 nm wavelength to serve as a pump beam. The pump beam is modulated at 500 Hz by an optical chopper which is synchronized with the laser pulses such that every second pulse is blocked. The attenuated OPA output serves as a wavelength-

tunable probe and reference. The time delay between the pump and the probe is set by a computer-controlled delay line which can be continuously tuned from 0 to 2.8 ns. The combined pump and probe beams are focused into the sample with a 200-mm focal length spherical mirror (SM1). At the sample the probe beam is slightly smaller in diameter than the pump beam. The pump and the probe beams are aligned to exact spatial overlap with the help of three computer-controlled alignment mirrors (M1-M3) and one computer-controlled beam splitter (BS1). Two InGaAs photodiode quad detectors (EOS IGA-030-Quad-E4, QD1 and QD2) are used to monitor the overlap of the beams on the sample. The sample is placed in a 2 mm thick quartz cuvette and is constantly stirred with a magnet bar. The transmitted pump beam is blocked after the sample with a color filter, while the transmitted probe beam is directed onto a Si/InGaAs sandwich detector (ThorLabs DSD2, PD1). The second sandwich detector (PD2) measures the probe pulses energy before the sample and is used as a reference. The sandwich detectors are specially designed photo-diodes consisting from two light-sensitive layers stacked one after another. The first, Silicon, layer allows detection of the wavelength in the range 400–1100 nm, and the second, Indium-Gallium-Arsenide, layer allows detection of the wavelength in the range 900–1700 nm. Two continuously-variable neutral density filter wheels (NDFW) are placed in front of the sandwich detectors in order to compensate for the wavelength-dependent variation of the probe pulse energy.

The detector outputs are digitized at a 2.5Msample/second rate using a 14-bit acquisition board (GaGe CS8420-128MS) for further analysis. Computer-controlled shutters are used to block the beams in order to minimize the exposure of the sample

during the experiment. The measurements, including beam alignment, control of the pulse delay, and control of the OPA wavelength are accomplished through LabView routines.

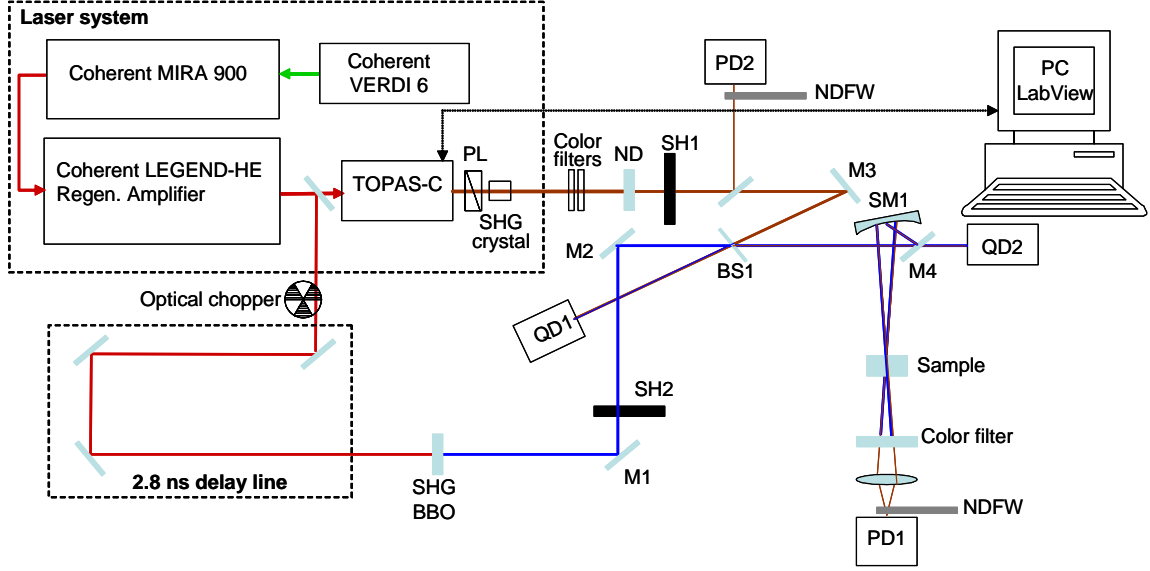


Figure 3.2. Schematic of the pump-probe experimental setup: Second harmonic of the amplified Ti:Sapphire beam is used as the pump to excite the sample, and the tunable output of the OPA is used as the probe beam. Both beams are automatically aligned using computer controlled motorized mirrors (M1-M3) and computer controlled motorized beam splitter (BS1). InGaAs photodiode quad detectors (QD1 and QD2) are used to monitor the beam overlap at the sample. Computer controlled flipping mirror (M4) directs beams either to QD2 or to the sample. SM1 – spherical mirror, NDFW – neutral density filter wheel, SH1, and SH2 – shutters

Change of optical density of the sample in the transient pump-probe absorption experiments is determined from the following expression [90]:

$$\Delta OD(\lambda) = \log_{10} \left( \frac{I_{ref}^0(\lambda) I_{sam}^1(\lambda)}{I_{sam}^0(\lambda) I_{ref}^1(\lambda)} \right), \quad (3.1)$$

where  $I_{ref}^0(\lambda)$  and  $I_{sam}^0(\lambda)$  are the energies of the probe pulse measured respectively by the reference and the sample detectors when the pump pulse is blocked, and  $I_{ref}^1(\lambda)$  and

$I_{sam}^1(\lambda)$  are the corresponding probe pulse energy values when the pump pulse is on. The change  $\Delta OD$  is evaluated according to (3.1) for each pair of the probe pulses (with and without the pump pulse) and then averaged over 10–100 acquisitions for each probe wavelength.

The extinction coefficient corresponding to the ESA is determined relative to that of a known reference compound, similar to the technique described in Ref. [91]. We use fullerene  $C_{60}$  in toluene as the reference ( $\varepsilon_{ref}(759nm) = 3700 M^{-1}cm^{-1}$ ) [92]. The optical densities of the sample and reference are adjusted to about equal values at the pump wavelength. The excited-state extinction coefficient  $\varepsilon_{sample}(\lambda_0)$  at a given wavelength  $\lambda_0$ , for which the reference excited-state extinction coefficient  $\varepsilon_{ref}(\lambda_0)$  is known, can be calculated as:

$$\varepsilon_{sample}(\lambda_0) = \varepsilon_{ref}(\lambda_0) \frac{\Delta OD_{sample}(\lambda_0)}{\Delta OD_{ref}(\lambda_0)}, \quad (3.2)$$

where  $\Delta OD_{sample}(\lambda_0)$  and  $\Delta OD_{ref}(\lambda_0)$  are the changes of the optical densities of the sample and the reference upon switching the pump on and off. The spectrum  $\varepsilon_{tr}(\lambda)$  is obtained by normalizing  $\Delta OD_{sample}(\lambda)$  using the known extinction at the wavelength  $\lambda_0$ .

Carbon tetrachloride is usually used for measurements of the spectra. This choice of solvent insures the absence of artifacts in the transient absorption spectra at long wavelengths, 1000–1600 nm, where most other solvents absorb laser light.

By integrating the transient extinction over frequency we obtain the transition dipole moment between the excited states as follows [85, 93]:

$$|\tilde{\mu}_{12}|^2 = \frac{3 \cdot 10^3 \ln(10) hcn}{8N_A \pi^3 f^2} \int \frac{\varepsilon_{tr}(\bar{\nu})}{\bar{\nu}} d\bar{\nu}, \quad (3.3)$$

where  $\bar{\nu}$  are the wavenumbers, and the integration is carried out over the frequency range of the electronic transition of interest.

We measure singlet-singlet ESA. If the time delay between the pump and the probe is short,  $<10$  ps, then the probe absorption is predominantly due to the absorption from  $S_1$  to higher excited singlet states. Triplet states do not populate significantly at such a short time scale. Increasing the delay between the pump and the probe pulses allows measuring temporal dynamics of the ESA to determine lifetimes of the initial excited states.

Usually the samples are prepared with an optical density of 0.1–0.4 at the pump wavelength. The pump beam diameter at the sample is about 5–10 micrometers. Under these conditions the accuracy of the transient absorption measurements is better than  $\Delta OD = 0.001$ .

#### 4. MEASUREMENTS OF TWO-PHOTON ABSORPTION SPECTRA AND CROSS SECTIONS: REFERENCE STANDARDS IN 550–1600 NM EXCITATION RANGE

A robust reliable technique of measurements of 2PA spectra is crucial for quantitative 2PA spectroscopy. Measuring 2PA cross sections and spectra of new compounds in a broad range of wavelengths is usually a tedious task, especially because it requires careful characterization of the temporal and spatial profile of the laser pulse. On the other hand, if there were available reference compounds with well-characterized 2PA spectra, then one could determine the 2PA cross sections of the unknown compounds by comparing the 2PA efficiency to that of the reference and thus automatically correct for the temporal- and spatial beam profile variations of the excitation pulse. Furthermore, if the reference compound is chosen such that its fluorescence spectrum overlaps with that of the new sample, one can record the signal at the same wavelength and thus overcome the necessity of knowing the detector spectral sensitivity and even the fluorescence quantum yields of the compounds. Thus, it is desirable to develop a set of standard reference dyes covering the whole visible and near-IR range of fluorescence wavelengths.

As an important ever step in establishing such reference compounds, W.W. Webb and co-authors [94, 95] published 2PA spectra of 16 commercial dyes. However, these data cover only a limited spectral range, 690–1050 nm. Moreover, only for three of them were the absolute 2PA cross sections measured. Evaluation of the absolute cross sections for the rest of the compounds requires knowledge of the fluorescence quantum yield, which is not always available and often varies from one solvent to another. In the entire spectral range used in the measurements, Webb and co-authors assumed that the spatial

and temporal laser beam profile is wavelength independent. This work remained so far the most reliable collection of 2PA spectra of the commercial dyes for reference purposes which many groups used.

The 2PA cross sections of common organic dyes, such as Anthracene, Fluorescein, and some Rhodamines, also have been reported in the literature at selected wavelengths [96-116]. However, these previous results vary by a large margin, which means that there is still a need for accurate 2PA cross section reference data.

This chapter presents an improved set of reference 2PA data, based on an extended collection of commercial organic dyes. The reference compounds are selected such that their 2PA spans the range 550–1600 nm, and the fluorescence emission spectra span from 375 to 900 nm, i.e. most of the visible, as well as the near-IR range of wavelengths. Our absolute 2PA spectra are corrected for the variations of the laser photon flux, pulse duration, and beam spatial profile. The measurement technique used here is presented in chapter 3 and appendix C. Briefly, the initial raw 2PA spectra are obtained by measuring 2PA-excited fluorescence normalized to a square of the excitation laser power in a particular range of excitation wavelengths. Then the raw spectra are corrected for the wavelength-dependent spatial and temporal laser profile. The absolute spectra are then obtained by calibrating the unknown efficiency of fluorescence detection, fluorescence quantum yield, and sample concentration.



Correction Curve for Measurements  
of Two-Photon Absorption Spectra  
and Cross Sections  
in Wide Range of Excitation Wavelengths

The 2PA-induced fluorescence signal collected over period of time  $T$ , and spectrally integrated over the interval of wavelengths between  $\lambda_{\min}$  and  $\lambda_{\max}$  depends on the temporal and spatial profile of the excitation laser pulses according to the following expression (see appendix C):

$$F_2(\lambda) = \frac{\alpha C \sigma_2(\lambda) W_2^2 T}{2g(h\nu)^2 \tau(\lambda) \Delta x(\lambda) \Delta y(\lambda)} \left( \frac{2 \ln 2}{\pi} \right)^{3/2} \int_{\lambda_{\min}}^{\lambda_{\max}} \phi(\lambda') \eta(\lambda') d\lambda' \quad (4.1)$$

where  $C$  is the concentration of the molecules,  $\sigma_2(\lambda)$  is the 2PA cross section at the excitation wavelength (in  $\text{cm}^4 \cdot \text{s}/\text{photon}$ ),  $\phi(\lambda')$  is the differential fluorescence quantum yield,  $\alpha$  is the collection geometry factor,  $\eta(\lambda')$  is a differential efficiency of photon collection (including geometrical factor, transmission of collecting optics and the detector quantum efficiency),  $g$  is the laser repetition rate (in Hz),  $\nu = c/\lambda$  is the laser frequency (in Hz),  $W_2$  is the laser average power (in Watts),  $\tau(\lambda)$  is the pulse duration FWHM (in seconds), and  $\Delta x(\lambda)$  and  $\Delta y(\lambda)$  are the beam diameters FWHM in horizontal and vertical directions respectively (in centimeters).

Thus, in order to establish a set of reliable 2PA standards, one needs first to do careful characterization of the laser system in the whole range of wavelengths used. The experimental setup, shown in figure 3.1 is used for 2PA measurements, and the laser pulse characterization (measurements of laser pulse duration and beam spatial profile) is

done in the whole tuning range. These data are used, first, for evaluation of 2PA cross section at some selected wavelengths and, second, for calibration of relative 2PA spectra.

The pulse duration in the whole region from 550 to 1600 nm is measured with an SHG autocorrelator. The beam shape and diameter is measured by imaging a laser beam scattered from a piece of paper with a CCD video camera. The absolute beam size is obtained by comparing the images of laser beam with an Edmund Scientific Magnifier Quality Resolution Chart placed in the same spot. At longer wavelengths, 1150–1600 nm, where the CCD sensitivity drops abruptly, the beam profile is characterized by imaging the fluorescence spot obtained upon the two- or three-photon excitation of a thin polymer film doped with multi-photon absorbing fluorophores. Further details are described in appendix C.

The results of the characterization of our laser system are summarized in terms of a correction function,  $C(\lambda) = \tau(\lambda)\Delta x(\lambda)\Delta y(\lambda)$  (see appendix C for more details). The corrected 2PA spectrum is then obtained by multiplying the raw 2PA spectrum based on the measured 2PA-induced fluorescence by the correction function. Thus, the knowledge of the correction function allows accurate measurements of the relative 2PA spectra corrected for wavelength-dependent laser properties. Figure 4.1 presents the correction function, inherent to our particular OPA working regime during the measurements of the standards.

The values of the correction curve vary with the wavelength by almost 300%. The 2PA spectrum is proportional to the correction curve. Therefore, assuming wavelength-independent temporal and spatial laser profiles and thus ignoring the correction curve

may result in up to 300% errors in the 2PA measurements, if the whole range of excitation wavelengths is used. Since for all the previous measurements of the 2PA spectra, including Webb's work, such a careful characterization of the employed laser beam was not performed, there is no big surprise in significant uncertainties in 2PA measurements and deviations of the measured data between the research groups.

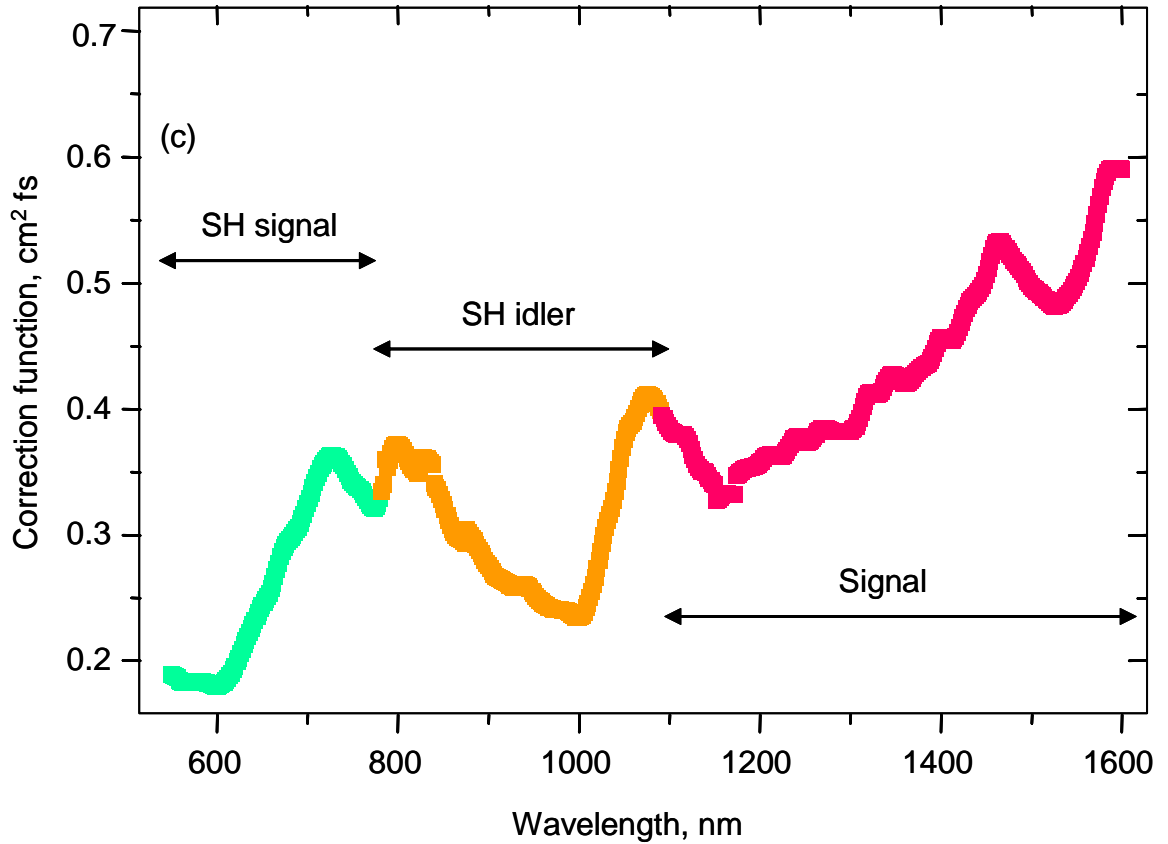


Figure 4.1. Correction function in 550–1600 nm range: green symbols correspond to second harmonic of the OPA signal, orange symbols correspond to second harmonic of the OPA idler, and red symbols correspond to the fundamental OPA signal

Two-Photon Absorption Spectra of the  
Reference Standards and their  
Comparison with the Literature Data

For almost 10 years the 2PA spectra published by W.W. Webb and co-authors [94, 95] were the only references widely used for measurements of absolute 2PA spectra. Thus, we studied a set of 16 commercially available dyes, which were selected such that the 2PA excitation wavelengths of the set would cover the range 550–1600 nm, and their fluorescence spectra would cover the whole visible and part of near IR-range, 375-900 nm. Therefore, the set covers most of the practical excitation and fluorescence wavelengths available for current femtosecond lasers and detectors. Most of the organic chromophores known so far have their 2PA excitation and fluorescence wavelengths in these ranges.

Figure 4.2 shows the normalized corrected fluorescence spectra of the studied dyes. Table D.1 summarizes the maximum extinction coefficients with the corresponding peak wavelengths and optimal ranges for the fluorescence wavelengths of the reference standards. The absorption and emission cover very broad wavelength range, such that almost any unknown chromophore spectra would match with these of at least one or two reference dyes.

Figures 4.3–4.5 present, as an example, the 2PA cross section spectra of three most intensively studied dyes, *Fluorescein*, *Rhodamine 6G* (*Rhodamine 590*), and *Rhodamine B* (*Rhodamine 610*). *Fluorescein* is dissolved in pH11 water, and *Rhodamines* are dissolved in methanol. The bottom axis represents the 2PA laser wavelength, and the top axis represents the transition wavelength (1PA wavelength). Additional symbols also

show the cross sections measured previously by other groups. Our results agree reasonably well with the majority of data obtained by the fluorescence method.

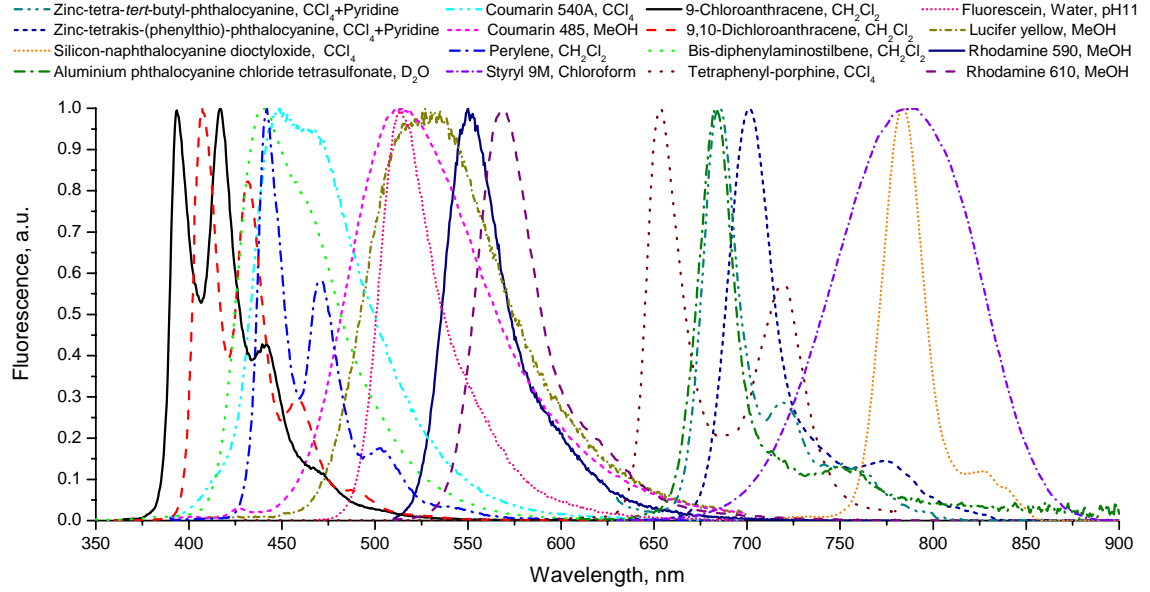


Figure 4.2. Normalized fluorescence spectra of the reference dyes

We estimate that our experimental error in the absolute cross section values is about 15%. The main contributions to the uncertainty of absolute 2PA come from: 1) pulse-to-pulse intensity variations during the 2PA-excited fluorescence signal measurements ( $\sim 10\%$ ), 2) fit error in the pulse duration determination ( $\sim 5\%$ ), and 3) fit errors in the beam diameter measurement ( $\sim 4\%$  for both  $\Delta x$  and  $\Delta y$ ). The experimental errors of the previously available 2PA cross section values vary from 30% (Webb) to  $\sim 50\text{--}100\%$  (other groups). Our spectra are measured with 2 nm wavelength steps (resolution), while the spectra by Webb [94, 95] are measured with 10 nm steps, and spectra by Clay [117] are measured with 10–20 nm steps.

In the case of *Fluorescein* (figure 4.3) in alkaline water solution, we observe almost quantitative agreement with the data of Webb, Xu and co-authors [94, 95, 109],

especially in the region of laser wavelengths from 700 to 900 nm. The result of Song et al. [111], obtained at 800 nm ( $\sigma_2 = 54$  GM), is also in a fair agreement with our measurement ( $\sigma_2(800) = 36$  GM). At 1064 nm, the cross section of Bradley et al. [101] is  $\sim 2$  times larger than our value. This discrepancy occurs most probably because Bradley et al. use neutral ethanol solution, where different spectral forms of Fluorescein are present.

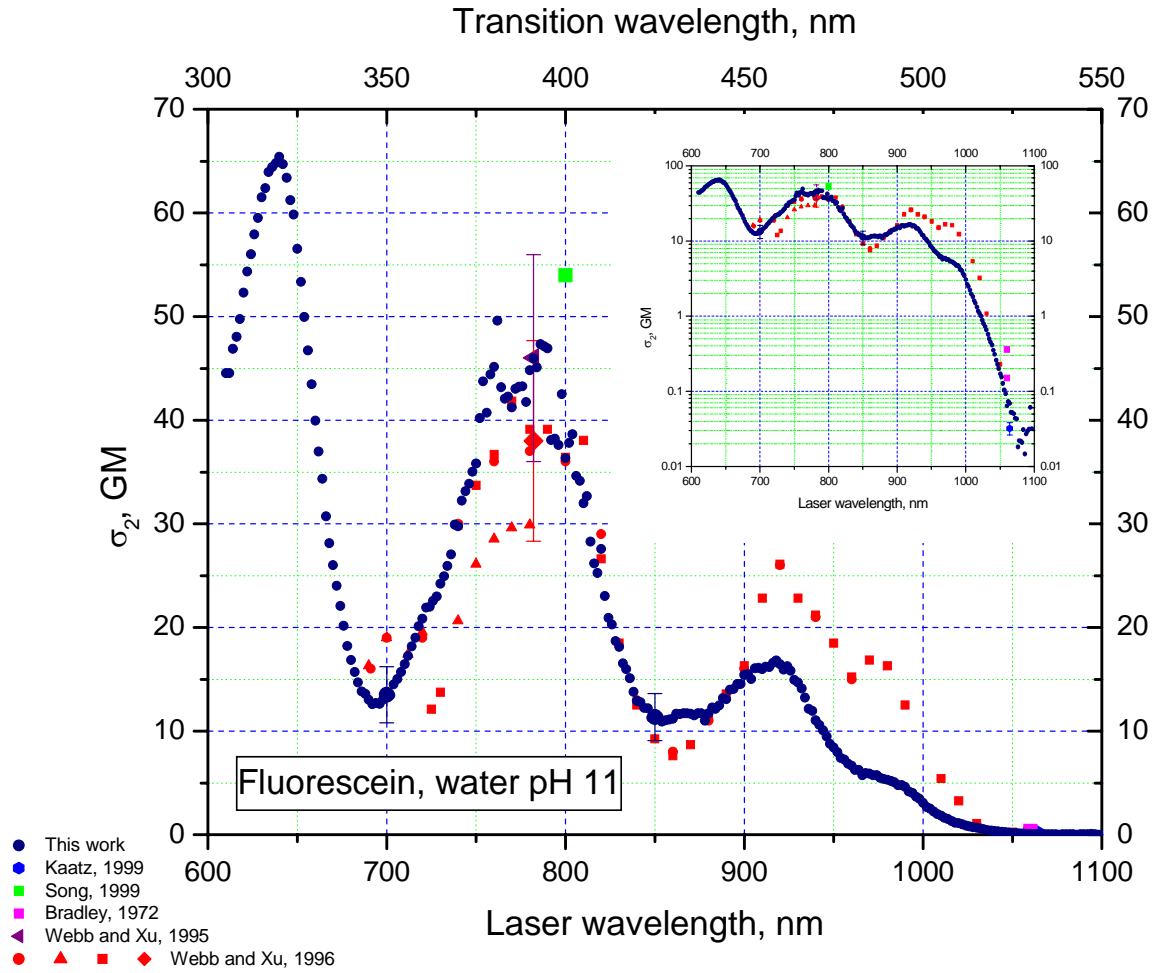


Figure 4.3. Two-photon absorption spectrum of the *Fluorescein* (dark blue symbols). Additional data points are shown based on the data available in literature

Our results for *Rhodamine 6G* (figure 4.4) generally agree with those of Webb, Albota and co-authors [95]. However, our cross sections are systematically lower at 690–

700 nm and larger at 720–900 nm. In the 920–960 nm region the two sets of data quantitatively match within error margins. We suspect that the Webb data deviate from ours because the spatial and temporal laser profiles were assumed to be wavelength-independent in their work.

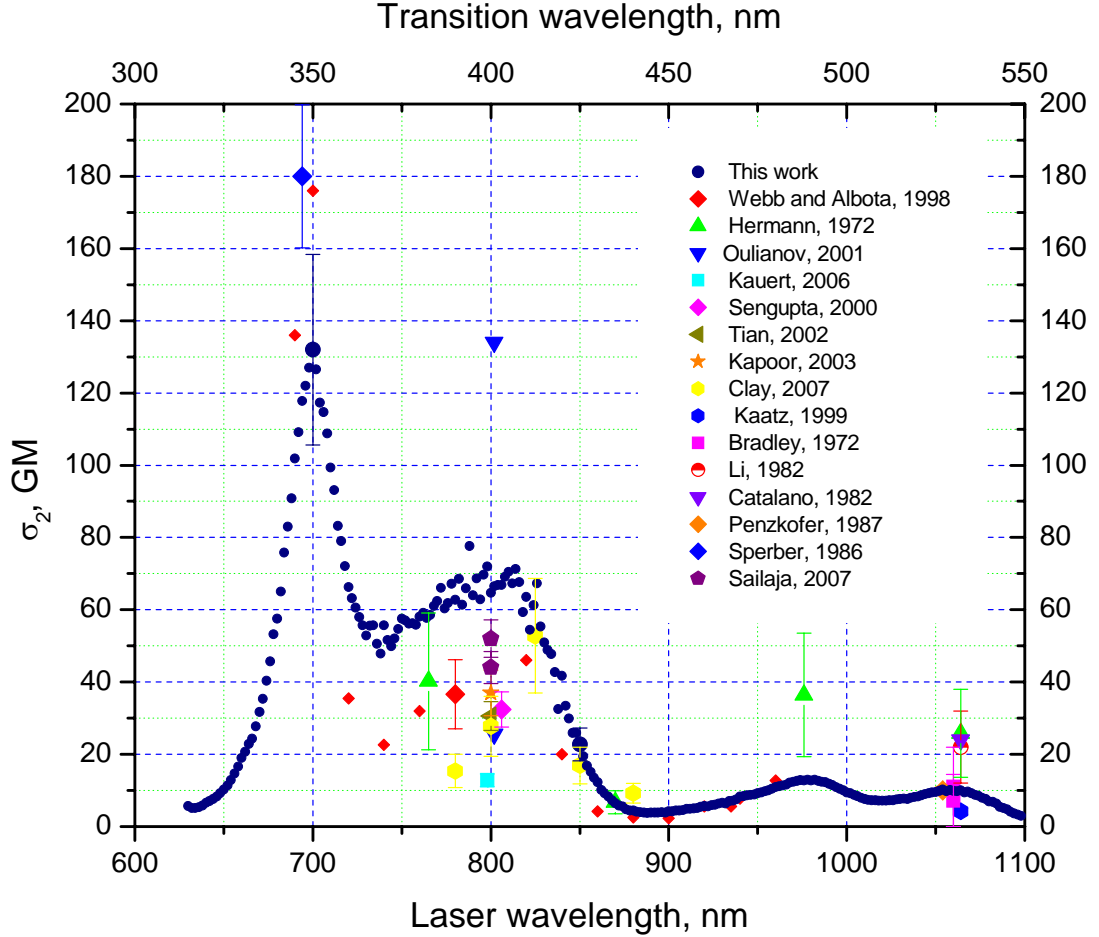


Figure 4.4. Two-photon absorption spectrum of the *Rhodamine 6G* (dark blue symbols). Additional data points are shown based on the data available in literature

Several data points for 2PA cross section of *Rhodamine 6G* are obtained at ~800 nm. Rentzepis and co-authors [113] evaluate  $\sigma_2$  relative to *Rhodamine B*, for which they use the cross section  $\sigma_2 = 150$  GM from Ref. [94]. The measurements were done using the integrated fluorescence spectrum, such that the fluorescence quantum yield of

*Rhodamine B* is required to obtain  $\sigma_2$ . The quantum yield of fluorescence ( $\phi = 0.71$ ) was used from Ref. [118]. The resulting value for *Rhodamine 6G*,  $\sigma_2(800) = 134$  GM, is two times larger than measured by us. However, the quantum yield of fluorescence of the reference *Rhodamine B* is probably overestimated in Ref. [118]. More recent and revised data [119, 120], as well as our own measurements give  $\phi = 0.45$ . With this correction, one would get  $\sigma_2(800) = 85$  GM, which is in fairly good agreement with our result ( $\sigma_2(800) = 65 \pm 9$  GM).

Other  $\sigma_2$  values are obtained at 800 nm with the NLT technique. The results are always 2.5–5 times lower (13–26 GM). This discrepancy between the fluorescence and NLT results can be explained [113] as being due to the contribution from several other linear and nonlinear effects, such as stimulated emission, amplified spontaneous emission, Raman scattering, self-phase modulation, and continuum and plasma generation, which can take place in addition to 2PA. These side effects cannot be separated from 2PA and usually result in underestimation of  $\sigma_2$  [113].

The 2PA spectrum of *Rhodamine B* in methanol published by Webb, Xu and co-authors [94] consists of several sets of data, taken in different spectral regions. The two such sets (upper and lower branches) differ from each other in the 800–850-nm region by a factor of  $\sim 2$ , which presents an ambiguity in choosing the reference value in this region. The upper branch coincides quantitatively with our results (figure 4.5) in the region from 690 to 850 nm, but the lower does so only from 880 to 1030 nm.



Similarly to the case of *Rhodamine 6G*, most of the data obtained in the 780–880 nm region with NLT technique are underestimated probably because of other possible linear and nonlinear processes, [113].

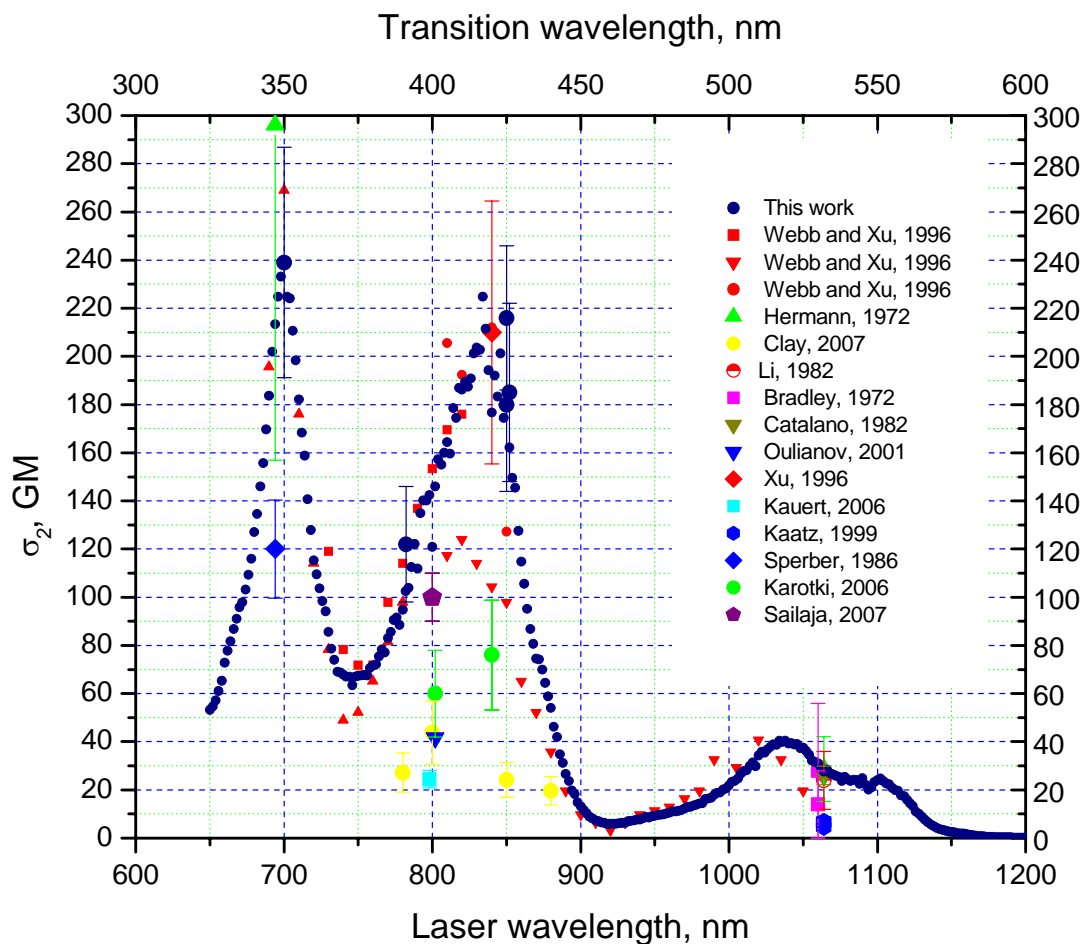


Figure 4.5. Two-photon absorption spectrum of the *Rhodamine B* (dark blue symbols). Additional data points are shown based on the data available in literature

At 1060 nm, we observe a rather good correlation (always within experimental error margins) of our data with fluorescence-based results of Refs. [99, 101, 103, 104].

The 2PA spectra and cross sections of the full set of the reference dyes are shown in appendix C and tables D.3–D.6.

In conclusion, this chapter presents absolute two-photon absorption spectra of a set of sixteen commercially-available dyes measured in a broad range of excitation wavelength 550–1600 nm, with high fidelity ( $\sim 2\text{--}4\times$  better than before) and high wavelength resolution ( $\sim 5\times$  better than before). The emission spectra of the dyes cover the range of sensitivity of standard detectors, such as a CCD sensor.

The 2PA spectra and cross sections presented here are used as reference standards for relative measurements of 2PA cross sections in the following chapters of the dissertation. The same data are starting to be used by other groups for 2PA measurements.

## 5. APPLICATION OF THE FEW-ESSENTIAL ENERGY LEVELS MODEL FOR QUANTITATIVE DESCRIPTION OF THE TWO-PHOTON ABSORPTION SPECTRA AND CROSS SECTIONS

The possibility of reliable and accurate measurements of 2PA is the imperative prerequisite for quantitative interpretation of the measured 2PA spectra. This chapter addresses the question whether the 2PA spectra of organic chromophores can be quantitatively explained, at least for low-energy transitions, based on the few-essential-levels approach. As discussed before, in such an approach, individual bands of the 2PA spectra are thought to be due to transitions from the ground state of the molecules to one of the low-energy excited states, either without interaction with any other energy states (two-level model) or with the interaction with some intermediate states (three- and more level model), and the influence of higher-lying energy levels is neglected.

To answer the above question we evaluate the 2PA spectra and cross sections for a selection of different compounds by two alternative methods. First, we directly measure absolute 2PA spectra. Second, we determine the key molecular parameters, such as transition dipole moments and permanent dipole moment differences from independent measurements. Then we insert the measured molecular parameters into the expressions (2.6) or (2.8) depending on whether the two- or three- level model is assumed (see chapter 2), and compare the calculated values with the directly measured 2PA cross sections.

### Two-Level Model

As a first step, we examine under what conditions the expression (2.6) describing the 2PA in the two-level approximation can be applied. The cross section is proportional to three important terms: square of the transition dipole moment between the ground and the excited states ( $|\vec{\mu}_{01}|^2$ ), square of the permanent dipole moment difference between the ground and the excited states ( $|\Delta\vec{\mu}_{01}|^2$ ), and the normalized transition line shape function ( $g(2\nu)$ ). The dependence of the expression (2.6) on the angle  $\beta$  may results in up to  $3\times$  variations of the cross section values. The angle can be measured as described in the second part of this chapter or it can be derived from the chemical structure of the molecules as is done in this part of the chapter. Three important conclusions can be immediately drawn from the expression (2.6): (1) The 2PA cross section is proportional to the square of transition dipole moment  $|\vec{\mu}_{01}|^2$ ; (2) The 2PA cross section is nonzero only if the permanent dipole moments in the ground and excited states are different ( $|\Delta\vec{\mu}_{01}| \neq 0$ ); (3) The line shape of the transition is the same for 1PA and 2PA.

Based on conclusions (1)–(3) one first might anticipate that if the molecule has a center of symmetry, then the two-level model is unlikely to be valid since parity selection rules predict that  $|\Delta\vec{\mu}_{01}| = 0$  (at least for non-degenerate states). However, as we shall show below, the concept of strict parity needs to be applied with some caution, especially in large molecules with complex electron-vibrational interactions. Second, if the 1PA and 2PA show an overlapping transition, then this transition is a good candidate for the two-

level model. Thirdly, for the two-level model (see figure 2.1) it is preferred that there are no intermediate levels in the 1PA spectra before the initial and final states. Therefore, we may be looking first of all for the lowest energy dipole-allowed  $S_0 \rightarrow S_1$  transition in non-symmetrical molecules.

For this particular study we select 14 molecules and group them into 3 sets according to their apparent symmetry properties as follows from the molecular structures. Our initial idea was to compare less symmetrical molecules with those with more symmetrical structure, and show that the two-level model works better in the former ones. To our surprise, however, it turned out that the two-level description at least for the lowest energy transition is quite independent of the type of symmetry of the molecular structure.

We first discuss the 2PA spectra of each set measured as described in chapter 4. Then we measure  $|\Delta\vec{\mu}_{01}|$  and  $|\vec{\mu}_{01}|$  for each of the molecules and apply expression (2.6). Further details about these measurements are given in appendix B. Briefly, we determine  $|\vec{\mu}_{01}|^2 g(2\nu)$  directly from the 1PA spectra and extinction coefficients. For the measurements of  $|\Delta\vec{\mu}_{01}|$  two common techniques may be applied. A frequency shift between the  $S_0 \rightarrow S_1$  transition maxima in the 1PA and fluorescence emission spectra, called solvatochromic shifts, can be used. Solvatochromic shifts are typical to organic molecules, where the distribution of vibronic levels in the ground- and the first excited electronic states is usually the same. The fluorescence spectrum, therefore, usually represents a mirror image of the 1PA spectrum with a small frequency shift, which depends on the polarity of the solvent and molecular properties. Solvatochromic shifts in

a series of solvents with varying polarity are proportional to  $|\Delta\vec{\mu}_{01}|^2$ , if the shifts are predominantly due to dipole-dipole interaction [122]. Alternatively, one may use the Stark effect in external electric field, e.g. in combination with spectral hole burning, where the last requires low temperatures, and the  $|\Delta\vec{\mu}_{01}|$  value is determined based on the spectral changes of the transition [123] due to application of the external electric field. For our study we prefer the solvatochromic shift approach as this does not require low temperatures.

Figures 5.1 a-c show the 1PA (right vertical scale) and 2PA (left vertical scale) spectra of the molecules. The horizontal scale at the bottom of the graphs corresponds to the transition wavelength (i.e. half of the 2PA laser wavelength), and the scale at the top corresponds to the transition frequency. Inserts show chemical structures of the molecules.

Group (i) comprises six non-centrosymmetrical substituted diphenylaminostilbenes with strongly asymmetrical structures. They show qualitatively very similar 1PA and 2PA spectra (figure 5.1a). The lowest-energy 1PA absorption shows a very broad peak with the width about  $5000\text{ cm}^{-1}$  and with the maximum around 360–410 nm. Since the fluorescence emission (table D.7) for all six compounds follows the corresponding 1PA peak, it is safe to conclude that the observed transition corresponds to the  $S_0 \rightarrow S_1$  transition between the ground and excited singlet states.

The next important experimental fact to discuss is that the measured 2PA has in all six molecules a distinct peak that nearly overlaps within the accuracy of the measurement with the  $S_0 \rightarrow S_1$  transition. The discontinuity in the 2PA spectrum of the molecule **2**

occurs at the wavelengths corresponding to the change of the OPA tuning range from second harmonic of signal to second harmonic of idler.

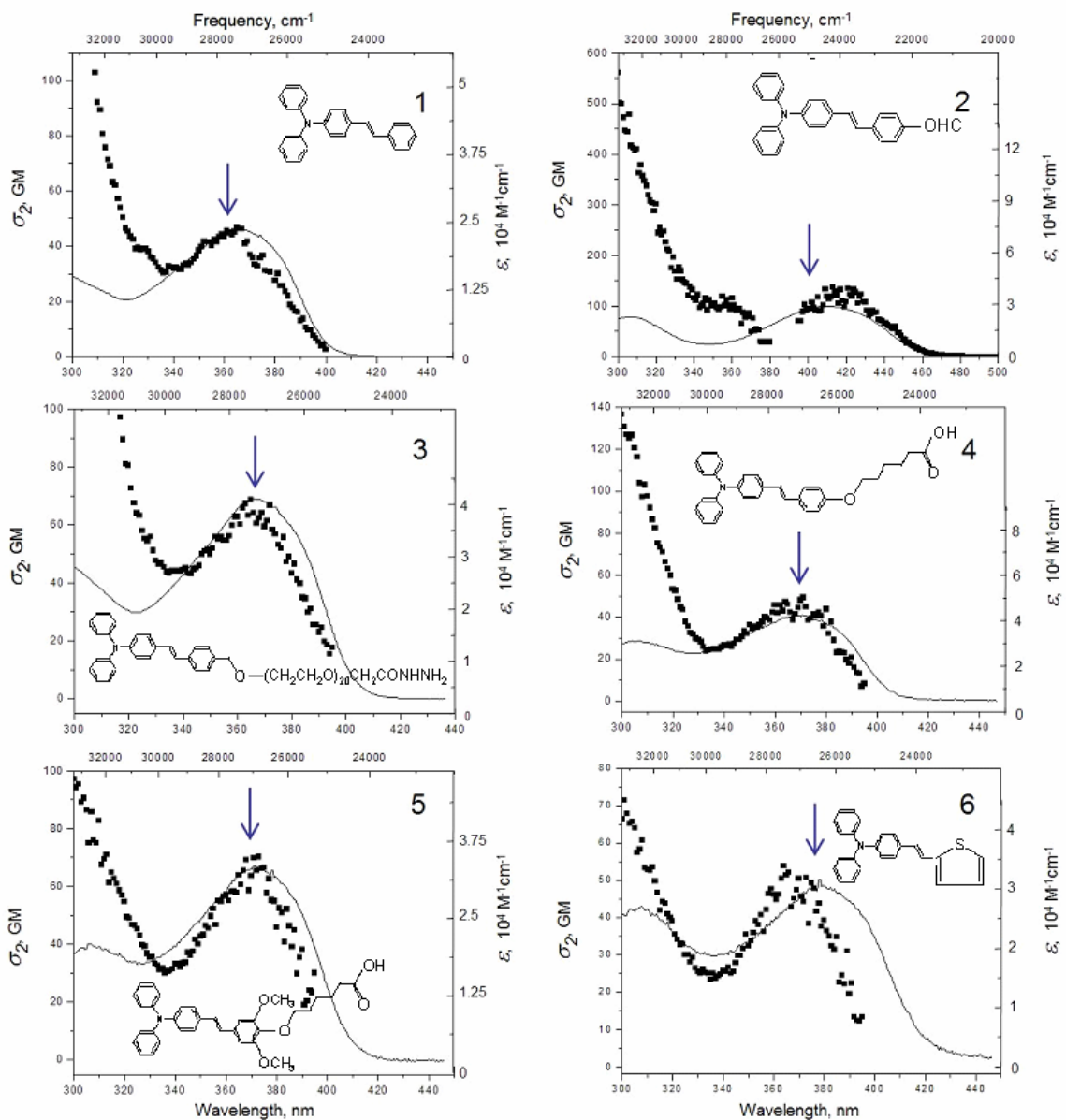


Figure 5.1a. 2PA (symbols) and 1PA (lines) spectra of substituted diphenylaminostilbenes. In 2PA spectrum of the molecule 2 one can see the OPA tuning gap around the wavelengths  $\lambda \approx 380\text{--}400 \text{ nm}$ . Vertical arrow indicates the wavelength, where  $\sigma_2^{ex}$  is evaluated (corresponding to the maximum of the lowest-energy 1PA transition)

For the molecule **5**, the 2PA peak is slightly narrower than the corresponding 1PA peak, while the maxima still coincide. For the molecule **6**, the 2PA peak is slightly blue-shifted and narrowed compared to the 1PA peak. However, in all cases, the 1PA and 2PA profiles are basically very similar, which is a strong indication that we must be dealing here with the same transition. We attribute these deviations between the 1PA and 2PA bands mostly to experimental errors in the 2PA measurements. The shift of the 2PA band relative to 1PA band in the molecules **5** and **6** can also be due to redistribution of the permanent dipole moment difference within the absorption band due to possibly strong charge transfer.

Therefore we use the peak wavelength of the 1PA  $S_0 \rightarrow S_1$  transition to select the values of  $\sigma_2$  for further comparison with the two-level model. Blue vertical arrows on the figure 5.1a show the corresponding wavelength for each molecule. A significant difference between the 1PA and 2PA spectra is observed only at shorter wavelengths,  $\lambda < 310$  nm, where the 2PA increases sharply, whereas 1PA shows some other weaker peaks. The increase of 2PA may be attributed to a resonance enhancement effect, of higher-lying electronic transitions.

The maximum 2PA cross section values at the peak of the 2PA bands vary from  $\sigma_2 = 40$  to 140 GM, which correlate with the earlier reported data for similar molecules [124-128].

The values of the maximum extinction coefficients of the molecules of group (i) are collected in table D.7 and vary from  $24000 \text{ M}^{-1}\text{cm}^{-1}$  for **1** to  $43000 \text{ M}^{-1}\text{cm}^{-1}$  for **3**. The  $|\Delta\vec{\mu}_{01}|$  values vary from 9 D for **3** to 15 D for **2** and are also collected in table D.7.



Note that this group of molecules satisfies our initial assumption that the non-centrosymmetrical molecules with the overlapping 1PA and 2PA transitions of the same line shape are the best candidates to be used for justification of the two-level model.

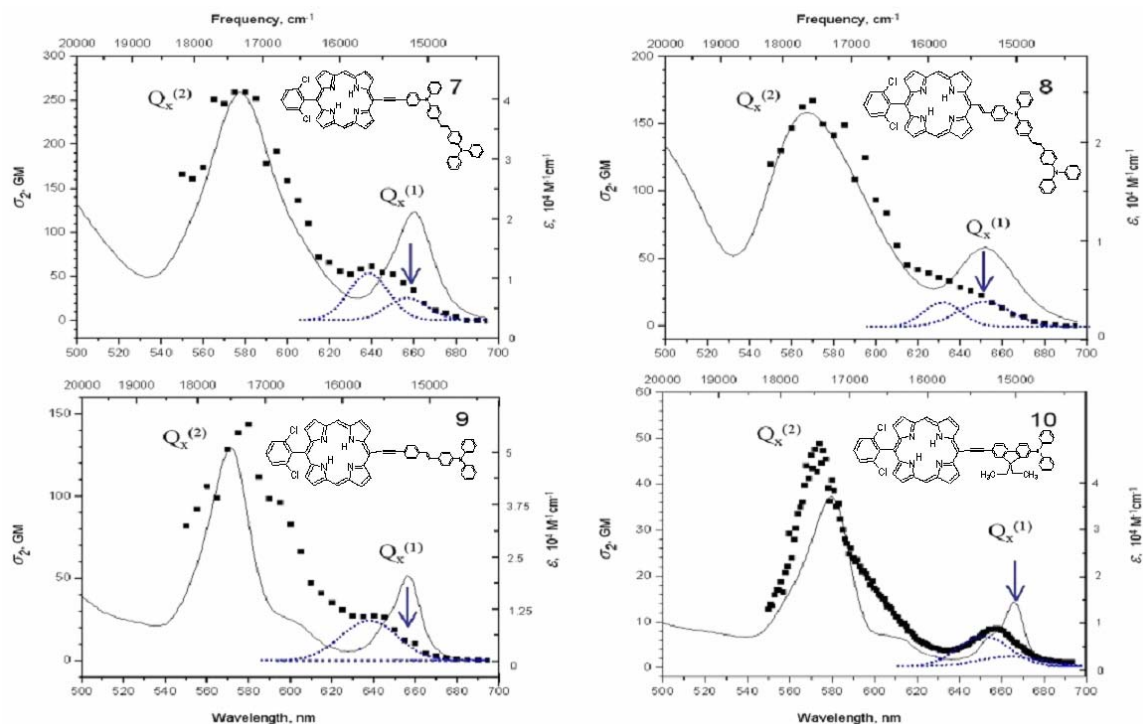


Figure 5.1b. 2PA (symbols) and 1PA (lines) spectra of meso-DPAS and BDPAS-substituted porphyrins. Dashed lines show decomposition of the long-wavelength portion of the 2PA spectrum into two Gaussians. Vertical arrow indicates the wavelength, where  $\sigma_2^{ex}$  is evaluated (corresponding to the maximum of the lowest-energy 1PA transition)

The group (ii) contains four substituted dipolar porphyrins. Those molecules comprise complex structures made of a symmetrical porphyrin core connected with a molecule similar in structure to the molecules of group (i). This results in push-pull character of their electronic structure. The spectra of the group (ii) are presented in figure 5.2b. The main two 1PA peaks belong to the Q-bands, inherent in tetrapyrroles.

Following the notation of Ref. [129], the longer wavelength band at 650–670 nm is  $Q_x^{(1)}$ , and the shorter wavelength band at 560–580 nm is  $Q_x^{(2)}$ .

It was shown in Ref. [129] that  $Q_x^{(1)}$  and  $Q_x^{(2)}$  bands have parallel transition dipole vectors, and that the  $Q_x^{(1)}$  band is a superposition of at least three vibronic transitions: purely electronic  $Q_x^{(1)}(0-0)$  and two vibronic satellites,  $Q_x^{(1)}(0-1)$  and  $Q_x^{(1)}(0-1')$ . The width of the  $Q_x^{(1)}$  peak is about 500–1000  $\text{cm}^{-1}$ . The  $Q_x^{(1)}$  peak corresponds to the  $S_0 \rightarrow S_1$  transition and the  $Q_x^{(2)}$  peak corresponds to the  $S_0 \rightarrow S_2$  transition.

The 2PA spectra of molecules **7-9** show a relatively narrow peak that closely matches the  $Q_x^{(2)}$  1PA transition and a shoulder at the wavelengths of the  $Q_x^{(1)}$  transition, while the molecule **10** shows peaks corresponding to both  $Q_x^{(2)}$  and  $Q_x^{(1)}$  transitions. As compared to the group (i), the overlap between the 1PA and 2PA transitions is much less obvious in the porphyrins. In fact, the 2PA of  $Q_x^{(1)}$  appears more like a shoulder, and is ~20 nm blue-shifted with respect to the corresponding 1PA peak. We attribute this change of shape to the vibronic satellites, where the 2PA may be much stronger than that of the pure electronic lowest energy 0-0 transition [129]. Note also that the peak 2PA cross section values in the lowest energy transition ( $Q_x^{(1)}$ ),  $\sigma_2 = 5 - 20$  GM, are about one order of magnitude smaller than the corresponding values in the group (i).

To take this circumstance into account we use two Gaussian peaks to fit the 2PA spectra of the  $Q_x^{(1)}$  transition with the transition frequency of 0-0 fixed and equal to that of 1PA spectra, as shown in figure 5.1b by vertical arrows. This allows us to extract the correct 2PA cross section from the Gaussian peak corresponding to the 0-0 transition and neglect the influence of vibronic satellites on the 2PA. The peak values of the 0-0 2PA

transition are collected in table D.7. We further use these numbers for comparison with the two-level model.

Table D.7 also contains the values of the maximum extinction coefficients and  $|\Delta\tilde{\mu}_{01}|$  of the molecules of group (ii). The extinctions vary from 8000 M<sup>-1</sup>cm<sup>-1</sup> for the molecule **8** to 25000 M<sup>-1</sup>cm<sup>-1</sup> for the molecule **9** and are smaller compared to the values of group (i). The  $|\Delta\tilde{\mu}_{01}|$  values vary from 0.4 D for the molecule **9** to 7 D for the molecule **8** and are also smaller than those of group (i).

Figure 5.1c shows the spectra of substituted stilbenes **11-14**. The 1PA consist of a strong S<sub>0</sub>→S<sub>1</sub> transition with a peak at 300–350 nm, accompanied by a weaker peak at shorter wavelengths, 300–320 nm, similar to the molecule **5** and **6** in group (i). The molecule **14** is a well-known chromophore, bis-diphenylaminostilbene (BDPAS), which is often considered as a benchmark example of a symmetrical 2PA system. Indeed, the main 2PA peak is clearly at a higher energy than the S<sub>0</sub>→S<sub>1</sub> transition and has no distinguishable counterpart in the 1PA spectrum. It has been shown that the 2PA peak at 335 nm is due to a higher-energy *g*-parity electronic state [117, 130]. Similar arguments can be made for the other three molecules, indicating that the underlying symmetry properties are close to that of BDPAS rather than group (i). For this reason, as mentioned before, initially this group of molecules was chosen as a counterexample to show that for a centro-symmetrical molecule the two-level model is not applicable. Nevertheless, a close inspection of the spectra presented in figure 5.1c shows that in addition to the strong 2PA peak, there is a weaker shoulder, which strongly overlaps with the S<sub>0</sub>→S<sub>1</sub> 1PA transition. Decomposing the measured 2PA spectra into two Gaussians allows us to

extract the 2PA peak corresponding to the lowest energy transition. While fitting the 2PA spectra of group (iii) molecules we do not fix the frequency of the lowest energy 2PA transition.

Table D.7 contains the values of the maximum extinction coefficients and  $|\Delta\bar{\mu}_{01}|$  of the molecules of group (iii). The extinctions are close to that of the group (i), and vary from 32000  $\text{M}^{-1}\text{cm}^{-1}$  for the molecule **11** to 53000  $\text{M}^{-1}\text{cm}^{-1}$  for the molecule **13**. The  $|\Delta\bar{\mu}_{01}|$  values are also similar to that of the group (i), and vary from 5.5 D for the molecule **14** to 11 D for the molecule **11**.

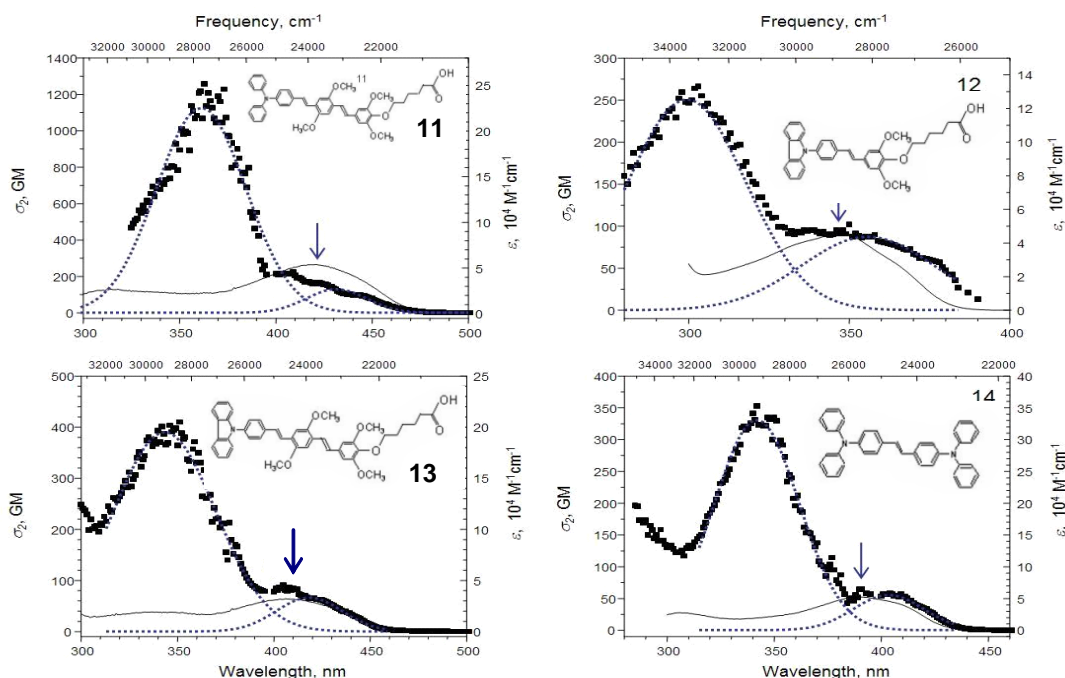


Figure. 5.1c. 2PA (symbols) and 1PA (lines) spectra of substituted diphenylaminostilbenes (group (iii)). Dashed lines show decomposition of the long-wavelength portion of the 2PA spectrum into two Gaussians. Vertical arrow indicates the wavelength, where  $\sigma_2^{ex}$  is evaluated (corresponding to the maximum of the lowest-energy 1PA transition)

The  $\sigma_2^{ex}$  values, corresponding to the lowest-energy component (along with the original experimental value at the same wavelength for groups (ii) and (iii)), are collected in table D.7. We estimate that  $\sigma_2^{ex}$  has overall 20% experimental error.

The next step is to obtain an estimate of the peak value of  $\sigma_2$  for the lowest energy transition in all 14 compounds by using expression (2.6). From chemical structure considerations, we assume here that the angle between  $\vec{\mu}_{01}$  and  $\Delta\vec{\mu}_{01}$  is zero,  $\beta \approx 0$ .

The peak 2PA cross sections,  $\sigma_2^{th}$ , obtained from the two-level model (see expression (2.6)) are collected in table D.7. We estimate that the calculated cross section values have 30% error.

In figure 5.2 we compare the calculated and the measured 2PA cross sections. The horizontal axis shows the 2PA cross sections obtained from the expression (2.6) with the Onsager local field model, and the vertical axis shows the corresponding experimental values. The experimental cross sections correspond to the wavelength of the lowest-energy 1PA transition maximum, as indicated by vertical arrow in figure 5.1.

The dashed diagonal line represents a situation where the measured and calculated cross sections coincide. The fact that the most accurate coincidence between  $\sigma_2^{th}$  and  $\sigma_2^{ex}$  is obtained in the group (i) is not very surprising, because those chromophores have low degree of symmetry. However, the fact that the data points of two other groups also lie close to the diagonal almost within the experimental error disregarding the higher symmetry of the chromophores supports the initial suggestion that in the case of organic chromophores the lowest energy  $S_0 \rightarrow S_1$  2PA transition can be well described using the two-level model.

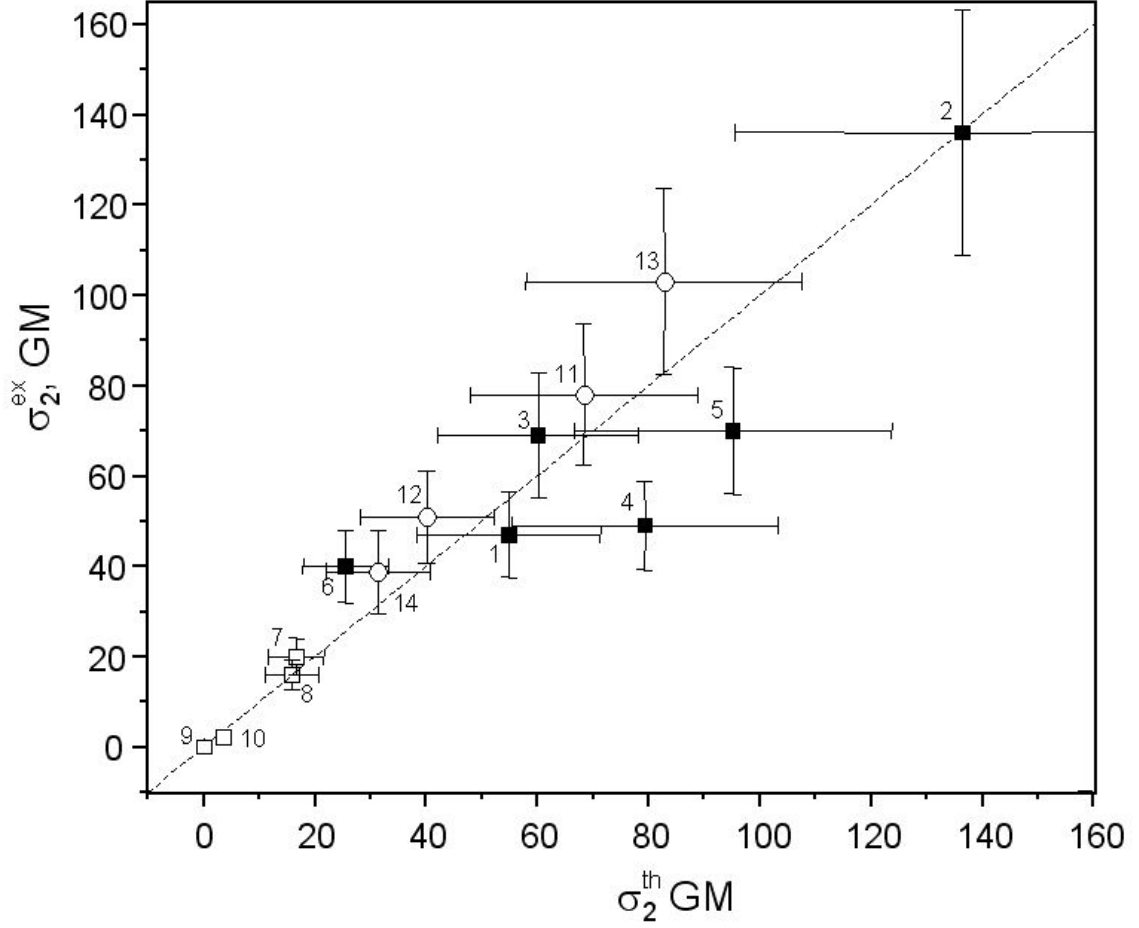


Figure 5.2. Comparison between the cross sections predicted by the two-level model (horizontal axis) and that measured in experiment (vertical axis). Solid rectangles – group (i), empty rectangles – group (ii), empty circles – group (iii). Vertical 20% error bars are due to the experimental uncertainty in the direct measurement of  $\sigma_2^{ex}$ . Horizontal 30% error bars are due to the uncertainty in the determination of the dipole moment values (see text for details)

It is possible to better quantify the degree of correlation by using  $\chi^2$ -minimization criterion:

$$\chi_R^2 = \frac{1}{N-1} \sum_{i=1}^N \left( \frac{\sigma_i^{th} - \sigma_i^{ex}}{\Delta_i} \right)^2, \quad (5.1)$$

where  $\sigma_i^{th}$  and  $\sigma_i^{ex}$ , are, correspondingly, the theoretical and the experimental cross sections,  $\Delta_i$  is the standard deviation, and the summation is over all  $N$  molecules. Smaller  $\chi_R^2$  means higher correlation. For the data points shown in figure 5.2, we calculate from (5.1)  $\chi_R^2=0.15$ . The same calculation with the Lorentz local field model gives  $\chi_R^2=0.21$ . This justifies our preference of the Onsager model, although the correlation is very good in both cases.

Of course, the current approach does not have the power to forecast the full 2PA spectrum. Nevertheless, our result suggests that the current method can be used to estimate the peak 2PA cross section of the lowest-energy transition with accuracy comparable to that obtained in direct nonlinear absorption measurements.

Most noteworthy is the conclusion that the simple two-level model gives a rather accurate approximation for the 2PA in the lowest energy dipole-allowed singlet-singlet transition independent of the structure and the symmetry of the molecules. This property can be also used to determine  $|\Delta\vec{\mu}_{01}|$  from the measured peak 2PA cross section in the given transition, which might eventually be considered as an alternative method to the Stark effect for determining of this important molecular parameter, if there is an alternative indication that the two-level model can be applied for the transition.

### Three-Level Model

In this part of the chapter we examine under what conditions a three-level model (2.8) can be applied to quantitatively describe the 2PA cross sections. In this approximation, the cross section is proportional to the square of the transition dipole

moment between the ground and the intermediate excited states  $|\vec{\mu}_{01}|^2$  times the square of the transition dipole moment between the intermediate and the final excited states  $|\vec{\mu}_{12}|^2$ . The cross section also depends on the resonance enhancement factor,  $1/(1 - \nu_{01}/\nu)^2$ , and the normalized transition line shape function  $g(2\nu)$ . For demonstration of applicability of the three-level model we select centrosymmetrical molecules where the states have definite parity. Parity selection rules help to avoid possible quantum interference effects such as shown on figure 2.1d. A candidate three-level system, therefore, would be such where the transition to the final level is prohibited in 1PA due to the parity selection rules (*gerade-gerade* transition with  $|\vec{\mu}_{02}| = 0$ ).

For those molecules the  $|\vec{\mu}_{01}|^2$  value can again be determined from the 1PA spectra. Measurements of the  $|\vec{\mu}_{12}|^2$  may be accomplished by using femtosecond pump-probe experiments described in chapter 3. The transition dipole moment between the excited states is obtained using expression (3.3).

The choice of the molecules for this part of the chapter is not trivial because very little quantitative information is available about *g*-parity excited states in organic dyes. Furthermore, one needs to find molecules where the transition frequency between the excited energy levels is accessible with our existing laser system (550–1700 nm). In this regard molecules **13** and **14** are not suitable because their excited state transition occurs at  $\sim 2000$  nm). We found a suitable candidate among tetrapyrroles, called free-base tribenzotetraazachlorin (**TBTAC**). It turned out to satisfy both requirements, showing a distinct peak in the 2PA spectrum and in the transient absorption spectrum in suitable



wavelength range. It is also interesting that the structure nominally lacks a center of symmetry. Nevertheless, effective symmetry is preserved and well manifested as shown below. The permanent dipole moments of **TBTAC** are negligible small,  $|\Delta\vec{\mu}_{0j}| \approx 0$ , for accessible excited state levels  $j$ , such that the two-level model predicts  $\sigma_2 \approx 0$ .

Figure 5.3 presents the 1PA and 2PA spectra of **TBTAC**. The 2PA spectrum is shown in transition wavelengths (equals to one-half of the laser 2PA wavelength). The figure also shows fluorescence anisotropy of the molecule as a function of the excitation wavelengths. The fluorescence anisotropy spectrum allows decomposing the 1PA spectrum into components with the transition dipole moments parallel (dash red line) and perpendicular (dot blue line) to the  $S_0 \rightarrow S_1$  transition [131], which allows revealing overlapping transitions hidden in the 1PA spectrum. Thus, if there is a 1PA transition corresponding to the 2PA transition, not visible in the 1PA spectrum, it may become visible after decomposing the 1PA spectrum into the two perpendicular components. The figure inserts show the chemical structure and the energy level diagram of **TBTAC**.

Similarly to most tetrapyrroles, the 1PA spectrum shows the Soret band around 300–400 nm ( $S_0 \rightarrow S_n$  on the energy level diagram, where  $S_n$  denotes the Soret band), and the Q-band around 700–760 nm. The Q-band consists of a strong peak at 753 nm ( $S_0 \rightarrow S_1$  on the energy level diagram), with two vibronic satellites (at 714 nm and 679 nm). A much weaker band at 605 nm may be attributed to a purely electronic transition to the next electronic state ( $S_0 \rightarrow S_2$  on the energy level diagram) [132, 133], which is polarized orthogonally to the  $S_0 \rightarrow S_1$  transition, according to the anisotropy measurements.

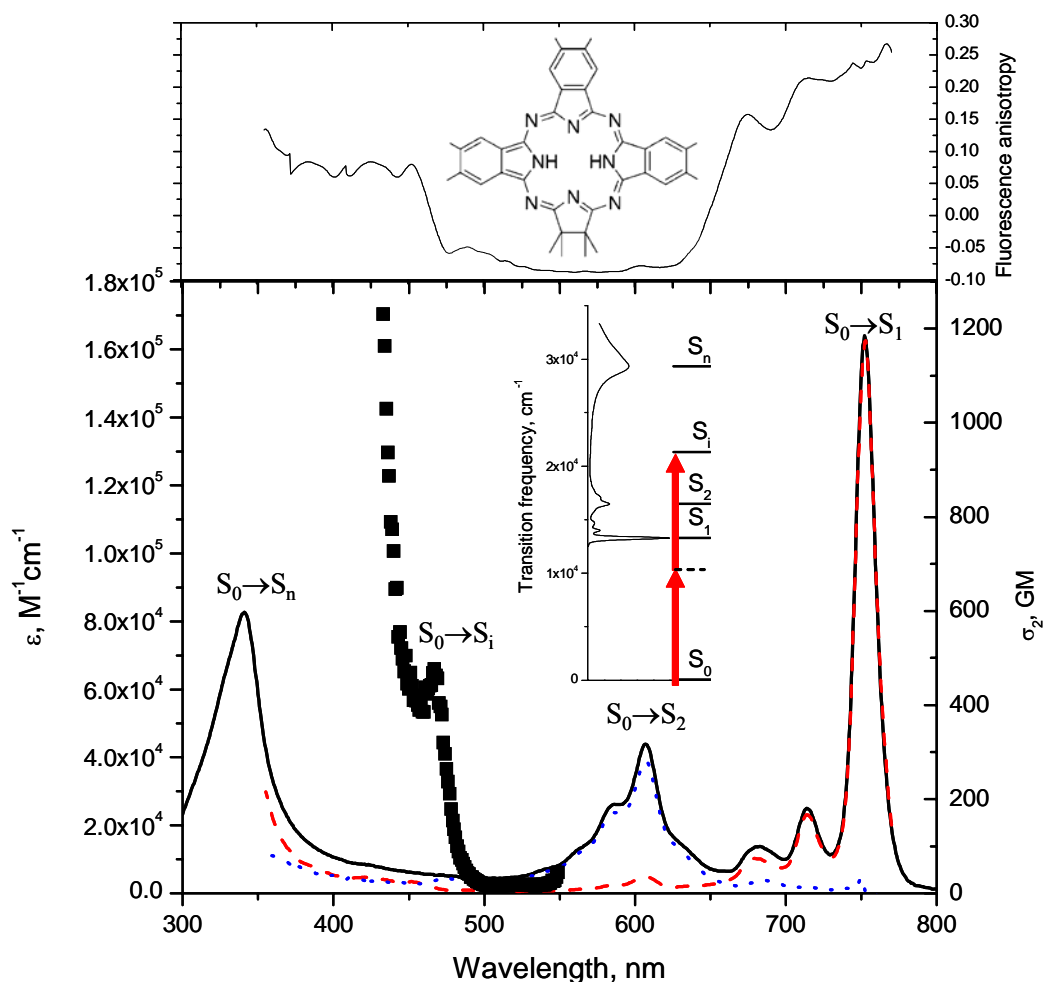


Figure 5.3. One-photon absorption (solid black line, left scale), two-photon absorption (black squares, right scale), fluorescence anisotropy (solid black line on the upper panel), and decomposition of the one-photon absorption spectra into transitions parallel (red dash line) and perpendicular (blue dot line) to the  $S_0 \rightarrow S_1$  transition of the free-base tribenzotetraazachlorin. Also shown is the chemical structure of the molecule. Level diagram shows possible energy transitions. Red arrows indicate a laser frequency needed to excite the  $S_0 \rightarrow S_i$  2PA transition

The 2PA spectrum in the region of laser wavelengths 800–1100 nm corresponds to the transition wavelengths between the Soret- and Q-bands. In this region the 1PA is very weak ( $\varepsilon < 10^4$ ) and does not show any distinct transitions. On the other hand, the 2PA

spectrum shows a very distinct narrow feature ( $S_0 \rightarrow S_i$  on the energy level diagram) corresponding to the laser wavelength of 935 nm, which we attribute to a  $g$ - $g$  transition. Note that the  $S_0 \rightarrow S_2$  transition, present in the 1PA spectrum, is red-shifted almost 150 nm from the observed 2PA transition. The detailed energy level structure above  $S_2$  is not established yet. Therefore, we denote the 2PA transition as  $S_i$ , where  $2 < i < n$ . At shorter wavelengths the 2PA cross sections increase rapidly due to the resonance enhancement effect [86, 87]. At longer wavelengths,  $\lambda > 1000$  nm, the cross sections are relatively small,  $\sigma_2 < 10$  GM.

Note that the position of the  $S_0 \rightarrow S_i$  transition appears 3 nm blue-shifted and the cross sections are enhanced by the resonance effect. The apparent peak of the  $S_0 \rightarrow S_i$  transition occurs at 935 nm, and the real peak occurs at 938 nm. As the laser wavelength approaches the maximum wavelength of the one-photon  $S_0 \rightarrow S_1$  transition (red arrow on the energy diagram) the resonance enhancement factor  $1/(1 - \nu_{01}/\nu)^2$  increases from 9.2 for  $\lambda = 1000$  nm through 17 for the  $S_0 \rightarrow S_i$  transition and up to 40 for  $\lambda = 870$  nm. Therefore, actually the whole 2PA spectrum is resonantly enhanced.

As a next step, we measure the transient absorption spectrum of **TBTAC**, as shown in figure 5.4. As described in chapter 3, we use the second harmonic of the Ti:Sapphire amplifier to excite molecules into their higher energy state,  $S_0 \rightarrow S_n$  (blue arrow on level diagram in the figure 5.4) from which the population quickly relaxes into the first excited state,  $S_1$  (wavy black arrow down). The tunable laser pulses, 550–1600 nm, probe the transitions from the first excited state  $S_1$  to higher-lying excited states (red arrow on the energy diagram).

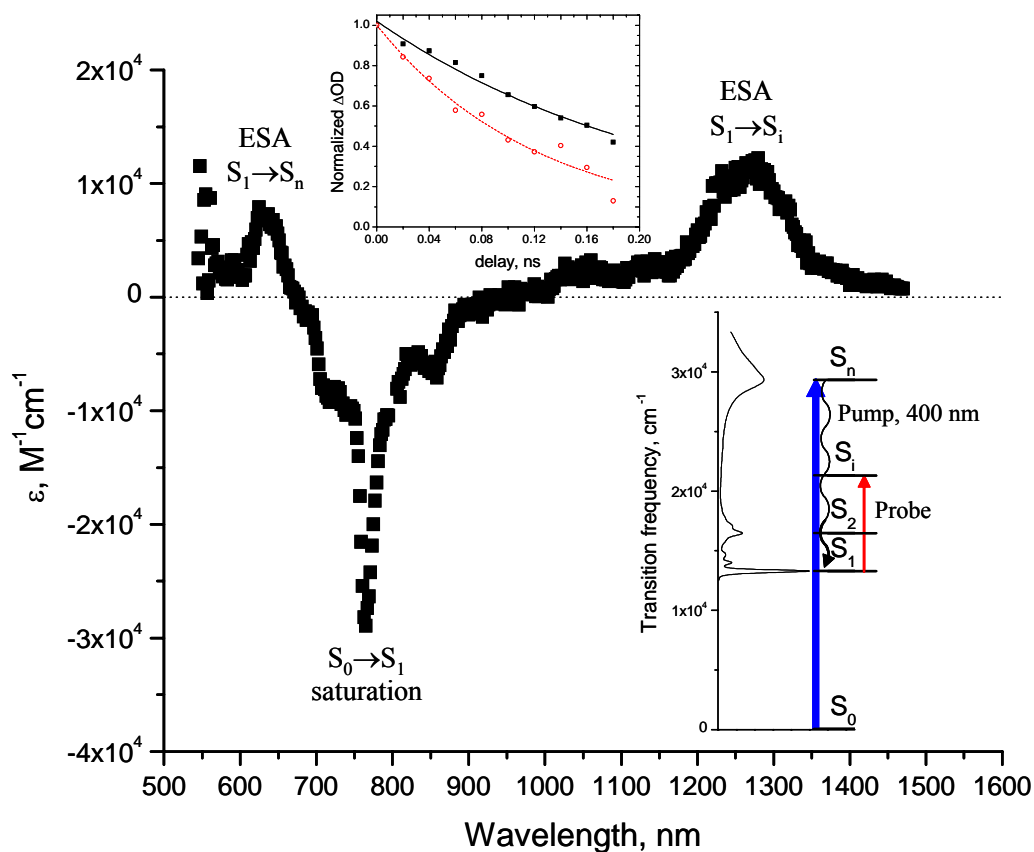


Figure 5.4. Transient absorption spectrum of the free-base tribenzotetraazachlorin. Negative values of extinction correspond to a saturation of absorption, and positive values correspond to a singlet-singlet excited state absorption. Level diagram shows possible energy transitions. Blue arrow represents the pump laser pulse, red arrow represents the probe laser pulse, and black arrow represents fast population decay from the higher-energy excited states to the first excited state. Insert on the top shows the decay of the normalized  $\Delta OD$  at two wavelengths: 1250 nm (black squares) and 1125 nm (red circles). Lines show exponential fits to the decays

The transient absorption spectrum of *TBTAC* shows ESA (positive values of the molar extinction) at wavelengths shorter than 650 nm, which is typical to tetrapyrroles [134]. The ESA peak at 600 nm corresponds to the  $S_1 \rightarrow S_n$  transition. The spectrum range between 650 and 800 nm corresponds to the Q-bands single-photon absorption, and the

transient absorption change is negative, meaning that the  $S_0 \rightarrow S_1$  absorption is saturated in this range of wavelengths due to a strong absorption of the pump. At longer wavelengths, the transient absorption spectrum shows a single peak at 1270 nm and a shoulder at 1000–1150 nm. The peak does not correspond to any transition in the 1PA spectra, but it does coincide in energy with the 2PA peak at 935 nm 2PA laser wavelength ( $S_0 \rightarrow S_i$  transition). This suggests that we see the same transition in both 2PA and transient absorption spectra.

The shoulder at 1000–1150 nm in the ESA of *TBTAC* is probably rather wide and too weak to be explained by a single transition. To elucidate its origin we measured temporal dependence of the transient absorption spectrum of *TBTAC* in the range 1100–1400 nm by varying the time delay between the pump and the probe. Since the decay rate of the ESA is proportional to the lifetime of the initial excited state, then if the decay rates of the shoulder and the peak are the same, they probably originate from the same excited state. If the decay rates are different, however, it is a clear sign of different initial excited states. Our measurement (see top insert of the figure 5.4) shows that the decay of the shoulder is twice as fast as the decay of the peak. This suggests that the shoulder and the peak most likely originate from different excited states. For example, if the peak represents a transition from the lowest vibrational level of the first excited state  $S_1$ , then the shoulder may be due to a transition from a vibrationally excited state of the  $S_1$  to some higher energy state other than  $S_i$ .

Before we turn to our final goal of comparison of the 2PA cross section in the  $S_0 \rightarrow S_i$  peak with the value predicted by the three-level model, let us note that the

expression (2.8) suggests that the line shapes of the transitions in the 2PA and the ESA spectra are the same. The line shape of the 2PA spectrum can be determined if one multiplies the measured spectrum by the resonance enhancement factor:

$$\tilde{\sigma}_2(\nu) = \sigma_2(\nu) \left( \frac{\nu_{01} - \nu}{\nu} \right)^2. \quad (5.2)$$

Figure 5.5 compares the reduced 2PA (expression (5.2)) and the ESA line shapes. The reduced 2PA line shape peaks at transition frequency of  $21370 \text{ cm}^{-1}$ . The peaks have almost the same width,  $\sim 800 \text{ cm}^{-1}$  and overlap quite well within experimental error in the transition frequency range  $\sim 20100\text{--}21500 \text{ cm}^{-1}$ . At the higher frequencies, the 2PA spectrum shows a strong increase, probably due to a higher energy transition. The origin of this higher energy transition is not established yet. It could be the  $S_0 \rightarrow S_n$  transition, in which case its peak is expected at  $\sim 29300 \text{ cm}^{-1}$  and is not accessible for 2PA measurements due to competing strong 1PA originating in the same frequency range. There also could be another transition at  $\sim 25800\text{--}26600 \text{ cm}^{-1}$  that is also not accessible for 2PA measurements. This last transition would not be visible in the ESA spectrum because it overlaps with the spectral region of the saturation of the  $S_0 \rightarrow S_1$  absorption.

Our next step is to compare the experimental peak cross section with the value estimated from the expression (2.8). We use expressions (3.3) to determine the transition dipole moment  $\tilde{\mu}_{12}$ . The following expression (see appendix B for further details) is used to determine  $\tilde{\mu}_{01}$ :

$$|\tilde{\mu}_{01}|^2 = \frac{3 \cdot 10^3 \ln(10) h c n}{8 N_A \pi^3 f^2} \int \frac{\varepsilon(\bar{\nu})}{\bar{\nu}} d\bar{\nu}, \quad (5.3)$$

where the integration is done over the whole  $S_0 \rightarrow S_1$  transition.

The 2PA cross section in expression (2.8) depends on the peak value of the line shape function,  $g(2\nu)$ , which, as discussed above, is the same for the 2PA and the ESA transitions. To determine this value we fit the observed ESA peak with a Gaussian peak and normalize its area to unity. The results are presented in table D.8. We estimate the experimental errors to be  $\sim 20\%$  for the transient absorption and extinction measurements,  $15\%$  for the 1PA and extinction measurements, and  $15\%$  for the line shape function determination.

So far, the only parameter that is unknown is the angle  $\alpha$  between the transition dipole moments  $\vec{\mu}_{01}$  and  $\vec{\mu}_{12}$ . The symmetry of the chemical structure of the molecule (figure 5.3) suggests that the transition dipole moments should be aligned along the axes passing through the opposite inner nitrogen atoms (vertical or horizontal directions in the figure), therefore the angle  $\alpha$  can be either  $\alpha \approx 0^\circ$  or  $\alpha \approx 90^\circ$ . This angle can be measured experimentally by comparing the two-photon fluorescence excited with the linearly and circularly polarized light as shown below.

Expression (2.5) shows that the 2PA cross section depends on the angles between the dipole moments and the optical electric field. Because of random orientation of the molecules in the solution, one needs to average expressions of the form  $(\vec{\mu}_{im} \cdot \vec{e})(\vec{\mu}_{mj} \cdot \vec{e})$  over the all possible orientations of the molecules (isotropic averaging). An example of such an averaging for the two-level model and linearly polarized light is given in appendix A.

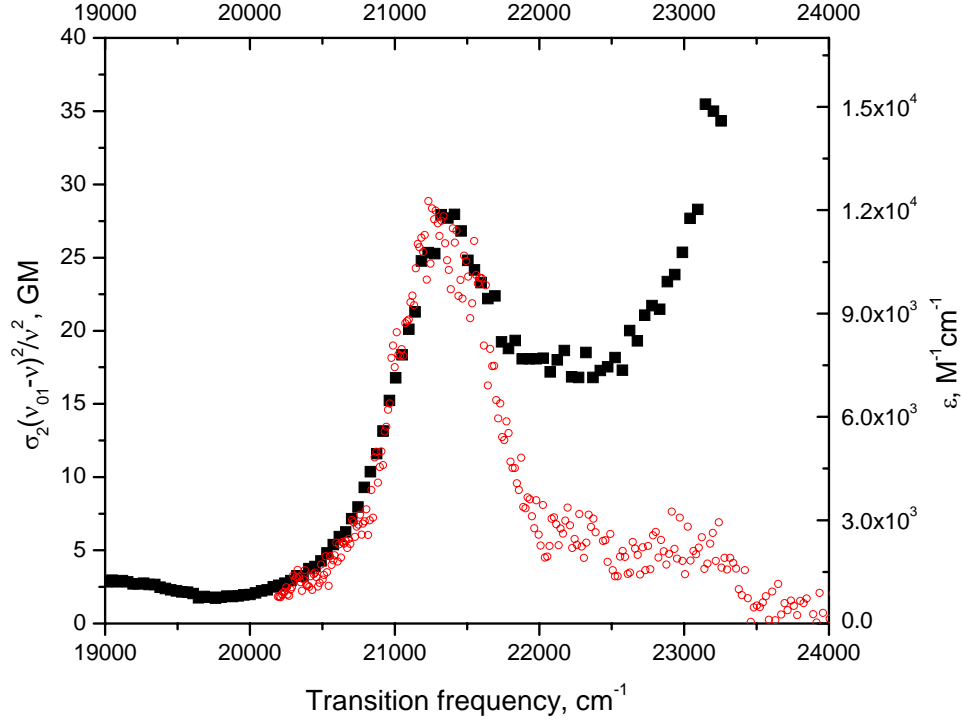


Figure 5.5. Two-photon (black squares) and excited state (red circles) line shapes of the free-base tribenzotetraazachlorin. Excited state absorption spectrum is plotted in the full (pump+probe) transition frequencies for easier comparison of the transitions

The averaging yields  $\left\langle (\vec{\mu}_{01} \cdot \vec{e})^2 (\vec{\mu}_{12} \cdot \vec{e})^2 \right\rangle_{\hat{\Omega}} = \frac{2(2\cos^2 \alpha + 1)}{15} |\vec{\mu}_{01}|^2 |\vec{\mu}_{12}|^2$  for linearly polarized light and  $\left\langle (\vec{\mu}_{01} \cdot \vec{e})^2 (\vec{\mu}_{12} \cdot \vec{e})^2 \right\rangle_{\hat{\Omega}} = \frac{(\cos^2 \alpha + 3)}{15} |\vec{\mu}_{01}|^2 |\vec{\mu}_{12}|^2$  for circularly polarized light [135, 136]. Therefore, the 2PA-induced fluorescence intensity will be different depending whether it is excited with linearly or circularly polarized light. The angle  $\alpha$  can be evaluated from the relation:

$$2 \frac{2(\cos \alpha)^2 + 1}{(\cos \alpha)^2 + 3} = \frac{F_{\text{vert}}}{I_{\text{vert}}^2} \frac{I_{\text{circ}}^2}{F_{\text{circ}}}, \quad (5.4)$$



where  $F_{vert}$  and  $F_{circ}$  are the 2PA-excited fluorescence signals, obtained upon excitation with linearly and circularly polarized pulses, respectively, and  $I_{vert}$  and  $I_{circ}$  are the corresponding pulse intensities. We measure the angle to be close to  $\alpha = 0 \pm 10^\circ$ .

Now we plug all the measured parameters into the expression (2.8) and obtain  $\sigma_2 = 34 \pm 10$  GM. This value compares very well with the 2PA cross section measured experimentally ( $\sigma_2 = 28 \pm 6$  GM). The values are also presented in D.8. It is quite remarkable that the 2PA cross section values agree quantitatively within the experimental errors. This result suggests that a) the measured 2PA cross section in the  $S_0 \rightarrow S_i$  peak can be explained in terms of the three-level model, b) the observed 2PA and ESA transitions are indeed the same, and c) the  $S_0 \rightarrow S_i$  transition can be attributed to the g-g transition.

Such a good correspondence between the experimental and theoretical peak cross sections makes us attempt simulating the entire 2PA spectrum based on the linear and ESA measurements. As shown in figure 5.5 one can use ESA to determine line shape functions for the g-g transition. Then, one can use the following expression to simulate the 2PA spectrum of the g-g transition:

$$\sigma_2(\nu) = \frac{\nu^2}{(\nu_{01} - \nu)^2} \tilde{\sigma}_2 \tilde{g}(\nu), \quad (5.5)$$

where  $\tilde{\sigma}_2$  is the peak 2PA cross section of the transition, obtained using expressions (2.8) and (5.2) and listed in table D.8, and  $\tilde{g}(\nu)$  is the line shape function determined from the ESA spectrum and normalized to unity in the maximum.

Figure 5.6 shows the measured 2PA spectrum overlapped with the simulations based on the expression (5.5). The simulated spectrum agrees well with the experimental data for the  $g$ - $g$  transition, but shows quite significant disagreement at frequencies higher than  $22000\text{ cm}^{-1}$ . This may be because the second 2PA peak of the *TBTAC* is not yet included in our model.

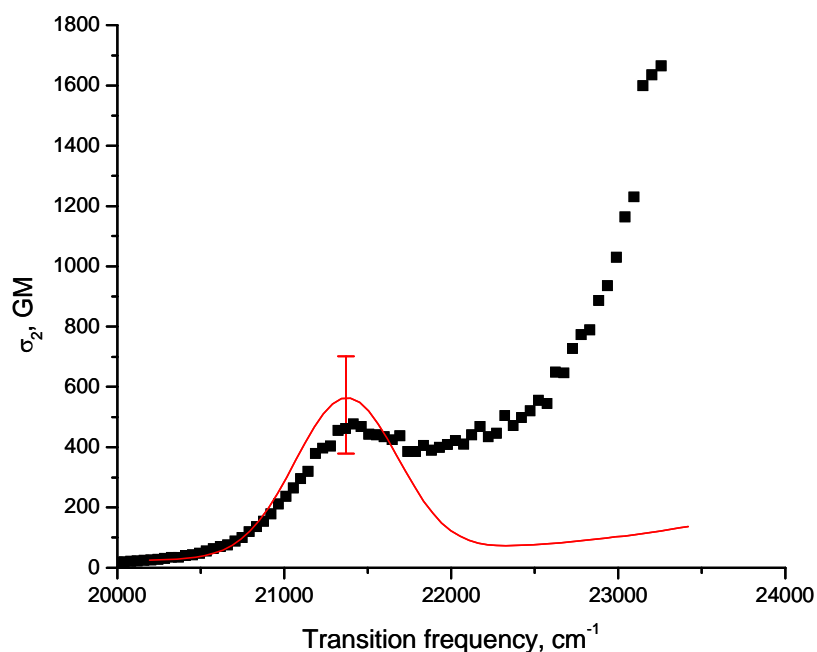


Figure 5.6. Comparison of the experimentally measured two-photon absorption spectrum (from figure 5.3, black squares) with the prediction (red line) based on the excited state absorption measurements and three-level model

Even though the analysis presented here may seem to be rather straightforward, it is to our best knowledge the first time that such good quantitative agreement between  $\sigma_2$  values and ESA data has been shown for large organic chromophores. A similar approach was recently explored in our work to explain the 2PA spectra of symmetrical

phthalocyanines [82]; however, in this work we did not have directly measured values of the transition dipole moments between the excited states of phthalocyanines.

Surprisingly, the nominally non-centrosymmetrical molecule, **TBTAC**, preserves the  $g$ - $g$  transition typical of symmetric compounds. Such an observation allows us to conclude that despite the formal symmetry break, the wavefunctions remain quasi-centrosymmetrical in **TBTAC**. This is in line with the quantum chemical calculations suggesting that the electronic wavefunctions in tetraazoporphyrins do not encounter the outer part of the two pyrroline rings [137, 138] and thus remain quasi-centrosymmetrical.

To conclude, a systematic quantitative study of the applicability of the few-essential-levels model is presented. We showed that the perturbation theory applied to two- and three-level systems quantitatively predicts the 2PA cross sections, provided that the necessary molecular parameters such as transition- and permanent dipole moments are known from independent measurements.

First, we have analyzed three different types of dipolar chromophores: substituted diphenylaminostilbenes, push-pull porphyrins, and carbazol-substituted stilbenes. We determined the 2PA cross section values in two alternative ways: (a) by direct measurements using the femtosecond fluorescence method and (b) by using perturbation theory formula for two-level system with non-zero permanent dipole moment difference between the ground- and excited states. For at least half of the systems studied, the discrepancy between (a) and (b) was less than 20%, and for all molecules was less than 50%. This is the first time when such direct quantitative correspondence was

demonstrated for different classes of molecules. Our results show that relatively straightforward linear spectroscopic measurements can predict the nonlinear absorption in the lowest-energy transition with an appreciable absolute accuracy.

Then we extended this approach to a model three-level system. We obtained the higher excited state transition dipole moments from transient absorption measurements. An interesting conclusion was drawn that even though **TBTAC** nominally lacks center of symmetry, the molecule displays a pronounced two-photon allowed, but one-photon forbidden transition near 2PA laser wavelength of 940 nm, which we assign as a *gerade-gerade* transition. The transition to the same state was also observed in the ESA and the corresponding transition dipole moment was determined from the pump-probe experiment. The applicability of the three-level model for 2PA in **TBTAC** was supported by the fact that the 2PA cross section in the above mentioned transition is in good quantitative agreement with that calculated using expression (2.8).

## 6. APPLICATION OF TWO-PHOTON ABSORPTION: 3D OPTICAL MEMORY

There is a growing demand for low cost rewritable terabyte (TB) data storage that would supersede current optical disks. Volumetric optical storage [39-59] takes advantage of the third dimension – thickness of the medium – to provide up to  $10^2$ – $10^3$  times increase over maximum capacity of current two-dimensional optical disks. Diffraction-limited focusing with a large NA objective has the ability to efficiently concentrate the incident laser power in a tight 3D volume (voxel). Because the rate of 2PA increases as a square of the instantaneous power density, the 2PA will occur only in this illuminated focal volume. It has been proposed that, by using 2PA-induced photochromic switching for the writing and 2PA-induced fluorescence for the readout, one can potentially address a large number of data layers inside an optical disk [41, 53]. However, assuming typical 2PA cross sections of photochromic molecules,  $\sigma_2 = 1 - 100$  GM, and practical limitations on the maximum laser power density,  $I < 10^8$  W/cm<sup>2</sup>, the efficiency and speed of such 2PA recording and readout still remain relatively small. The small 2PA cross section of known photochromic materials constitutes a fundamental challenge for the technology, especially because terabyte storage implies fast writing and readout. Simple estimations show that for a 1 TB-disk, the writing/readout speed should be at least  $>100$  Mbit/s. The challenge is therefore consists in finding photochromic materials that satisfy simultaneously stringent requirements for high 2PA cross section as well as high efficiency and fidelity of photo-induced switching.

Some tetrapyrroles have very large 2PA cross sections,  $\sigma_2 > 10^3 - 10^4$  GM, in the near-IR range of wavelengths [88, 129, 139-142]. This fact, in combination with the possibility to switch non-symmetrical free-base tetrapyrroles optically between two spectrally distinct tautomeric forms [143-147], makes them attractive candidates for high capacity storage.

It was also shown that at frequencies just below the lowest energy  $S_0 \rightarrow S_1$  band, where the resonance enhancement is the largest, 1PA from thermally-excited vibrational levels in the electronic ground state may efficiently compete with resonantly-enhanced 2PA [142, 148]. This concurrent 1PA poses a serious problem for TB storage, because it causes chromophores to switch not only in the focus voxel, but rather in the whole illuminated volume. In a disk, comprising a large number of data layers, the out of focus 1PA is especially damaging because it strongly reduces the signal-to-background ratio (SBR). For this reason, in all previous work comprising 2PA 3D memory systems [39, 40-55] the laser frequencies were detuned far to the red from the 1PA resonance. On the other hand, if the frequency detuning is too large, then the signal-to-noise ratio (SNR) is reduced because of decreasing 2PA cross section. The goal of the study presented in this chapter is to find out whether a compromise can be achieved between these mutually exclusive requirements.

### Basic Principles of Two-Photon Volumetric Recording and Readout

Our first step is to build a quantitative model of volumetric memory. Figure 6.1 shows the principle of writing and readout of a two-photon volumetric optical disk [41,

53]. Each data bit is recorded in one voxel (volumetric pixel). The voxel (parallelepiped for simplicity) has vertical and horizontal sizes,  $d_v$  and  $d_h$ , respectively. The vertical and horizontal safeguard intervals between the voxels are  $h_v$  and  $h_h$ . The voxels are arranged in  $M$  vertically stacked layers. If  $T$  is the thickness of the disk, then the number of layers is  $M_{\max} = T(d_v + h_v)^{-1}$ . The bit area density (per layer) is  $R_{\max} = (d_h + h_h)^{-2}$ .

The photochromic molecules can be present in two discernibly different states denoted here as form A and form B. In the electronic ground state, the spontaneous transformation between A and B is prevented by a potential energy barrier (figure 6.1). The barrier height is much less or absent in the excited electronic state, allowing for the switching from A to B to take place upon absorption of light.

The molecules are evenly dispersed in a homogeneous optically-transparent polymer (such as polycarbonate). If the concentration of molecules is  $C$  (molecules per  $\text{cm}^3$ ), then each voxel contains, on average,  $N_0 = Cd_v d_h^2$  molecules.

A large numerical aperture ( $\text{NA} > 0.5$ ) lens focuses the laser beam into a small 3D diffraction-limited spot that matches the shape and dimensions of the voxel (figure 6.1a). Initially, i.e. before writing, the chromophores are all assumed to be in the form A. Bit value “1” is recorded by illuminating the corresponding voxel with brief laser pulses. The laser frequency  $\nu_L$  is usually close to one-half of the 2PA peak frequency of the form A. The illumination causes the molecules to switch to the form B, which is considered as bit value “1”. The bit value “0” corresponds to form A. Subsequent bits are written by rotating the disk and/or by moving the focus to the next voxel. Under ideal circumstances the intensity outside of the focus voxels is not sufficiently high to cause 2PA at any

appreciable level. However, as we will discuss below, in practice, a long-wavelength tail of 1PA absorption can cause an appreciable background in the whole illuminated volume of the disk.

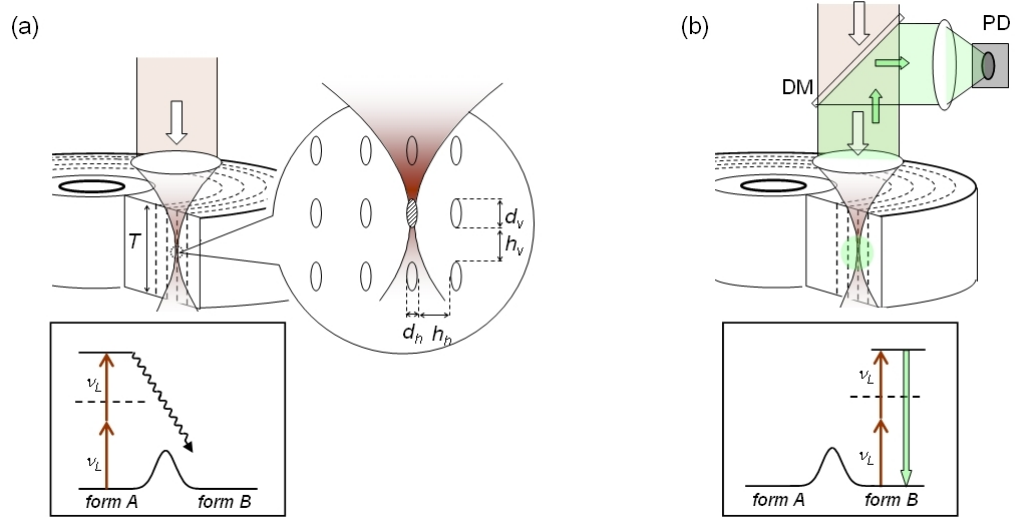


Figure 6.1. Basic principle of 2PA-based volumetric optical disk.  $T$ ,  $d_h$ ,  $d_v$  are the thickness, horizontal and vertical sizes of the voxel, respectively,  $h_h$  is the distance between two neighboring voxels in a layer,  $h_v$  is the distance between layers. (a) Writing. Upon 2PA excitation, form A switches to form B, which is separated by energy barrier (insert). (b) Readout. 2PA of form B results in its fluorescence that is collected by the focusing lens. Dichroic mirror (DM) reflects the fluorescence to a photo detector (PD)

For the readout (figure 6.1b), the laser is focused consequently on each voxel. 2PA-induced fluorescence of the form B is collected by the same large NA lens, and reflected onto a photo-detector. Bit value “1” is assigned when the sufficiently large number of photons is detected. Otherwise the assigned bit value is “0”.

### Fast Bit Access Rate and Single Femtosecond Pulse Recording

The above bit-by-bit storage idea is worthwhile only if the information can be written and read out at a sufficiently high rate. It is therefore reasonable to require that



the minimum bit rate be at least 100 MHz or higher (100 MHz is a typical pulse rate of mode-locked lasers such as Ti:Sapphire femtosecond oscillators). This is the same as saying that the maximum time allotted for recording of one bit is about 10 ns, in which case, the minimum time for recording of 1 TB ( $8 \cdot 10^{12}$  bits) will already be about one day.

Let us consider the laser source to be typical femtosecond Ti:Sapphire oscillator. To estimate the peak power let us assume for simplicity that the pulse has a rectangular shape of duration  $t_L = 100$  fs. Then the peak intensity is,  $I = n_L h\nu_L t_L^{-1}$ , where  $h\nu_L$  is the photon energy and  $n_L$  is the average number of photons in one pulse.

While the higher intensity results in stronger 2PA, there is a practical upper limit due to competing nonlinear-optical processes such as self-focusing, white light generation, optical breakdown, etc. These processes occur above the typical threshold intensity,  $I_{\max} \approx 10^{11}$  W·cm<sup>-2</sup> [63] (in a polymer medium and for 100-fs pulses). At 800 nm wavelength this corresponds to about  $10^{30}$  photons·s<sup>-1</sup>·cm<sup>-2</sup>. If we suppose, that the focus spot area  $d_h^2 \approx (3\mu m)^2$ , then the maximum allowed pulse energy will then be  $E = Id_h^2 t_L \sim 10^{-9}$  J.

Another practical limitation is due to thermal effects. Exposure of a small volume to high average optical power raises the sample temperature, which, in turn may lead to the thermal destruction of the chromophores and polymer matrix. To minimize the thermal effects, the average incident power of the laser beam, tightly focused on the voxel area should be below ~100 mW. Combining this with the previous estimate of the maximum pulse energy, we arrive again at the 100 MHz maximum pulse repetition rate.

Using Resonance Enhancement of Two-Photon  
Absorption to Increase Signal-to-Noise

The discrimination between "1" and "0" is only practical if the signal-to-noise ratio is sufficiently large, e.g.  $SNR \geq 4$ . Assuming an ideal situation, the photo-detector is limited only by shot-noise. If we also assume that the 2PA takes place only inside the focus voxel, and that the contribution from 1PA, either inside or outside of the focus is negligibly small, then the signal-to-noise ratio can be expressed as (see appendix E for details):

$$SNR = \frac{1}{2\sqrt{2}} I_w I_r NA t_L \sqrt{\eta N_0} \sqrt{\varphi_{A \rightarrow B} \varphi^B} \sigma_2, \quad (6.1)$$

where  $I_w$  and  $I_r$  refer to the intensity of the laser pulses used for bit writing and read out respectively,  $\sigma_2 = \sqrt{\sigma_2^A \sigma_2^B}$  is the geometric mean of the 2PA cross section of the two forms,  $\varphi_{A \rightarrow B}$  is the quantum efficiency of photochemical transformation,  $N_0$  is the number of molecules in the voxel,  $\varphi^B$  is the form B quantum efficiency of fluorescence, and  $\eta$  is the quantum efficiency of the detector.

Expression (6.1) shows that the SNR can be expressed in terms of the laser and molecular parameters. All of them, except for the 2PA cross section,  $\sigma_2$ , are limited in practice by values shown below. Therefore, increasing the 2PA cross sections is essential for higher SNR values. Substituting realistic values of the parameters into (6.1),  $N_0 = 10^8$ ,  $\varphi_{A \rightarrow B} = 0.1$ ,  $\varphi^B = 0.1$ ,  $\eta = 0.5$ ,  $I_w = 5 \times 10^{29}$  photons·cm<sup>-2</sup>·s<sup>-1</sup>,  $I_r = 5 \times 10^{28}$  photons·cm<sup>-2</sup>·s<sup>-1</sup>,  $t_L = 100$  fs, and  $NA = 0.75$ , we see, that for volumetric memory to be

practical ( $SNR \geq 4$ ), the minimum required molecular 2PA cross section is  $\sigma_2 > 10^3$  GM.

The question now arises whether current 2PA materials can meet this requirement, and if not, then what can be done to achieve this goal.

In order to compare 2PA materials, one can introduce effective molecular figure of merit (FOM). The FOM can show which molecule is the best for 2PA memory, assuming that the recording and readout conditions are kept the same. Inspection of expression (6.1) suggests  $FOM = \sqrt{\sigma_2^A \sigma_2^B \varphi^B \varphi_{A \rightarrow B}}$  be used. Table D.9 summarizes the 2PA data for some of the current 2PA photochromic materials including spiropyrans [149], fulgides [150], and diarylethenes [151, 152]. We see that, most of the reported  $\sigma_2$  values are considerably below  $10^3$  GM. Table D.9 lists also the quantum yields of the  $A \rightarrow B$  photo-transformation and of fluorescence of form B, along with the FOM.

As a rule, photochromic molecules (including those listed in table D.9), lack a center of inversion. In chapter 5 of this dissertation we showed that under certain conditions, if the laser frequency is close to one-half of the first electronic transition energy, then the 2PA cross section is well described by the two-level model (figure 2.1a).

Indeed, using typical parameter values for photochromic molecules (table D.9),  $|\Delta\vec{\mu}_{01}| = 10$  D,  $|\vec{\mu}_{01}| = 10$  D, and a 2PA linewidth of  $\sim 1000$   $\text{cm}^{-1}$  in expression (2.6) gives an upper limit of the peak 2PA cross section  $\sigma_2 \sim 500$  GM. We must thus conclude that for current chromophores the required minimum  $\sigma_2$  values are most likely not attainable, at least not within the framework of large detuning from any intermediate resonances.

Orders of magnitude larger  $\sigma_2$  value can be obtained if the laser is tuned closer to some intermediate 1PA resonance, acting as a third (intermediate) energy level. Ideally, this level should occur slightly higher in energy than half-way between the ground and final states (see chapter 2) [87, 88, 129, 139-142, 153, 154]. This provides the maximum resonance enhancement effect, while still maintaining true instantaneous character of the two-photon process. Expression (2.8) describes resonance enhancement in the three-level system.

Assuming realistic parameters for transition dipole moments,  $|\Delta\vec{\mu}_{01}|=10$  D,  $|\vec{\mu}_{01}|=10$  D, and relative detuning,  $\nu_{01}/\nu \sim 1.2$ , peak 2PA cross section could be  $\sigma_2 \sim 10^3 - 10^5$  GM, which is much closer to the required minimum value. Below we analyze the performance of the memory with an assumption that the 2PA cross section is enhanced by nearby intermediate resonance.

#### Numerical Simulations: Tradeoff between Signal-to-Noise and Signal-to-Background Ratios

Although the photon budget for single-pulse-per-bit memory access is exceptionally tight, our estimates of the high cross section values available in three-level systems have a good chance of meeting the minimum SNR requirement. On the other hand, by tuning closer to the intermediate resonance, we may no longer safely assume that the 1PA is negligible. In particular, if the writing laser frequency is too close to the 1PA resonance, then this may give rise to unintentional switching of the molecules due to 1PA outside of the focus. Our next goal is to quantify the most important tradeoff between 2PA and 1PA,

in which, on the one hand, one would like to enhance SNR by tuning the laser frequency closer to the 1PA resonance, but on the other hand, one would like to enhance signal-to-background ratio (SBR) by detuning further from the resonance.

Here we need to be able to model the 1PA and 2PA spectra of arbitrary chromophores such that the small (relative to the peak 1PA) effect of the 1PA background would be quantitatively described by the model in order to compare it with the 2PA. Most critically, we need to be able to model a dependence of the 1PA on the temperature, detuning from the resonance, and laser power. The details of the analysis of the dependence of the 1PA and the 2PA and associated SNR and SBR on intrinsic molecular parameters, and external factors such as laser frequency and intensity, as well as spectral shape of 1PA and 2PA, are presented in appendix E. Briefly, we use the following expressions to calculate SBR and SNR for a hypothetical chromophore:

$$SBR = \frac{N_w}{N_B} = \frac{2}{M} \frac{P_{2PA}^w}{P_{1PA}^w}, \quad (6.2)$$

$$SNR = \sqrt{P_{2PA}^w P_{2PA}^r N_0 \varphi^B \varphi_{A \rightarrow B} \frac{(NA)^2}{2} \eta}. \quad (6.3)$$

To find the probability rates for the 1PA writing ( $P_{1PA}^w$ ) and 2PA writing ( $P_{2PA}^w$ ) and readout ( $P_{2PA}^r$ ) we simulate a complete 1PA spectrum of the chromophore by using a phenomenological model of absorption, assuming that the 1PA depends on detuning from the transition frequency,  $\nu_{01} - \nu$ , peak 1PA cross section,  $\sigma_1^{\max}$ , temperature  $T$ , and the intensity of laser pulses. The 2PA spectrum of the chromophore is simulated by using a

phenomenological model, which assumes dependence of the spectrum on the peak 2PA cross section,  $\sigma_2(\nu_{0I})$ , laser frequency, 2PA line shape, and the laser intensity.

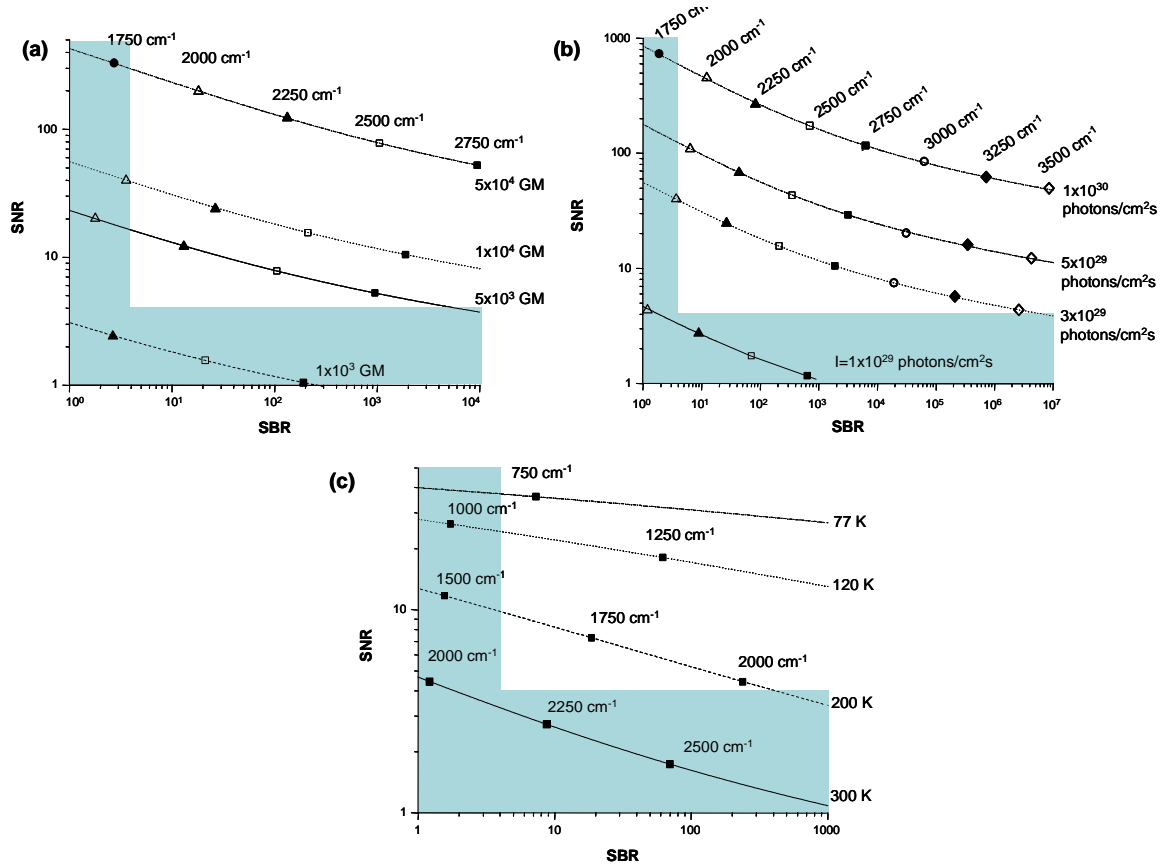


Figure 6.2. SNR versus SBR diagrams obtained for an “ideal” molecule as a result of model simulations for a set of parameters described in appendix E and presented in table D.10. Each marked data point represents a particular integer value of detuning,  $\nu_{0I}-\nu$ , with the corresponding value in  $\text{cm}^{-1}$  shown on top of the curve. The desired parameter space, where  $\text{SNR} > 4$  and  $\text{SBR} > 4$ , is shown as non-shaded area. Figure 6.2a shows a family of curves with different peak 2PA cross section values,  $\sigma_2(\nu_{0I})$  with fixed temperature (300 K) and peak laser intensity ( $3 \times 10^{29} \text{ photons} \cdot \text{cm}^{-2} \cdot \text{s}^{-1}$ ). In figure 6.2b we vary laser intensity, while the temperature (300 K) and the peak 2PA cross section ( $10^4 \text{ GM}$ ) are fixed. Figure 6.2c presents the effect of temperature variation with constant cross section ( $10^4 \text{ GM}$ ) and intensity ( $I = 10^{29} \text{ photons} \cdot \text{cm}^{-2} \cdot \text{s}^{-1}$ )

The resulting SNR and SBR depend on many parameters, of which the most important are the detuning, temperature, peak 2PA cross section, and the laser intensity.

For simplicity the results of our simulations are presented in figure 6.2 in the form of

SNR vs. SBR diagrams. The diagrams show values of SNR and SBR as continuous functions of detuning with all other parameters fixed. Each marked data point represents a particular value of detuning,  $\nu_{01} - \nu$ , with the corresponding value in  $\text{cm}^{-1}$  shown on top of the curve. The sets of curves are plotted for varied values of the peak 2PA cross section (figure 6.2a), laser intensity (figure 6.2b), and temperature (figure 6.2c). The allowed parameter space is given by the  $SNR > 4$  and  $SBR > 4$  conditions and is shown as the non-shaded area, whereas shaded regions show that at least one of the two key requirements is not fulfilled. All the parameters used in these simulations are summarized in table D.10. In our simulations we are pushing the memory capacity towards a 1TB disk, assuming the number of data layers to be  $M = 1000$ .

Figure 6.2a shows how, for the same writing and readout intensity,  $I_w = I_r = 3 \times 10^{29} \text{ photons} \cdot \text{cm}^{-2} \cdot \text{s}^{-1}$ , SNR and SBR vary as a function of the detuning from the 1PA resonance at room temperature, 300K. Each curve corresponds to a particular peak 2PA cross section value,  $\sigma_2(\nu_{01})$ . As discussed above, for these particular conditions, the peak 2PA cross section needs to be at least,  $\sigma_2(\nu_{01}) = 5 \times 10^3 \text{ GM}$ . Optimal detuning varies with the cross section, and for  $\sigma_2(\nu_{01}) = 5 \times 10^3 \text{ GM}$  is in the range 2100–3000  $\text{cm}^{-1}$ . The SBR increases drastically with detuning from the intermediate level, since 1PA falls nearly exponentially with the detuning, but 2PA decreases much slower, approximately as  $(\nu_{01} - \nu)^{-2}$ . It is also worth noting that in case of far off-resonance 2PA, the corresponding data points will fall into the shaded region (at the far right-hand side of the graphs). This is because at large detuning,  $\nu_{01} - \nu > 3000 \text{ cm}^{-1}$ , SBR is large, while

SNR becomes very small due to weak 2PA even for large  $\sigma_2(\nu_{01})$ . This supports our assertion above that the resonance enhancement of 2PA is indispensable for fast >100 MHz storage. The result shows that even though tuning the laser frequency closer to an intermediate resonance increases background, it is still possible to achieve desirable values of SNR and SBR at ambient temperature with reasonable high laser intensity and 2PA cross sections.

Figure 6.2b shows the variation of SNR versus SBR as a function of intensity. In this case, the cross section ( $\sigma_2(\nu_{01})=10^4$  GM) and the temperature ( $T=300$  K) were the two fixed parameters. The plot reveals that the minimum required intensity is of the order of  $I_w = I_r = 3 \times 10^{29}$  photons·cm<sup>-2</sup>·s<sup>-1</sup>. This value is important because it provides some flexibility in choosing the laser power below the critical threshold. On the other hand, even with a rather high peak 2PA cross section, the abovementioned maximum intensity threshold,  $I = 3 \times 10^{29}$  photons·cm<sup>-2</sup>·s<sup>-1</sup>, is still quite high, thus justifying our previous assumption that 2PA storage requires femtosecond laser excitation. The optimal detuning varies in the range from 2000 to 3500 cm<sup>-1</sup>.

Finally, figure 6.2c shows SNR and SBR for different working temperatures, while the peak cross section and intensity are fixed at  $\sigma_2(\nu_{01})=10^4$  GM and  $I = 10^{29}$  photons·cm<sup>-2</sup>·s<sup>-1</sup>, respectively. At room temperature, the 1PA low frequency tail extends far from the transition maximum, and 1PA can still be significant at detunings of  $\sim 2000$  cm<sup>-1</sup>. At  $T < 100$  K, on the other hand, the probability of population of vibrational levels with detunings  $> 500$  cm<sup>-1</sup> is less than  $e^{-7.5}$ , and 1PA becomes negligibly small at



the given detuning. Thus, with the parameters chosen in figure 6.2c, the desired SNR and SBR cannot be achieved at room temperature. However, lowering the temperature just below 250 K can already give the required improvement.

Our data suggest that lowering of the temperature of the storage medium provides a significant improvement of the performance of the fast 3D memory disk. For example, by reducing the temperature from 300 to 200 K, the SBR at  $\nu_{01} - \nu = 2000 \text{ cm}^{-1}$  is improved by two orders of magnitude. We note that  $T = 200 \text{ K}$  is well within the operation range of solid state thermoelectric cooling elements.

#### Experimental Characterization of a Model Compound for 3D Optical Memory

Next we perform experiments with a model 2PA chromophore, non-symmetrical metal-free phthalo-naphthalocyanine ( $\text{Pc}_3\text{Nc}$ ) [146].  $\text{Pc}_3\text{Nc}$  can be switched between tautomer  $T_1$  and tautomer  $T_2$  by photo-excitation. At room temperature, the ground state energy barrier is less than  $kT$ , and nearly all molecules are in the form  $T_1$  because of its lower energy. To avoid spontaneous switching from  $T_2$  back to  $T_1$ , we perform our measurements at  $T < 100 \text{ K}$ , where both forms are stable in the ground state. Also, lowering the temperature helps to increase SBR by reducing the long-wavelength absorption (see above). The quantum efficiencies of the switching measured at 77 K [155] are:  $\phi_{T_2 \rightarrow T_1} = 0.014 \pm 0.003$  and  $\phi_{T_1 \rightarrow T_2} = 0.0025 \pm 0.0005$ . Details on the 2PA-induced photo-tautomerization in  $\text{Pc}_3\text{Nc}$  are given in appendix E.

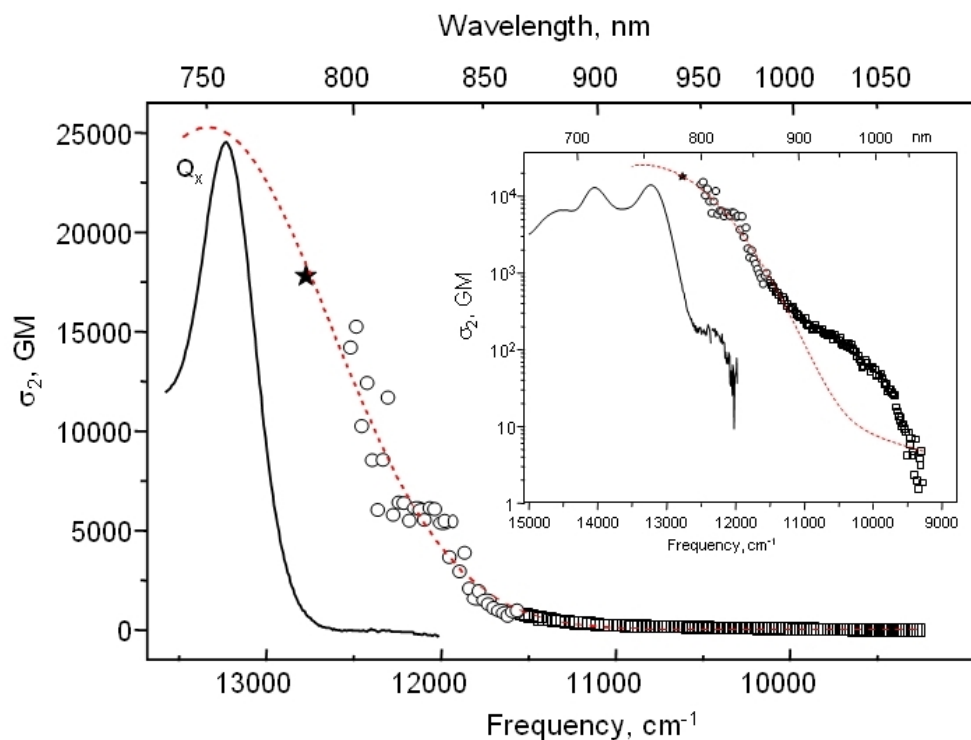


Figure 6.3. 1PA (solid line) and 2PA (symbols) spectra of  $\text{Pc}_3\text{Nc}$ . 1PA spectrum is measured in methylene chloride at room temperature. The open squares present 2PA data obtained at room temperature in methylene chloride, open circles – at 77 K in polyethylene film, and the asterisk corresponds to the datum obtained at 77 K from the rate of photochemical transformation. Dashed line is the best fit of experimental 2PA spectrum to the Voigt function with central frequency fixed at  $13330 \text{ cm}^{-1}$ . Inset shows semi-logarithmic presentation of the spectra

Figure 6.3 shows the 2PA spectrum of  $T_1$  measured at 77K (open circles) and room temperature (open squares). The measurements at room temperature were done as described in chapter 3. For the low temperature measurements  $\text{Pc}_3\text{Nc}$  was evenly dispersed in thin polyethylene film. The film was fixed inside the variable temperature cryostat and cooled to liquid nitrogen temperature,  $T = 77 \text{ K}$ . The cryostat was added to the experimental setup presented in figure 3.1 in place of the sample, and the 2PA spectrum was measured as described in previous chapters. The low temperature spectrum was measured in the wavelength region overlapping the spectrum measured at room

temperature. The 2PA cross sections were assumed to be the same in the overlapping region, so that the shorter wavelength part of the low temperature spectrum was normalized to the cross sections obtained at room temperature.

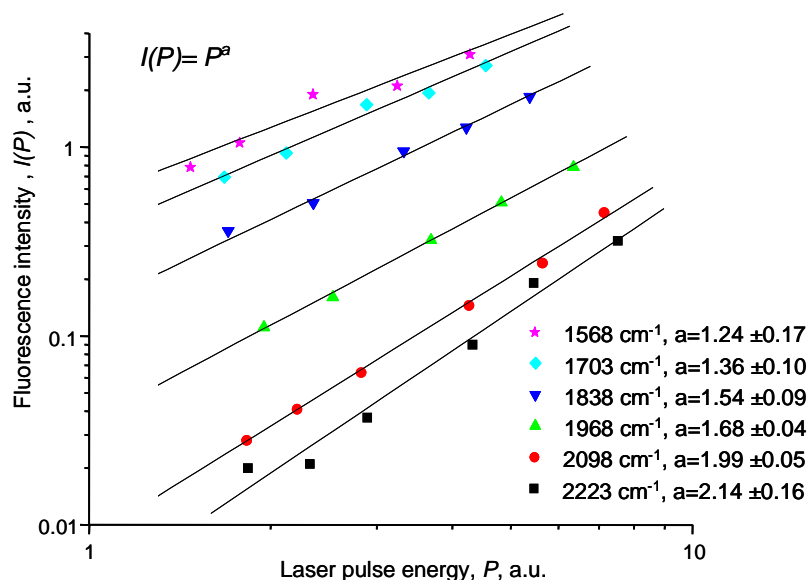


Figure 6.4. Dependence of fluorescence signal intensity ( $I$ ) on excitation laser pulse energy ( $P$ ) at different laser wavelengths, presented in double logarithmic scale. Solid lines are the best fits of data to power dependence,  $I = P^a$ . Inset shows the detuning values and the corresponding power exponent for each detuning

The data clearly show a dramatic increase of the 2PA efficiency when the laser frequency approaches the  $Q_x(0-0)$  resonance. In fact,  $\sigma_2$  grows by more than two orders of magnitude, from  $1 \times 10^2$  GM to  $1.6 \times 10^4$  GM, upon decreasing the detuning from  $3800 \text{ cm}^{-1}$  to  $800 \text{ cm}^{-1}$ . The data point shown as an asterisk was obtained [155] from fitting the measured time dependence of photoswitching  $T_1 \rightarrow T_2$  dynamics of  $\text{Pc}_3\text{Nc}$  (see appendix E and figure E.3). The corresponding value at  $783 \text{ nm}$ ,  $\sigma_2 = 1.8 \times 10^4 \text{ GM}$ , correlates well with the data obtained by the standard fluorescence method. Note that the  $\sigma_2$  values

obtained here are well within the range required for fast access 3D memory (see previous sections).

To investigate the behavior of the background (hot-band) 1PA we measured the fluorescence intensity of  $T_1$  as a function of laser power at room temperature, and fitted the data with the power law,  $I(P) = P^a$ . Figure 6.4 illustrates the set of these dependences obtained at different frequency detuning values from the 1PA maximum. Since the 2PA rate increases as the square of the laser power, while 1PA has a linear power dependence, one can conclude that at large detunings,  $\nu_{01} - \nu > 2100 \text{ cm}^{-1}$ , the fluorescence is excited through 2PA. At smaller detunings, where the dependence becomes closer to linear,  $a \approx 1$ , the fluorescence is excited through 1PA. Intermediate detunings with  $1 < a < 2$  correspond to fluorescence excited by a combination of 1PA and 2PA processes.

#### Simulation of Signal-to-Background and Signal-to-Noise Ratios Using Experimentally Obtained Molecular Parameters

Having measured and characterized the key parameters of the model chromophore Pc3Nc, our next task is to analyze the performance of the memory using these data.

Figure 6.5 shows the SNR vs. SBR curves, calculated for Pc<sub>3</sub>Nc at 77 K at different photon flux densities, assuming the same values for recording and readout ( $I_w = I_r$ ). As was discussed above, the  $T_2$  form of Pc<sub>3</sub>Nc is only stable at  $T < 100 \text{ K}$ . As in the above simulations, the number of layers is set to  $M = 1000$ . We consider the  $T_2 \rightarrow T_1$  tautomerization reaction for writing, because its quantum efficiency is much larger than

that of the  $T_1 \rightarrow T_2$  reaction. In the simulation we use the fluorescence spectrum weighted with the appropriate Boltzmann factor to simulate the 1PA spectrum of  $\text{Pc}_3\text{Nc}$  (see appendix E, figure E1). We also use a fit to the experimental 2PA spectrum (figure 6.3, dashed line) to describe the 2PA in the whole range of wavelengths. We consider for simplicity that both forms,  $T_1$  and  $T_2$  have similar 1PA and 2PA spectra. Other parameters used in this simulation are presented in table D.10. Our results show that the minimum photon intensity required for obtaining  $SBR > 4$  and  $SNR > 4$  is rather high,  $I = 4 \times 10^{29} \text{ photons} \cdot \text{cm}^{-2} \cdot \text{s}^{-1}$ . Although it is less than the destructive nonlinearity threshold ( $10^{30} \text{ photons} \cdot \text{cm}^{-2} \cdot \text{s}^{-1}$ ), the allowed parameter space is rather limited. Note also that rather large values of SBR can be achieved in a vast range of detunings from 600 to  $3000 \text{ cm}^{-1}$ , meaning that the SNR is more critically affected by the power density than SBR.

Even though the simulations presented above use a strongly simplified model, we may conclude that we have gained a useful insight into the most critical processes involved in facilitating a fast rewritable volumetric memory. In the following, we will briefly discuss some important parameters that were not included in the basic model, but which should also be considered in building a practical storage system.

We assumed above that reading out does not erase the memory, i.e. form B does not transform back to A upon illumination. In tetrapyrroles this assumption is in part justified by much lower quantum efficiency of the backward ( $T_1 \rightarrow T_2$ ) reaction [146]. We also assumed a rather high concentration of the chromophore molecules,  $10^{-2} - 10^{-1} \text{ M}$ . At such concentrations, both the exciting laser beam and emitted fluorescence may be

significantly attenuated during propagation through the disk (the so-called inner filter effect). To overcome this, larger detuning values and/or molecules with larger a Stokes shift might be required.

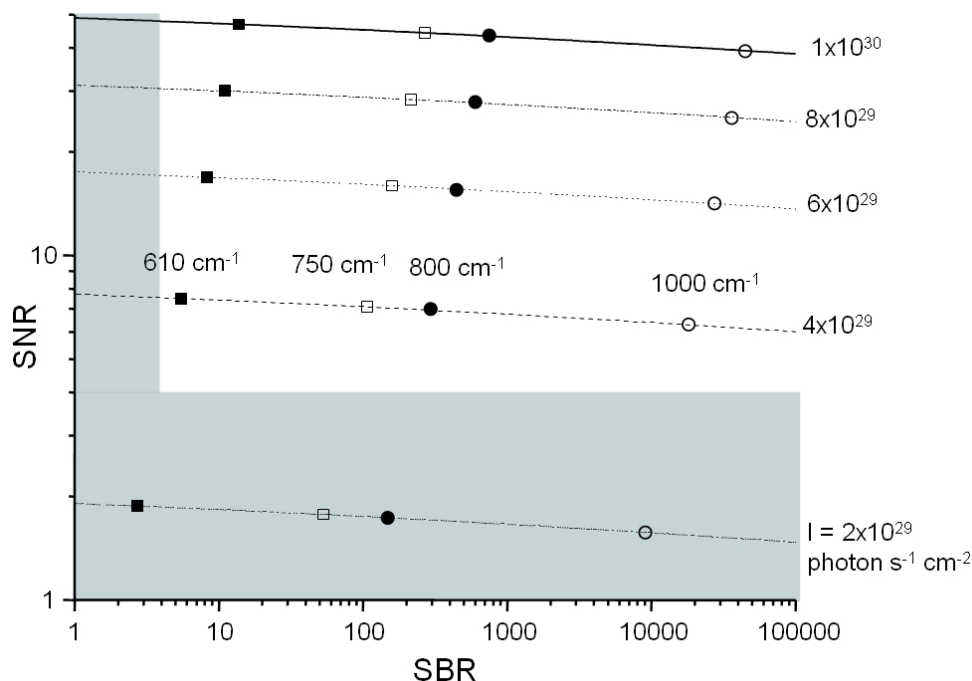


Figure 6.5. SNR versus SBR diagram, obtained as a result of numerical simulations for  $\text{Pc}_3\text{Nc}$  at  $T = 77 \text{ K}$ . Each curve corresponds to a particular laser peak intensity, indicated on top of the curve. Different symbols on the curves label the particular values of frequency detuning from 1PA maximum. Shaded regions correspond to forbidden values of  $\text{SNR} < 4$  or/and  $\text{SBR} < 4$ . Other parameters used in simulation are summarized in table D.10, third column

### Non-Centrosymmetrical Phthalocyanines for Volumetric Optical Memory

Although the principles of the 2PA-based volumetric optical memory have been known for more than twenty years, there is still a lack of a systematic study of the 2PA properties of materials considered for this technology.

In the rest of this chapter we present a summary of experimental characterization of a series of asymmetrical phthalocyanines promising for volumetric optical storage. The molecules are provided by CIBA Specially Chemicals Inc (Bazel, Switzerland). We measure their 2PA spectra, 2PA cross sections, temperature stability, tautomerization, and fluorescence quantum yields. We describe the effect of substituents and the influence of different isomers on the 2PA properties. We find that among the set of studied molecules, there is one that is the most promising for rewritable 3D optical memory. Measurements were done in carbon tetrachloride, methylene chloride, and octane solutions, poly(vinylbutyral) (PVB) and polyethylene (PE) films.

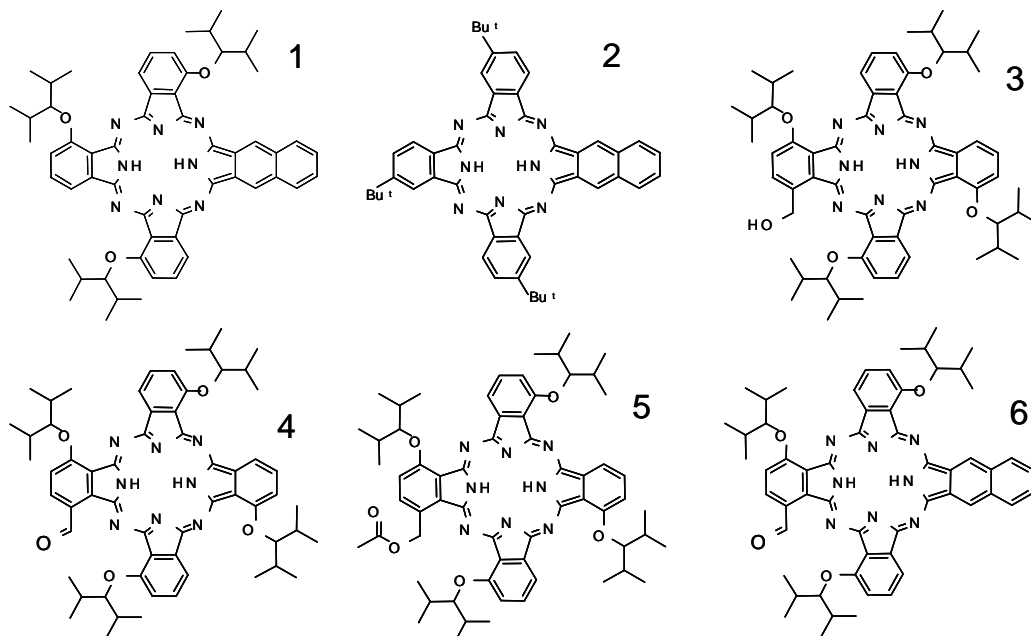


Figure 6.6. Chemical structures of the molecules

Figure 6.6 shows the chemical structures of the molecules studied. The molecules are based on a centro-symmetrical metal-free phthalocyanine core with different substituents on the periphery, which break the symmetry for all the molecules.

Compounds 1, 2, and 6 have an extra benzene ring, attached to the core, as one of the substituents (phthalonaphthalocyanines). The presence of the benzene substituent makes these molecules have a lower degree of symmetry compared to compounds 3-5. Compound 2 has three *tert*-butyl substituent groups at the  $\beta$ -positions. Molecules 1 and 6 have three alkoxy group substituents at the  $\alpha$ -positions, and the molecules 3-5 have four alkoxy groups. Also, molecules 3-6 have an additional substituent group at the  $\alpha$ -position. For molecules 6 and 4 this is the CHO group, while for molecules 3 and 5 these are CH<sub>2</sub>OH, and CH<sub>2</sub>OCOCH<sub>3</sub> groups, respectively. Molecule 1 is Pc<sub>3</sub>Nc considered above.

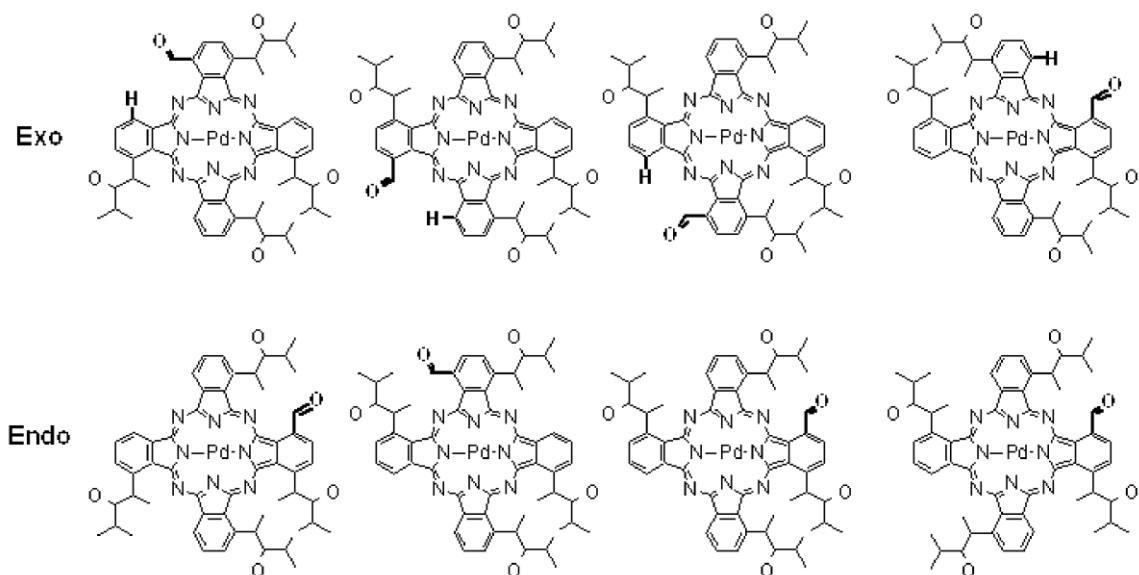


Figure 6.7. Possible isomers of Pd-substituted version of molecule 4

Compounds 3-6 have several isomers depending on mutual positions of OR-groups and additional substituents. Exo and endo isomers are defined as follows: in exo-isomers the additional substituent, for example the aldehyde group, is in close proximity to the  $\alpha$ -hydrogen atom and in endo-isomers it is in a close proximity to one of the alkoxy groups.



An example of structures for isomers of the metallo-version of compound 4 is shown in figure 6.7. Similar structures are possible for other molecules. The isomers were separated by flash chromatography.

Below we refer to versions **a** and **b** of molecules 1 and 6. These versions were synthesized using a starting material with a slightly different distribution of isomers. They also contain small a (but not specified) amount of compound 4.

### Spectra of the Non-Centrosymmetrical Phthalocyanines

Figures 6.8–6.10 show the 1PA and 2PA spectra of the studied phthalocyanines plotted versus transition frequency. The 2PA cross sections of compounds 2–6 were measured relative to Pc<sub>3</sub>Nc (1). The 1PA spectra can be partitioned into Q-bands in the red part of the spectrum ( $600 < \lambda < 800$  nm) and a Soret band in the blue part ( $\lambda < 500$  nm). The 2PA transitions in general repeat these spectral features. We analyze spectra in the Q- and Soret-regions separately.

Two intense and relatively narrow 1PA electronic transitions of perpendicular polarizations,  $S_0 \rightarrow S_1$  ( $Q_x$ ) and  $S_0 \rightarrow S_2$  ( $Q_y$ ), in the red – near-IR wavelength region are typical for metal-free phthalocyanines. We define the  $x$ -axis as directed along the polarization of the lowest,  $S_0 \rightarrow S_1$ , transition. The widths of the  $Q_x$  peaks for molecules 1–6 are:  $275\text{ cm}^{-1}$ ,  $405\text{ cm}^{-1}$ ,  $480\text{ cm}^{-1}$ ,  $<774\text{ cm}^{-1}$ ,  $470\text{ cm}^{-1}$ , and  $430\text{ cm}^{-1}$ , respectively. The extinction coefficients of the  $Q_x$  peaks are of the order of  $10^5\text{ M}^{-1}\text{cm}^{-1}$  for all the molecules (see table D.11).

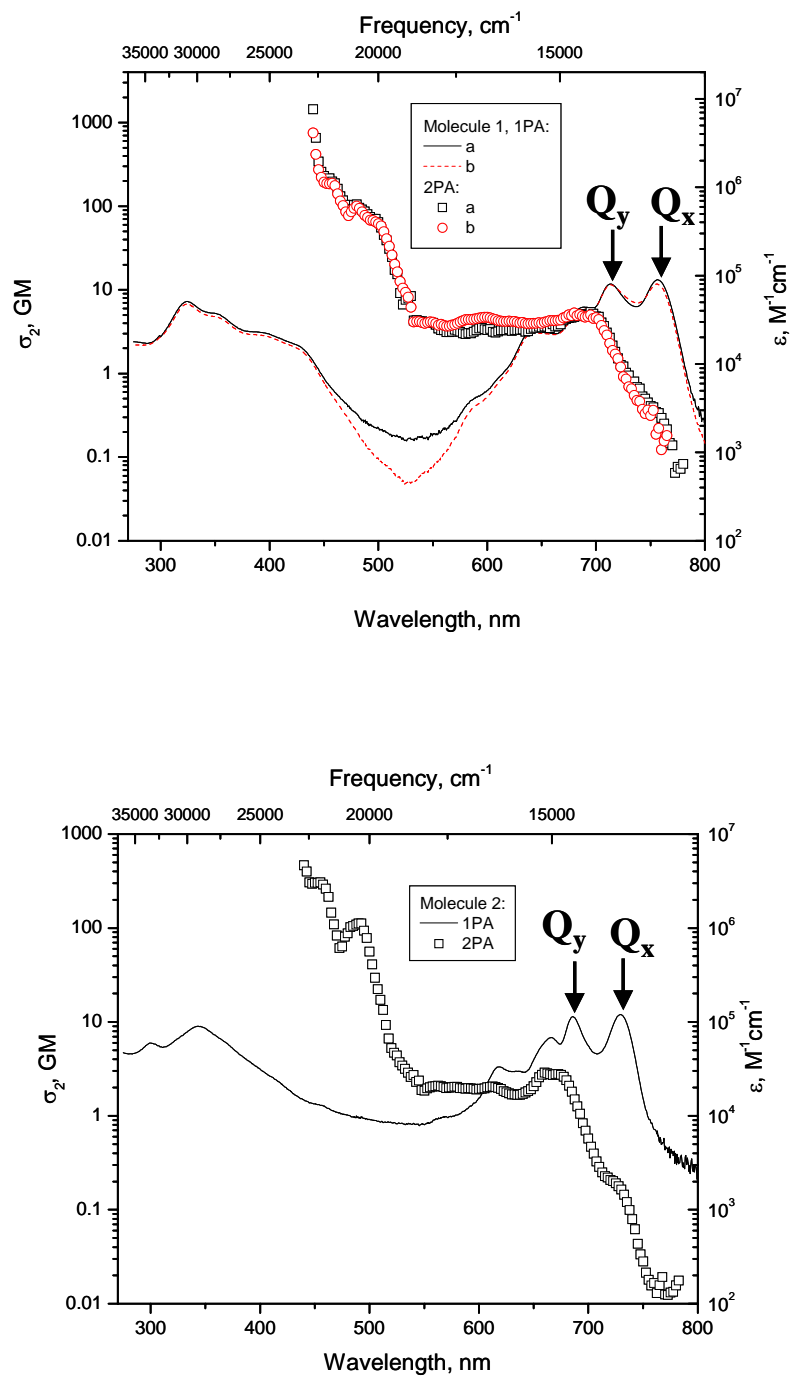


Figure 6.8. 1PA (lines) and 2PA (symbols) spectra of phthalocyanines 1 (Pc<sub>3</sub>Nc) and 2 in carbon tetrachloride at room temperature. The two near-IR peaks in 1PA spectra correspond to the  $Q_x$  and  $Q_y$  bands

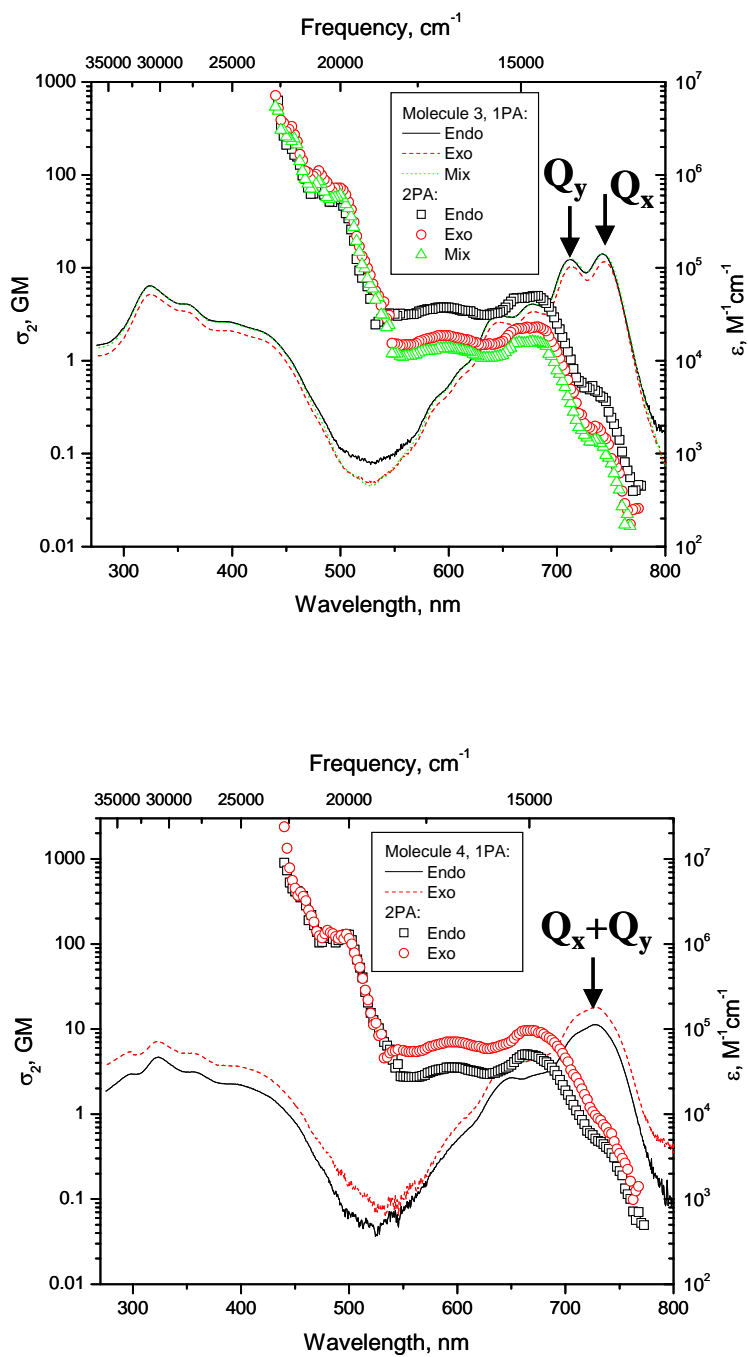


Figure 6.9. 1PA (lines) and 2PA (symbols) spectra of isomers of phthalocyanines 3 and 4 in carbon tetrachloride at room temperature. The two near-IR peaks in 1PA spectrum correspond to the  $Q_x$  and  $Q_y$  bands

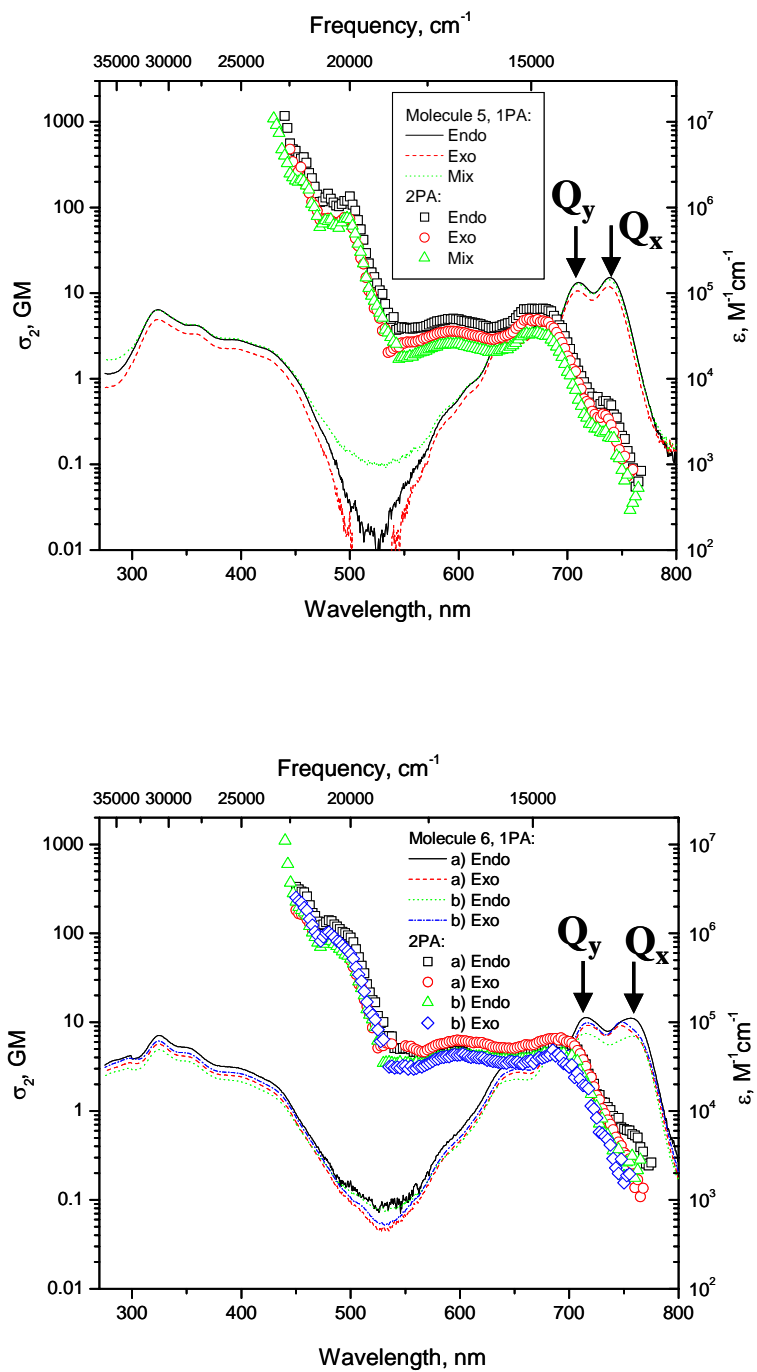


Figure 6.10. 1PA (lines) and 2PA (symbols) spectra of isomers of phthalocyanines 5 and 6 in carbon tetrachloride at room temperature. The two near-IR peaks in 1PA spectrum correspond to the  $Q_x$  and  $Q_y$  bands

The 2PA spectra in the Q-region generally follow the 1PA spectra. The 2PA cross sections of the Q-transitions are rather small, not larger than  $\sigma_2 \sim 4$  GM. Since the excitation corresponding to the Q band is far from any intermediate resonance ( $\lambda_{2PA} \approx 1400-1500$  nm, and  $\lambda_{01} \approx 750$  nm), and the molecules possess a relatively high degree of symmetry compared to the molecules in groups (i) and (ii) of chapter 4, the low values of the 2PA cross section may be explained by the low values of the dipole moment difference  $\Delta\vec{\mu}_{01}$ . The relative intensities of the 2PA peaks corresponding to the  $Q_x$  and  $Q_y$  transitions are different from the 1PA ones: In the 1PA spectra both the  $Q_x$  and  $Q_y$  bands have nearly the same peak extinction coefficient values, and in the 2PA spectra, the cross section values of the  $Q_x$  peak are several times less than those of the  $Q_y$  peak. This supports the idea of perpendicular polarizations for these transitions, and hence for one of them the angle  $\beta \approx 0^\circ$ , while for the second transition  $\beta \approx 90^\circ$ . Then, the 2PA cross sections may differ by a factor of three (if  $\Delta\vec{\mu}_{01}$  are equal for both transitions). Additional difference is possible due to the line shape function.

By comparing the spectra of the different molecules in the Q-bands, one can make the following observations: Even though the molecules are rather similar, the 2PA cross sections vary by a large factor, from 0.3 GM to 3.4 GM for the  $Q_y$ -transition and from 0.12 GM to 0.55 GM for the  $Q_x$ -transition.

- The change of substituents from *tert*-butyl groups at  $\beta$ -positions (molecule 2) to alkoxy groups at  $\alpha$ -positions (molecule 1) results in the red shift of the entire 1PA spectrum by 30 nm ( $500\text{ cm}^{-1}$ ). The 2PA spectrum also experiences the red shift and the 2PA cross sections increase nearly by a factor of 2. These effects can be attributed

to a stronger electron-accepting ability of alkoxy groups in the  $\alpha$ -position versus *tert*-butyl groups in the  $\beta$ -position, resulting in the increase of  $\Delta\bar{\mu}_{01}$  for the molecule 1.

- The addition of an extra CHO group (molecule 6) changes the 1PA spectrum very little, but results in a slight decrease of the 2PA cross sections (as compared to the better purified compound 1) and in a slight increase of the cross sections (compared to 1a and 1b). We can put forward two different explanations of this fact: The slight decrease of  $\sigma_2$  could be caused by the steric interaction of the added CHO-group with the adjacent alkoxy group, which reduces  $\pi$ -conjugation; Further, the reduction of the cross sections of 6 can be trivially explained by a small contamination of 6 with compound 4. Alternatively, if we compare 6 with 1a and 1b only, then we can see that the addition of the CHO-group slightly reduces the degree of symmetry and increases the difference in dipole moments.
- The exchange of the external benzene ring of molecule 4 with an alkoxy group (molecule 6) produces a nearly symmetrical structure. This substitution shifts the  $Q_x$  and  $Q_y$  peaks closer to each other, such that the bands start to overlap. Similar shifts are observed in the 2PA spectrum. The 2PA cross section values diminish nearly by a factor of 2, which is probably due to smaller  $\Delta\bar{\mu}_{01}$  in the more symmetrical molecule 4.
- The reduction of the double bond in the aldehyde substituent group of molecule 3 vs. 4 does not change 1PA but does slightly (~25%) increase the peak 2PA cross section. However, the resulting value is still smaller than that of 1 or 6. The likely reason is the change of  $\Delta\bar{\mu}_{01}$ . It is also interesting that the peak cross sections of the isomers of

molecule 3 differ by a factor of three, while the extinction coefficients remain the same. This again may be attributed to variations of  $\Delta\tilde{\mu}_{01}$ .

- The change of substituent in 3, giving compound 5, makes the latter less symmetrical and thus increases the 2PA cross section due to increased  $\Delta\tilde{\mu}_{01}$ . However, molecules 6, and especially 1 still have larger asymmetry, and, thus, possess the highest 2PA cross sections among all the studied compounds.

One of the main conclusions of the above comparison is that the alkoxy substituents at  $\alpha$ -positions significantly ( $\sim 2\times$ ) increase the 2PA cross section as compared to *tert*-butyl groups at  $\beta$ -positions.

A question which remains unclear is how the substitution isomerism changes the value of the 2PA cross section. Endo-isomers of molecules 3, 5, and 6 show higher cross sections, and, surprisingly, the mixture of isomers shows the lowest one. In principle, this could be attributed to the fact that for the endo-isomer (right bottom corner of figure 6.7), the bulky alkoxy groups do not clash. On the other hand, in exo-isomers they always experience steric interaction, which reduces the planarity of the molecule. In contrast to 3, 5, and 6, the endo-isomers of 4 show a lower cross section than the exo-isomers. For this latter molecule, the comparison is not well justified because of the strong overlap of the  $Q_x$  and  $Q_y$  peaks.

The 1PA Soret band of the studied molecules is weaker and broader than the Q-bands. The 2PA strength in this region monotonically increases with decreasing wavelength. This can be at least partially explained by the resonance enhancement effect, caused by the presence of Q-transition(s) (at  $\lambda \approx 730 - 760$  nm) acting as near-resonance

intermediate states. The shoulder in the 2PA spectra appearing at transition wavelengths  $\lambda = 475 - 500$  nm is probably an indication of a 1PA-forbidden *gerade-gerade* transition [82] similar to that observed in **TBTAC** (see chapter 5). In molecule 2, this transition appears as a clear peak at  $\lambda = 490$  nm. For all the molecules studied, the cross sections obtained far from the resonance region ( $\lambda > 745$  nm) are of the order of  $\sigma_2 \sim 10^2$  GM. On the other hand, the narrowness of the  $Q_x$  band allows the laser frequency to be tuned very close to the  $Q_x$  resonance. Approaching the resonance ( $\lambda \rightarrow 800$  nm) results in a substantial enhancement of 2PA, while the presence of the hot-band absorption starts to contribute to the excitation, causing the laser power dependence of the fluorescence signal to change from the quadratic law, as demonstrated in figure 6.4.

#### Photoinduced Tautomerization of the Non-Centrosymmetrical Phthalocyanines

Two protons in the center of the molecules can be aligned along diagonal pairs of either identically or differently substituted benzopyrrolic rings. This makes two tautomeric forms possible in each isomer. The tautomers have different absorption and fluorescence spectra. As for  $Pc_3Nc$ , the form  $T_1$  is more stable at room temperature. At lower temperatures,  $T < 100$  K, the  $T_2$  form becomes stable. The molecules can be optically switched via 1PA or 2PA between the two forms. Since structural changes occur inside the core of the molecule, this does not alter the shape and the volume of the molecule much. Alternation of the molecular volume stresses the polymer matrix and lead to destruction of the optical disk. Tautomerization of phthalocyanines is promising



for 3D optical memory, since the molecules can be switched many times without substantial influence or damage on the surrounding polymer.

The measurements of the tautomerization transformation were performed with a mixture of isomers as follows [57]: The molecules were uniformly dispersed in polyethylene (PE) films. The films were mounted inside a variable-temperature cryostat and cooled down to 77K. The molecules were illuminated by a laser tuned to the maximum of the  $Q_x$  band of the  $T_1$  form with the beam diameter  $\sim 8$  mm, and the average power  $\sim 1\text{--}4$  mW, and the 1PA spectra of the molecules were measured after 10, 30, 190 and 1900 seconds of illumination. Then the laser wavelength was tuned to the maximum of the  $Q_x$  band of the  $T_2$  form and the backward transformation was measured.

Figures 6.11 and 6.12 show the linear absorption spectra of the free-base phthalocyanines (1, 3, 4, and 5) before and after illumination of the Q-bands by a laser beam. The solid line shows 1PA spectra of molecules before illumination, dashed line – after 10 seconds, dotted line – after 30 seconds, dash-dotted line – after 190 seconds, and dash-dot-dotted line – after 1090 seconds of illumination. One can see a gradual transformation of each molecule from  $T_1$  into  $T_2$  upon irradiation, as the peaks of  $T_1$  decrease with the illumination time, and the peaks of  $T_2$  increase.

The inserts in the figures show the changes in optical density of the  $T_2$  form with irradiation dose (in photons per  $\text{cm}^2$ ). The dose was changed by increasing irradiation time at constant light intensity. The rate of transformation,  $\tau_{T_1 \rightarrow T_2}$ , allows obtaining the tautomerization quantum yields,  $\phi_{T_1 \rightarrow T_2}$ , which are presented in table D.12, according to:

$$\varphi_{T_1 \rightarrow T_2} = \frac{1}{\sigma_1 \tau_{T_1 \rightarrow T_2}}, \quad (6.4)$$

where  $\sigma_1$  refers to the 1PA cross section of  $T_1$  at the excitation wavelength.

The narrow absorption lines of molecule 1 (Pc<sub>3</sub>Nc) allow rather good spectral separation of the  $T_1$  and  $T_2$  forms. Molecules 3 and 5 have the highest tautomerization quantum yield in the series. This can be explained by the fact that the molecules with higher symmetry have higher tautomerization quantum yield [57].

Unfortunately, in symmetrical tetrapyrroles the  $T_1$  and  $T_2$  spectra overlap, which makes it difficult to distinguish one from the other. Molecule 4 is unique in the series: the  $Q_x$  band of the low-temperature form  $T_2$  appears red-shifted from the  $Q_x$  band of  $T_1$  form, while for all other molecules a blue shift is observed. Also, for molecule 4, the  $Q_x$  and  $Q_y$  peaks are well resolved in PE at 77 K in contrast to carbon tetrachloride solution at room temperature.

The temperature at which the amount of  $T_2$  molecules, produced at 77 K, reduces by half in dark (the stability temperature  $T_{1/2}$  of the  $T_2$  form) was also measured. For this we first illuminated the PE samples as described above to transform the phthalocyanines in the  $T_2$  form. Then the temperature of the films was gradually increased while monitoring the 1PA spectra, and the temperature at which the  $Q_x$  peak of  $T_2$  was half of its initial value was recorded. The stability temperature is found to be in the range of  $T_{1/2} = 115\text{--}134$  K, but can be raised to  $T_{1/2} = 150$  K by deuteration of the molecular center.

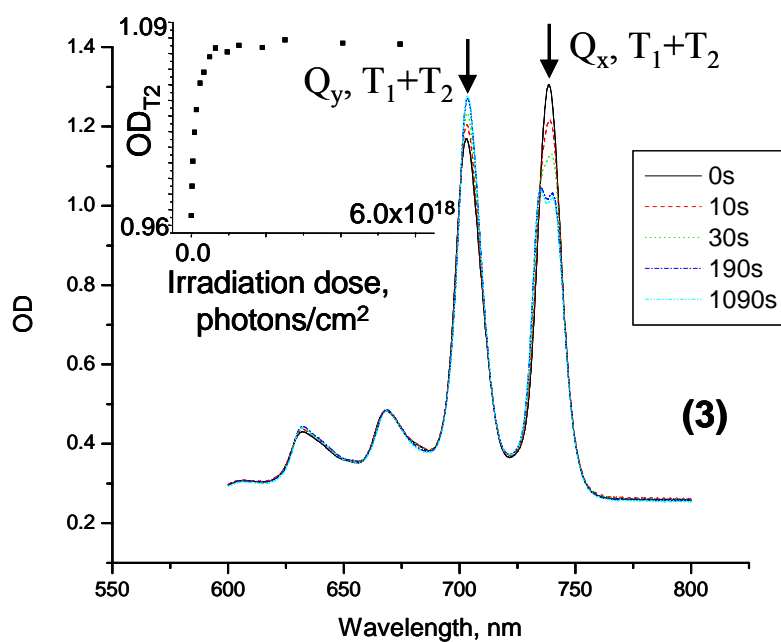
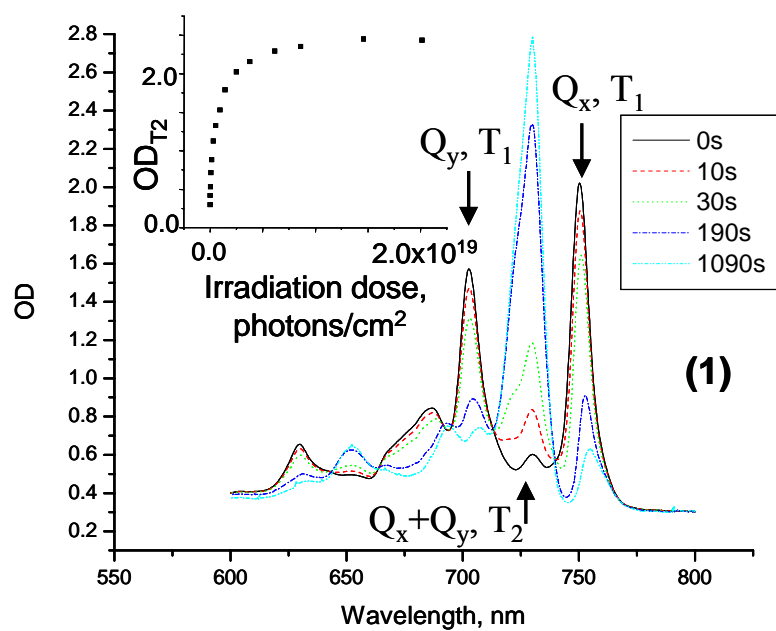


Figure 6.11. Transformation of tautomer  $T_1$  into tautomer  $T_2$  in phthalocyanines 1 and 3 in polyethylene film at 77K. Main figure – absorption spectra at different illumination times at constant laser intensity. Insert shows the increase of the  $T_2$  peak absorption with irradiation dose

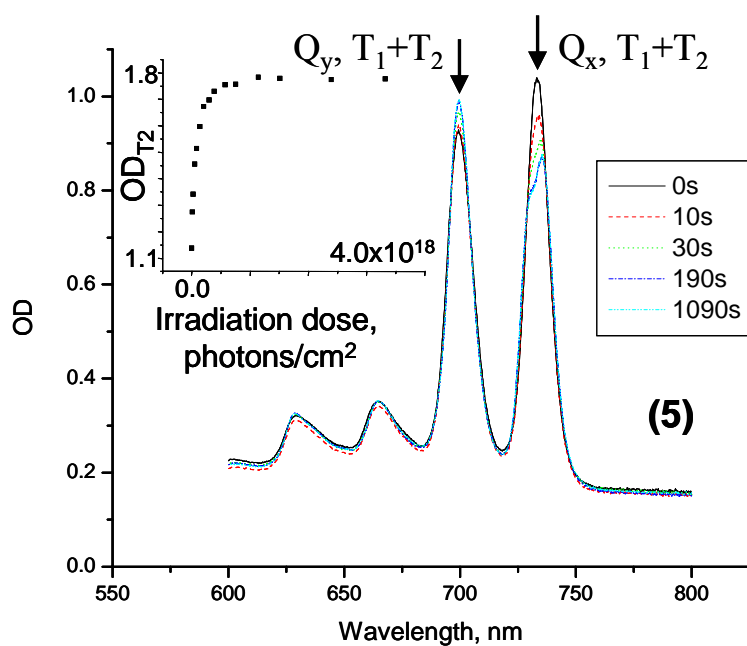
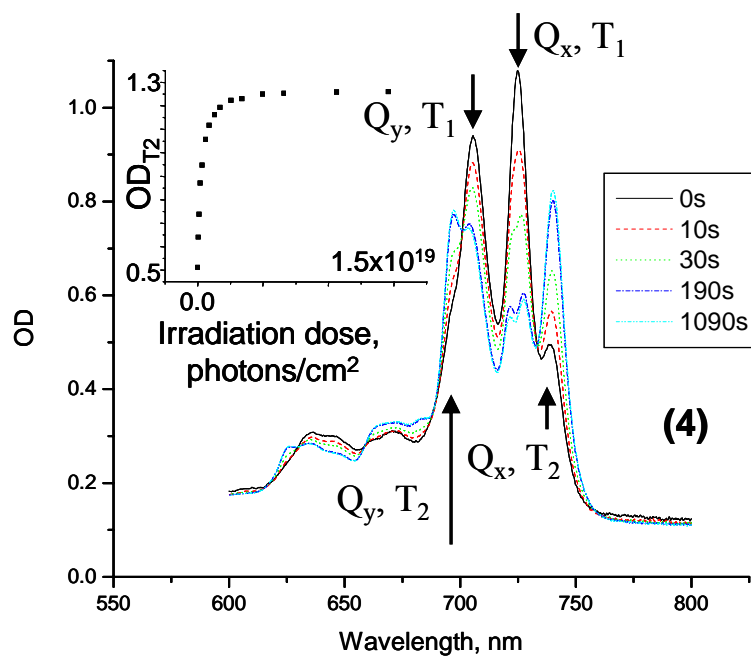


Figure 6.12. Transformation of tautomer  $T_1$  into tautomer  $T_2$  in phthalocyanines 4 and 5 in polyethylene film at 77K. Main figure – absorption spectra at different illumination times at constant laser intensity. Insert shows the increase of the  $T_2$  peak absorption with irradiation dose

Fluorescence quantum yields were measured in octane relative to free-base tetra-*tert*-butyl-phthalocyanine. These data are also presented in table D.12. The highest quantum yield is found for 4 ( $\varphi^B = 0.38$ ), and the lowest for 3 ( $\varphi^B = 0.14$ ).

### Comparison of the Studied Phthalocyanines in Connection with Optimization of the Volumetric Memory

According to the expressions given earlier for SNR (6.3) and SBR (6.2), we need to maximize the following quantities relevant for 3D optical memory applications:

$$\frac{\sigma_2(\lambda_w)}{\sigma_1(\lambda_w)} \rightarrow \max; \quad \sqrt{\sigma_2(\lambda_w)\sigma_2(\lambda_r)\varphi^B\varphi_{A \rightarrow B}} \rightarrow \max, \quad (6.5)$$

where  $\sigma_1$  and  $\sigma_2$  are the 1PA and 2PA cross sections at the reading and writing wavelengths, respectively. In the following comparison, we assume that the identical wavelengths are used for the readout and write access.

Below we use expressions (6.5) to select the best molecular systems studied here. In particular we need to compare the 1PA and 2PA cross sections at low temperature where the excitation wavelength is close to the intermediate resonance in order to maximize resonance enhancement. However, because such low temperature measurements of the 2PA were done only for chromophore 1 (Pc<sub>3</sub>Nc), we here compare cross sections measured at room temperature at the wavelength  $\lambda = 900$  nm. The calculated figures of merit for SBR and SNR are summarized in table D.13. Note that while showing impressive tautomerization quantum yields, molecules 3 and 5 are not practical since the absorption spectra of their tautomeric forms overlap. Since the fluorescence quantum yield of 2, and the tautomerization quantum yields of 2 and 6 were not measured, we

estimated these values by averaging the data obtained for other molecules. According to table D.13, the best SBR is obtained for molecule 1. Molecules 3 and 5 show slightly smaller SBR values. The lowest SBR is obtained for 2, 4, and 6. The ratio between the highest and the lowest values of SBR is near 5-fold. From the SNR point of view, molecules 3 and especially 5 are the best, essentially because of their high tautomerization quantum yields. For practical applications, the best value of SNR is found for compound 4; however 1, 2, 4, and 6 all show very similar results. We expect that the picture would not change at low temperature and if we tune the laser wavelength closer to the intermediate resonance, making molecule 1 ( $\text{Pc}_3\text{Nc}$ ) probably still the best out of the whole set of systems studied here.

Finally, we formulate here some other target approaches, which can be used for optimization of novel 2PA photochromes: (1) It is very much preferred that the photochromic 2PA storage materials demonstrate an intense intermediate 1PA resonance. Phthalocyanines and some other tetrapyrroles possess relatively narrow  $S_0 \rightarrow S_1$  transitions ( $\sim 500\text{--}1000\text{ cm}^{-1}$ ). Much narrower resonances will not bring a significant improvement, because at room temperature the background is due to the hot-band absorption. A wider resonance, however, increases background 1PA and prevents the values of SBR to be practical. (2) SBR and SNR will improve if sufficiently large 2PA cross sections would extend at least  $1500\text{ cm}^{-1}$  to lower frequencies from the 1PA peak. The advantage would be even larger if, instead of the smooth and featureless 2PA spectrum considered here, a molecule would display a sharp 2PA peak, preferably just below the 1PA maximum. Some of the phthalocyanines synthesized from  $\text{Pc}_3\text{Nc}$  with

only slight modifications indeed demonstrate such a peak. Their optical properties and applicability to 2PA memory are summarized in the chapter. (3) To suppress the 1PA background it would be beneficial if vibronic coupling to low-frequency vibrational modes is weak.

One potential drawback of the systems considered here consists in relatively low quantum efficiency of the phototautomerization ( $\phi_{T_1 \rightleftharpoons T_2} < 0.01$ ). To overcome this impediment, one needs to study in more detail the mechanism of switching between H<sub>2</sub>-tautomers of tetrapyrroles. It has been proposed [146] that the product form T<sub>2</sub> is formed in the vibrationally relaxed triplet state via the tunneling of a single proton, which results in an intermediate state with cis-configuration of protons. Rather slow population of the triplet state reduces the value of tautomerization quantum yield. It has also been shown [146] that the lower the symmetry of a molecule the smaller is the phototautomerization rate. It would therefore be important to study the relationship between the rate of tautomerization and molecular structure.

We also note that a similar approach in principle can be applied for optimization of two-photon microscopy. Based on similar treatment of SNR and SBR, one can introduce a specific figure of merit to choose the optimum fluorescent marker at each required wavelength. We consider this problem as one of the possibilities for future research.

## 7. APPLICATION OF TWO-PHOTON ABSORPTION SPECTROSCOPY FOR DETECTION OF CANCER CELLS

Early detection of tumors is imperative for successful treatment of cancer. Preventative treatments may be applied if the tumors could be discovered at their earliest possible stage, i.e. when they have not yet grown beyond just a few malignant cells. Fluorescence-based detection of cancer cells *in-vivo* is a highly promising technique for early non-invasive cancer diagnostic and malignant tumor localization [156-160]. The majority of current fluorescence-based diagnostic techniques use special targeting agents, such as synthetic peptide-based antibodies, which help attach fluorophores to the cancer cells. For initial diagnostics screening, it would be however desirable to avoid using the targeting agents, because of high cost and possible harmful side effects, including immune responses [161]. Our goal is to study whether an inexpensive commercial fluorescent dye could be used for imaging of cancer cells *in vivo* environment. We also address the issue of the fidelity of the discrimination between the tumor and the surrounding healthy tissues. Recently, some improvement of the signal-to-background ratio in cancer tumor detection has been achieved by using specifically targeted-activatable fluorescent probes, such as pH-activatable molecules [160], cathepsin-mediated dequenching-based molecules [157], etc. However, identifying a malignant tumor in surrounding of a large number of healthy cells is still associated with large margins of error, and therefore fundamentally new approaches are required.

In application for biological imaging, 2PA-excited fluorescence has important advantages over the conventional one-photon excited fluorescence, consisting in its inherent 3D resolution [9, 162], larger penetration depth [9, 163], lower scattering [162],



and less photodamage [162]. Recently we have shown that the photodynamic therapy of cancer can be successfully used in a mouse body at an effective depth of 2 cm upon irradiation with 795-nm laser light [164]. However, the 2PA imaging inside live tissue has been limited so far to about 1 mm, mostly due to absorption and scattering of the visible fluorescence inside biological tissues [162].

Here we show that femtosecond two-photon excitation of a commercial near-IR fluorescent dye Styryl-9M can be used to improve the sensitivity and the fidelity of detection of cancer cells surrounded by healthy tissue cells, deep inside the tissue.

In chapter 4, we have shown that the ionic dye, Styryl-9M, has a relatively high 2PA cross section,  $\sigma_2 \sim 750 \text{ GM}$ , in the near-infrared wavelength region, 1150–1250 nm [165]. Styryl-9M is highly photostable, and is used as a laser dye [166]. The family of Styryl dyes has also been shown to have low toxicity, good biocompatibility [167, 168], and also sensitivity of the 1PA and the fluorescence emission spectra to the local environment [169, 170], membrane potential [171, 172], metal ions [173, 174], and presence of DNA [167, 175]. Another interesting property of these molecules, which has been shown only recently by us, is that the 2PA spectrum of Styryl-9M is even more sensitive to the local environment than the corresponding 1PA and one-photon-excited fluorescence spectra [170].

Here we take an advantage of these unique properties of Styryl-9M to demonstrate that near-IR femtosecond-pulse excitation can be used for detection of a very small number of living cancer cells surrounded by a large number of healthy cells.

Proof-of-principle experiments involving imaging of tumors are usually extremely difficult to conduct on live animals. Therefore, in our preliminary studies we are using so-called biological phantoms. These are artificial samples containing living cells, embedded in a collagen matrix, which simulates key optical properties of opaque biological tissues. Tissue phantoms may also contain specific tissue culture medium that helps keeping cells alive and provide them with the required nutrients. The phantoms used in this study were prepared by mixing of collagen type I with the setting solution in disposable 1×1 cm plastic spectroscopic cuvettes, and the cells were uniformly dispersed in the mixture. Styryl-9M dye dissolved in DMSO was added to the phantoms 16 hours before imaging experiments were performed. Further details on preparation of the phantoms are found in appendix F.

#### Experimental Setup for Two-Photon Imaging of Cancer Cells in Tissue Phantoms

The experimental setup for imaging of the tissue phantoms and solutions containing Styryl-9M is shown on figure 7.1a. The same 1 KHz wavelength-tunable OPA femtosecond laser as described in chapter 3 is employed for the excitation of the sample. The laser beam is passed through an iris diaphragm 1 and is slightly focused, ~1 cm behind the sample with a lens 2 ( $f=10$  cm). The sample consists of a 1×1 cm spectroscopic cuvette 3. The fluorescence excited in the sample is collected at the direction perpendicular to the excitation beam using a 75-mm  $f/1.4$  objective lens 4 and is imaged using a CCD detector 6 (Xillix MicroImager PMI1400). The detection

wavelength is selected with a variable liquid-crystal spectral filter 5 (VariSpec, CRI). A Helium-Neon laser 7 is used for the initial alignment and focusing of the CCD camera.

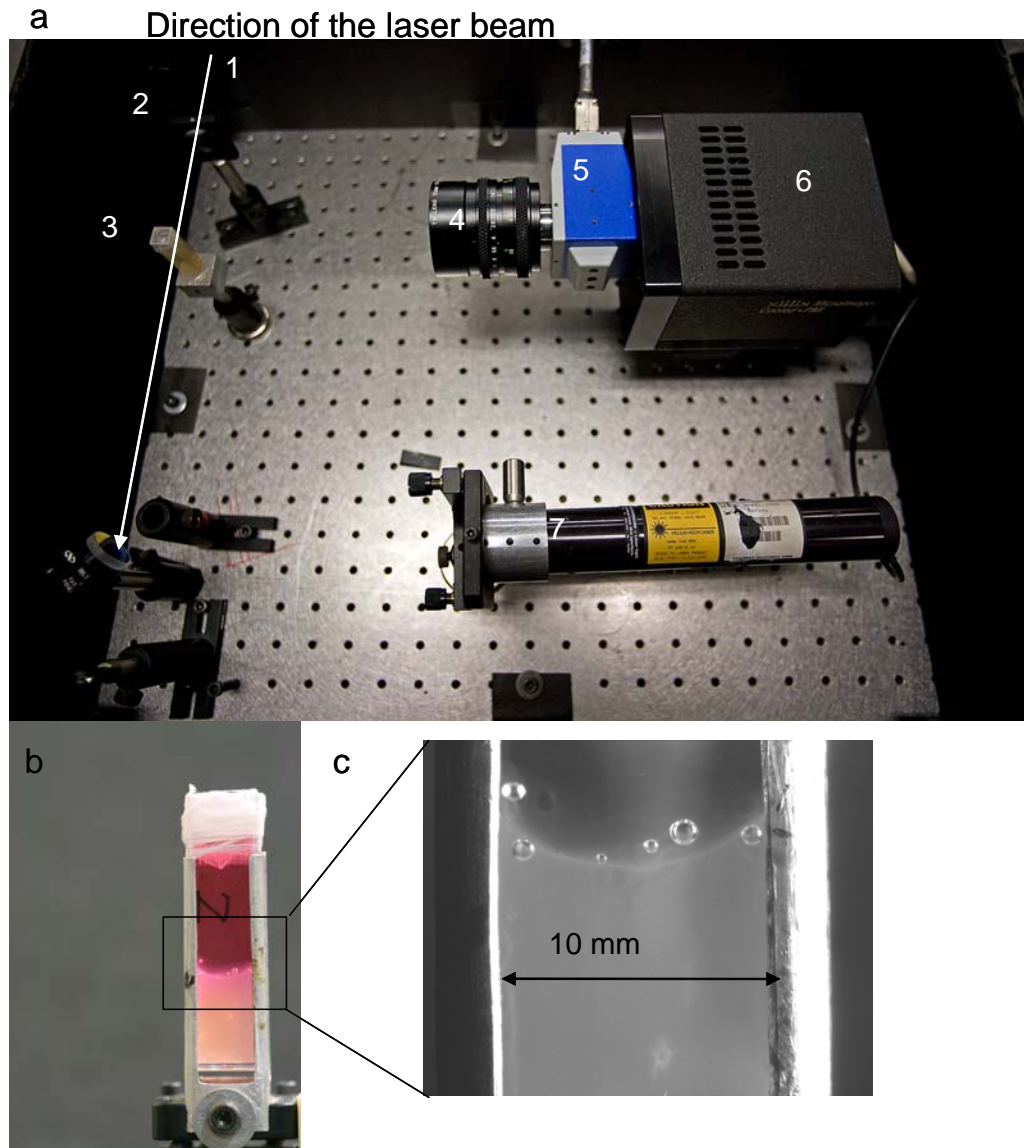


Figure 7.1. (a) Experimental setup for imaging of biological phantoms with Styryl-9M: (1) Laser beam entrance, (2) focusing lens, (3) sample cuvette (4) 75 mm f/1.4 objective lens, (5) variable wavelength filter, (6) – CCD camera, (7) He-Ne laser. (b) Sample cuvette with a phantom. (c) Field of view of the CCD camera with a 75-mm objective lens

The VariSpec transmission wavelength is set near the fluorescence maximum of the dye ( $\sim 730\text{-}750\text{ nm}$ ). The sample holder is placed  $\sim 28\text{ cm}$  from the CCD, such that the field of view of the camera is about  $\sim 2\text{ cm}$  wide. Addition of an extension tube between the objective and the CCD provides  $5\times$  magnification and reduces the field of view to  $\sim 4\text{ mm}$ . Further magnification along with corresponding reduction of the field of view to  $\sim 3\text{ mm}$  is achieved when the camera objective is replaced by a  $4\times$  microscope objective. The combination of the CCD camera, the variable wavelength filter and the objective allows the fluorescence image to be captured, while blocking the most of the laser scattering.

Figure 7.1b shows the tissue phantom in the sample holder, and figure 7.1c shows a part of the phantom that is typically captured within the CCD camera field of view (without additional magnification).

### Spectroscopy of Styryl-9M in Tissue Phantoms

As a preliminary step of our study, we performed 1PA and 2PA spectroscopy of Styryl-9M in various solvents. We examined the dependency of the 1PA and 2PA spectra on the solvent polarity, and the 1PA and fluorescence spectra on the solvent pH. We found that the peak of the  $S_0 \rightarrow S_1$  1PA experiences a large shift of  $\sim 3000\text{ cm}^{-1}$  with the change of the solvent polarity function from 0.35 to 0.5. On the other hand, the fluorescence emission spectrum of Styryl-9M barely changes under the same conditions. The 2PA spectrum shifts depending on the solvent polarity in a similar manner as the 1PA  $S_0 \rightarrow S_1$  peak. We also observe a very significant  $\sim 170\times$  absorption intensity change and a  $\sim 50\times$  fluorescence intensity change when the pH of water solution varies from 8 to

11. Further details on the spectroscopy of Styryl-9M in solutions are presented in appendix F. These preliminary results suggest that the 2PA spectrum of Styryl-9M can be used to sense the local environment, which in turn could be used to distinguish between cancer cells and normal (healthy) cells.

Next we measure relative 2PA spectra of Styryl-9M in tissue phantoms using the setup and method described in chapter 3. The following phantom samples are investigated: (a) phantoms containing no cells (we call these references), (b) phantoms containing only normal cells, and (c) a phantom containing only cancer cells. Figure 7.2 shows the corresponding 2PA spectra, in arbitrary relative units. To highlight the significant differences between three types of samples, the spectra are normalized such that data points overlap at wavelengths  $\lambda < 1100$  nm. The spectra have essentially the same shape at wavelengths  $\lambda < 1100$  nm, but differ from each other substantially at longer wavelengths,  $\lambda > 1100$  nm. At 1200 nm, the relative 2PA of the phantom with normal cells is about  $\sim 1.2\times$  stronger, and the relative 2PA of the phantom with cancer cells is about  $\sim 1.8\times$  stronger than that of the reference sample without cells. If we calculate the ratio of the 2PA-excited fluorescence intensities at 1100 and 1200 nm,  $F(1100)/F(1200)$ , then we can use this value as a quantitative measure to differentiate between normal cells and cancer cells. Note also that both the excitation and the fluorescence wavelengths fall well within the tissue transparency window, 800–1200 nm, [176], which is an important advantage for deep tissue diagnostics, because the absorption and scattering of the light by the tissue is minimal.

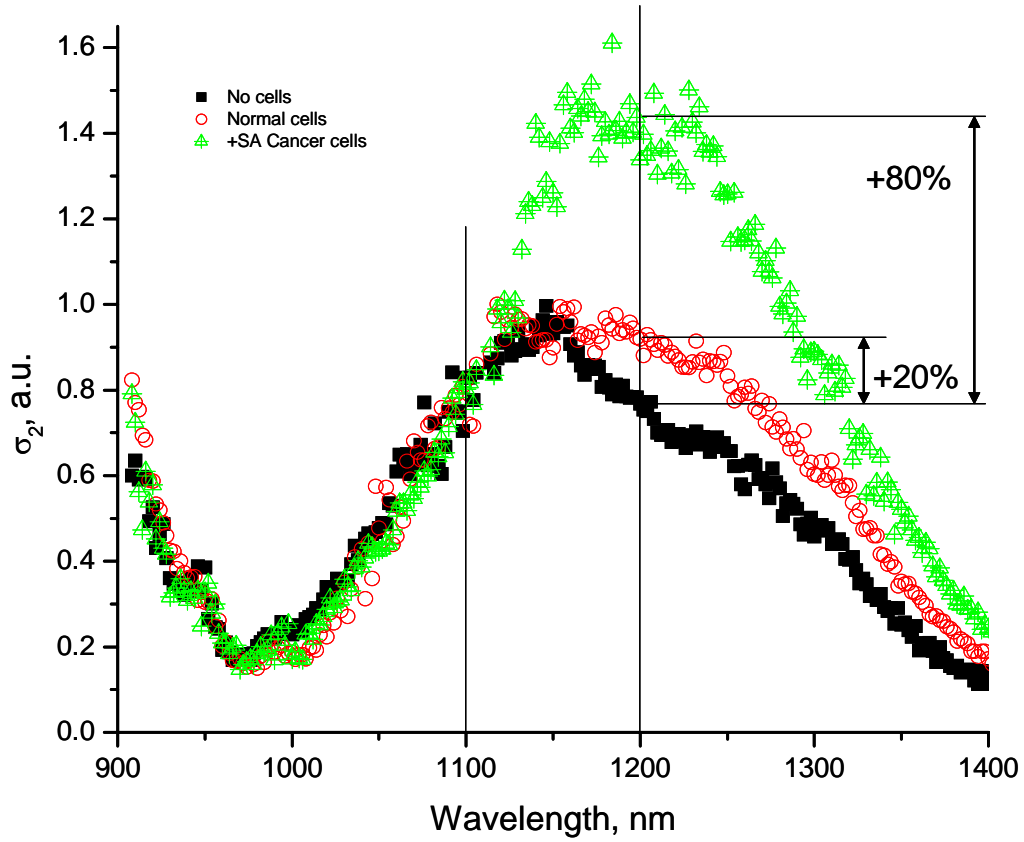


Figure 7.2. 2PA spectra of Styryl-9M in tissue phantoms with no cells (black squares), with normal cells (red circles), and with cancer cells (green triangles), all in relative units

It is interesting to note that the 2PA spectrum of Styryl-9M in a phantom with cancer cells (figure 7.2) can be represented as a linear superposition of two distinct spectral bands, which we call “blue” and “red”. The “blue” component corresponds to Styryl-9M dissolved in water, and the “red” component is similar to Styryl-9M dissolved in ethanol (see figure F.4). The decomposition of the spectrum of the phantom with cancer cells into the “blue” and “red” components is shown in figure 7.3. We normalize the “red” and “blue” forms such that in the spectrum of the phantom with cancer cells the

proportion of the two spectral components is close to 1:1. Then the ratio of the “red” to the “blue” forms in the 2PA spectra of phantoms with normal cells and without cells can equals 0.6 and 0.45, respectively.

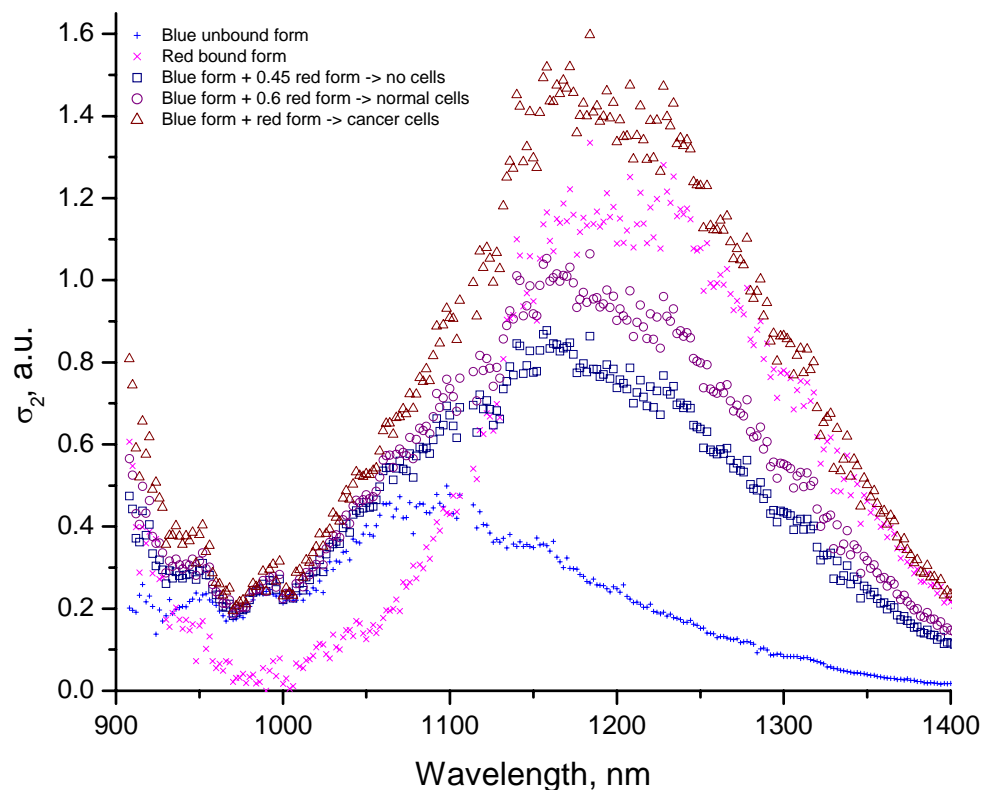


Figure 7.3. 2PA spectra of Styryl-9M in water, “blue” form (blue +), in ethanol, “red” form, (pink ×), and their linear superpositions with different weights (described in the inset), corresponding to a phantom without cells (dark blue squares), a phantom with normal cells (purple circles) and a phantom with cancer cells (brown triangles)

The important point is that the balance between the two spectral forms of Styryl-9M appears to indicate the biological environment, e.g. some receptor site that may be present in cancer cells but absent in normal cells. In order to quantify this dependence later in this chapter we try to describe the changing balance in terms of thermodynamic

equilibrium between the two states. Suppose that one form is that corresponding to the Styryl-9M molecule dissolved in water (most probably the “blue” form, since it is the spectrum of Styryl-9M in water) and another form corresponds to Styryl-9M molecules that are bound (attached) to the cell membrane (“red” form).

It has been shown that a dye with very similar structure, LDS-751 (Styryl-8), experiences a spectral shift corresponding to a transition to a less polar environment upon binding to the P-glycoprotein (Pgp) [177]. The Pgp is one of the specific, so called, drug-resistant proteins, which are often produced by cancer cells in high numbers, while in most normal tissues their number is greatly reduced [178]. The Pgp is located in the cell membrane. These issues will be discussed in detail in a later section.

#### Analysis of the Two-Photon-Excited Fluorescence Images Helps to Identify Cancer Cells

Encouraged by the fact that the phantoms with the cancer and normal cells can be distinguished, we propose using the 2PA spectrum of Styryl-9M as an optical imaging technique for detection of cancer cells in biological tissues. Let us consider a tissue phantom containing uniformly distributed normal cells. A small colony ( $\sim 1 \mu\text{m}^3$ ,  $\sim 10^5 - 10^6$  cells) of cancer cells is inserted in the phantom with the help of a micropipettor to mimic a small malignant tumor embedded inside healthy tissue. Our goal is to be able to determine the presence of the cancer cell colony in the phantom and pinpoint its location.

The procedure that we use consists of four steps. As a first step, we acquire two images of the 2PA-excited fluorescence in a phantom using a CCD camera and 1100-nm and 1200-nm laser wavelengths for the excitation. We also acquire a background image,



using the same CCD sensitivity settings, exposure time, etc., but with the laser excitation blocked.

As a second step, we analyze the digital images. We sum up pixels intensity over the vertical direction of the CCD sensor (for each horizontal pixel) and separately over the horizontal direction of the CCD sensor (for each vertical pixel) according to the following expression:

$$\begin{aligned} \left\{ F(x_i, \lambda) \right\}_{i=0}^{N-1} &= \sum_{j=0}^{M-1} F(x_i, y_j, \lambda) \\ \left\{ F(y_j, \lambda) \right\}_{j=0}^{M-1} &= \sum_{i=0}^{N-1} F(x_i, y_j, \lambda) \end{aligned} \quad (7.1)$$

where  $F(x_i, y_j)$  is the pixel intensity value at the  $x_i$ -th horizontal and  $y_j$ -th vertical CCD pixel,  $N$  is the number of the CCD pixels in horizontal direction,  $M$  is the number of the CCD pixels in vertical direction, and  $\lambda$  corresponds to the excitation wavelength (we define  $\lambda = 0$  for background image).

Figure 7.4 shows the raw images of the tissue phantom, where a cancer colony is present somewhere around the horizontal CCD pixels #400–450 in the region of the bright line, created by the laser beam. Note that the presence of the colony cannot be detected based on the fluorescence images alone. Further data processing described in this section allows us to find whether the cancer colony is present in the phantom and where it is located. The integral along the horizontal direction as a function of vertical direction (black line in figure 7.4) has almost Gaussian shape and corresponds to the Gaussian laser beam profile used to excite the 2PA-induced fluorescence. The integral along the vertical direction as a function of horizontal direction (red line in figure 7.4)

shows how the fluorescence intensity changes as the laser beam travels through the sample.

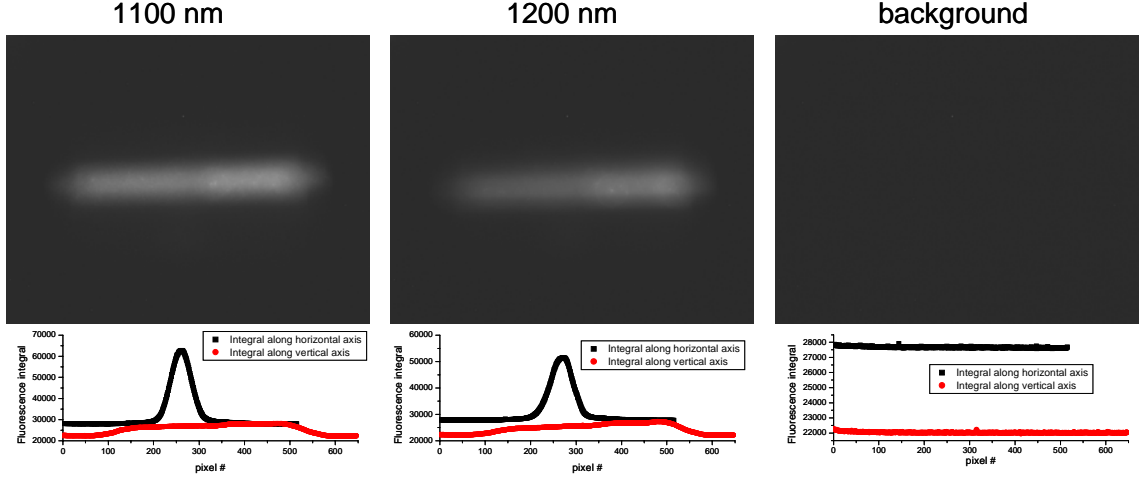


Figure 7.4. First two steps of the optical imaging technique for cancer localization (black line – integral along horizontal direction of the CCD sensor, red line – integral along vertical direction of the CCD sensor)

As a third step, we calculate the difference between the integral fluorescence signal and the integral background along the vertical direction of the CCD sensor for both excitation wavelengths according to the expression

$$\begin{aligned} \Delta \{F(x_i, 1100)\}_{i=0}^{N-1} &= \{F(x_i, 1100) - F(x_i, 0)\}_{i=0}^{N-1} \\ \Delta \{F(x_i, 1200)\}_{i=0}^{N-1} &= \{F(x_i, 1200) - F(x_i, 0)\}_{i=0}^{N-1} \end{aligned} \quad (7.2)$$

An example of this calculation is shown in figure 7.5. The resulting curves represent the pure integral signal of the 2PA-excited fluorescence along the laser propagation path.

In the forth and final step, we normalize the curves to the square of the incident laser power. This helps to minimize fluctuations caused by variation from sample-to-

sample and also day-to-day fluctuations of the laser power. We then calculate the fluorescence ratio,  $F(1100)/F(1200)$ , by dividing the two normalized curves obtained above:

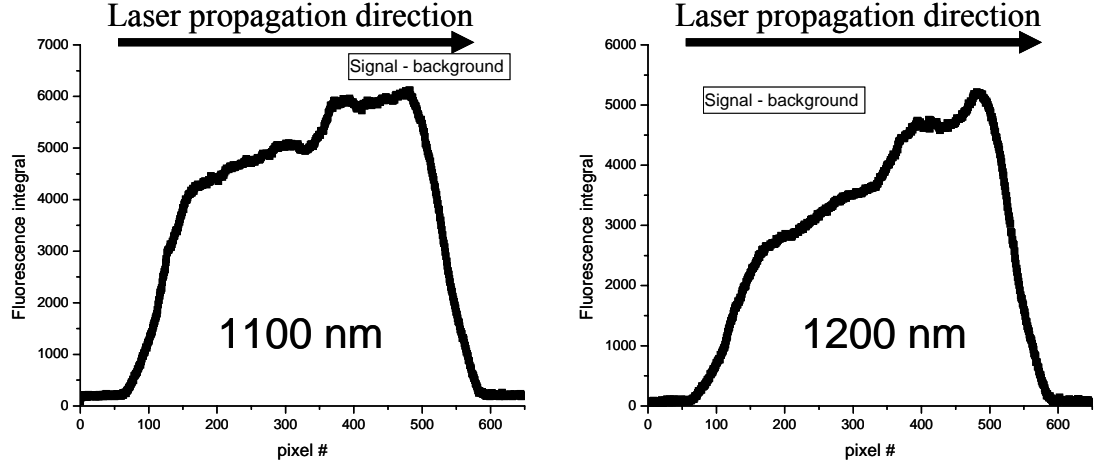


Figure 7.5. Third step of the optical imaging technique used for detecting cancer cells: the curves show the integral fluorescence signal at two excitation wavelengths along the vertical direction of the CCD sensor with subtracted background

$$\left\{ \frac{F(1100)}{F(1200)}(x_i) \right\}_{i=0}^{N-1} = \frac{\Delta \{F(x_i, 1100)\}_{i=0}^{N-1} W_{1200}^2}{\Delta \{F(x_i, 1200)\}_{i=0}^{N-1} W_{1100}^2}, \quad (7.3)$$

where  $W_{1100}$  and  $W_{1200}$  are the values of the laser power at 1100 nm and 1200 nm, respectively.

Expression (7.3) represents the change of the fluorescence intensity as a function of the laser propagation distance through the phantom. The expression is used in the next section to calculate the fluorescence ratio,  $F(1100)/F(1200)$ , for several tissue phantoms.

In the rest of this section we demonstrate spatial location detection of a cancer cell colony surrounded by a large number of normal cells. A typical cell count in an early pre-cancer stage of malignancy is about  $5 \times 10^5$  cells. Based on the 2PA spectra shown in figure 7.2 we expect that the ratio of fluorescence signals excited at 1100 and 1200 nm,  $F(1100)/F(1200)$ , will be smaller in the presence of cancer cells, because at 1200 nm the 2PA of phantoms with cancer cells is stronger than that without cancer cells, while the 2PA at 1100 nm does not depend on the phantom composition. The cancer colonies  $\sim 1 \mu\text{l}$  volume ( $\sim 1 \mu\text{m}^3$  colony size,  $\sim 10^5$  cells) were introduced in the middle of the phantom cuvettes with an adjustable volume pipette. The samples contained cancer colonies of MBA-MD-231 (human breast carcinoma cells), 4T1 (mouse mammary carcinoma cells), and +SA (mouse mammary carcinoma cells) cancer lines.

Figure 7.6 shows the fluorescence ratio,  $F(1100)/F(1200)$ , for five different samples measured as a function of spatial coordinate along the laser beam propagation direction in the region near the center of the cuvette. The first two phantoms contain uniformly distributed normal cells and +SA cancer cells. Three other samples contain the small cancer colony (MBA-MD-231, 4T1 and +SA) surrounded by a large number of normal cells.

The two curves corresponding to the phantoms with uniformly distributed cells have similar shapes, but the fluorescence ratio value,  $F(1100)/F(1200)$ , in the phantom with cancer cells is systematically lower.

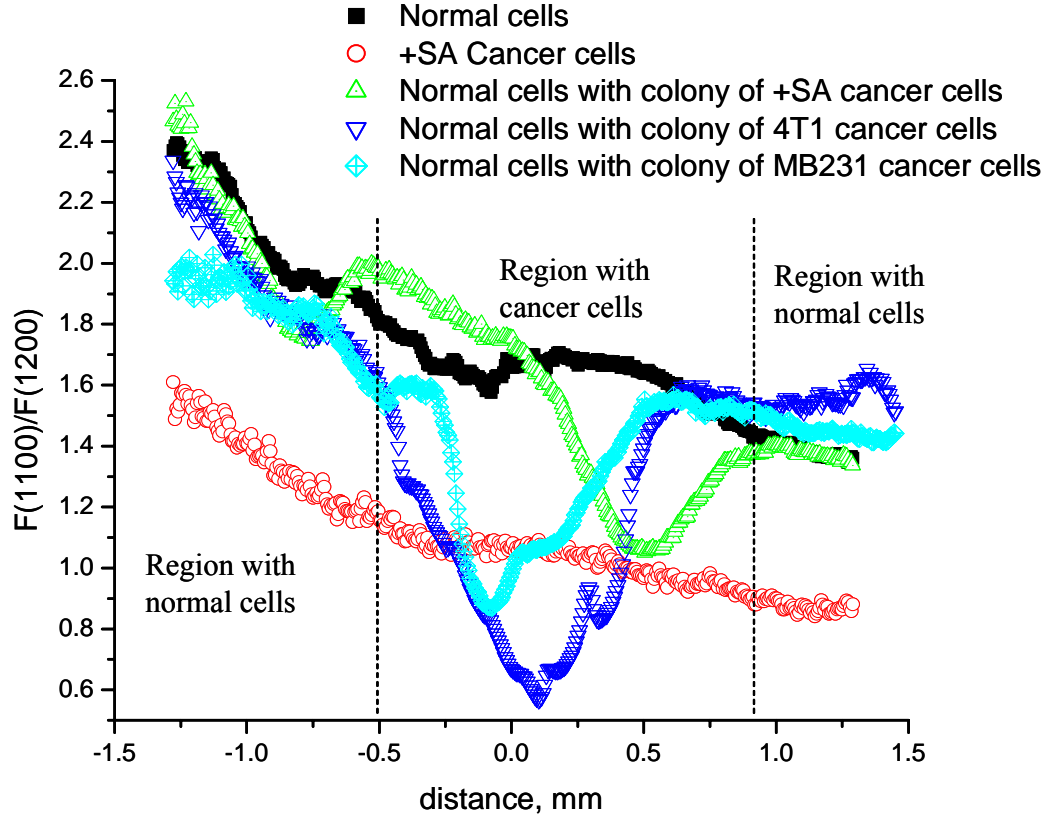


Figure 7.6. Dependence of the  $F(1100)/F(1200)$  fluorescence ratio on the laser propagation distance inside the phantom: black curve corresponds to the uniform phantom with normal cells; red curve corresponds to the uniform phantom with +SA cancer cells; green curve corresponds to the phantom with normal cells and introduced +SA cancer colony; blue curve corresponds to the phantom with normal cells and introduced 4T1 cancer colony; cyan curve corresponds to the phantom with normal cells and introduced MB231 cancer colony. Distance is measured from the middle point of the cuvette containing phantom. Vertical dashed lines show approximate location of the cancer colony introduced in the phantoms

A systematic decrease of the ratio with the distance (from  $F(1100)/F(1200) \approx 2.4$  to  $F(1100)/F(1200) \approx 1.4$  for the phantom containing normal cells, and from  $F(1100)/F(1200) \approx 1.6$  to  $F(1100)/F(1200) \approx 0.8$  for the phantom containing cancer

cells) is attributed to the effects of scattering and absorption of the laser light as it propagates through the phantom. In the samples with the small cancer colony surrounded by uniformly distributed normal cells, the fluorescence ratio shows a distinct feature exactly at the location where the cancer colony was introduced.

For this feature, the fluorescence ratio value approaches the values observed in the phantom uniformly filled with cancer cells. Outside of the feature, the fluorescence ratio value approaches that of the phantom uniformly filled with normal cells. The minimum value of the  $F(1100)/F(1200)$  ratio coincides with the predetermined position of the cancer colony. The width of the feature varies from  $\sim 0.5$  mm for MB-231 cancer line (green triangles) and +SA cancer line (black squares) to  $\sim 0.75$  mm for 4T1 cancer line (red circles), which is  $\sim 5\text{--}7\times$  the size of the colony. The values of the fluorescence ratio stay in the range  $F(1100)/F(1200) > 1.4$  for the places with normal cells and  $F(1100)/F(1200) < 1.3$  for the places with cancer cells.

This result demonstrates that Styryl-9M can be indeed used for distinguishing between the normal and cancer cells inside the tissue phantoms and even for localizing small cancer colonies surrounded by normal cells.

#### Evaluation of Ultimate Sensitivity of Cancer Cell Detection

The next point is to show that the 2PA excited fluorescence technique can be used for detection of extremely small colonies containing just a few cancer cells. For this demonstration we compare +SA cancer cell line used above with a different cancer line, NIHOVCAR3. The NIHOVCAR3 cancer line [179] is used because it is known to

produce the largest number of Pgp molecules per cancer cell. Here we assume that the binding of Styryl-9M to Pgp is responsible for the cancer sensitivity and expect that because the sensitivity to the two cancer lines will be different, it should be possible to detect a significantly smaller number of cancer cells in the phantoms with NIHOVCAR3 cancer colony than in the phantoms with +SA cancer colony.

In this experiment, the cancer colonies were introduced in the same place of the phantoms with uniformly distributed normal cells. First, the position of the cancer colony was detected by using a sample with the biggest number of cells, as described in the previous section. The fluorescence ratio  $F(1100)/F(1200)$  was measured at the position of the cancer colony. The  $F(1100)/F(1200)$  ratio had the minimum at the same position for all the phantoms where the presence of the cancer colony was detected. Figure 7.7 shows the dependence of the  $F(1100)/F(1200)$  ratio exactly at the location of the cancer colony as a function of the amount of cancer cells in the colony. Using the  $F(1100)/F(1200)$  ratio obtained in the previous section (see figure 7.6) we can introduce the following phenomenological criteria: We consider that the cancer colony is present (detected) if the fluorescence ratio is  $F(1100)/F(1200) < 1.35$ , and is not present (only normal cells are detected) if  $F(1100)/F(1200) > 1.57$ . The range of the fluorescence ratios  $1.35 < F(1100)/F(1200) < 1.57$  is considered to be a boarder line case. Figure 7.7 shows that in the phantoms containing NIHOVCAR3 cancer cells the  $F(1100)/F(1200)$  ratio falls in the “cancer colony detected” region,  $F(1100)/F(1200) < 1.35$ , for all the sizes of the cancer colonies with ten and more

cells. This data suggests that we are able to detect the colonies consisting of only about ten NIH3T3 cancer cells.

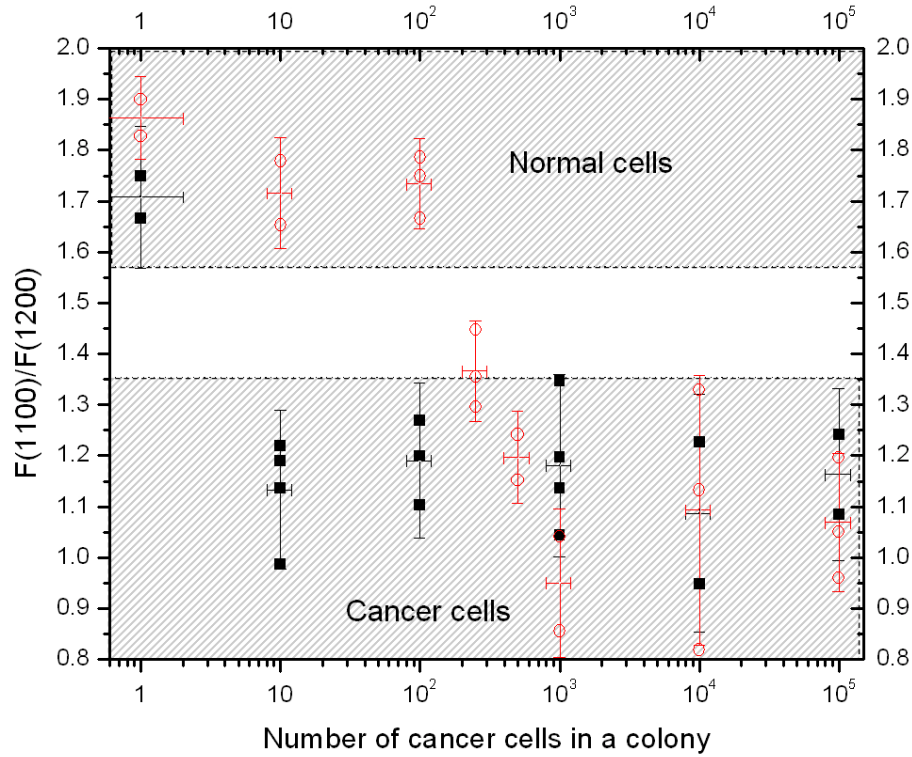


Figure 7.7. Determination of the sensitivity of cancer cell localization based on the phantoms containing a known number of cancer cells: black squares – NIH3T3 cancer line, and red circles – +SA cancer line

This is to our best knowledge the first time such high sensitivity is demonstrated for *in vivo* sample. In comparison, for the +SA cancer cells this minimum cell count increases to almost five hundred. The ability to detect 10-500 cancer cells is not exceptional for standard histology microscopic techniques [180, 181], where single cancer cells are routinely identified based on the well established morphological difference from the normal cells in stained tissue samples. The current result is remarkable in the sense that we can virtually image living cells in their natural



environment, without any special sample preparation or tissue slicing. For comparison, currently available non-invasive fluorescent techniques [182] are able to detect malignant tissues only if they contain more than  $10^5$ – $10^7$  cancer cells.

Finally, we attempt to get one more clue about what mechanism might be responsible for the very high cancer detection sensitivity. If the change of the 2PA spectrum of Styryl-9M upon binding to Pgp is responsible, then the dye should exist in two distinct forms, and the following thermo-dynamic model could be considered: The  $F(1100)/F(1200)$  fluorescence ratio should have two distinct values, the first corresponding to Styryl-9M molecules bound to Pgp, and the second to free Styryl-9M molecules in water. The dependence of the fluorescence ratio on the Pgp concentration could be expressed using the Langmuir equation, which usually describes a relationship between the concentration of a compound and the fractional occupancy (availability) of the binding sites to which this compound can bind or adsorb at a constant temperature:

$$\frac{F(1100)}{F(1200)}(x) = A + (B - A) \frac{1 - Cx}{1 + Cx}, \quad (7.4)$$

where  $A$  is the fluorescence ratio for the bound state,  $B$  is the fluorescence ratio for the unbound state,  $x$  is the number of cancer cells in the colony, and  $C$  is the thermodynamic equilibrium factor,

$$C = Ne^{-\frac{\Delta E}{kT}}, \quad (7.5)$$

where  $N$  is the average number of the Pgp molecules per one cancer cell,  $\Delta E$  is the binding energy between Styryl-9M and Pgp,  $k$  is the Boltzmann constant, and  $T$  is the temperature.

If the experimentally observed dependence of the  $F(1100)/F(1200)$  ratio on the number of cancer cells can be fitted with (7.4), then this would support our hypothesis of the binding of Styryl-9M to Pgp. If, on the other hand, the experimental dependence cannot be fitted with (7.4), then it would suggest that another mechanism is responsible for the observed sensitivity.

The solid line in figure 7.8 shows the fit of the  $F(1100)/F(1200)$  obtained for +SA cancer cells (from figure 7.7) with the expression (7.4). The dashed curves indicate the estimated uncertainty range of the current fit function. We can perform the fitting procedure only for the +SA cancer line, since its concentration dependence has at least 1 intermediate point, between the cancer and normal region. A similar fit to the NIHOVCAR3 cancer line is complicated due to an insufficient number of experimental points. Those points are hard to measure, mostly because of the complexity of preparation of the phantoms containing just 2–5 cancer cells keeping in mind that the number of the cancer cells should be known with reasonable accuracy. The fact that the measured concentration dependence is consistent with the model expression (7.4) is in accord with our initial hypothesis that binding of Styryl-9M molecules to the Pgp is responsible for the described cancer sensitivity.

The best fit of the experimental data with the expression (7.4) gives an estimate of the binding energy of Styryl-9M to Pgp:

$$\Delta E = (4.8 + \ln N \pm 0.7)kT. \quad (7.6)$$

Unfortunately, we were unable to determine the average number  $N$  of the Pgp molecules per one cancer cell, because this information is not available from the

literature, and also because determining this value from the experiment presents a tedious task, probably worth a separate study. We estimate this value to be somewhere in the range  $10^1 < N < 10^4$ . We conclude that the binding energy is on the order of  $\Delta E \sim 10kT$ .

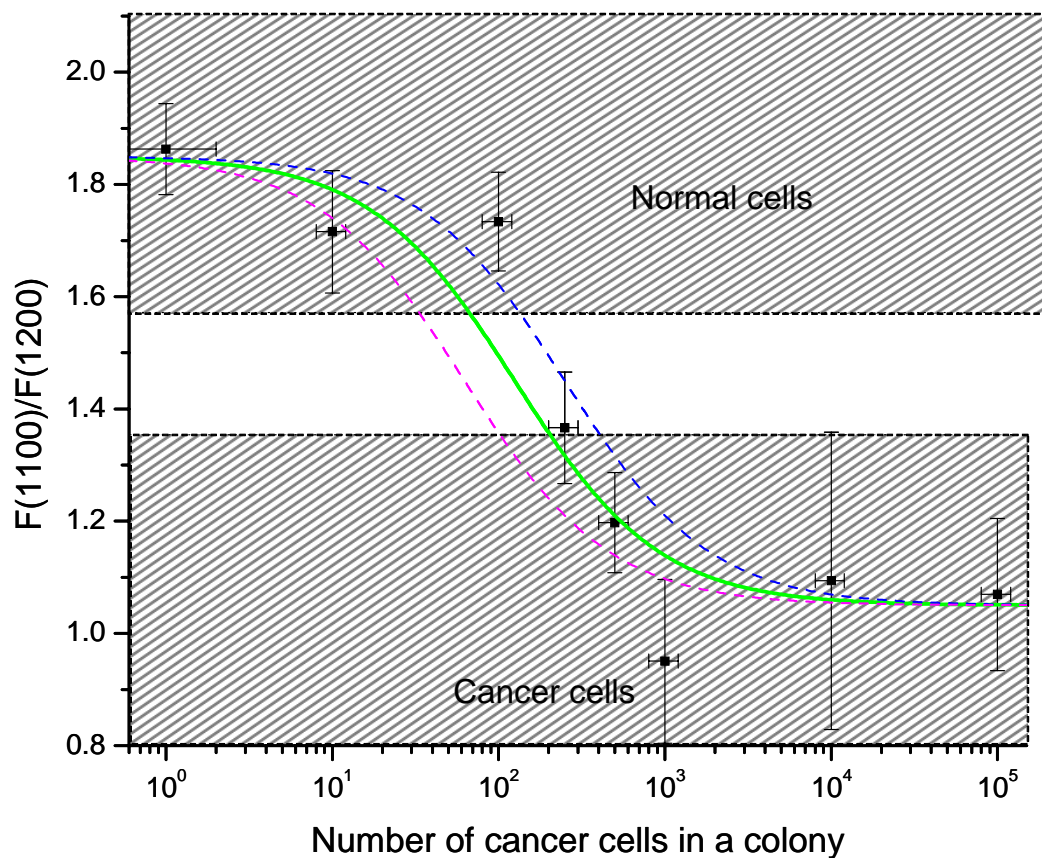


Figure 7.8. Determination of the binding energy of Styryl-9M to cancer cells of the +SA cancer line: Parameters obtained from the expression (7.4) are:  $A = 1.05$ ,  $B = 1.85$ ; The best fit gives  $C = 0.008$  (solid green line), and the corresponding fitting errors give:  $C = 0.004$  (dashed blue line), and  $C = 0.016$  (dashed pink line)

This value suggests that the binding between the ligand (Styryl-9M) and receptor (Pgp) is most probably due to electrostatic interaction. The energy value (0.25 eV)

correlates well with the ligand-receptor binding energies typical to biological systems,  $\Delta E \sim 0.12 - 1.2$  eV.

To conclude, we have shown that the commercially available dye, Styryl-9M, can be used as a sensitive fluorescent marker for detection of cancer cell colonies embedded in biological tissue phantoms. The method we propose and implement is based on the quantitative analysis of the fluorescence signals obtained with two-photon excitation at two different wavelengths in the near-IR range. By comparing normalized ratios of the signal intensity at different wavelengths we are able to distinguish between samples with cancer cells, without cells, and with normal cells. We show that this ratiometric imaging allows for first time the spatial localization of as few as 10 cancer cells inside a tissue phantoms. The proposed method seems promising for non-invasive deep optical detection of cancer. It can be applied for cancer diagnostics by differentiation of cancer vs. normal cells, as well as for precise localization of tumors.

## 8. SUMMARY AND CONCLUSIONS

The work presented in this dissertation includes results in the following four main areas: a) establishment of the 2PA reference standards in 550–1600 nm excitation range, b) quantitative analysis of the experimentally measured 2PA spectra and cross sections and the comparison with the predictions of the few-essential-levels model, c) applications of 2PA for volumetric optical memory, and d) applications of 2PA for cancer detection.

### Measurements of Two-Photon Absorption Spectra and Cross Sections: Reference Standards in 550–1600 nm Excitation Range (Chapter 4)

This dissertation, for the first time, establishes a set of reference dyes for measurements of 2PA in the broad excitation range of wavelengths, 550–1600 nm. The absolute 2PA spectra of commercial organic dyes presented here are measured with an estimated accuracy  $\pm 15\%$  using an improved femtosecond fluorescence excitation method, which accounts for the variations of the pulse duration and the beam profile with the excitation wavelength. The data are in good agreement with previously available yet inaccurate literature data at selected wavelengths, especially those measured with the fluorescence techniques. These results facilitate accurate quantitative relative measurements of the 2PA spectra and cross sections.

Application of the Few-Essential Energy Levels  
Model for Quantitative Description of the Two-Photon  
Absorption Spectra and Cross Sections (Chapter 5)

This dissertation presents a systematic study of the applicability of the few-essential-levels model to the quantitative interpretation of 2PA spectra and cross sections. The study shows, for the first time, that the model gives accurate quantitative results in the low-energy transitions in a broad class of organic dye molecules, such as substituted diphenylaminostilbenes, push-pull and symmetrical tetrapyrroles (porphyrins and tetraazachlorin), and carbazol-substituted stilbenes. The 2PA cross section values are determined in two alternative ways: (a) by direct measurement with the femtosecond fluorescence excitation method and (b) by measuring the values of the permanent dipole moment differences between the ground- and the excited states and the transition dipole moments between the states involved in the transitions in separate linear and pump-probe spectroscopic experiments, and by using perturbation theory for two- and three-level systems.

The 2PA cross sections obtained with the two-level model by methods (a) and (b) in the lowest-energy dipole-allowed transitions agree with better than 50% absolute accuracy, whereas in the case of at least half of the systems studied, the discrepancy is less than 20%.

The absolute 2PA spectra and cross sections obtained with the three-level model in the lowest-energy *gerade-gerade* transition of **TBTAC** agree with better than 30% absolute accuracy.

This is the first time that such direct quantitative correspondence is demonstrated for a wide range of molecules. The result shows that relatively straightforward linear and nonlinear spectroscopic measurements can be used to accurately predict the nonlinear absorption in the low energy transitions and vice versa – measurements of 2PA spectra and cross sections can be used to estimate the value and spectra of  $\Delta\vec{\mu}_{01}$  and  $\vec{\mu}_{12}$ .

### Applications of Two-Photon Absorption for Volumetric Optical Memory (Chapter 6)

This dissertation studies both theoretically and experimentally the requirements imposed on the photophysical characteristics of photochromes used for 2PA terabyte volumetric optical data storage. The dissertation presents a quantitative analysis model of the signal-to-noise ratio (SNR) and the signal-to-background ratio (SBR) when writing of the data bits is performed by means of 2PA-induced photochromic switching, and the readout is performed by 2PA-induced fluorescence. The model assumes a single-channel data access rate  $>100$  MHz with reasonable  $SNR > 4$  and leads to a minimum required intrinsic 2PA cross section value,  $\sigma_2 > 10^3$  GM. The model shows that due to practical limitations on chromophore, such high  $\sigma_2$  values can be achieved only by using near-resonance excitation. However, the near-resonance enhancement of 2PA cross sections raises questions about undesired side effects due to competing 1PA on the low-frequency side of the lowest-frequency transition band. The dissertation investigates the critical trade-off between the 2PA and the 1PA as a function of the laser detuning from the 1PA resonance, laser intensity, and sample temperature. The simulations show that fast writing and readout with acceptable SNR and SBR may be achieved by carefully choosing all the

above variables. The proposed concepts are verified by performing experiments with non-symmetrical phthalocyanine molecule, which shows a near-resonance 2PA cross section,  $\sigma_2 \sim 10^4$  GM, and efficient 2PA-induced photochromic switching between two tautomer forms. According to the model presented, molecules of this type have potential for high capacity data storage.

#### Applications of Two-Photon Absorption for Cancer Detection (Chapter 7)

A novel way is presented for optical detection of malignant cancer cell colonies embedded in tissue phantoms by using near-IR femtosecond two-photon excitation of fluorescent dye Styryl-9M. The two-photon excited fluorescence from the dye is shown to depend on the type of cells, i.e. whether the cells are malignant or healthy, as well as on the composition of the phantoms. The ratio between the fluorescence intensities excited at 1100 and 1200 nm is used to distinguish between the samples containing no cell colonies, samples with colonies of normal cells, and samples with cancer cells. The proposed method is a promising tool for non-invasive deep tissue photodetection diagnostics and for precise localization of malignant cells.

#### Quantitative Nonlinear Spectroscopy

In conclusion, the approach presented in the dissertation explores the idea of quantitative two-photon absorption spectroscopy of organic chromophores as a powerful and versatile experimental tool. The methodology described here can be applied for studying individual transitions in organic and biological chromophores, and also to



functionalize organic materials for various applications. Our approach suggests a step-by-step procedure for the interpretation of the 2PA spectra and cross sections based upon the few-essential-levels model. Typical steps of this procedure are shown in figure 8.1.

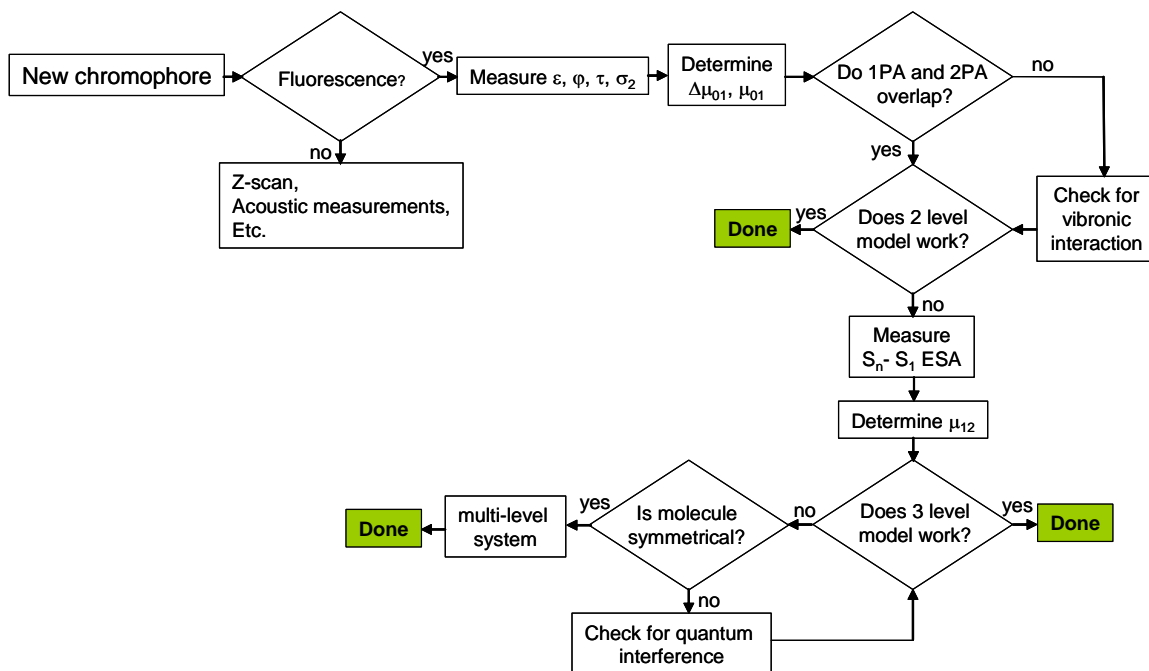


Figure 8.1. Flowchart showing typical approach to independently justify the 2PA cross section of a new compound

As a first step, one needs to measure linear properties of a molecule, comprising absorption and emission spectra, maximum extinction coefficient, and fluorescence/phosphorescence quantum yield. One also needs to check for possible complications, such as dual fluorescence, existence of conformers, etc. As a next step, one measures the relative 2PA spectrum and uses the differential quantum yield and concentration of the sample and reference compounds to determine the absolute 2PA cross sections. One also determines transition dipole moments between the ground and excited states using 1PA extinctions, and permanent dipole moment difference between

the ground and the first excited states using the Lippert-Mataga equation and solvatochromic shift measurements, as described in appendix B.

As an important step, one compares 1PA and 2PA spectra to determine if there are overlapping bands that would indicate a lack of inversion symmetry. For these systems, one attempts using the two-level model to describe the 2PA strength of the overlapping transition. Sometimes a disagreement between the two-level model and experimental data can be due to incorrectly determined permanent dipole moment difference. That can happen if the Stokes shift is due to solute-solvent interactions, other than dipole-dipole, for example, hydrogen bonding. Alternatively, a cavity volume entering the Lippert-Mataga equation can be overestimated due to nonspherical shape of a solute molecule. If vibronic components in the 2PA spectrum are more pronounced than in the 1PA spectrum, this effect should also be taken into account.

For the other transitions, the three-level model can be applied to describe the 2PA strength. The excited state transition dipole moment can be determined from femtosecond pump-probe experiments. If the three-level model fails, then there are two further possibilities: (a) If the molecule lacks a center of symmetry, then quantum interference between alternative pathways may need to be taken into account. (b) If the molecule is centro-symmetrical, then the influence of even higher energy levels on the 2PA strength is significant.

Future studies may combine the quantitative nonlinear spectroscopy with microscopic methods in applications to biological objects and nanoscale structures.

## REFERENCES CITED

1. M. Göppert-Mayer, "Über elementarakte mit zwei quantensprüngen", *Annalen der Physik*, **401**, 273-294 (1931).
2. W. Kaiser, C.G. Garrett, "Two-photon excitation in  $\text{CaF}_2\text{:Eu}^{2+}$ ", *Phys. Rev. Lett.*, **7**, 229-231 (1961).
3. W. Denk, J.H. Strickler, W.W. Webb, "Two-photon laser scanning fluorescence microscopy", *Science*, **248**, 73-76 (1990).
4. R.M. Williams, D.W. Piston, W.W. Webb, "Two-photon molecular excitation provides intrinsic 3-dimensional resolution for laser-based microscopy and microphotochemistry", *FASEB J.*, **8**, 804-813 (1994).
5. B.R. Masters, P.T.C. So, E. Gratton, "Multiphoton excitation fluorescence microscopy and spectroscopy of in vivo human skin", *Biophys. J.*, **72**, 2405-2412 (1997).
6. P.T.C. So, H. Kim, I.E. Kochevar, "Two-photon deep tissue ex vivo imaging of mouse dermal and subcutaneous structures", *Opt. Expr.*, **3**, 339-350 (1998).
7. R. Gauderon, C.J.R. Sheppard, "Effect of a finite-size pinhole on noise performance in single-, two-, and three-photon confocal fluorescent microscopy", *Appl. Opt.*, **38**, 3562-3564 (1999).
8. G.H. Patterson, D.W. Piston, "Photobleaching in two-photon excitation microscopy", *Biophys. J.*, **78**, 2159-2162 (2000).
9. W.R. Zipfel, R.M. Williams, W.W. Webb, "Nonlinear magic: multiphoton microscopy in the biosciences", *Nat. Biotechnol.*, **21**, 1369-1377 (2003).
10. Z.-Q. Liu, Q. Fang, D. Wang, D.-X. Cao, G. Xue, W.-T. Yu, H. Lei, "Trivalent boron as an acceptor in donor- $\pi$ -acceptor-type compounds for single- and two-photon excited fluorescence", *Chem. Eur. J.*, **9**, 5074-5084 (2003).
11. M. Oheim, D.J. Michael, M. Geisbauer, D. Madsen, R.H. Chow, "Principles of two-photon excitation fluorescence microscopy and other nonlinear imaging approaches", *Adv. Drug Deliv. Rev.*, **58**, 788-808 (2006).
12. Y. Imanishi, K.H. Lodowski, Y. Koutalos, "Two-photon microscopy: shedding light on the chemistry of vision", *Biochem.*, **46**, 9674-9684 (2007).
13. G.S. He, J.D. Bhawalkar, C.F. Zhao, P.N. Prasad, "Optical limiting effect in a two-photon absorption dye doped solid matrix", *Appl. Phys. Lett.*, **67**, 2433-2435 (1995).

14. G.S. He, G.C. Xu, P.N. Prasad, B.A. Reinhardt, J.C. Bhatt, A.G. Dillard, "Two-photon absorption and optical-limiting properties of novel organic compounds", *Opt. Lett.*, **20**, 435-437 (1995).
15. D.I. Kovsh, S. Yang, D.J. Hagan, E.W. Van Stryland, "Nonlinear optical beam propagation for optical limiting", *Appl. Opt.*, **38**, 5168-5180 (1999).
16. J. Oberlé, L. Bramerie, G. Jonusauskas, C. Rullière, "Optical-limiting properties of a push-pull diphenyl-butadiene", *Opt. Comm.*, **169**, 325-352 (1999).
17. C.W. Spangler, "Recent development in the design of organic materials for optical power limiting", *J. Mater. Chem.*, **9**, 2013-2020 (1999).
18. Y. Morel, A. Ibanez, C. Nguefack, C. Andraud, A. Collet, J-F. Nicoud, P.L. Baldeck, "Nonlinear absorption spectra of transparent organic crystals for optical limiting applications at visible wavelengths" *Synt. Met.*, **115**, 265-268 (2000).
19. F.E. Hernández, S. Yang, E.W. Van Stryland, D.J. Hagan, "High-dynamic-range cascaded-focus optical limiter", *Opt. Lett.*, **25**, 1180-1182 (2000).
20. H. Lei, H.Z. Wang, Z.C. Wei, X.J. Tang, L.Z. Wu, C.H. Tung, G.Y. Zhou, "Photophysical properties and TPA optical limiting of two new organic compounds", *Chem. Phys. Lett.*, **333**, 387-390 (2001).
21. R. Lepkowicz, A. Kobaykov, D.J. Hagan, E.W. Van Stryland, "Picosecond optical limiting in reverse saturable absorbers: a theoretical and experimental study", *J. Opt. Soc. Am. B*, **19**, 94-101 (2002).
22. M.G. Silly, L. Porrès, O. Mongin, P.-A. Chollet, M. Blanchard-Desce, "Optical limiting in the red-NIR range with soluble two-photon absorbing molecules", *Chem. Phys. Lett.*, **379**, 74-80 (2003).
23. C. Li, C. Liu, Q. Li, Q. Gong, "Broadband optical limiting and nonlinear optical absorption properties of a novel hyperbranched conjugated polymer", *Chem. Phys. Lett.*, **400**, 569-572 (2004).
24. T.-C. Lin, G.S. He, P.N. Prasad, L.-S. Tan, "Degenerate nonlinear absorption and optical power limiting properties of asymmetrically substituted stilbenoid chromophores", *J. Mater. Chem.*, **14**, 982-991 (2004).
25. M. Charlot, N. Izard, O. Mongin, D. Riehl, M. Blanchard-Desce, "Optical limiting with soluble two-photon absorbing quadrupoles: Structure-property relationships", *Chem. Phys. Lett.*, **417**, 297-302 (2006).

26. P.-A. Bouit, G. Wetzel, G. Berginc, B. Loiseaux, L. Toupet, P. Feneyrou, Y. Bretonnière, K. Kamada, O. Maury, C. Andraud, "Near IR nonlinear absorbing chromophores with optical limiting properties at telecommunication wavelengths", *Chem. Mater.*, **19**, 5325-5335 (2007).
27. T. Karu, V. Letokhov, "Possible benefits of two-quantum excitation in ALA-PDT", *J. Photochem. Photobiol. B*, **23**, 261-262 (1994).
28. D. Leupold, I.E. Kochevar, "Multiphoton photochemistry in biological systems. Introduction", *Photochem. Photobiol.*, **66**, 562-565 (1997).
29. J.D. Bhawalkar, N.D. Kumar, C.F. Zhao, P.N. Prasad, "Two-photon photodynamic therapy", *J. Clin. Laser Med. Surg.*, **15** (5), 201-204 (1997).
30. M.W. Berns, Z. Wang, A. Dunn, V. Wallace, V. Venugopalan, "Gene inactivation by multiphoton-targeted photochemistry", *Proc. Nat. Acad. Sci. USA*, **97**, 9504-9507 (2000).
31. P.K. Frederiksen, M. Jorgensen, P.R. Ogilby, "Two-photon photosensitizes production of singlet oxygen", *J. Am. Chem. Soc.*, **123**, 1215-1221 (2001).
32. A. Karotki, M. Kruk, M. Drobizhev, A. Rebane, E. Nickel, C.W. Spangler, "Efficient singlet oxygen generation upon two-photon excitation of new porphyrin with enhanced nonlinear absorption", *IEEE J. Sel. Top. Quantum Electron.*, **7**, 971-975 (2001).
33. J. Liu, Y.W. Zhao, J.Q. Zhao, A.D. Xia, L.J. Jiang, S. Wu, L. Ma, Y.Q. Dong, Y.H. Gu, "Two-photon excitation studies of hypocrellins for photodynamic therapy", *J. Photochem. Photobiol. B*, **68**, 156-164 (2002).
34. A. Karotki, "Simultaneous two-photon absorption of tetrapyrrolic molecules: from femtosecond coherence experiments to photodynamic therapy", Ph.D. Thesis, Montana State University, Bozeman, Montana, (2003).
35. K. Ogawa, H. Hasegawa, Y. Inaba, Y. Kobuke, H. Inouye, Y. Kanermitsu, E. Kohono, T. Hirano, S. Ogura, I. Okura, "Water-soluble bis(imidazolylporphyrin) self-assemblies with large two-photon absorption cross sections as potential agents for photodynamic therapy", *J. Med. Chem.*, **49**, 2276-2283 (2006).
36. A. Karotki, M. Khurana, J.R. Lepock, B.C. Wilson, "Simultaneous two-photon excitation of photofrin in relation to photodynamic therapy", *Photochem. Photobiol.*, **82**, 443-452 (2006).
37. D. Gao, R.R. Agayan, H. Xu, M.A. Philbert, R. Kopelman, "Nanoparticles for two-photon photodynamic therapy in living cells", *Nano Lett.*, **6**, 2383-2386 (2006).

38. T.J. Beck, M. Burkanas, S. Bagdonas, Z. Krivickiene, W. Beyer, R. Sroka, R. Baumgartner, R. Rotomskis, "Two-photon photodynamic therapy of C6 cells by means of 5-aminolevulinic acid induced protoporphyrin IX", *J. Photochem. Photobiol. B*, **87**, 174-182 (2007).
39. D.A. Parthenopoulos, P.M. Rentzepis, "Three-Dimensional Optical Storage", *Science*, **245**, 843-845 (1989).
40. D.A. Parthenopoulos, P.M. Rentzepis, "Two-photon volume information storage in doped polymer systems", *J. Appl. Phys.*, **68**, 5814-5818 (1990).
41. J.H. Strickler, W.W. Webb, "3-D optical data storage by two-photon excitation", *Adv. Mater.*, **5**, 1479-481 (1993).
42. A.S. Dvornikov, J. Malkin, P.M. Rentzepis, "Spectroscopy and kinetics of photochromic materials for 3D optical memory devices", *J. Phys. Chem.*, **98**, 6746-6752 (1994).
43. A.S. Dvornikov, I. Cokgor, F. McCormick, R. Piyaket, S. Esener, P.M. Rentzepis, "Molecular transformation as a means for 3D optical memory devices", *Opt. Commun.*, **128**, 205-210 (1996).
44. R.R. Birge, B. Parsons, Q.W. Song, J.R. Tallent, "Protein-based three-dimensional memories and associative processors", in: *Molecular Electronics*, ed.: M.A. Ratner and J. Jortner, Blackwell Science, 1997.
45. A.S. Dvornikov, P.M. Rentzepis, "Novel organic ROM materials for optical 3D memory devices", *Opt. Commun.*, **136**, 1-6 (1997).
46. B.H. Cumpston, S.P. Ananthavel, S. Barlow, D.L. Dyer, J.E. Ehrlich, L.L. Erskine, A.A. Heikal, S.M. Kuebler, I.-Y.S. Lee, D. McCord-Maughon, J. Qin, H. Rockel, M. Rumi, X.-L. Wu, S.R. Marder, J.W. Perry, "Two-photon polymerization initiators for three-dimensional optical data storage and microfabrication", *Nature*, **398** (6722), 51 (1999).
47. D. Day, M. Gu, A. Smallridge, "Use of two-photon excitation for erasable-rewritable three-dimensional bit optical data storage in a photorefractive polymer", *Opt. Lett.*, **24**, 948-950 (1999).
48. H.E. Pudavar, M.P. Joshi, P.N. Prasad, B.A. Reinhardt, "High-density three-dimensional optical data storage in a stacked compact disk format with two-photon writing and single photon readout", *Appl. Phys. Lett.*, **74**, 1338-1340 (1999).
49. S. Kawata, Y. Kawata, "Three-dimensional optical data storage using photochromic materials", *Chem. Rev.*, **100**, 1777-1788 (2000).

50. "Photochromism: Memories and switches," *Chem. Rev.*, **100**, Spec. Iss. 5, Guest ed.: M. Irie, (2000).
51. Y. Shen, J. Swiatkiewicz, D. Jakubczyk, F. Xu, P.N. Prasad, R.A. Vaia, B.A. Reinhardt, "High-density optical data storage with one-photon and two-photon near-field fluorescence microscopy", *Appl. Opt.*, **40**, 938-940 (2001).
52. K.D. Belfield, K. J. Schafer, "A new photosensitive polymer material for WORM optical data storage", *Chem. Mater.*, **14**, 3656-3662 (2002).
53. G.W. Burr, "Volumetric storage" in *Encyclopedia of Optical Engineering*, ed.: R.B. Johnson and R.G. Driggers, Marcel Dekker, New York, 2003.
54. A.S. Dvornikov, Y.C. Liang, P.M. Rentzepis, "Ultra-high-density non-destructive readout, rewritable molecular memory", *Res. Chem. Intermed.*, **30**, 545-561 (2004).
55. W.-Y. Liao, S.-S. Wang, H.-H. Yao, C.-W. Chen, H.-P. Tasi, W.-P. Chu, J.-H. Chen, S.-B. Lee, "Three-dimensional optical disks using fluorescent oligomer recording material", *IEEE Trans. Magn.*, **41**, 1019-1021 (2005).
56. C. Corredor, Z.-L. Huang, K.D. Belfield, "Two-photon 3-D optical data storage in a photochromic diarylethene polymer composite", *Polym. Prepr.*, **47**, 1058-1059 (2006).
57. N.S. Makarov, M. Drobizhev, A. Rebane, D. Peone, H. Wolleb, H. Spahni, "Experimental characterization of two-photon materials for fast rewritable optical data storage", *Proc. SPIE*, **6330**, 63300K (2006).
58. E. Walker, A. Dvornikov, K. Coblenz, S. Esener, P. Rentzepis, "Toward terabyte two-photon 3D disk", *Opt. Expr.*, **15**, 12264-12276 (2007).
59. N.S. Makarov, A. Rebane, M. Drobizhev, H. Wolleb, H. Spahni, "Optimizing two-photon absorption for volumetric optical data storage", *J. Opt. Soc. Am. B*, **24**, 1874-1885 (2007).
60. S. Maruo, S. Kawata, "Two-photon-absorbed near-infrared photopolymerization for three-dimensional microfabrication", *J. Microelectromech. Syst.*, **7**, 411-415 (1998).
61. H.-B. Sun, T. Kawakami, Y. Xu, J.-Y. Ye, S. Matuso, H. Misawa, M. Miwa, R. Kaneko, "Real three-dimensional microstructures fabricated by photopolymerization of resins through two-photon absorption", *Opt. Lett.*, **25**, 1110-1112 (2000).
62. K.D. Belfield, K.J. Schafer, Y. Liu, J. Liu, X. Ren, E.W. Van Stryland, "Multiphoton-absorbing organic materials for microfabrication, emerging optical



- applications and non-destructive three-dimensional imaging”, *J. Phys. Org. Chem.*, **13**, 837-849 (2000).
63. M. Miwa, S. Juodkazis, S. Matsuo, H. Misawa, “Femtosecond two-photon stereolithography”, *Appl. Phys. A*, **73**, 561-566 (2001).
  64. I. Wang, M. Bouriau, P.L. Baldeck, C. Martineau, C. Andraud, “Three-dimensional microfabrication by two-photon-initiated polymerization with a low-cost microlaser”, *Opt. Lett.*, **27**, 1348-1350 (2002).
  65. W. Zhou, S.M. Kuebler, K.L. Braun, T. Yu, J.K. Cammack, C.K. Ober, J.W. Perry, “An efficient two-photon-generated photoacid applied to positive-tone 3D microfabrication”, *Science*, **296**, 1106-1109 (2002).
  66. T. Yu, C.K. Ober, S.M. Kuebler, W. Zhou, S.R. Marder, J.W. Perry, “Chemically amplified positive resists for two-photon three-dimensional microfabrication”, *Adv. Mater.*, **15**, 517-521 (2003).
  67. K.-S. Lee, D.-Y. Yang, S.H. Park, R.H. Kim, “Recent developments in the use of two-photon polymerization in precise 2D and 3D microfabrications”, *Polym. Adv. Technol.*, **17**, 72-82 (2006).
  68. Y. Zhao, X. Li, F. Wu, X. Fang, “Novel multi-branched two-photon polymerization initiators of ketocoumarin derivatives”, *J. Photochem. Photobiol. A*, **177**, 12-16 (2006).
  69. A.C. Young, J. Dragavon, T. Strovas, T. Molter, L. Zheng, L. Burgess, A.K.-Y. Jen, M.E. Lidstrom, D.R. Meldrum, “Two-photon lithography of platinum-porphyrin oxygen sensor”, *IEEE Sens. J.*, **7**, 931-936 (2007).
  70. A. Tünnermann, H. Eichmann, R. Henking, K. Mossavi, B. Wellegehausen, “Single-shot autocorrelator for KrF subpicosecond pulses based on two-photon fluorescence of cadmium vapor at  $\lambda=508$  nm”, *Opt. Lett.*, **16**, 402-404 (1991).
  71. O. Lammel, A. Penzkofer, “Femtosecond pulse duration measurement by two-photon fluorescence detection”, *Opt. Quant. Electr.*, **32**, 1147-1160 (2000).
  72. K. Ogawa, “Real-time spectrogram measurement of ultrashort optical pulses using two-photon absorption in semiconductor”, *Opt. Expr.*, **10**, 262-267 (2002).
  73. F. Theberge, S.M. Sharifi, S.L. Chin, H. Schroder, “Simple 3-D characterization of ultrashort laser pulses”, *Opt. Expr.*, **14**, 10125-10131 (2006).
  74. A. Kosuge, T. Sekikawa, X. Zhou, T. Kanai, S. Adachi, S. Watanabe, “Frequency-resolved optical gating of isolated attosecond pulses in the extreme ultraviolet”, *Phys. Rev. Lett.*, **97**, 263901 (2006).

75. V.I. Bredikhin, M.D. Galanin, V.N. Genkin, "Two-photon absorption and spectroscopy", *Sov. Phys.-Usp.*, **16**, 299-321 (1973).
76. R.M. Hochstrasser, H.N. Sung, "Electronic and vibrational states of biphenyl crystals using two-photon excitation spectroscopy", *J. Chem. Phys.*, **66**, 3265-3274 (1977).
77. M.F. Granville, G.R. Holtom, B.E. Kohler, R.L. Christensen, K.L. D'Amico, "Experimental confirmation of the dipole forbidden character of the lowest excited singlet state in 1,3,5,7-octatetraene", *J. Chem. Phys.*, **70**, 593-594 (1979).
78. D.M. Friedrich, W.M. McClain, "Two-photon molecular electronic spectroscopy", *Ann. Rev. Phys. Chem.*, **31**, 559-577 (1980).
79. T.J. Barker, R.G. Denning, J.R.G. Thorne, "Applications of two-photon spectroscopy to inorganic compounds. 1. Spectrum and electronic structure of  $\text{Cs}_2\text{UO}_2\text{Cl}_4$ ", *Inorg. Chem.*, **26**, 1721-1732 (1987).
80. T. Plakhotnik, D. Wasler, "Time resolved single molecule spectroscopy", *Phys. Rev. Lett.*, **80**, 4064-4067 (1998).
81. M. Drobizhev, A. Rebane, Z. Suo, C.W. Spangler, "One-, two- and three-photon spectroscopy of  $\pi$ -conjugated dendrimers: cooperative enhancement and coherent domains", *J. Luminesc.*, **111**, 291-305 (2005).
82. M. Drobizhev, N.S. Makarov, Y. Stepanenko, A. Rebane, "Near-infrared two-photon absorption in phthalocyanines: enhancement of lowest gerade-gerade transition by symmetrical electron-accepting substitution", *J. Chem. Phys.*, **124**, 224701 (2006).
83. M. Drobizhev, N.S. Makarov, A. Rebane, G. de la Torre, T. Torres, "Strong two-photon absorption in push-pull phthalocyanines: role of low symmetry and permanent dipole moment change upon excitation", *J. Phys. Chem. B*, **112**, 848-859 (2008).
84. J.B. Birks, *Photophysics of aromatic molecules*, Wiley-Interscience: London, 1970.
85. A. Rebane, N.S. Makarov, M. Drobizhev, B. Spangler, E.S. Tarter, B.D. Reeves, C.W. Spangler, F. Meng, Z. Suo, "Quantitative prediction of two-photon absorption cross section based on linear spectroscopic properties", *J. Phys. Chem. C*, **112**, 7997-8004 (2008).
86. W. Demtroder, *Laser spectroscopy. Basic concepts and instrumentation*, Springer-Verlag: Berlin, Heidelberg, New York, 1982.

87. M. Drobizhev, A. Karotki, M. Kruk, A. Rebane, "Resonance enhancement of two-photon absorption in porphyrins", *Chem. Phys. Lett.*, **355**, 175-182 (2002).
88. M. Drobizhev, Y. Stepanenko, Y. Dzenis, A. Karotki, A. Rebane, P.N. Taylor, H.L. Anderson, "Understanding strong two-photon absorption in  $\pi$ -conjugated porphyrin dimers via double-resonance enhancement in a three-level model," *J. Am. Chem. Soc.*, **126**, 15352-15353 (2004).
89. A. Rebane, M. Drobizhev, N.S. Makarov, E. Beuerman, C. Nacke, J. Pahapill, "Modeling non-Lorentzian two-photon absorption line shape in dipolar chromophores", *J. Lumin.*, in press (2010).
90. J.F. Shepanski, R.W. Anderson Jr., "Chlorophyll-a excited singlet state absorption measured in the picosecond time regime", *Chem. Phys. Lett.*, **78**, 165-173 (1981).
91. I. Carmichael, G.L. Hug, "Triplet-triplet absorption spectra of organic molecules in condensed phases", *J. Phys. Chem. Ref. Data*, **15**, 1-31 (1986).
92. T.W. Ebbesen, K. Tanigaki, S. Kuroshima, "Excited state properties of C<sub>60</sub>", *Chem. Phys. Lett.*, **181**, 501-504 (1991).
93. D. Toptygin, "Effects of the solvent refractive index and its dispersion on the radiative decay rate and extinction coefficient of a fluorescent solute", *J. Fluoresc.*, **13**, 201-219, (2003).
94. C. Xu, W.W. Webb, "Measurement of two-photon excitation cross sections of molecular fluorophores with data from 690 to 1050 nm", *J. Opt. Soc. Am. B*, **13**, 481-491 (1996).
95. M.A. Albota, C. Xu, W.W. Webb, "Two-photon fluorescence excitation cross sections of biomolecular probes from 690 to 960 nm", *Appl. Opt.*, **37**, 7352-7356 (1998).
96. W.L. Peticolas, R. Norris, K.E. Rieckhoff, "Polarization effects in the two-photon excitation of anthracene fluorescence", *J. Chem. Phys.*, **42**, 4164-4169 (1965).
97. M. D. Galanin, Z. A. Chizhikova, "Effective cross sections of two-photon absorption in organic molecules", *JETP Lett.*, **4** (2), 27-28 (1966).
98. A.P. Aleksandrov, V.I. Bredikhin, "Measurement of the absolute value of the cross-section for two-photon absorption in anthracene molecules", *Opt. Spectr.*, **30**, 37-38 (1971).
99. J.P. Hermann, J. Ducuing, "Dispersion of the two-photon cross section in rhodamine dyes", *Opt. Comm.*, **6**, 101-105 (1972).

100. J.P. Hermann, J. Ducuing, "Absolute measurement of two-photon cross sections", *Phys. Rev. A*, **5**, 2557-2568 (1972).
101. D.J. Bradley, M.H.R. Hutchinson, H. Koetser, "Interactions of picosecond laser pulses with organic molecules", *Proc. R. Soc. Lond. A*, **329**, 105-119 (1972).
102. I.M. Catalano, A. Cingolani, "Multiphoton cross-section measurements with low-power cw laser-induced luminescence", *Appl. Opt.*, **21**, 477-480 (1982).
103. I.M. Catalano, A. Cingolani, "Absolute two-photon fluorescence with low-power cw lasers", *Appl. Phys. Lett.*, **38**, 745-747 (1981).
104. S. Li, C.Y. She, "Two-photon absorption cross-section measurements in common laser dyes at 1.06  $\mu\text{m}$ ", *Optica Acta*, **29**, 281-287 (1982).
105. S.M. Bachilo, S.L. Bondarev, "Spectral and polarization features of two-photon absorption in retinal and retinyl acetate", *Zhurnal Prikladnoi Spektroskopii*, **45**, 623-629 (1985).
106. A.P. Blokhin, A.V. Povedailo, V.A. Tolkachev, "Polarization of two-photon excited fluorescence of vapors of complex organic molecules", *Opt. Spectr.*, **60**, 60-64 (1986).
107. P. Sperber, A. Penzkofer, " $S_0$ - $S_n$  two-photon absorption dynamics of rhodamine dyes", *Opt. and Quant. Electr.*, **18**, 381-401 (1986).
108. A. Penzkofer, W. Leupacher, " $S_0$ - $S_1$  two photon absorption dynamics of organic dye solutions", *Opt. and Quant. Electr.*, **19**, 327-349 (1987).
109. C. Xu, J. Guild, W.W. Webb, W. Denk, "Determination of absolute two-photon excitation cross sections by in situ second-order autocorrelation", *Opt. Lett.*, **20**, 2372-2374 (1995).
110. P. Kaatz, D.P. Shelton, "Two-photon fluorescence cross-section measurements calibrated with hyper-Rayleigh scattering", *J. Opt. Soc. Am. B*, **16**, 998-1006 (1999).
111. J.M. Song, T. Inoue, H. Kawazumi, T. Ogawa, "Determination of two photon absorption cross section of fluorescein using a mode locked titanium sapphire laser", *Anal. Sc.*, **15**, 601-603 (1999).
112. P. Sengupta, J. Balaji, S. Banerjee, R. Phillip, G.R. Kumar, S. Maiti, "Sensitive measurement of absolute two-photon absorption cross sections", *J. Chem. Phys.*, **112**, 9201-9205 (2000).

113. D.A. Oulianov, I.V. Tomos, A.S. Dvornikov, P.M. Rentzepis, "Observations on the measurement of two-photon absorption cross-section", *Opt. Comm.*, **191**, 235-243 (2001).
114. P. Tian, W.S. Warren, "Ultrafast measurement of two-photon absorption by loss modulation", *Opt. Lett.*, **27**, 1634-1636 (2002).
115. R. Kapoor, C.S. Friend, A. Parta, "Two-photon-excited absolute emission cross-sectional measurements calibrated with a luminance meter", *J. Opt. Soc. Am. B*, **20**, 1550-1554 (2003).
116. M. Kauert, P.C. Stoller, M. Frenz, J. Rička, "Absolute measurement of molecular two-photon absorption cross-sections using a fluorescence saturation technique", *Opt. Expr.*, **14**, 8434-8447 (2006).
117. G.O. Clay, C.B. Schaffer, D. Kleinfeld, "Large two-photon absorptivity of hemoglobin in the infrared range of 780-880 nm", *J. Chem. Phys.*, **126**, 025102 (2007).
118. J.N. Demas, G.A. Crosby, "The measurement of photoluminescence quantum yields. A review", *J. Phys. Chem.*, **75** (8), 991-1024 (1971).
119. T. Karstens, K. Kobs, "Rhodamine B and Rhodamine 101 as reference substances for fluorescence quantum yield measurements", *J. Phys. Chem.*, **84** (14), 1871-1872 (1980).
120. O.S. Finikova, T. Troxler, A. Senes, W.F. DeGrado, R.M. Hochstrasser, S.A. Vinogradov, "Energy and electron transfer in enhanced two-photon-absorbing systems with triplet cores", *J. Phys. Chem. A*, **111** (30), 6977-6990 (2007).
121. R. Sailaja, P.B. Bisht, C.P. Singh, K.S. Bindra, S.M. Oak, "Influence of multiphoton events in measurement of two-photon absorption cross-sections and optical nonlinear parameters under femtosecond pumping", *Opt. Commun.*, **277**, 433-439 (2007).
122. P. Suppan, "Invited review: Solvatochromic shifts: the influence of the medium on the energy of electronic states", *J. Photochem & Photobio. A*, **50**, 293-330 (1990).
123. Vauthey E., Holliday K., Changjiang W., Renn A., Wild U.P., "Stark-effect and spectral hole-burning - solvation of organic-dyes in polymers", *Chem. Phys.* **171**, 253-263 (1993).
124. P.N. Day, K.A. Nguyen, R. Pachter, "TDDF study of one- and two-photon absorption properties: donor- $\pi$ -acceptor chromophores", *J. Phys. Chem. B*, **109**, 1803-1814 (2005).

125. P. Shao, B. Huang, L. Chen, Z. Liu, J. Qin, H. Gong, S. Ding, Q. Wang, "Synthesis and two-photon absorption properties of novel heterocycle-based organic molecules", *J. Mater. Chem.*, **15**, 4502-4506 (2005).
126. S. Lee, K.R.J. Thomas, S. Thayumanavan, C.J. Bardeen, "Dependence of two-photon absorption cross section on the conjugation of the phenylacetylene linker in dipolar donor-bridge-acceptor chromophores", *J. Phys. Chem. A*, **109**, 9767-9774 (2005).
127. L. Antonov, K. Kamada, K. Ohta, F.S. Kamounah, "A systematic femtosecond study on the two-photon absorbing D- $\pi$ -A molecules- $\pi$ -bridge nitrogen insertion and strength of the donor and acceptor groups", *Phys. Chem. Chem. Phys.*, **5**, 1193-1197 (2003).
128. S. Polyutov, I. Minkov, F. Gel'mukhanov, H. Agren, "Interplay of one- and two-step channels in electrovibrational two-photon absorption", *J. Phys. Chem. A*, **109**, 9507-9513 (2005).
129. M. Drobizhev, F. Meng, A. Rebane, Y. Stepanenko, E. Nickel, C.W. Spangler, "Strong two-photon absorption in new asymmetrically substituted porphyrins: interference between charge-transfer and intermediate-resonance pathways", *J. Phys. Chem. B*, **110**, 9802-9814 (2006).
130. M. Drobizhev, A. Karotki, Y. Dzenis, A. Rebane, Z.Y. Suo, C.W. Spangler, "Strong cooperative enhancement of two-photon absorption in dendrimers", *J. Phys. Chem. B*, **107** (31), 7540-7543 (2003).
131. J.R. Lakowicz, *Principles of fluorescence spectroscopy*, Plenum Press: New York, 1983.
132. T. Fukuda, E.A. Makarova, E.A. Luk'yanets, N. Kobayashi, "Synthesis and spectroscopic and electrochemical studies of novel benzo- or 2,3-naphtho-fused tetraazachlorins, bacteriochlorins, and isobacteriochlorins", *Chem. Eur. J.*, **10**, 117-133 (2004).
133. S.M. Arabei, J.-P. Galaup, A.P. Stupak, T.A. Pavich, E.A. Makarova, K.N. Solovyov, "Spectral and luminescent properties of triareno-substituted tetraazochlorins", *J. Appl. Spect.*, **76**, 352-361 (2009).
134. J. Rodriguez, C. Kirmaier, D. Holten, "Optical properties of metalloporphyrin excited states", *J. Am. Chem. Soc.*, **111**, 6500-6506 (1989).
135. W.J. Meath, E.A. Power, "On the importance of permanent moments in multiphoton absorption using perturbation theory", *J. Phys. B: At. Mol. Phys.*, **17**, 763-781 (1984).

136. C. Wan, C.K. Johnson, "Time-resolved anisotropic two-photon spectroscopy", *Chem. Phys.*, **179**, 513-531 (1994).
137. Y.B. Vysotsky, V.A. Kuzmitsky, K.N. Solovyov, " $\pi$ -Electron ring currents and magnetic properties of porphyrin molecules in the MO LCAO SCF method", *Theor. Chim. Acta*, **59**, 467-485 (1981).
138. Y.B. Vysotsky, V.A. Kuzmitsky, K.N. Solovyov, "Calculation of the magnetic properties of porphyrin molecules using MO LCAO SCF method", *J. Struct. Chem.*, **22**, 22-30 (1981) (in Russian).
139. M. Drobizhev, Y. Stepanenko, Y. Dzenis, A. Karotki, A. Rebane, P.N. Taylor, H.L. Anderson, "Extremely strong near-IR two-photon absorption in conjugated porphyrin dimers: quantitative description with three-essential-states model", *J. Phys. Chem. B*, **109**, 7223-7236 (2005).
140. M. Drobizhev, Y. Stepanenko, A. Rebane, C.J. Wilson, T.E.O. Screen, H.L. Anderson, "Strong cooperative enhancement of two-photon absorption in double-strand conjugated porphyrin ladder arrays", *J. Am. Chem. Soc.*, **128**, 12432-12433 (2006).
141. M. Drobizhev, A. Karotki, M. Kruk, N. Zh. Mamardashvili, A. Rebane, "Drastic enhancement of two-photon absorption in porphyrins associated with symmetrical electron-accepting substitution", *Chem. Phys. Lett.*, **361**, 504-512 (2002).
142. A. Karotki, M. Drobizhev, Y. Dzenis, P.N. Taylor, H.L. Anderson, A. Rebane, "Dramatic enhancement of intrinsic two-photon absorption in a conjugated porphyrin dimer", *Phys. Chem. Chem. Phys.*, **6**, 7-10 (2004).
143. S.F. Shkirman, S.M. Arabei, G.D. Egorova, "Photoinduced molecular transformations of tetrapropylchlorin in an n-octane matrix", *J. Appl. Spectr.*, **31**, 1370-1373 (1980).
144. S. Völker, R. Macfarlane, "Laser photochemistry and hole-burning of chlorine in crystalline n-alkanes at low temperatures", *J. Chem. Phys.*, **73**, 4476-4482 (1980).
145. E.I. Zenkevich, A.M. Shulga, I.V. Filatov, A.V. Chernook, G.P. Gurinovich, "NH tautomerism and visible absorption spectra of porphyrins with asymmetrical substitution: oscillator model and MO calculations", *Chem. Phys. Lett.*, **120**, 63-68 (1985).
146. I. Renge, H. Wolleb, H. Spahni, U.P. Wild, "Phthalonaphthalocyanines: New Far-Red Dyes for Spectral Hole Burning", *J. Phys. Chem. A*, **101**, 6202-6213 (1997).

147. M. Drobizhev, C. Sigel, A. Rebane, "Photo-tautomer of Br-porphyrin: A new frequency-selective material for ultrafast time-space holographic storage", *J. Lumin.*, **86**, 391-397 (2000).
148. M. Drobizhev, A. Karotki, M. Kruk, A. Krivokapic, H.L. Anderson, A. Rebane, "Photon energy upconversion in porphyrins: one-photon hot-band absorption versus two-photon absorption", *Chem. Phys. Lett.*, **370**, 690-699 (2003).
149. V.F. Mandzhikov, V.A. Murin, V.A. Barachevskii, "Nonlinear coloration of photochromic spiropyran solutions", *Quant. Electron. (Moscow)*, **3**, 128-129 (1973).
150. A.A. Angeluts, N.I. Koroteev, S.A. Magnitskii, M.M. Nazarov, I.A. Ozheredov, A.P. Shkurinov, "An experimental setup for studying photochromic compounds exposed to two-photon excitation", *Instruments and Experimental Techniques*, **41**, 94-98 (1998).
151. S. Saita, T. Yamaguchi, T. Kawai, M. Irie, "Two-photon photochromism of diarylethene dimer derivatives", *Chem. Phys. Chem.*, **6**, 2300-2306 (2005).
152. Y. Feng, Y. Yan, S. Wang, W. Zhu, S. Qian, H. Tian, "Photochromic thiophene oligomers based on bithienylethene: synthesis, photochromic and two-photon properties", *J. Mater. Chem.*, **16**, 3685-3692 (2006).
153. K. Kamada, K. Ohta, Y. Iwase, K. Kondo, "Two-photon absorption properties of symmetric substituted diacetylene: drastic enhancement of the cross section near the one-photon absorption peak", *Chem. Phys. Lett.*, **372**, 386-393 (2003).
154. J.M. Hales, D.J. Hagan, E.W. Van Stryland, K.J. Schafer, A.R. Morales, K.D. Belfield, P. Pacher, O. Kwon, E. Zojer, J.L. Bredas, "Resonant enhancement of two-photon absorption in substituted fluorine molecules", *J. Chem. Phys.*, **121**, 3152- 3160 (2004).
155. M. Drobizhev, N.S. Makarov, A. Rebane, H. Wolleb, H. Spahni, "Very efficient two-photon induced photo-tautomerization in non-symmetrical phthalocyanines", *J. Lumin.*, **128**, 217-222 (2008).
156. S. Montan, K. Svanberg, S. Svanberg, "Multicolor imaging and contrast enhancement in cancer-tumor localization using laser-induced fluorescence in hematoporphyrin-derivative-bearing tissue", *Opt. Lett.*, **10**, 56-58 (1985).
157. R. Weissleder, C.H. Tung, U. Mahmood, A. Bogdanov, "In vivo imaging of tumors with protease-activated near-infrared fluorescent probes", *Nat. Biotechnol.*, **17**, 375-378 (1999).



158. X. Wu, H. Liu, J. Liu, K.N. Haley, J.A. Treadway, J.P. Larson, N. Ge, F. Peale, M.P. Bruchez, "Immunofluorescent labeling of cancer marker Her2 and other cellular targets with semiconductor quantum dots", *Nat. Biotechnol.*, **21**, 41-46 (2003).
159. C. Loo, A. Lowery, N. Halas, J. West, R. Drezek, "Immunotargeted nanoshells for integrated cancer imaging and therapy", *Nano. Lett.*, **5**, 709-711 (2005).
160. Y. Urano, D. Asanuma, Y. Hama, Y. Koyama, T. Barrett, M. Kamiya, T. Nagano, T. Watanabe, A. Hasegawa, P.L. Choyke, H. Kobayashi, "Selective molecular imaging of variable cancer cells with pH-activatable fluorescence probes", *Nat. Med.*, **15**, 104-109 (2009).
161. D. Artemov, N. Mori, B. Okolli, Z.M. Bhujwalla, "MR molecular imaging of the Her-2/*neu* receptor in breast cancer cells using targeted iron oxide nanoparticles", *Magn. Reson. Med.*, **49**, 403-408 (2003).
162. G.J. Brakenhoff, M. Müller, R.I. Ghauharali, "Analysis of efficiency of two-photon versus single-photon absorption for fluorescence generation in biological objects", *J. Microsc.*, **183**, 140-144 (1996).
163. S. Lévêque-Fort, M.P. Fontaine-Aupart, G. Roger, P. Georges, "Fluorescence-lifetime imaging with a multifocal two-photon microscope", *Opt. Lett.*, **29**, 2884-2886 (2004).
164. J.R. Starkey, A.K. Rebane, M.A. Drobizhev, F. Meng, A. Gong, A. Elliott, K. McInnerney, C.W. Spangler, "New two-photon activated photodynamic therapy sensitizers induce xenograft tumor regressions after near-IR laser treatment through the body of the host mouse", *Clin. Cancer Res.*, **14**, 6564-6573 (2008).
165. N.S. Makarov, M. Drobizhev, A. Rebane, "Two-photon absorption standards in the 550-1600 nm excitation wavelength range", *Opt. Expr.*, **16**, 4029-4047 (2008).
166. V.S. Antonov, K.L. Hohla, "Dye stability under excimer-laser pumping. II. Visible and UV dyes", *Appl. Phys. B*, **32**, 9-14 (1983).
167. V.P. Tokar, M.Yu. Losytsky, V.B. Kovalska, D.V. Kryvorotenko, A.O. Balanda, V.M. Prokopets, M.P. Galak, I.M. Dmytruk, V.M. Yashchuk, S.M. Yarmoluk, "Fluorescence of styryl dyes-DNA complexes induced by single- and two-photon excitation", *J. Fluoresc.*, **16**, 783-791 (2006).
168. R. Ramadass, J. Bereiter-Hahn, "Photophysical properties of DASPMI as revealed by spectrally resolved fluorescence decays", *J. Phys. Chem. B*, **111**, 7681-7690 (2007).

169. D.K. Palit, A.K. Singh, A.C. Bhasikuttan, J.P. Mittal, "Relaxation dynamics in the excited states of LSD-821 in solution", *J. Phys. Chem. A*, **105**, 6294-6304 (2001).
170. N.S. Makarov, E. Beuerman, M. Drobizhev, J. Starkey, A. Rebane, "Environment-sensitive two-photon dye", *Proc. SPIE*, **7049**, 70490Y (2008).
171. R.K. Gupta, B.M. Salzberg, A. Grinvald, L.B. Cohen, K. Kamino, S. Leshner, M.B. Boyle, A.S. Waggoner, C.H. Wang, "Improvements in optical methods for measuring rapid changes in membrane potential" *J. Membrane Biol.*, **58**, 123-137 (1981).
172. A. Grinvald, R. Hildesheim, I.C. Farber, L. Anglister, "Improved fluorescent probes for the measurement of rapid changes in membrane potential", *Biophys. J.*, **39**, 301-308 (1982).
173. E.V. Tulyakova, O.A. Fedorova, Yu.V. Fedorov, G. Jonusauskas, L.G. Kuz'mina, J.A.K. Howard, A.V. Anisimov, "Synthesis, complexation, and E-Z photoisomerisation of azadithiacrown-containing styryl dyes as new optical sensors for mercury cations", *Rus. Chem. Bull. Int. Ed.*, **56**, 513-526 (2007).
174. F. Huang, Y. Tian, C-Y. Chen, Y-J. Cheng, A.C. Young, A.K.-Y. Jen, "Cross-conjugated polymers with large two-photon absorption cross-sections for metal ion sensing", *J. Phys. Chem. C*, **111**, 10673-10681 (2007).
175. J.W. Lee, M. Jung, G.R. Rosania, Y-T. Chang, "Development of novel cell-permeable DNA sensitive dye using combinatorial synthesis and cell-based screening", *Chem. Comm.*, 1852-1853 (2003).
176. *Handbook of biological confocal microscopy*, Ed. J.B. Pawley, Science, 2006.
177. M.R. Lugo, F.J. Sharom, "Interaction of LDS-751 with P-glycoprotein and mapping of the location of the R drug binding site", *Biochem.*, **44**, 643-655 (2005).
178. P.D.W. Eckford, F.J. Sharom, "P-glycoprotein (ABCB1) interacts directly with lipid-based anti-cancer drugs and platelet-activating factors", *Biochem. Cell Biol.*, **84**, 1022-1033 (2006).
179. A.R. Günthert, C. Gründker, T. Bongertz, T. Schlott, A. Nagy, A.V. Schally, G. Emons, "Internalization of cytotoxic analog AN-152 of luteinizing hormone-releasing hormone induces apoptosis in human endometrial and ovarian cancer cell lines independent of multidrug resistance-1 (MDR-1) system", *Am J Obstet Gynecol.*, **191**, 1164-1172 (2004).
180. P.S. Adusumilli, B.M. Stiles, M.-K. Chan, D.P. Eisenberg, Z. Yu, S.F. Stanziale, R. Huq, R.J. Wong, V.W. Rusch, Y. Fong, "Real-time diagnostic imaging of tumors

- and metastases by use of a replication-competent herpes vector to facilitate minimally invasive oncological surgery”, *FACEB*, 10.1096/fj.05-5316fje (2006).
181. F.S. Cohen, E. Taslidere, D.S. Hari, “Tissue characterization and detection of dysplasia using scattering light”, *3<sup>rd</sup> IEEE Int. Symp. on Biomed. Imaging: Nano to Macro*, 590-593 (2006).
  182. P.T. Winnard Jr., J.B. Kluth, V. Raman, “Noninvasive optical tracking of breast cancer metastasis with tdTomato red fluorescent protein”, *Clontech Lab. Inc.*, (2008).
  183. R.W. Boyd, *Nonlinear optics*, Academic Press: San Diego, 2003.
  184. R. Pantell, H. Puthoff, *Fundamentals of Quantum electronics*, John Wiley & Sons, New York, 1969.
  185. J.P. Lavoine, “Effects of permanent dipole moments in transient four-wave mixing experiments,” *J. Phys. Chem.* **127**, 094107 (2007).
  186. A. Singh, W.-Y. Huang, L.W. Johnson, “Determination of the ground state, excited state and change in dipole moments of magnesium and zinc chlorin”, *Spectrochim. Ac. Pt. A*, **58**, 2177-2183, (2002).
  187. G.D. Egorova, V.N. Knyukshto, K.N. Solovev, M.P. Tsvirko, “Intramolecular spin-orbital perturbations in ortho- and meta-halogeno-derivatives of tetraphenylporphin”, *Opt. Spektrosk.*, **48**, 1101-1109 (1980).
  188. A. Karotki, M. Drobizhev, M. Kruk, C. Spangler, E. Nickel, N. Mamardashvili, A. Rebane, “Enhancement of two-photon absorption in tetrapyrrolic compounds”, *J. Opt. Soc. Am. B*, **20**, 321-332 (2003).
  189. A. Rebane, N. Christensson, M. Drobizhev, Y. Stepanenko, C. W. Spangler, “Quantum interference in organic solid”, *Optics Express*, **13** (16) 6033-6038 (2005).
  190. G.A. Reynolds, K.H. Drexhage, “New coumarin dyes with rigidized structure for flashlamp-pumped lasers”, *Chem. Phys. Lett.*, **13** (3), 222-225 (1975).
  191. A. Fischer, C. Cremer, E.H.K. Stelzer, “Fluorescence of coumarins and xanthenes after two-photon absorption with a pulsed titanium-sapphire laser”, *Appl. Opt.*, **34**, 1989-2003 (1995).
  192. Z. Huang, X. Wang, B. Li, C. Lv, J. Xu, W. Jiang, X. Tao, S. Qian, Y. Chui, P. Yang, “Two-photon absorption of new multibranched chromophores based on bis(diphenylamino)stilbene”, *Opt. Mater.*, **29**, 1084-1090 (2007).

193. W.W. Stewart, "Synthesis of 3,6-disulfonated 4-aminonaphthalimides", *J. Am. Chem. Soc.*, **103** (25), 7615-7620 (1981).
194. M. Kruk, A. Karotki, M. Drobizhev, V. Kuzmitsky, V. Gael, A. Rebane, "Two-photon absorption of tetraphenylporphyrin free base", *J. Lumin.*, **105**, 45-55 (2003).
195. M. Morone, L. Beverina, A. Abbotto, F. Silvestri, E. Collini, C. Ferrante, R. Bozio, G. A. Pagani, "Enhancement of two-photon absorption cross-section and singlet-oxygen generation in porphyrins upon  $\beta$ -functionalization with donor-acceptor substituents", *Org. Lett.*, **8** (13), 2719-2722 (2006).
196. T. Ishi-i, Y. Taguri, S. Kato, M. Shigeiva, H. Gorohmaru, S. Maeda, S. Mataka, "Singlet oxygen generation by two-photon excitation of porphyrin derivatives having two-photon-absorbing benzothiadiazole chromophores", *J. Mater. Chem.*, **17**, 3341-3346 (2007).
197. Y. Liang, A.S. Dvornikov, P.M. rentzepis, "Photochemistry of photochromic 2-indolylfulgides with substituents at the 1'-position of the indolylmethylene moiety", *J. Photochem. Photobiol. A: Chem.*, **146**, 83-93 (2001).
198. K. Teuchner, A. Pfarrherr, H. Stiel, W. Freyer, D. Leupold, "Spectroscopic properties of potential sensitizers for new photodynamic therapy start mechanisms via 2-step excited electronic states", *Photochem. Photobiol.*, **57**, 465-471 (1993).
199. K.K. Rebane, *Impurity Spectra of Solids* (Plenum, 1970).
200. A.S. Davydov, A.F. Lubchenko, "Urbach rule for localized excitations in crystals", *Sov. Phys. - Doklady*, **13**, 325-327 (1968).
201. M.D. Frank-Kamenetskii, A.V. Lukashin, "Electron-oscillatory interactions in polyatomic-molecules", *Uspekhi Fiz. Nauk*, **116**, 193-229 (1975) (in Russian).
202. D.W. Posener, "The shape of spectral lines: Tables of the Voigt profile", *Austr. J. Phys.*, **12**, 184-196 (1959).
203. I. Rückmann, A. Zeug, R. Herter, B. Röder, "On the influence of higher excited states in the ISC quantum yield of octa- $\alpha$ -alkyloxy-substituted Zn-phthalocyanine molecules studied by nonlinear absorption", *Photochem. Photobiol.*, **66**, 576-584 (1997).
204. J.S. Shirk, R.G.S. Pong, S.R. Flom, H. Heckmann, M. Hanack, "Effect of axial substitution on the optical limiting properties of indium phthalocyanines", *J. Phys. Chem. A*, **104**, 1438-1449 (2000).
205. E.M. Maya, A.W. Snow, J.S. Shirk, R.G.S. Pong, S.R. Flom, G.L. Roberts, "Synthesis, aggregation, behavior and nonlinear absorption properties of lead

- phthalocyanines substituted with siloxane chains”, *J. Mater. Chem.*, **13**, 1601-1613 (2003).
206. A. Zeug, M. Meyer, P.-C. Lo, D.K.P. Ng, B. Röder, “Fluorescence anisotropy and transient absorption of halogenated silicon(IV) phthalocyanines with axial poly(ethyleneglycol) substituents”, *J. Porph. Phthalocyanines*, **9**, 298-302 (2005).
  207. M. Gouterman, “Spectra of porphyrins”, *J. Mol. Spectr.*, **6**, 138-163 (1961).
  208. P. Fromherz, “Monopole-dipole model for symmetrical solvatochromism of hemicyanine dyes”, *J. Phys. Chem.*, **99**, 7188-7192 (1995).
  209. Z. Wang, A. Bonoiu, M. Samoc, Y. Cui, P.N. Prasad, “Biological pH sensing based on surface enhanced Raman scattering through a 2-aminothiophenol-silver probe”, *Biosens. Bioelectr.*, **23**, 886-891 (2008).
  210. H. Sun, F. Jacquey, J.C. Bernengo, “A micro-spectrophotometric study on the spectral properties of phenol red injected into cytoplasm for pH determination”, *Biophys. Chem.*, **48**, 91-100 (1993).
  211. N.P. Robertson, J.R. Starkey, S. Hamner, G.G. Meadows, “Tumor cell invasion of three-dimensional matrices of defined composition: evidence for a specific role for heparin sulfate in rodent cell lines”, *Cancer Res.*, **49**, 1816-1823 (1989).
  212. K.G. Danielson, L.W. Anderson, H.L. Hosick, “Selection and characterization in culture of mammary tumor cells with distinctive growth properties in vivo”, *Cancer Res.*, **40**, 1812-1819 (1980).
  213. U.K. Ehmann, W.D. Peterson Jr., D.S. Misfeldt, “To grow mouse mammary epithelial cells in culture”, *J Cell Biol.*, **98**, 1026-1032 (1984).

## APPENDICES

APPENDIX A

DERIVATION OF THE EXPRESSION FOR TWO-PHOTON  
CROSS SECTION IN CASE OF TWO-LEVEL MODEL

Consider the density matrix equations of motion, which describes the interaction of the molecule with the monochromatic electric field,  $\vec{E}(t) = \vec{e}E_0 \cos(\omega t)$  [183]:

$$\dot{\rho}_{nm} = \frac{1}{i\hbar} [\hat{H}, \hat{\rho}]_{nm} - \gamma_{nm} (\rho_{nm} - \rho_{nm}^{eq}), \quad (\text{A.1})$$

where  $\hat{\rho}$  is the density matrix,  $\gamma_{nm}$  are the relaxation constants,  $\hat{H}$  is the Hamiltonian, and  $\hat{\rho}^{eq}$  are the equilibrium values of the density matrix.

We will find a perturbation solution of Schrödinger equation with perturbed Hamiltonian  $\hat{H} = \hat{H}_0 + \hat{V}(t)$ , where the interaction energy,  $\hat{V}(t) = -\hat{\mu}\vec{E}(t)$ , is given by the dipole moment  $\hat{\mu}$ , and perturbation series expansion is:

$$\hat{\rho} = \hat{\rho}^{(0)} + \hat{\rho}^{(1)} + \hat{\rho}^{(2)} + \hat{\rho}^{(3)} + \dots \quad (\text{A.2})$$

In the two-level model the density matrix is:

$$\hat{\rho} = \begin{pmatrix} \rho_{00} & \rho_{01} \\ \rho_{10} & \rho_{11} \end{pmatrix}, \quad (\text{A.3})$$

with the ground-state and the equilibrium matrix

$$\hat{\rho}^{eq} = \hat{\rho}^{(0)} = \begin{pmatrix} 1 & 0 \\ 0 & 0 \end{pmatrix}, \quad (\text{A.4})$$

and the matrix of dipole moments

$$\hat{\mu} = \begin{pmatrix} \bar{\mu}_{00} & \bar{\mu}_{01} \\ \bar{\mu}_{01} & \bar{\mu}_{11} \end{pmatrix}, \quad (\text{A.5})$$

where indices 0 correspond to ground state and 1 correspond to first excited state.

We can calculate the perturbed values of the density matrix as:

$$\rho_{nm}^{(i)}(t) = \frac{e^{-(i\omega_{nm} + \gamma_{nm})t}}{i\hbar} \int_{-\infty}^t \sum_v [V_{nv}(t') \rho_{vm}^{(i-1)} - \rho_{nv}^{(i-1)} V_{vm}(t')] e^{(i\omega_{nm} + \gamma_{nm})t'} dt'. \quad (\text{A.6})$$

It is simple to show that the first three orders of the perturbation series are:

$$\begin{cases} \rho_{00}^{(1)} = 0 \\ \rho_{01}^{(1)} = \frac{\bar{\mu}_{01} \vec{E}_0}{2\hbar} \left[ \frac{e^{-i\omega t}}{(\omega - \omega_0 + i\gamma_{01})} - \frac{e^{i\omega t}}{(\omega + \omega_0 - i\gamma_{01})} \right] \\ \rho_{11}^{(1)} = 0 \end{cases} \quad (\text{A.7})$$



$$\left\{ \begin{aligned}
\rho_{00}^{(2)} &= \frac{(\hat{e}\bar{\mu}_{01})^2 E_0^2}{2\hbar^2} \left[ \frac{-2\gamma_{01}(\omega^2 + \omega_0^2 + \gamma_{01}^2)}{\gamma_{00}(\omega - \omega_0 - i\gamma_{01})(\omega - \omega_0 + i\gamma_{01})(\omega + \omega_0 - i\gamma_{01})(\omega + \omega_0 + i\gamma_{01})} + \right. \\
&\quad \left. \frac{(\omega - i\gamma_{01})e^{2i\omega t}}{2\omega(\omega - \omega_0 - i\gamma_{01})(\omega + \omega_0 - i\gamma_{01})} + \frac{(\omega + i\gamma_{01})e^{-2i\omega t}}{2\omega(\omega - \omega_0 + i\gamma_{01})(\omega + \omega_0 + i\gamma_{01})} \right] \\
\rho_{01}^{(2)} &= \frac{\hat{e}\bar{\mu}_{01}\hat{e}(\bar{\mu}_{00} - \bar{\mu}_{11})E_0^2}{4\hbar^2} \left[ \frac{2}{(\omega - \omega_0 + i\gamma_{01})(\omega + \omega_0 - i\gamma_{01})} e^{-2i\omega t} \right. \\
&\quad \left. \frac{(\omega - \omega_0 + i\gamma_{01})(2\omega - \omega_0 + i\gamma_{01})}{e^{2i\omega t}} \right] \\
\rho_{11}^{(2)} &= \frac{(\hat{e}\bar{\mu}_{01})^2 E_0^2}{2\hbar^2} \left[ \frac{2\gamma_{01}(\omega^2 + \omega_0^2 + \gamma_{01}^2)}{\gamma_{00}(\omega - \omega_0 - i\gamma_{01})(\omega - \omega_0 + i\gamma_{01})(\omega + \omega_0 - i\gamma_{01})(\omega + \omega_0 + i\gamma_{01})} - \right. \\
&\quad \left. \frac{(\omega - i\gamma_{01})e^{2i\omega t}}{2\omega(\omega - \omega_0 - i\gamma_{01})(\omega + \omega_0 - i\gamma_{01})} - \frac{(\omega + i\gamma_{01})e^{-2i\omega t}}{2\omega(\omega - \omega_0 + i\gamma_{01})(\omega + \omega_0 + i\gamma_{01})} \right] , \quad (A.8)
\end{aligned} \right.$$

$$\rho_{01}^{(3)} = \frac{\hat{e}\bar{\mu}_{01}E_0^3}{8\hbar^3} \left[ \begin{aligned}
&e^{-3i\omega t} \left( \frac{2(\hat{e}\bar{\mu}_{01})^2(\omega + i\gamma_{01})}{\omega(\omega + \omega_0 + i\gamma_{01})} + \frac{(\hat{e}(\bar{\mu}_{00} - \bar{\mu}_{11}))^2}{(2\omega - \omega_0 + i\gamma_{01})} \right) \frac{1}{(\omega - \omega_0 + i\gamma_{01})(3\omega + \omega_0 - i\gamma_{01})} - \\
&e^{3i\omega t} \left( \frac{2(\hat{e}\bar{\mu}_{01})^2(\omega - i\gamma_{01})}{\omega(\omega - \omega_0 - i\gamma_{01})} + \frac{(\hat{e}(\bar{\mu}_{00} - \bar{\mu}_{11}))^2}{(2\omega + \omega_0 - i\gamma_{01})} \right) \frac{1}{(\omega + \omega_0 - i\gamma_{01})(3\omega + \omega_0 - i\gamma_{01})} + \\
&e^{i\omega t} \left( \frac{8(\hat{e}\bar{\mu}_{01})^2\gamma_{01}(\omega^2 + \omega_0^2 + \gamma_{01}^2)}{\gamma_{00}(\omega - \omega_0 - i\gamma_{01})(\omega - \omega_0 + i\gamma_{01})(\omega + \omega_0 + i\gamma_{01})} + \frac{3(\hat{e}(\bar{\mu}_{00} - \bar{\mu}_{11}))^2}{(2\omega + \omega_0 - i\gamma_{01})} \right) \frac{1}{(\omega + \omega_0 - i\gamma_{01})(\omega - \omega_0 + i\gamma_{01})} \\
&e^{-i\omega t} \left( \frac{8(\hat{e}\bar{\mu}_{01})^2\gamma_{01}(\omega^2 + \omega_0^2 + \gamma_{01}^2)}{\gamma_{00}(\omega - \omega_0 - i\gamma_{01})(\omega - \omega_0 + i\gamma_{01})(\omega + \omega_0 + i\gamma_{01})} + \frac{3(\hat{e}(\bar{\mu}_{00} - \bar{\mu}_{11}))^2}{(2\omega - \omega_0 + i\gamma_{01})} \right) \frac{1}{(\omega + \omega_0 - i\gamma_{01})(\omega - \omega_0 + i\gamma_{01})}
\end{aligned} \right] . \quad (A.9)$$

From the last element one can calculate the probability rate of 2PA,  $P_{2PA} = \frac{\sigma_2}{2} I^2$ ,

where  $\sigma_2$  is the 2PA cross section and  $I$  is the intensity of the electric field, as:

$$P_{2PA} = \frac{1}{i\hbar} \sum_{\nu} \left[ V_{1\nu} \rho_{\nu 1}^{(3)} - \rho_{1\nu}^{(3)} V_{\nu 1} \right] \approx \frac{(\hat{e} \vec{\mu}_{01})^2 (\hat{e} (\vec{\mu}_{00} - \vec{\mu}_{11}))^2 E_0^4 \gamma_{01}}{2\hbar^4 \omega_0^2 ((2\omega - \omega_0)^2 + \gamma_{01}^2)}, \quad (\text{A.10})$$

where only non-oscillating terms and near 2PA resonance conditions were used.

Substituting the electric field instead of the intensity:

$$P_{2PA} = \frac{\sigma_2}{2} \left( \frac{nc}{8\pi\hbar\omega} \bar{E}_0^2 \right)^2, \quad (\text{A.11})$$

and neglecting small quantities we receive intermediate result:

$$\sigma_2 = (\hat{e} \vec{\mu}_{01})^2 (\hat{e} (\vec{\mu}_{00} - \vec{\mu}_{11}))^2 \frac{2(2\pi)^3}{(n\hbar)^2} \left( \frac{E_0}{\bar{E}_0} \right)^4 \frac{\gamma_{01}}{\pi ((2\omega - \omega_0)^2 + \gamma_{01}^2)}. \quad (\text{A.12})$$

where we have introduced normalized line shape function:

$$g(2\omega) = \frac{\gamma_{01}}{\pi ((2\omega - \omega_0)^2 + \gamma_{01}^2)} \quad (\text{A.13})$$

$$\int_{-\infty}^{\infty} g(2\omega') d(2\omega') = 1$$

To describe isotropic media, such as solution, we perform averaging over all possible spherical orientations:

$$\begin{aligned} \left\langle (\hat{e} \vec{\mu}_{01})^2 (\hat{e} (\vec{\mu}_{00} - \vec{\mu}_{11}))^2 \right\rangle_{\bar{\Omega}} &= \int_0^{2\pi} d\phi \int_0^{\pi} \left( \begin{pmatrix} 0 \\ 0 \\ 1 \end{pmatrix} \cdot \begin{pmatrix} \sin \theta \cos \phi \\ \sin \theta \sin \phi \\ \cos \theta \end{pmatrix} \right) \left( \begin{pmatrix} \sin \beta \\ 0 \\ \cos \beta \end{pmatrix} \cdot \begin{pmatrix} \sin \theta \cos \phi \\ \sin \theta \sin \phi \\ \cos \theta \end{pmatrix} \right)^2 \times \\ &\times \sin \theta d\theta \frac{(|\vec{\mu}_{01}| |\Delta \vec{\mu}_{01}|)^2}{4\pi} = \frac{2 \cos^2 \beta + 1}{15} (|\vec{\mu}_{01}| |\Delta \vec{\mu}_{01}|)^2 \end{aligned} \quad (\text{A.14})$$

where

$$\Delta \vec{\mu}_{01} = \vec{\mu}_{00} - \vec{\mu}_{11}, \quad (\text{A.15})$$

Combining (A.12)–(A.15) we arrive at the final expression:

$$\sigma_2 = \frac{2(2\pi)^3 f^4}{15(n\hbar)^2} |\vec{\mu}_{01}|^2 |\Delta \vec{\mu}_{01}|^2 (2 \cos^2 \beta + 1) g(2\omega), \quad (\text{A.16})$$

where  $\beta$  is the angle between the dipole moment vectors  $\vec{\mu}_{01}$  and  $\Delta\vec{\mu}_{01}$ , and  $f = \frac{E_0}{\bar{E}_0}$  is

the local field factor, which is introduced to take into account the effects of the media.

Since

$$\begin{cases} \int g(2\omega) d2\omega = 1 = \int g(2\nu) d2\nu \\ \omega = 2\pi\nu \end{cases}, \quad (\text{A.17})$$

one can rearrange (A.16) to get:

$$\sigma_2 = \frac{2(2\pi)^4 f^4}{15(nch)^2} |\vec{\mu}_{01}|^2 |\Delta\vec{\mu}_{01}|^2 (2\cos^2 \beta + 1) g(2\nu). \quad (\text{A.18})$$

### Density Matrix Description of Two-Level System

Alternatively, the behavior of two-level molecules interacting with an external electric field  $\vec{E}(t)$ , can be described by a system of coupled differential equations of motion for the density matrix [184, 185]:

$$\begin{cases} \frac{d\rho_{11}}{dt} = \frac{2\vec{\mu}_{01}\vec{E} \text{Im}\rho_{01}}{\hbar} - \frac{\rho_{11}}{T_1} \\ \frac{d \text{Re}\rho_{01}}{dt} = \left( \frac{\Delta\vec{\mu}_{01}\vec{E}(t)}{\hbar} - \omega_{10} \right) \text{Im}\rho_{01} - \frac{\text{Re}\rho_{01}}{T_2} \\ \frac{d \text{Im}\rho_{01}}{dt} = - \left( \frac{\Delta\vec{\mu}_{01}\vec{E}(t)}{\hbar} - \omega_{10} \right) \text{Re}\rho_{01} - \frac{\vec{\mu}_{01}\vec{E}(t)(2\rho_{11}-1)}{\hbar} - \frac{\text{Im}\rho_{01}}{T_2} \end{cases} \quad (\text{A.19})$$

where  $\rho_{01}$  is the complex off-diagonal density matrix element,  $\rho_{11}$  is the population of the excited state,  $\omega_{10}$  is the resonance transition frequency and  $\hbar$  is the Planck's constant. The set of molecular parameters includes:  $\vec{\mu}_{01}$  – transition dipole moment,  $\Delta\vec{\mu}_{01}$  – permanent dipole moment difference in the ground- and excited states, and  $T_1$  and  $T_2$  – decay times of the excited state population and of the coherence between the two states,

respectively. Note that rotating wave approximation is not used here. The system (A.19) can be solved numerically directly without approximations of perturbation theory.

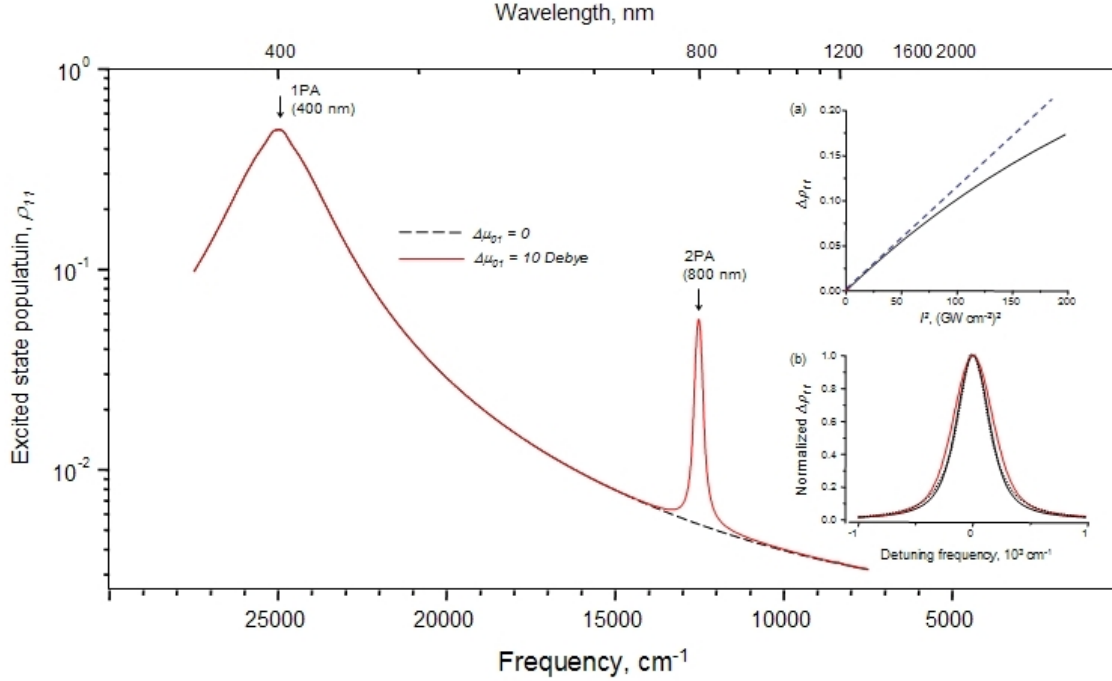


Figure A.1. Numerical simulations of 2PA in two-level system. Comparison of population of excited state for molecule with zero difference in dipole moments of ground and excited state  $\Delta\vec{\mu}_{01}$  (dashed line) and for molecule with  $\Delta\vec{\mu}_{01} = 10D$  difference (solid line). 2PA peak is well visible for the second case. On the inserts are: a) the comparison of the difference in excited state population due to 2PA ( $\Delta\rho_{11}$ ) vs. square of intensity, showing saturation effect; and b) the comparison of line shape of 1PA and 2PA peaks of excited state population and Lorentz function. The parameters were used as follow:  $T_1=1600$  fs,  $T_2=50$  fs, pulse duration=100 fs,  $\nu_{01}=25000$   $\text{cm}^{-1}$ ,  $\mu_{01}=10$  D. The detuning frequency is a difference between transition frequencies of the laser and absorption resonance

Suppose the molecule is illuminated with a brief Gaussian-shaped pulse of carrier frequency,  $\omega$ . If the duration of the pulse is much less than the upper energy level decay time,  $\tau \ll T_1$ , then the probability of absorption is proportional to  $\rho_{11}$ , where the last is measured shortly after the pulse. Figure A.1 presents the calculated absorption probability as a function of  $\omega$ . We assume that electric field is linearly polarized and is

parallel to both  $\vec{\mu}_{01}$  and  $\Delta\vec{\mu}_{01}$ . The peak intensity of the pulse is  $I = 45 \text{ GW cm}^{-2}$  and the pulse duration is  $\tau = 100 \text{ fs}$ . The molecular parameters are chosen to represent a typical dipolar organic system:  $\nu_{01} = 25000 \text{ cm}^{-1}$ ,  $\mu_{01} = \Delta\mu_{01} = 10 \text{ D}$ ,  $T_1 = 1 \text{ ns}$ ,  $T_2 = 50 \text{ fs}$ , and the value of excited state population  $\rho_{11}$  was taken 150 fs after the center of the pulse.

The excited state population (the main part of figure A.1) displays two resonances, one at 400 nm ( $\nu_{01}$ ) and another at 800 nm ( $\nu_{01}/2$ ). We note that the Lorentzian line shape follows from the exponential relaxation terms in expression (A.19). In reality, especially in the case of organic molecules, the 1PA falls off much more rapidly with increasing frequency detuning. The first resonance is much stronger and corresponds, as expected, to one-photon transition from the ground to excited state. The second significantly weaker peak corresponds to two-photon transition connecting the same states. Note that if we set  $\Delta\mu_{01} = 0$ , the 2PA vanishes (dashed curve), thus justifying the idea that only dipolar molecules exhibit 2PA in a two-level model.

The 2PA cross section can be expressed through the 2PA-induced excited state population as follow,

$$\sigma_2 = \frac{4\Delta\rho_{11}(h\nu)^2}{I^2\tau} \sqrt{\frac{2\ln 2}{\pi}}, \quad (\text{A.20})$$

where  $\Delta\rho_{11}$  is calculated as the difference between the population with- and without contribution from permanent dipole moment short after the pulse, assuming Gaussian pulse shape. Figure A.1, insert (a) shows that, up to a moderate intensity,  $I \sim 50 \text{ GW cm}^{-2}$ ,  $\Delta\rho_{11}$  increases linearly with  $I^2$  which allows for direct evaluation of  $\sigma_2$ . At higher intensities, the theory predicts saturation of 2PA, and, correspondingly, the effective

cross section decreases. Figure A.1, insert (b) shows that in the current model the 2PA resonance has the same width and Lorentzian shape as the 1PA resonance. This fact is used in the dissertation to verify if a two-level description of 2PA is applicable. Furthermore, if the measured 1PA line shape is Lorentzian, then we may expect the same line shape also for the 2PA. In practice, the absorption line shapes are often much more involved. The spectra may include multiple overlapping vibronic transitions, as well as inhomogeneous broadening.

In addition to a possibility of quantitative simulation of the 2PA spectrum, the density matrix formalism also offers a helpful physical insight into the origin of the 2PA effect itself. Indeed, it is easy to show that in the limit of moderate or low intensity ( $\rho_{11} \ll 1$ ), (A.2.1) may be reduced to a variant of classical harmonic oscillator equation:

$$\ddot{\rho}_{01} + \left[ \frac{\Delta \bar{\mu}_{01} \vec{E}(t)}{\hbar} - \omega_{10} \right]^2 \rho_{01} + \frac{\dot{\rho}_{01}}{T_2} = - \frac{\bar{\mu}_{01} \vec{E}(t) \omega_{10}}{\hbar}. \quad (\text{A.21})$$

The term enclosed in the square brackets may be interpreted as instantaneous resonance transition frequency. If the permanent dipole moment difference is not zero, then the transition is modulated at the optical frequency, leading to the nonlinear absorption resonance at  $\omega_{01}/2$ . We conclude that, at least in the case of two-level system, 2PA may be understood as a purely classical phenomenon, in which a harmonic oscillator is driven by a periodic external force, which is also modulating the resonance frequency. The 2PA resonance occurs when the two half-resonance frequencies combine, i.e. when  $2\omega = \omega_{10}$ .

APPENDIX B

DESCRIPTION OF THE STANDARD LINEAR MEASUREMENTS FOR  
DETERMINATION OF THE VALUES OF THE DIPOLE MOMENTS BETWEEN  
THE GROUND AND EXCITED STATES

### Measurements of the Extinction Coefficients

Spectrometer PerkinElmer Lambda 900 is used for UV-VIS absorption spectra measurements. The extinction coefficients ( $\varepsilon$ ) are measured for the lowest singlet-singlet transition by dissolving 1-10 mg of a compound in 25 ml of solvent. Then, the optical density in a 1-mm quartz spectroscopic cell is measured in a series of gradual dilutions, and the linear part of the Lambert-Beer plot is used to calculate the extinction coefficients.

Transition dipole moment can be obtained from the extinction coefficient using the following expression [129]:

$$|\vec{\mu}_{01}|^2 g(\bar{\nu}_{01}) = \frac{3 \cdot 10^3 \ln 10 h c \varepsilon(\bar{\nu}_{01}) n}{(2\pi)^3 N_A \bar{\nu}_{01} f^2}, \quad (\text{B.1})$$

where  $g(\bar{\nu}_{01})$  is the maximum of the normalized line shape function,  $\int_{\nu} g(2\nu) d\nu = 1$ ,  $\bar{\nu}_{01}$

is the frequency of the band maximum (in  $\text{cm}^{-1}$ ),  $\varepsilon(\bar{\nu}_{01})$  is the extinction coefficient at the maximum, and  $N_A$  is the Avogadro's number.

Alternatively, the transition dipole moment can be obtained using the following expression [85, 93]:

$$|\vec{\mu}_{01}|^2 = \frac{3 \cdot 10^3 \ln(10) h c n}{8 N_A \pi^3 f^2} \int \frac{\varepsilon(\bar{\nu})}{\bar{\nu}} d\bar{\nu}, \quad (\text{B.2})$$

where the integration is carried out over the entire electronic transition.



Measurements of Solvatochromic Shifts and determination  
of the Permanent Dipole Moment Difference

The value of  $|\Delta\vec{\mu}_{01}|$  can be measured directly via Stark effect. Here we take a more convenient, albeit indirect approach, where the dipole moment difference is found from the dependence of the solvatochromic shifts between the peak 1PA absorption and fluorescence frequencies,  $\Delta\bar{\nu}_s$ , on the solvent polarity [122] due to dipole-dipole interaction:

$$|\Delta\vec{\mu}_{01}|^2 = hca^3 \frac{\Delta\bar{\nu}_s}{\Delta f(D)}, \quad (\text{B.3})$$

where  $a$  is the molecular cavity radius,  $\Delta f(D) = \frac{2(D_2 - 1)}{2D_2 + 1} - \frac{2(D_1 - 1)}{2D_1 + 1}$  is the change of the Onsager polarity function between two solvents, where the last have similar refractive index values, but different dielectric constants,  $D_1$  and  $D_2$ . For the best accuracy one can use the slope of the solvatochromic shifts with respect to polarity function,  $\frac{\Delta\bar{\nu}_s}{\Delta f(D)}$ , with the measurements done in at least 4–6 different solvents with varying polarities.

The solvatochromic shifts are measured as a difference between the frequencies of the 1PA and fluorescence maximum,  $\Delta\bar{\nu}_s = \bar{\nu}_{abs}^{\max} - \bar{\nu}_{fluor}^{\max}$ . The frequency of the 1PA maximum is found from the zero of the derivative of the lowest energy peak of the 1PA spectrum measured in the samples with optical densities  $OD \sim 1$ . The frequency of the fluorescence maximum is found from the zero of the derivative of the fluorescence spectrum measured in the samples with low optical densities  $OD < 0.1$ , excluding possible spectral changes due to reabsorption of fluorescence. Spectrofluorimeter

PerkinElmer LS 50B is used for fluorescence emission spectra measurements. Fluorescence spectra are corrected to account for variations of the detector sensitivity with the wavelength.

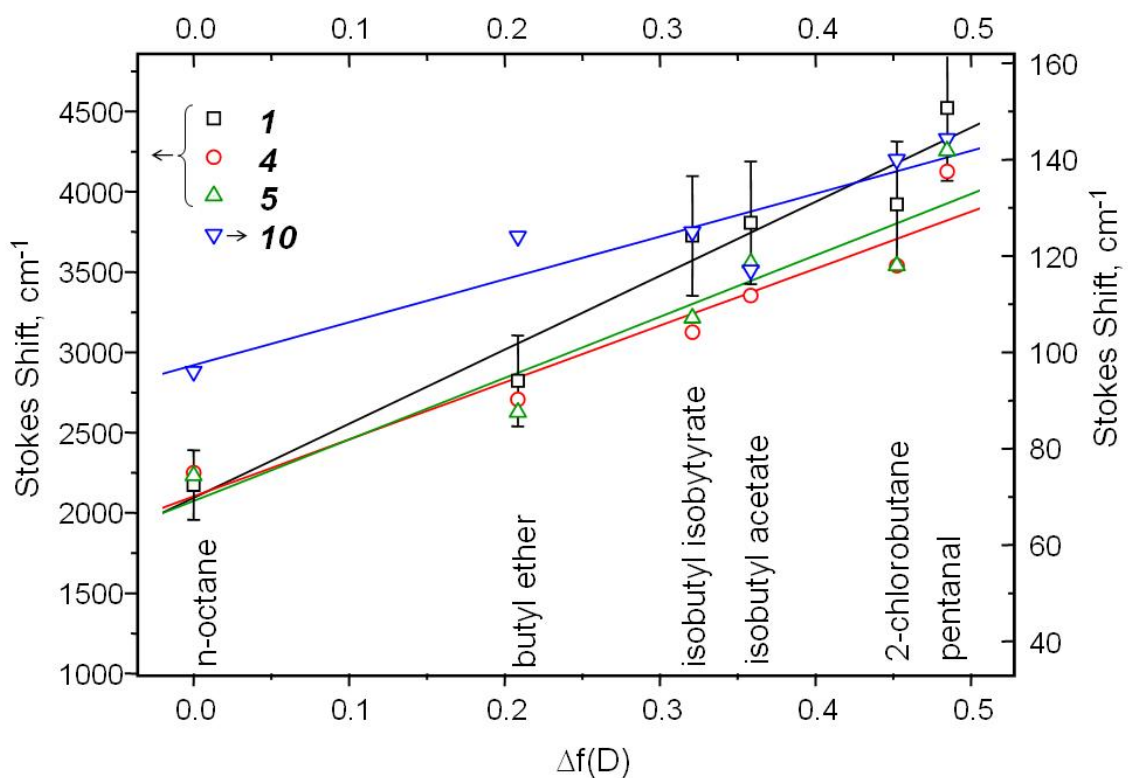


Figure B.1. Solvatochromic (Stokes) shifts in a series of solutions for compounds **1**, **4**, **5**, and **10**. The solvents are: *n*-octane, butyl ether, isobutyl isobutyrate, isobutyl acetate, 2-chlorobutane, and pentanal. Solid lines show linear fits

For compounds **3-6** (see chapter 5) the solvatochromic shifts were measured in toluene ( $D = 2.4$ ) vs. tetrahydrofuran ( $D = 7.58$ ); and for compounds **2**, **8-10** – in octane ( $D = 2.0$ ) vs. 2-chlorobutane ( $D = 8.06$ ). For compounds **1**, **4**, **5** and **10-14** a wider series of solvents was used, including *n*-octane, butyl ether, isobutyl isobutyrate, isobutyl acetate, 2-chlorobutane, and pentanal. It has been shown before [186] that these solvents interact with tetrapyrrolic molecules only via dipole-dipole interactions, which justifies

the use of Lippert-Mataga expression (B.3) for extraction of the difference in dipole moments.

Figure B.1 shows the solvatochromic shifts measured in a series of solvents for the molecules **1**, **4**, **5**, and **10** plotted versus polarity function. The magnitude of the shift increases with the solvent polarity, and is well described by a straight line. Table D.7 collects the normalized Stokes shifts (slopes) of the molecules studied. The typical experimental error of the solvatochromic shift values are about 10%, mostly due to fitting errors for the determination of the peak fluorescence and absorption frequencies, and increase for those molecules where the shift is the smallest. The fact that the Stokes shifts in group (ii) are much smaller than in other molecules, indicates that the substituted porphyrins have a relatively small permanent dipole moment change.

### Measurements of the Fluorescence Anisotropy

Determining the value of  $|\Delta\vec{\mu}_{01}|$  from the solvatochromic shifts data has been, up to recently, subject to considerable uncertainty due to significant uncertainties in the determination of the molecular cavity radius,  $a$ . Our approach is based on the assumption that the molecular cavity radius equals the hydrodynamic radius of a molecule. The last may be evaluated from Smolukhovsky-Einstein theory of rotational diffusion [129], which relates the radius to the fluorescence anisotropy [131]:

$$a^3 = \frac{3\tau_f kT}{4\pi\eta \left( \frac{0.4}{r} - 1 \right)}, \quad (\text{B.4})$$

where  $\eta$  is the solvent viscosity,  $\tau_f$  is the fluorescence life time,  $k$  is the Boltzmann constant; and  $T$  is the temperature.

Fluorescence anisotropy ( $r$ ) of **I-12** (see chapter 5) was measured in benzene according to standard procedure in L-configuration [131]: Excitation spectra of the lowest energy transitions are measured in a sequence with the following orientations of the polarizers on the entrance and on the exit: vertical-vertical ( $I_{VV}(\lambda)$ ); vertical-horizontal ( $I_{VH}(\lambda)$ ); horizontal-horizontal ( $I_{HH}(\lambda)$ ); and horizontal-vertical ( $I_{HV}(\lambda)$ ). Finally a second vertical-vertical measurement is made to check for the photostability of the samples. The fluorescence anisotropy is determined as:

$$r(\lambda) = \frac{I_{VV}(\lambda) - GI_{VH}(\lambda)}{I_{VV}(\lambda) + 2GI_{VH}(\lambda)}, \quad (\text{B.5})$$

where  $G$  is the constant value of the lowest energy part of the function  $G(\lambda) = \frac{I_{HV}(\lambda)}{I_{HH}(\lambda)}$ .

To minimize noise, the spectrometer scanning speed is chosen to be as slow as possible (10 nm/min). Since some of the compounds are photochemically not very stable, a special care is taken to insure that the fluorescence intensity does not change more than 5% during the measurements. For example, to avoid photodegradation of the compound **2** we had to increase the scan speed up to 100 nm/min.

Table D.7 collects the measured fluorescence anisotropies, along with the  $a$  values calculated from expression (B.4), and  $|\Delta\bar{\mu}_{01}|$  values calculated from expression (B.3). We estimate 20% error in the cavity radius.

### Fluorescence Lifetimes

Coherent Mira 900 laser is used for fluorescence excitation, and asynchroscan streak camera, Hamamatsu C5680-21, is employed for time-resolved detection of the emission (time resolution  $<20$  ps). Vertically polarized laser light is slightly focused in the sample, and the fluorescence is collected in the perpendicular direction. The scattered laser light is separated from the fluorescence signal by a stack of color cut-off filters. Because the maximum scan range of the streak camera is limited to 2 ns, we register the fluorescence in 6 overlapping time regions. The segments are combined into one 0–7 ns decay curve for further analysis.

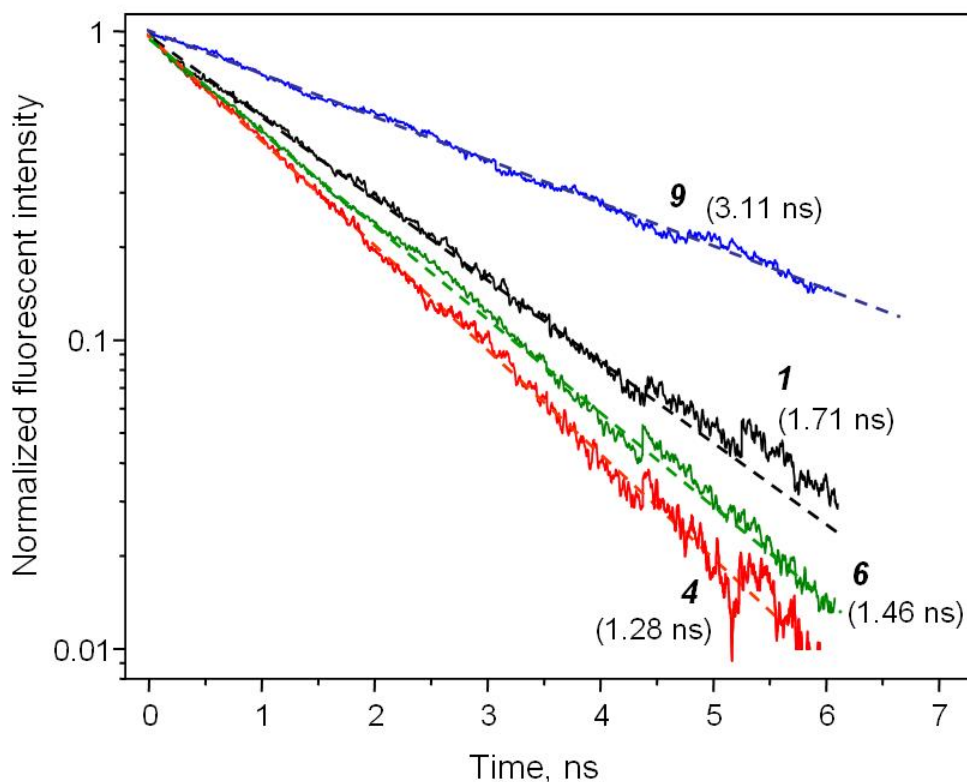


Figure B.2. Fluorescence decay curves for compounds **1**, **4**, **6**, and **9**: dashed lines show single exponential fits to extract fluorescence lifetimes

For molecules **1–6** (see chapter 5) we used 800 nm wavelength for 2PA-induced excitation of fluorescence, while the 1PA by second harmonic wavelength 400 nm was used for the excitation of molecules **7–9**.

Figure B.2 shows example of the fluorescence decay curves obtained for molecules **1**, **4**, **6**, and **9** dissolved in benzene. The curves are fitted with mono-exponential functions to determine the lifetimes.

### Fluorescence Quantum Yields

Fluorescence quantum yield is measured in diluted samples ( $OD_{\max} < 0.5$ ) using relative technique according to the expression

$$\varphi_{sample} = \frac{\left(n_{sample}^2 \int f_{sample}(\lambda) d\lambda\right) \left(1 - 10^{-OD_{ref}}\right)}{\left(n_{ref}^2 \int f_{ref}(\lambda) d\lambda\right) \left(1 - 10^{-OD_{sample}}\right)}, \quad (\text{B.6})$$

where  $f(\lambda)$  represents the fluorescence spectrum, corrected to account for variations of the detector sensitivity with the wavelength,  $OD$  represents the optical density at the excitation wavelength,  $n$  represents the refractive index of the solvent, and the indices *sample* and *ref* stand for the unknown and reference compounds respectively.

Fluorescence quantum yields for compounds **1–6** and **11–14** (see chapter 5) were measured in benzene relative to 9-methyl anthracene in benzene ( $\varphi = 0.49$  [84]); and relative to free-base tetraphenylporphyrin (*TPP*) in toluene ( $\varphi = 0.09$  [187]) for compounds **7–10**. Table D.7 collects the measured fluorescence lifetimes. We estimate 2% experimental error in the measurements.

APPENDIX C

MEASUREMENTS OF THE TWO-PHOTON CROSS SECTIONS

Fluorescent Method for the Measurements of the  
Two-Photon Absorption Spectra and Cross Sections

We evaluate absolute 2PA cross section by using a variant of the well known fluorescence method [97, 100, 101, 117, 188], in which the intensity of two-photon excited fluorescence is compared to the intensity of one-photon excited fluorescence of the same sample under the same detection conditions. The one-photon excitation is used to calibrate the unknown efficiency of registration channel and fluorescence quantum yield.

The fluorescence signal, collected over period of time  $T$ , and spectrally integrated over the interval of wavelengths between  $\lambda_{\min}$  and  $\lambda_{\max}$  is:

$$\begin{aligned} F_1 &= \alpha C \int_{\lambda_{\min}}^{\lambda_{\max}} \varphi(\lambda) \eta(\lambda) d\lambda \int_0^T dt \int_0^L dz \int_{\text{pulse profile}} P_1(x, y, z) ds \\ F_2 &= \alpha C \int_{\lambda_{\min}}^{\lambda_{\max}} \varphi(\lambda) \eta(\lambda) d\lambda \int_0^T dt \int_0^L dz \int_{\text{pulse profile}} P_2(x, y, z) ds \end{aligned} \quad (C.1)$$

where indexes 1 and 2 refer to 1PA and 2PA excitation, respectively,  $P$  is the probability rate of the excitation of the molecule,  $C$  is the concentration of the molecules,  $\eta(\lambda)$  is a differential efficiency of photon collection (including geometrical factor, transmission of collecting optics and the detector quantum efficiency), and  $\varphi(\lambda)$  is the differential fluorescence quantum yield.

If the spectral width of the laser pulse is much smaller than the width of the molecule absorption band, then the probability rates of one- and two-photon excitation are, respectively:



$$\begin{aligned} P_1 &= \sigma_1(\lambda_1)I_1 \\ P_2 &= \frac{\sigma_2(\lambda_2)}{2}I_2^2, \end{aligned} \quad (C.2)$$

where,  $I$  is the intensity of laser pulse,  $\sigma_1$  is the 1PA cross section (in  $\text{cm}^2$ ), and  $\sigma_2$  is the 2PA cross section (in  $\text{cm}^4 \cdot \text{s}/\text{photon}$ ).

If the 1PA- and 2PA-induced fluorescence is measured in the same conditions (acquisition time, spectrometer slit width and spectral region, chromophore concentration etc.), then the collection related coefficients can be expressed from 1PA-excited fluorescence. The 1PA and 2PA excitation intensities can be calculated from the laser average power and its spatial and temporal profiles. Assuming that the two-photon excitation laser beam has a Gaussian temporal and space profiles, with pulse duration FWHM  $\tau$  (in seconds) and beam diameters FWHM in horizontal and vertical directions  $\Delta x$  and  $\Delta y$ , respectively (in centimeters), the relations between intensity and power are:

$$\begin{aligned} \int_0^T dt \int_{\text{pulse profile}} I_1(x, y, t) ds &= \frac{W_1 T}{h \nu_1} \\ \int_0^T dt \int_{\text{pulse profile}} I_2^2(x, y, t) ds &= \frac{W_2^2 T}{(h \nu_2)^2} \frac{f_{\text{prof}}}{g}, \end{aligned} \quad (C.3)$$

$$f_{\text{prof}} = \frac{\int_{\text{pulse}} I_2^2(x, y, t) dx dy dt}{\left( \int_{\text{pulse}} I_2(x, y, t) dx dy dt \right)^2} = \frac{1}{\tau \Delta x \Delta y} \left( \frac{2 \ln 2}{\pi} \right)^{3/2}$$

where  $f_{\text{prof}}$  is the laser profile factor,  $g$  is the laser repetition rate (in Hz),  $\nu = c/\lambda$  is the laser frequency (in Hz),  $W$  is the laser average power (in Watts), and  $h$  is the Planck's constant.

The 2PA cross section can then be expressed from (C.1)–(C.3) as a function of experimentally measured quantities as:

$$\sigma_2 = \frac{\pi^{3/2}}{\sqrt{2}(\ln 2)^{3/2}} \frac{W_1}{(W_2)^2} \frac{(h\nu_2)^2}{h\nu_1} \frac{F_2}{F_1} g \tau \Delta x \Delta y \sigma_1 \frac{1-10^{-OD}}{\ln 10 OD}, \quad (\text{C.4})$$

where  $OD$  is the optical density of the sample at the one-photon excitation wavelength. Pulse duration and beam radius in expression (C.3), (C.4) refer to the two-photon excitation. Note that if one uses a sample with a low optical density ( $OD < 0.05$ ), then the last fraction in (C.4) tends to 1, which means that the exact value of  $OD$  does not need to be known.

#### Characterization of the Laser Pulse

The duration and the spatial profile of the excitation beam at the sample are characterized in the whole tuning range. These data is used, first, for evaluation of the 2PA cross section at selected wavelengths (for each region, second harmonic of the signal, second harmonic of the idler, and fundamental of the signal, one or two wavelengths where selected) and, second, for calibration of the relative 2PA spectra.

The pulse duration in the whole region from 550 to 1600 nm is measured with SHG autocorrelator (Clark MXR AC-150). In the region of wavelengths 700–1000 nm, an independent measurement of  $\tau$  using a Frequency resolved optical gating (FROG) device (Newport/SwampOptics GRENOUILLE 8-50) is done, yielding similar results.

Figure C.1 shows an example of the autocorrelation function at wavelength 1160 nm. Gaussian curve fits data with error  $< 3\%$ .

Figure C.2 shows that pulse duration (FWHM assuming Gaussian shape) decreases from 120–140 fs at 600–700 nm to 70–80 fs at 1500–1600 nm. Pulse shortening is typical for the fundamental and SH, and sum-frequency, and even at fourth harmonic when pumping TOPAS with >100 fs pulses. In case of our OPA, we observe that the pulse duration does change with the wavelength in a manner that is reproduced from one experiment to another. The wavelength dependence of the pulse duration for the fundamental signal and its second harmonic (figure C.2b) have similar shape curved upwards. The minimum pulse duration is at the longer wavelength edge of the tuning range and is about 35–40% smaller than the maximum value. The pulse duration at the lower wavelength edge of the tuning range is about 12–19% smaller than the maximum value. The wavelength dependence of the second harmonic of the idler is curved downwards. Its minimum is in the middle of tuning range, near 990 nm, and its maximum is at the red edge of the range, near 800 nm. The minimum value is about 33% smaller than the maximum. The pulse duration at the longer wavelength edge of the tuning range, near 1070 nm, and is about 22% smaller than the maximum. The full change in the pulse durations lies within 70–140 fs. We note that if the wavelength dependence of the pulse duration would be neglected, then that results in up to 50% error in the measurements of the 2PA cross section spectrum.

In the wavelength range 550–1150 nm, the beam shape and diameter is measured by imaging a scattered laser spot with a CCD video camera (Xillix MicroImager PMI1400), and compared to ES Magnifier Quality Resolution Chart (Edmund Scientific). Spatial beam profile is slightly elliptic, with Gaussian widths,  $\Delta x$  and  $\Delta y$ , in horizontal

and vertical directions, respectively. At longer wavelengths, 1150–1600 nm, where the CCD has negligibly low sensitivity, the beam profile is characterized by imaging the fluorescence spot obtained upon the two- or three-photon excitation of a thin polymer film, doped with multi-photon absorbing fluorophores [189]. The correcting multiplication of the observed beam diameters by a factor of  $\sqrt{2}$  or  $\sqrt{3}$  is done in these cases to obtain the real diameters from two- and three-photon data, respectively. The independent checks with the edge-blade method in both  $x$ - and  $y$ - directions gave similar results.

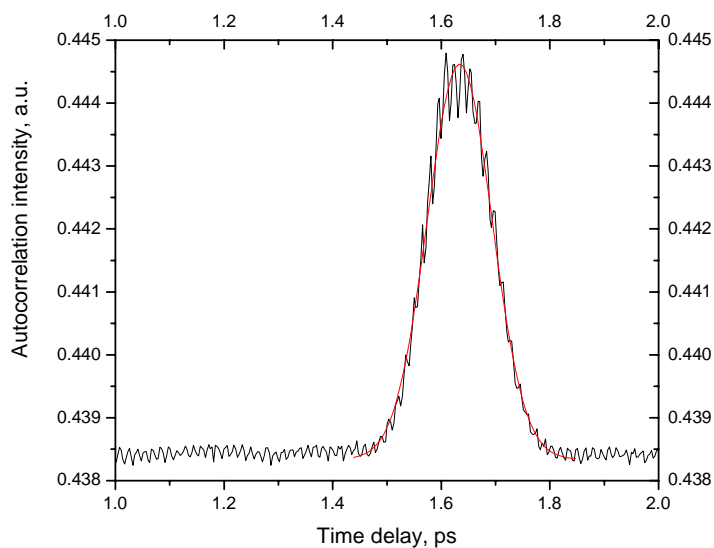


Figure C.1. An example of autocorrelation function (black) and its Gaussian fit (red) for  $\lambda=1160$  nm

Figure C.3 shows an example of the beam profile picture taken with the CCD at wavelength 1160 nm. Gaussian curves fits integrals along vertical and horizontal axis of the beam profile with error  $<1\%$ .

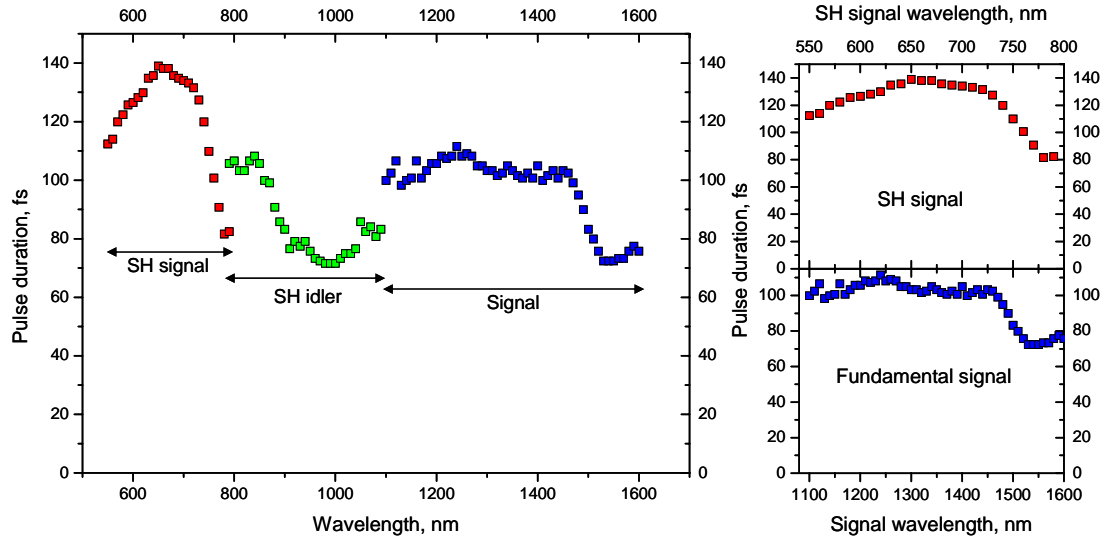


Figure C.2. OPA pulse duration in 550-1600 nm wavelength range (a) and comparison of OPA pulse duration of signal and its second harmonic (b)

Figure C.4 shows the measured vertical and horizontal beam diameters. The wavelength dependence can be thought of as a superposition of two curves: first is the curved downwards function similar to the pulse duration dependence in each of the tuning ranges. The second is the monotone increasing function due to the beam propagation. Dashed line shows the modeled beam divergence due to the propagation of the beam with an assumption that the beam waist is located 2 meters before the lens L1 (figure 3.1) and the diameter of the beam (FWHM=0.065 cm) is independent of the wavelength.

The maximum beam diameter is reached at 1600 nm. The minimum beam diameter is reached around 610 nm and is about 66% smaller than the maximum value. The beam diameter lies within 0.03–0.10 cm range. Therefore, neglecting the wavelength dependence of the beam diameter can result in up to 900% measurements error. The

beam ellipticity ( $e = 1 - D_{\min}/D_{\max}$ ) changes from 0.003 to 0.2. Ignoring this ellipticity can result in up to 25% error in the 2PA cross sections.

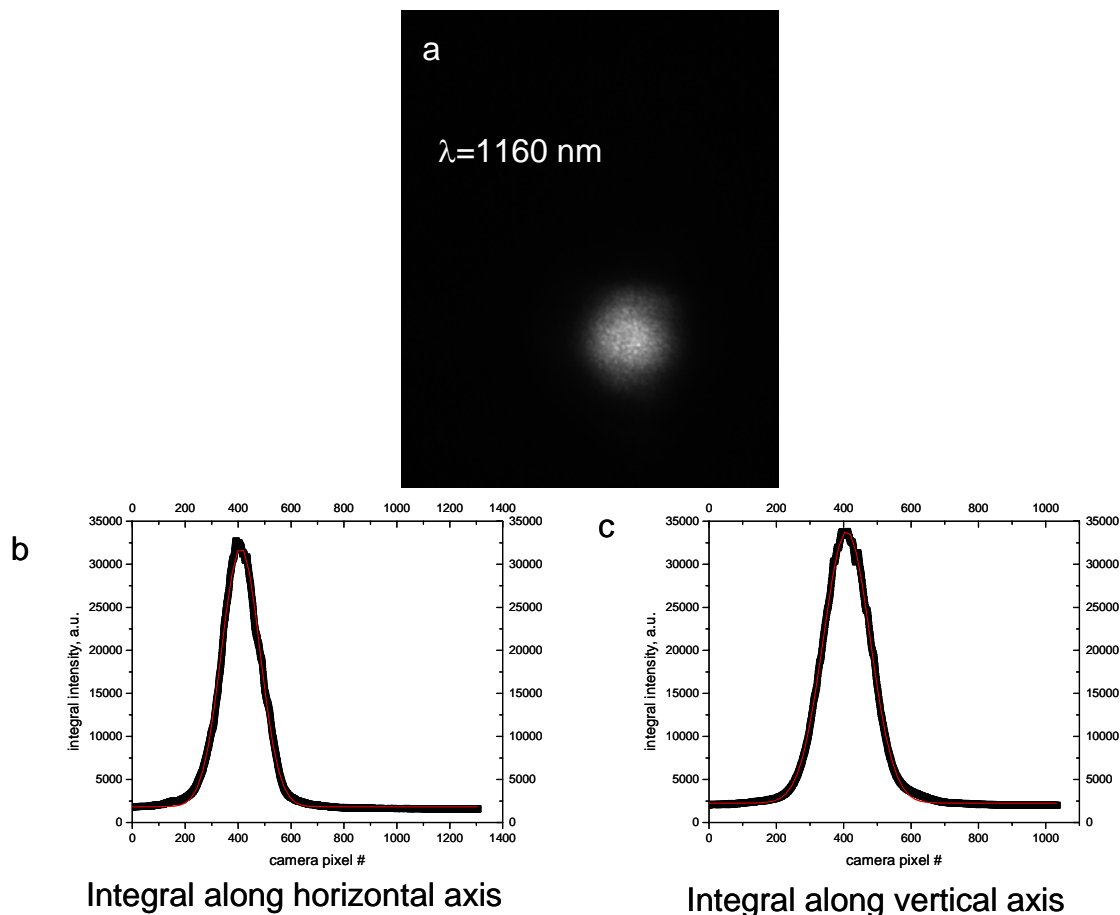


Figure C.3. CCD picture of the beam profile (a), integral of the beam intensity along horizontal axis (b), and integral of the beam intensity along vertical axis (c); pictures are shown for  $\lambda = 1160$  nm. Gaussian fits to beam profiles are also shown (red lines)

At each wavelength, where  $\sigma_2$  is measured, we always confirm that the fluorescence signal increases as a square of the excitation intensity. For this the excitation beam is gradually attenuated with a set of neutral filters, mounted on a motorized filter wheel, placed before the beam splitter (see figure 3.1). The beam splitter (thin glass plate) sends small part ( $\sim 4\%$ ) of the excitation beam onto the reference detector (Moletron J3-02). A

digital oscilloscope (Tectronix TDS 3052) is used to transfer the detector output to the computer. The LabView routine controls the filter wheel and acquires the fluorescence and the reference intensity signals. Power exponent  $\alpha$  is extracted by fitting the intensity dependence with appropriate function by Origin software. We consider the dependence quadratic, if  $\alpha$  is falling within the range between 1.9 and 2.1 with a standard deviation not larger than  $\pm 0.1$ .

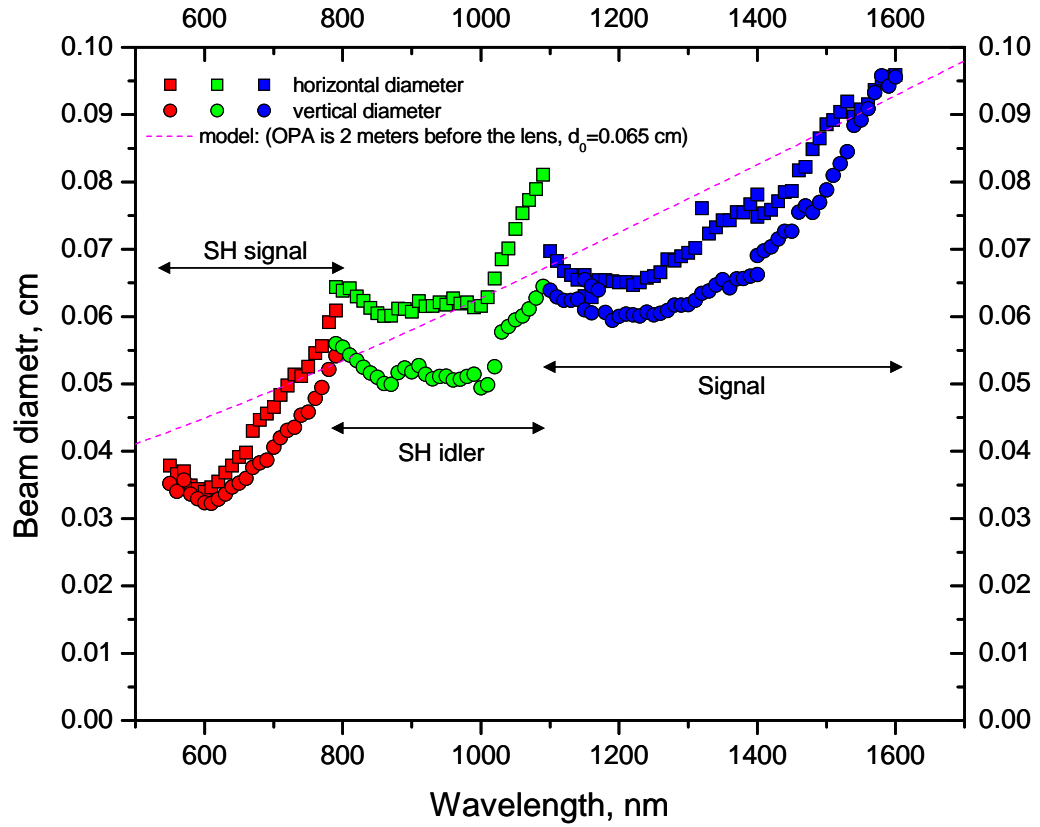


Figure C.4. Horizontal (squares), vertical (circles) beam diameter in 550-1600 nm range, and a model of a wavelength dependence of the constant beam diameter due to its propagation divergence

For the measurement of the relative 2PA spectrum, we use two-photon excitation with the tunable OPA and record the intensity of the fluorescence,  $F$ , as a function of the excitation wavelength. This intensity is equal to:

$$F(\lambda) = A \frac{\sigma_2(\lambda) W^2(\lambda)}{(h\nu)^2 \tau(\lambda) \Delta x(\lambda) \Delta y(\lambda)}, \quad (\text{C.5})$$

where  $A$  is a constant, including all the parameters, which are independent from excitation wavelength,  $\lambda$ . The relative 2PA spectrum,  $S_{2PA}(\lambda)$ , which is proportional to  $\sigma_2(\lambda)$ , can thus be presented as:

$$S_{2PA}(\lambda) = \frac{F(\lambda)}{W^2(\lambda)} (h\nu)^2 \tau(\lambda) \Delta x(\lambda) \Delta y(\lambda). \quad (\text{C.6})$$

By measuring the intensity of the fluorescence,  $F(\lambda)$ , the average power,  $W(\lambda)$ , the pulse duration,  $\tau(\lambda)$ , and the beam size,  $\Delta x(\lambda)$ , and  $\Delta y(\lambda)$ , all as a function of wavelength, one can obtain the corrected 2PA spectrum (C.6) in relative values.

At each wavelength step, the fluorescence signal from the sample  $F$  and the reference channel signal, proportional to  $W$ , are simultaneously acquired, as described before. The OPA tuning and the collection of these two signals are computer-controlled through the LabView routine. The methods of measurement of the pulse duration and the beam shape are described above and the results are shown on figures C.2, and C.4.

We define the correction function,

$$C(\lambda) = \tau(\lambda) \Delta x(\lambda) \Delta y(\lambda), \quad (\text{C.7})$$

to get the corrected 2PA spectrum. The raw 2PA spectrum  $F(\lambda)$  is multiplied by  $C(\lambda)$  and divided over  $(W^2 \lambda^2)$ . The absolute 2PA spectrum in a particular tuning region (SH of



signal, SH of idler, or signal) is obtained by calibrating the spectrum relative to the absolute cross section measured at one wavelength. The absolute cross sections are independently measured at either one of several wavelengths in each region, including 600, 700, 850, 900, 920, 950, and 1200 nm. Figure 4.1 (chapter 4) presents the correction function,  $C(\lambda)$ . Note that this particular correction function was characteristic to the particular OPA alignment and pump conditions at the time of the measurements, and may change when these conditions are altered. The total changes of the values of correction curve lie within 0.18–0.58 cm<sup>2</sup>fs. Wavelength dependence of the beam diameter and pulse duration partially compensate each other, however both changes are important. Ignoring the corrections may result in up to 300% errors in the 2PA measurements, if the whole range of excitation wavelengths is used.

The quadratic dependence of the fluorescence signal  $F$  on excitation power is checked for several selected wavelengths, as described before. Particular attention is paid to the short wavelengths region, where the hot-band 1PA may occur.

Water and some organic solvents absorb starting in the near-IR region. To minimize the absorption by the solvent a 1-mm thick sample (instead of 1 cm) was used for water from 930 to 1100 nm, and for chloroform from 1120 to 1600 nm. In the case of methanol, only <10% difference was observed between the 2PA spectra obtained in 1-mm versus 1-cm thick samples in the region 890< $\lambda$ <1300 nm. This allowed to use of the 1-cm path length because it gave a stronger signal and therefore less noise. In other cases, where either nonpolar solvent or longer wavelength region was needed, we used carbon tetrachloride, which is transparent at least up to 1600 nm.

### Measurement of the Two-Photon Cross Section Relative to Reference Standard

To obtain the unknown 2PA cross section we measure in exactly the same conditions of excitation and registration for the sample and the reference standard the intensity of two-photon excited fluorescence  $F_2$  in a narrow spectral region (1-3 nm) near a selected registration wavelength,  $\lambda_{reg}$ . The cross section is evaluated as follows:

$$\sigma_{2,s} = \frac{F_{2,s}(\lambda_{reg})C_r\varphi_r(\lambda_{reg})}{F_{2,r}(\lambda_{reg})C_s\varphi_s(\lambda_{reg})}\sigma_{2,r}, \quad (C.8)$$

where index  $r$  stands for the reference and  $s$  – for the new sample and other symbols are described earlier. The differential quantum efficiency  $\varphi(\lambda_{reg})$  can be obtained e.g. with a regular spectrofluorimeter in one-photon excitation mode, (set at the same registration wavelength  $\lambda_{reg}$  where  $F_2$  was measured). In a narrow spectral region, where the detector spectral response can be considered as a constant, this quantity cancels out in both  $F_{2,s}(\lambda_{reg})/F_{2,r}(\lambda_{reg})$  and  $\varphi_r(\lambda_{reg})/\varphi_s(\lambda_{reg})$  ratios, although both are obtained with different spectral instruments. To use this method, one needs an efficient overlap of the emission spectra of the new molecule and the reference. Our series of standards provides such possibility because it covers a very broad range of emission wavelengths, from 375 to 900 nm.

Finally, in order to determine the relative corrected 2PA spectrum of a new compound,  $S_{2PA,s}(\lambda)$ , one measures the uncorrected 2PA spectra of the new compound,  $F_{2,s}(\lambda)$ , and the reference,  $F_{2,r}(\lambda)$ , in the same experimental conditions, and then obtain the corrected spectrum, from the relation:

$$S_{2PA,s}(\lambda) = \frac{F_{2,s}(\lambda)}{F_{2,r}(\lambda)}S_{2PA,r}(\lambda), \quad (C.9)$$

where  $S_{2PA,r}(\lambda)$  is the corrected 2PA spectrum (in relative units) of one of the standards, presented in the chapter 4 and in the following section of the appendix.

Set of Reference Dyes for Relative  
Measurements of Two-Photon Absorption

Figure C.5 shows the chemical structures of the measured molecules ordered by the increasing fluorescence wavelength. These 16 compounds are: 9-Chloroanthracene (*ClAnt*), 9,10-Dichloroanthracene (*diClAnt*), Perylene, Fluorescein (*Fluoresc*), 5,10,15,20-Tetraphenyl-21H,23H-porphine (*TPP*), Zinc-2,9,16,23-tetra-*tert*-butyl-29H,31H-phthalocyanine (*tBuPcZn*), Zinc-2,9,16,23-tetrakis-(phenylthio)-29H,31H-phthalocyanine (*tPhTPcZn*), Silicon 2,3-naphthalocyanine dioctyloxide (*SiNc*), and Styryl 9M (purchased from Aldrich); Coumarin 540A (*Coum540*) and Coumarin 485 (*Coum485*) (purchased from Lambdachrome Laser Dyes); Rhodamine 590 (*Rh6G*), and Rhodamine 610 (*RhB*) (purchased from Exciton); Aluminium(III) phthalocyanine chloride (tetrasulfonate) (*AlPc*) (purchased from Frontier Scientific); Lucifer yellow (*LY*) (purchased from Molecular Probes); and Bis-diphenylaminostilbene (*BDPAS*) (synthesized previously [17] and available from MPA Technologies).

*ClAnt*, *diClAnt*, *BDPAS*, and *Perylene* are dissolved in dichloromethane (EMD Chemicals Inc.); *Coum540*, *TPP*, *tBuPcZn*, *tPhTPcZn*, and *SiNc* are dissolved in carbon tetrachloride (Sigma-Aldrich); *Coum485*, *LY*, *Rh6G*, and *RhB* are dissolved in methanol (Fisher Scientific); *Fluoresc* is dissolved in water, pH11 (Micro Essential Laboratory); *AlPc* is dissolved in heavy water (Cambridge Isotope Laboratories); *Styryl9M* is dissolved in chloroform (Fisher Scientific); 1% of pyridine (EM Science) is added for better solubility of *tBuPcZn* and *tPhTPcZn*. All compounds and solvents are used as obtained without further purification.

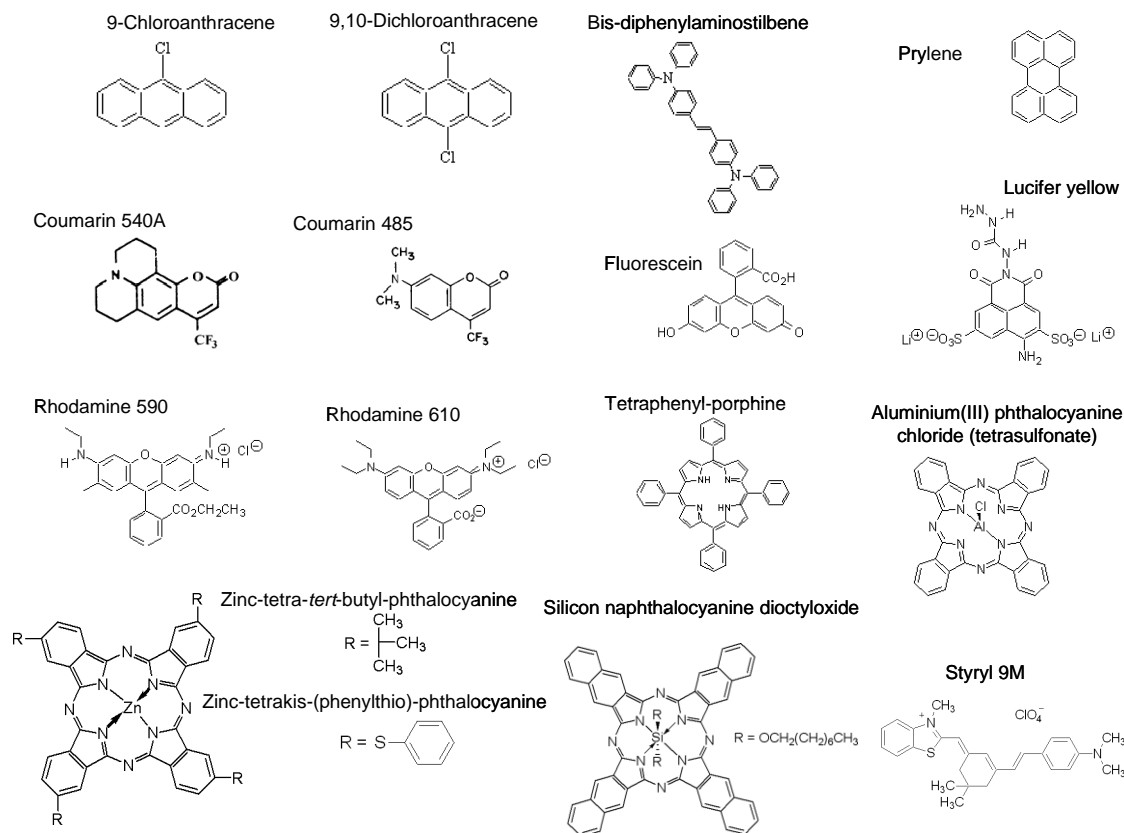


Figure C.5. Chemical structures of 16 standard reference compounds

### Two-Photon Absorption Spectra of the Reference Standards

Figures C.6–C.18 present the 2PA cross section (left vertical scale) and molar extinction (right vertical axis) spectra of the 13 dyes. The bottom axis represents the transition wavelength (1PA wavelength), and the top axis represents the 2PA laser wavelength.

There is a number of 2PA cross sections published on other molecules similar to shown here.

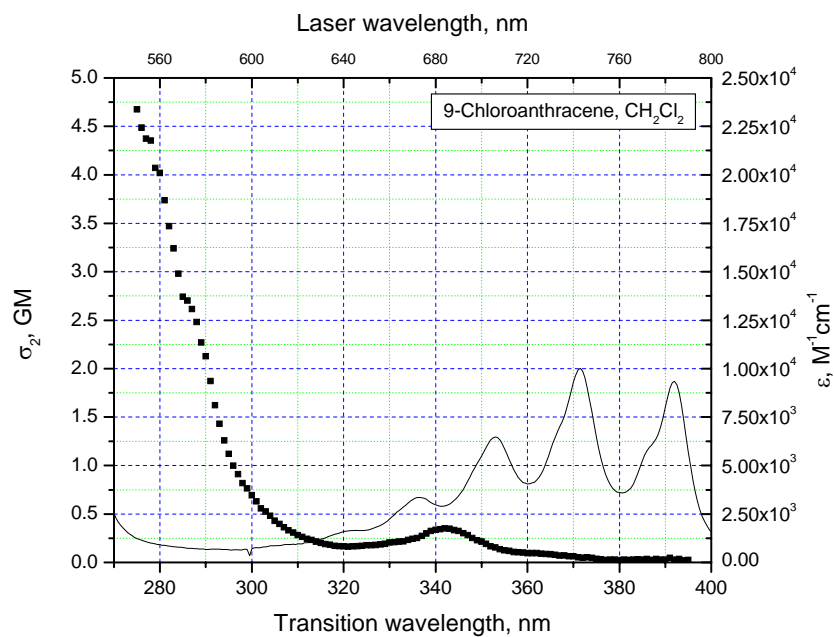


Figure C.6. Two-photon absorption (symbols) and one-photon absorption (solid lines) spectra of the *ClAnt*

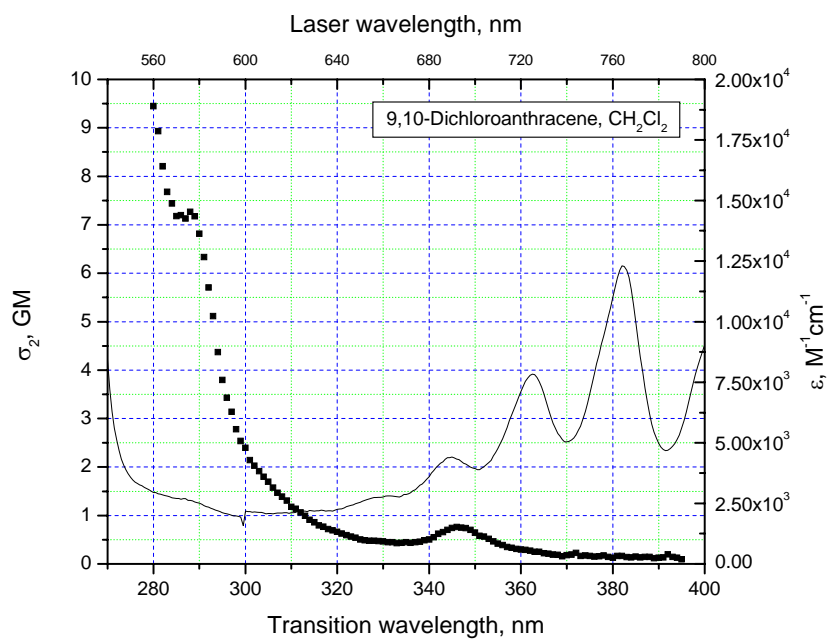


Figure C.7. Two-photon absorption (symbols) and one-photon absorption (solid lines) spectra of the *diClAnt*

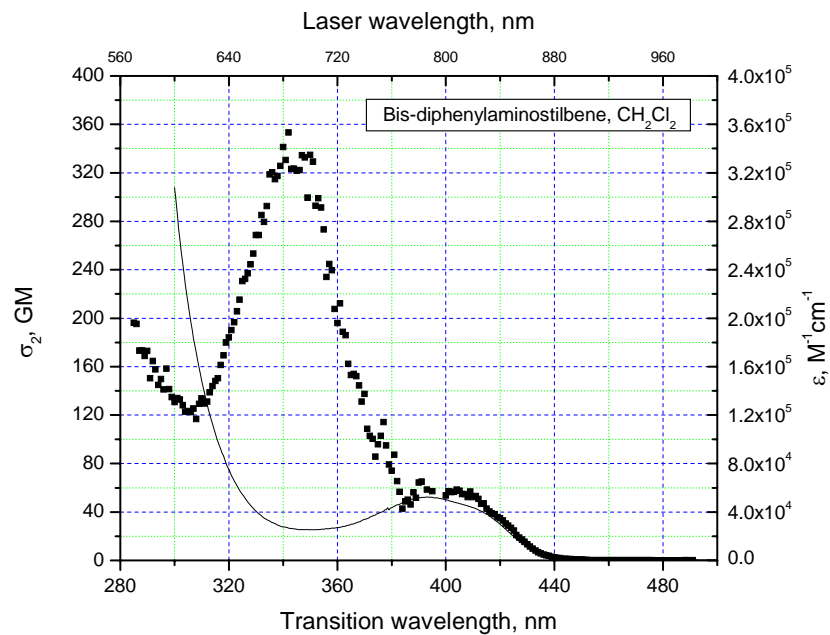


Figure C.8. Two-photon absorption (symbols) and one-photon absorption (solid lines) spectra of the *BDPAS*

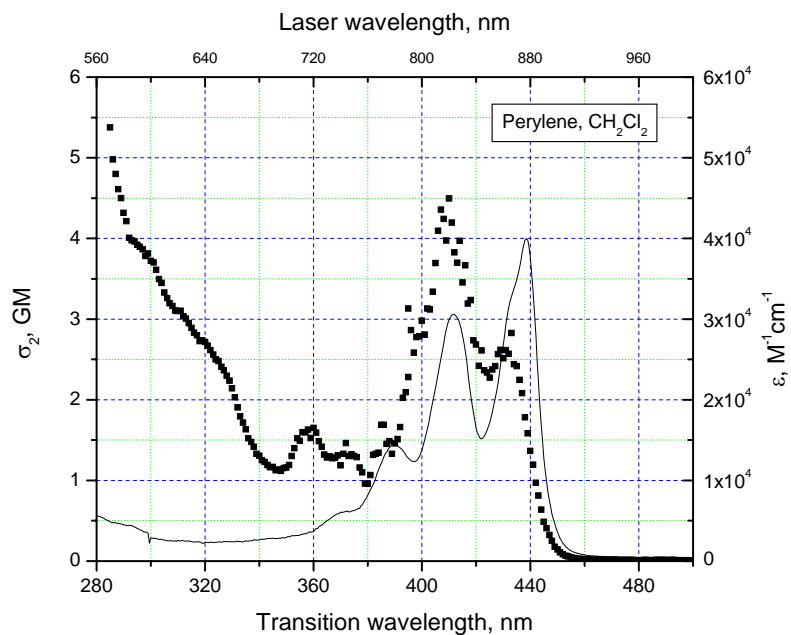


Figure C.9. Two-photon absorption (symbols) and one-photon absorption (solid lines) spectra of the *Perylene*

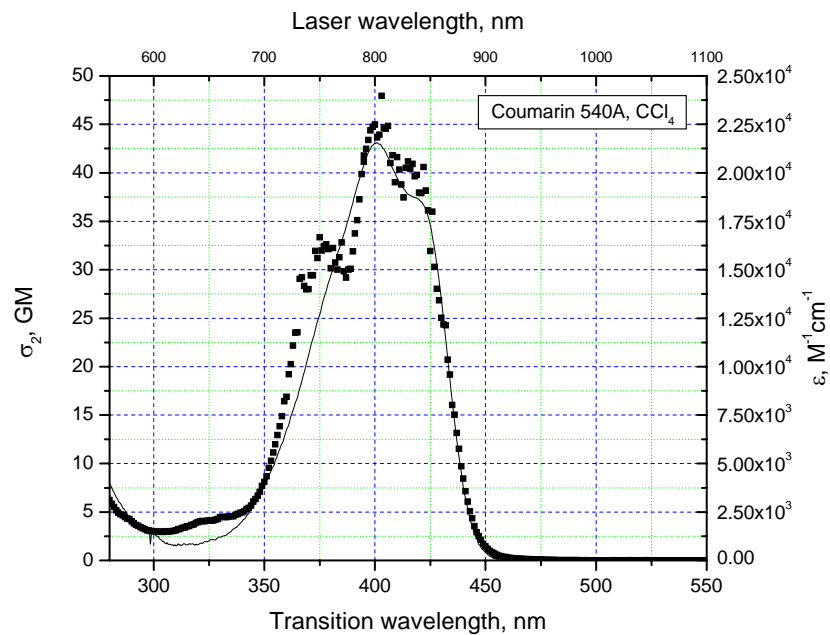


Figure C.10. Two-photon absorption (symbols) and one-photon absorption (solid lines) spectra of the *Coum540*

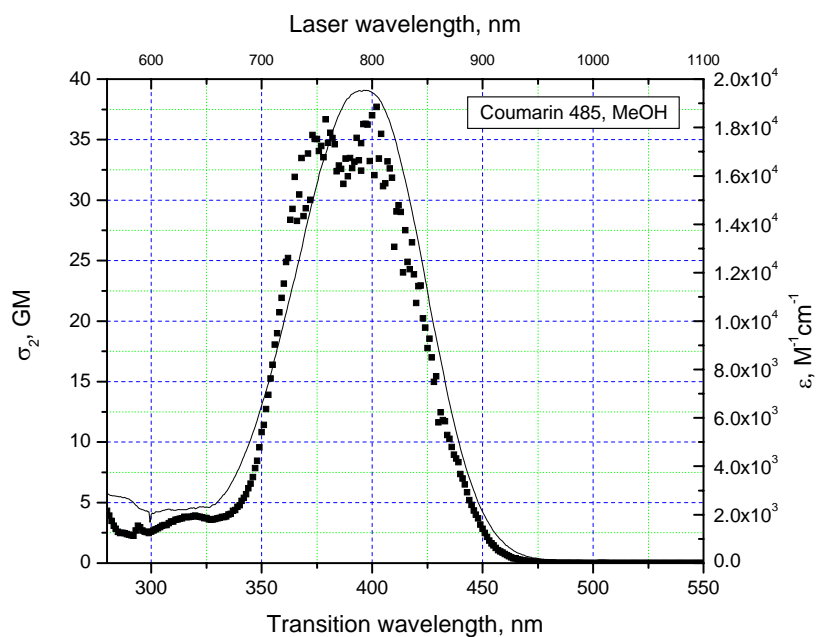


Figure C.11. Two-photon absorption (symbols) and one-photon absorption (solid lines) spectra of the *Coum485*

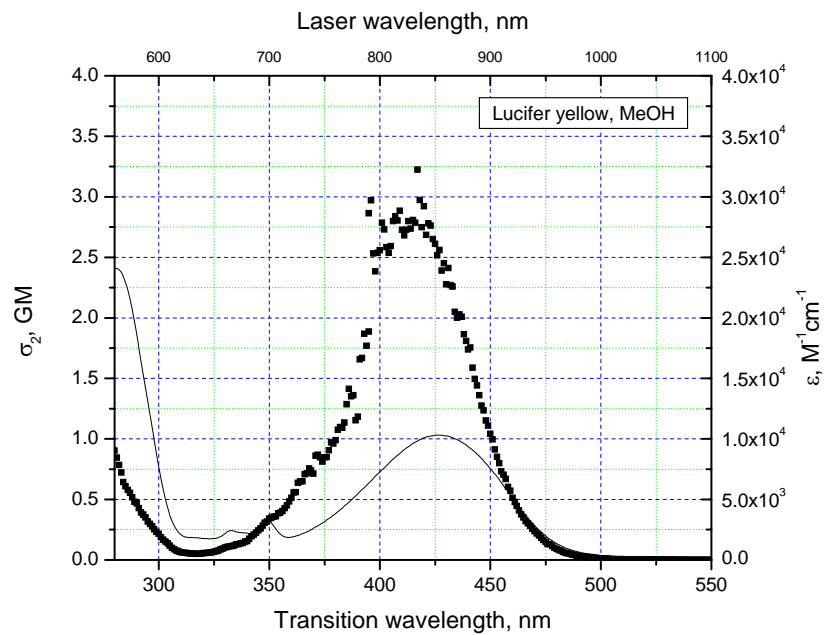


Figure C.12. Two-photon absorption (symbols) and one-photon absorption (solid lines) spectra of the *LY*

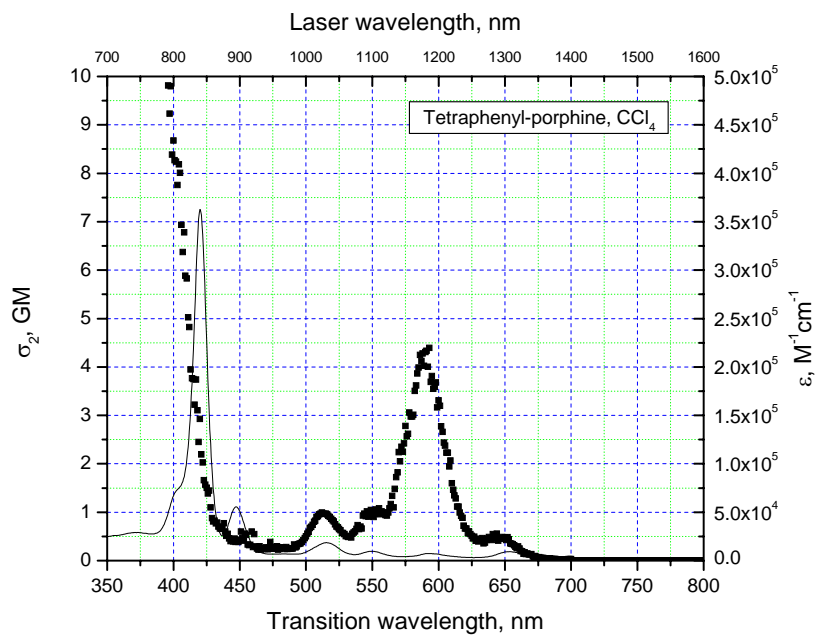


Figure C.13. Two-photon absorption (symbols) and one-photon absorption (solid lines) spectra of the *TPP*



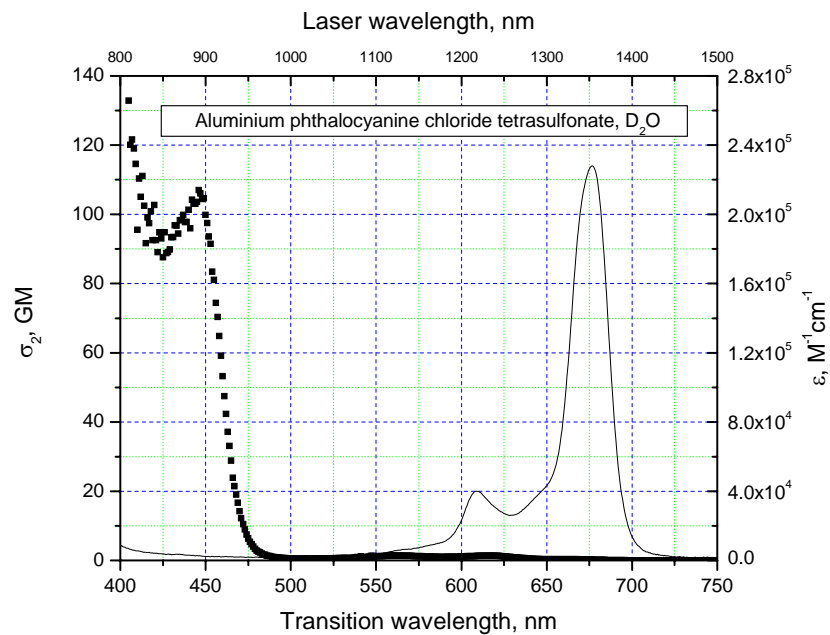


Figure C.14. Two-photon absorption (symbols) and one-photon absorption (solid lines) spectra of the *ALPc*

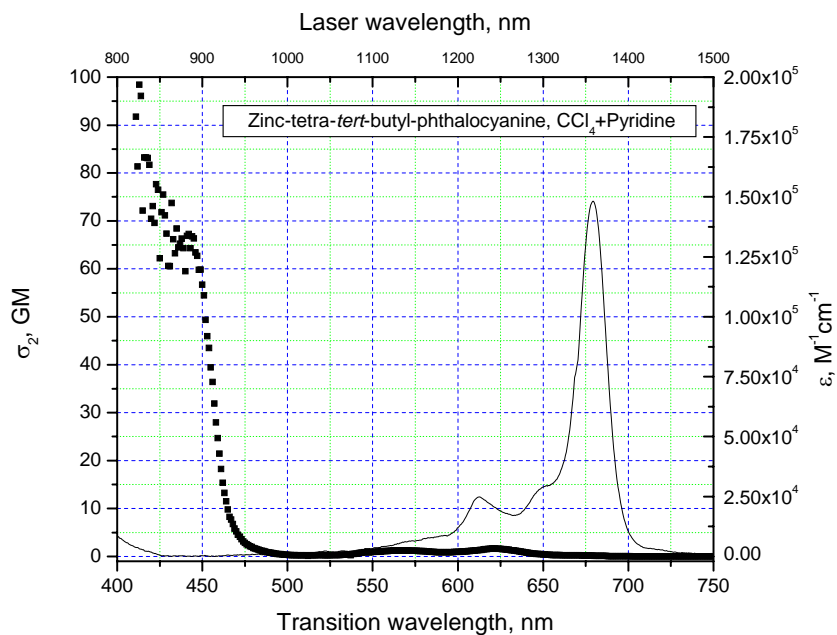


Figure C.15. Two-photon absorption (symbols) and one-photon absorption (solid lines) spectra of the *tBuPcZn*

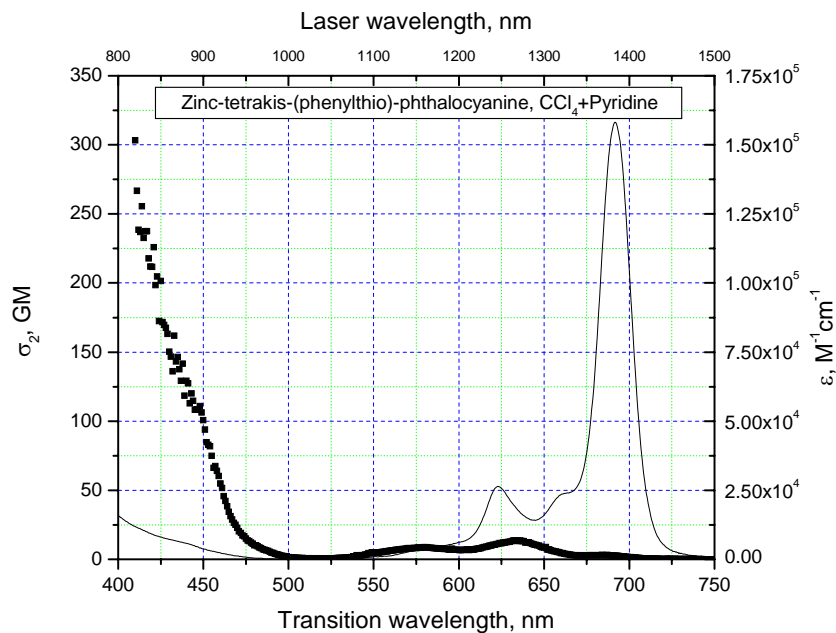


Figure C.16. Two-photon absorption (symbols) and one-photon absorption (solid lines) spectra of the *tPhTPcZn*

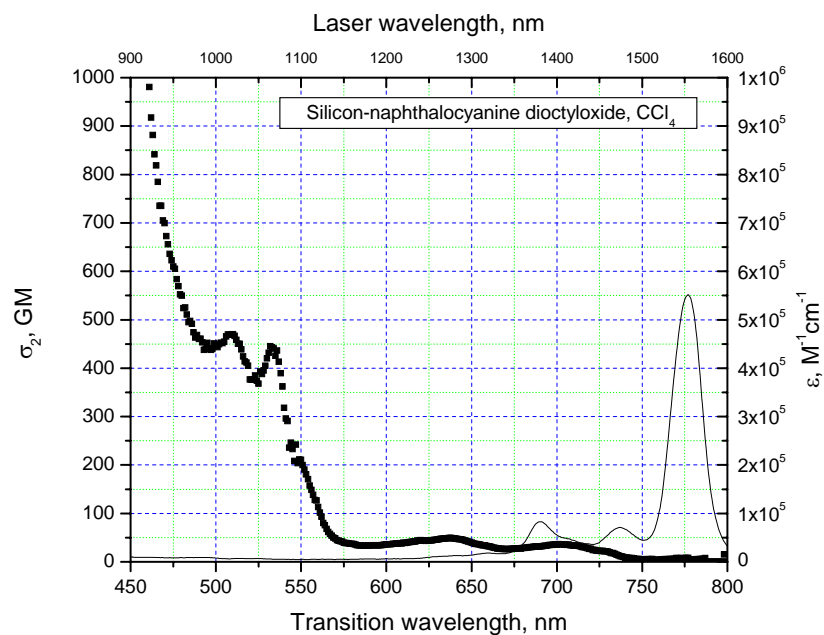


Figure C.17. Two-photon absorption (symbols) and one-photon absorption (solid lines) spectra of the *SiNc*

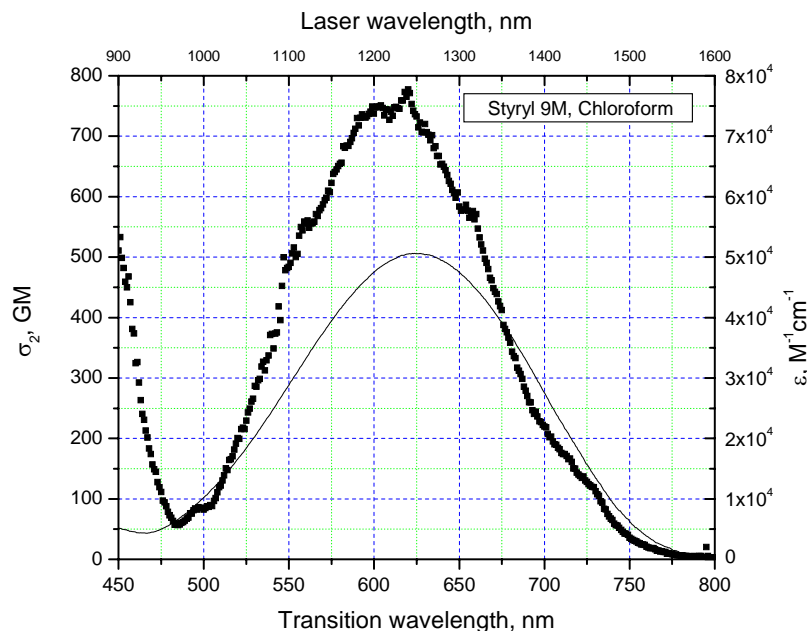


Figure C.18. Two-photon absorption (symbols) and one-photon absorption (solid lines) spectra of the *Styryl9M*

Webb and co-authors report  $\sigma_2\phi = 19 \pm 5.5$  GM for *Coumarin 307* (7-Ethylamino-6-methyl-4-trifluoromethylcoumarin) at 776 nm [94]. Assuming the quantum yield  $\phi = 0.56$  [190], this translates into  $\sigma_2 = 34 \pm 10$  GM, which correlates very well with our result for structurally close *Coumarin 485* (7-dimethylamino-4-trifluoromethylcoumarin),  $\sigma_2 = 33 \pm 4.6$  GM (at 776 nm). The absolute spectra of three other coumarins, obtained with fluorescence technique [191], also correlate well with our data for *Coumarin 485*. In particular, *Coumarin 151* (7-amino-4-trifluoromethylcoumarin) shows  $\sigma_2^{\max}(754) = 47$  GM vs.  $\sigma_2^{\max}(754) = 35 \pm 5$  GM for *Coumarin 485* (figure C.11).

Our cross section of *9-Chloroanthracene* ( $\sigma_2 = 0.28 \pm 0.04$  GM) obtained at 694 nm, is in good agreement with several previous fluorescence results for Anthracene in

solution: 0.18 GM [96],  $0.3 \pm 0.1$  GM [98],  $0.14 \pm 0.04$  GM [105], and in gas phase: 0.18 GM [106]. The *Perylene* cross section measured in a gas phase (2.4 GM at 694 nm) [106] also agrees with our result ( $1.1 \pm 0.2$  GM). Absolute 2PA spectrum of *BDPAS* is measured previously in toluene with picosecond fluorescence excitation [188]. It correlates quite well with that presented here, both in the shape and maximum absolute values ( $\sigma_2^{\max}(690) = 190 \pm 30$  GM in [188], vs.  $\sigma_2^{\max}(687) = 330 \pm 45$  GM here and  $320 \pm 65$  in [130]). Femtosecond NLT result for *BDPAS* in THF  $\sigma_2(800) = 33$  GM [192] is  $\sim 2$  folds less than our fluorescence-based value,  $\sigma_2(800) = 60$  GM, which again can be due to other than 2PA effects, taking place in NLT measurement.

Absolute two-photon excitation spectrum (in  $\sigma_2\phi$  values) of *Lucifer Yellow* in water is published in [94]. The authors report  $\sigma_2\phi = 0.95 \pm 0.3$  GM at 860 nm. Taking the quantum yield  $\phi = 0.21$  [193], one obtains  $\sigma_2 = 4.5 \pm 1.4$  GM, which compares to our result in methanol,  $\sigma_2 = 2.4 \pm 0.3$  GM. The result, recently published by Karotki et al [36]  $\sigma_2(860) = 2.8 \pm 0.8$  GM (in water) is in even better agreement with ours.

The 2PA spectrum of *TPP* in toluene is measured previously [189, 194] in a 1-cm cell without taking into account the toluene absorption in the near-IR region, and, therefore, its shape between 1120 and 1260 nm, presented there, is most probably distorted. On the other hand, the absolute cross section value, measured at 1205 nm,  $\sigma_2 = 3.3 \pm 0.7$  GM in a very thin ( $< 1$  mm) initial layer of sample, is correct. This value agrees rather well with that measured here in transparent carbon tetrachloride at the same wavelength ( $\sigma_2 = 2.8 \pm 0.4$  GM). Morone et al. [195] and Ishi-i et al. [196], report the

2PA cross sections for *TPP* measured by femtosecond open aperture z-scan method at 800 - 810 nm in chloroform. The value of Morone et al.,  $\sigma_2 = 16 \pm 4$  GM, agrees well with our measurements ( $\sigma_2 = 10 \pm 2$  GM) in toluene [189, 194] and  $\sigma_2 = 8 \pm 1$  GM in  $\text{CCl}_4$  (figure C.14). However, Ishi-i et al., report an underestimated cross section,  $\sigma_2 = 2.2$  GM, which can be explained by reasons discussed above for other molecules.

The 2PA spectra of *Zinc-tetra-tert-butyl-phthalocyanine* and *Zinc-tetrakis-(phenylthio)-phthalocyanine* previously obtained in dichloromethane in 800–1100 nm region [82] coincide within experimental errors with those obtained here for the same molecules in the same spectral region but in carbon tetrachloride with 1% of pyridine.

Finally, tables D.3–D.6 present 2PA cross sections of all the dyes from the set with the 10 nm wavelength step. The data can be used for relative measurements as described previously in the appendix.

APPENDIX D

DATA TABLES

Table D.1. Extinction coefficients at maximum wavelength, fluorescence wavelength range and 2PA wavelength range for the dyes

Compound	$\epsilon$ , M <sup>-1</sup> cm <sup>-1</sup>	$\lambda_{\epsilon}$ , nm	$\lambda_{\text{fluorescence}}$ , nm	$\lambda_{\text{2PA}}$ , nm
<i>ClAnt</i>	9340	392	385-475	550-790
<i>diClAnt</i>	12000	404	397-474	550-790
<i>BDPAS</i>	52400	393	414-528	570-980
<i>Perylene</i>	40000	438.5	431-515	570-1000
<i>Coum540</i>	21600	401	414-548	550-1100
<i>Coun485</i>	19500	394	459-632	550-1100
<i>Fluoresc</i>	92300	491.5	490-580	610-1100
<i>LY</i>	10300	426.5	473-636	560-1100
<i>Rh6G</i>	12600	528.5	524-620	630-1098
<i>RhB</i>	11100	546	540-640	650-1300
<i>TPP</i>	18500	515	638-745	790-1600
<i>AlPc</i>	228000	677	661-765	810-1500
<i>tBuPcZn</i>	148000	679	666-768	820-1500
<i>tPhTPcZn</i>	158000	692	678-788	820-1500
<i>SiNc</i>	552000	777	760-832	920-1600
<i>Styryl9M</i>	50600	627	704-859	900-1600

Table D.2. Comparison of two-photon cross sections of the reference standards with the literature data

$\lambda_{\text{laser}}$	Solvent	Pulse duration	Method	Conc., M	$\sigma_2$ , GM	Ref.
<i>Fluorescein</i>						
<b>782</b>	water, pH11	100 fs	L	$3 \cdot 10^{-6}$	$46 \pm 6$	This work
		cw	L	$8 \cdot 10^{-5}$	$38 \pm 9.7$	[94]
	Water, pH13	100-240 fs	LSOA		$46 \pm 10$	[109]
<b>800</b>	water, pH11	130 fs	L	$3 \cdot 10^{-6}$	$36 \pm 5$	This work
		180 fs	L	$10^{-4}$	54	[111]
	water, pH13	100 fs	L	$1.45 \cdot 10^{-5}$	$36 \pm 11$	[95]
<b>1060-1064</b>	water, pH11	100 fs	L	$3 \cdot 10^{-6}$	$0.069 \pm 0.010$	This work
	EtOH	60 ns	L	$10^{-5}$	$0.36^a$	[101]
		ps	L	$10^{-5}$	$0.15^a$	[101]
	CH <sub>3</sub> OD, pH10	125 ns	L vs. HRS	$2 \cdot 10^{-5}$	$0.032 \pm 0.006$	[110]
<i>Rhodamine 590 (6G)</i>						
<b>694</b>	MeOH	160 fs	L	$8 \cdot 10^{-6}$	$112 \pm 16$	This work
	MeOH, EtOH	30 ps	NLT	$4 \cdot 10^{-2}$	$180 \pm 20$	[107]
<b>765</b>	MeOH	120 fs	L	$8 \cdot 10^{-6}$	$55 \pm 8$	This work
	EtOH	40 ns	L		$40 \pm 19^a$	[99]
<b>780</b>	MeOH	100 fs	L	$8 \cdot 10^{-6}$	$60 \pm 8$	This work
		100 fs	L		$37 \pm 10$	[95]
		100-200fs	DMPP		$8 \pm 4$	[117]
<b>798-806</b>	MeOH	80-120 fs	L	$8 \cdot 10^{-6}$	$65 \pm 9$	This work
		1.2 ps	L	$3.26 \cdot 10^{-5}$	134	[113]
		440 fs	L	$4.3 \cdot 10^{-7}$	$12.8 \pm 1.8$	[116]
		1.2 ps	NLT	$2.33 \cdot 10^{-2}$	12.8	[113]
		100-200fs	DMPP	$8.3 \cdot 10^{-3}$	$13 \pm 4$	[117]
		70 fs	NLT	$3 \cdot 10^{-2}$	$15.3 \pm 2$	[114]
		115 fs	z-scan	$1.02 \cdot 10^{-2}$	$16.2 \pm 2.4$	[112]
		100 fs	NLT		$26 \pm 3$	[121]
		100 fs	z-scan	$10^{-2}$	$22 \pm 2$	[121]
<b>825</b>	MeOH	110 fs	L	$3.09 \cdot 10^{-4}$	$37 \pm 6$	[115]
<b>825</b>	MeOH	125 fs	L	$8 \cdot 10^{-6}$	$64 \pm 9$	This work
		100-200fs	DMPP	$8.3 \cdot 10^{-3}$	$26 \pm 7$	[117]
<b>870</b>	MeOH	120 fs	L	$8 \cdot 10^{-6}$	$6.4 \pm 0.9$	This work
	EtOH	40 ns	L		$6.74^a$	[99]
<b>880</b>	MeOH	110 fs	L	$8 \cdot 10^{-6}$	$4.4 \pm 0.6$	This work
		100-200fs	DMPP	$8.3 \cdot 10^{-3}$	$4.8 \pm 1.5$	[117]
<b>976</b>	MeOH	85 fs	L	$8 \cdot 10^{-6}$	$13 \pm 2$	This work
	EtOH	40 ns	L		$36.4^a$	[99]
<b>1054-1064</b>	MeOH	100 fs	L	$8 \cdot 10^{-6}$	$10 \pm 1$	This work
		5 ps	NLT	0.2	$10 \pm 1$	[108]
	MeOD	125 ns	L vs. HRS	$2.17 \cdot 10^{-6}$	$4.2 \pm 0.8$	[110]
	EtOH	ps	L	$10^{-3}$	$7.2^a$	[101]



		60 ns	L	$10^{-3}$	$11^a$	[101]
		110 ns	L	$10^{-6}$	$22 \pm 10$	[104]
		cw	L	$10^{-2}$	$24 \pm 4^a$	[102]
		40 ns	L		$25.8^a$	[99]
<i>Rhodamine 610 (B)</i>						
<b>694</b>	MeOH	160 fs	L	$6 \cdot 10^{-7}$	$213 \pm 30$	This work
	Acidic MeOH	30 ps	NLT	$4 \cdot 10^{-2}$	$120 \pm 20$	[107]
<b>780</b>	MeOH	100 fs	L	$6 \cdot 10^{-7}$	$95 \pm 13$	This work
		100-200 fs	DMPP	$8.3 \cdot 10^{-3}$	$14 \pm 4$	[117]
<b>798-802</b>	MeOH	130 fs	L	$6 \cdot 10^{-7}$	$140 \pm 20$	This work
		300 fs	L	$10^{-5}$	$60 \pm 14$	[36]
		100-200 fs	DMPP	$8.3 \cdot 10^{-3}$	$21 \pm 7$	[117]
		440 fs	L	$10^{-6}$	$24 \pm 3.6$	[116]
		1.2 ps	NLT	$2.56 \cdot 10^{-2}$	20.8	[113]
		100 fs	z-scan	$10^{-2}$	$50 \pm 5$	[121]
		100 fs	NLT		$50 \pm 4$	[121]
<b>840</b>	MeOH	130 fs	L	$6 \cdot 10^{-7}$	$195 \pm 25$	This work
		100 fs	L	$10^{-4}$	$210 \pm 55$	[94]
		300 fs	L	$10^{-5}$	$76 \pm 23$	[36]
<b>850</b>	MeOH	130 fs	L	$6 \cdot 10^{-7}$	$180 \pm 25$	This work
		100-200 fs	DMPP	$8.3 \cdot 10^{-3}$	$12 \pm 3$	[117]
<b>880</b>	MeOH	110 fs	L	$6 \cdot 10^{-7}$	$54 \pm 8$	This work
		100-200 fs	DMPP	$8.3 \cdot 10^{-3}$	$10 \pm 3$	[117]
<b>1060-1064</b>	MeOH	100 fs	L	$6 \cdot 10^{-7}$	$28 \pm 4$	This work
		ps	L	$10^{-5}$	$14^a$	[101]
		60 ns	L	$10^{-5}$	$28^a$	[101]
	EtOH	cw	L	$10^{-2}$	$26 \pm 4^a$	[103]
		40 ns	L		$29 \pm 13^a$	[99]
		110 ns	L	$10^{-6}$	$24 \pm 12^a$	[104]
	CH <sub>3</sub> OD	125 ns	L vs. HRS	$3 \cdot 10^{-6}$	$4.6 \pm 1.4$	[110]
		125 ns	L	$3 \cdot 10^{-6}$	$6.8 \pm 2$	[110]
		125 ns	L, abs	$3 \cdot 10^{-6}$	$6.2 \pm 2$	[110]

<sup>a</sup>Original value is multiplied by 2, because of different definition of  $\sigma_2$  (see text).

Abbreviations of the methods used:

L – luminescence (fluorescence);

NLT – nonlinear transmission;

LSOA – second order autocorrelation of luminescence;

L vs. HRS – luminescence signal calibrated versus hyper-Rayleigh scattering;

DMPP – double modulation pump-probe spectroscopy;

NLTM – nonlinear transmission modulation.

Table D.3. Two-photon cross sections (GM) of the dyes at selected wavelengths (nm). The relative error of numbers shown here is  $\pm 15\%$  (First four compounds)

Wavelength	9-Chloro-anthracene	9,10-Dichloro-anthracene	<i>Bis (diphenylamino)-stilbene</i>	<i>Perylene</i>
550	4.7	11		
560	4.0	9.4		
570	2.7	7.2	200	5.4
580	2.1	6.8	170	4.3
590	1.1	3.8	150	3.9
600	0.69	2.4	130	3.7
610	0.43	1.7	120	3.3
620	0.28	1.2	130	3.1
630	0.20	0.86	150	2.9
640	0.17	0.66	180	2.7
650	0.18	0.51	230	2.5
660	0.21	0.46	270	2.1
670	0.24	0.44	320	1.6
680	0.34	0.51	340	1.3
690	0.33	0.74	320	1.2
700	0.21	0.64	330	1.2
710	0.13	0.42	270	1.5
720	0.095	0.29	200	1.7
730	0.083	0.22	150	1.3
740	0.064	0.18	140	1.2
750	0.037	0.16	96	1.3
760	0.024	0.13	74	1.4
770	0.028	0.15	49	1.4
780	0.030	0.13	68	1.5
790	0.025	0.09	57	2.3
800			54	3.0
810			58	3.7
820			52	4.5
830			43	3.5
840			35	2.7
850			25	2.3
860			13	2.5
870			5.9	2.4
880			2.6	1.4
890			1.1	0.49
900			0.61	0.14
910			0.28	0.046
920			0.12	0.025
930			0.12	0.018
940			0.12	0.016
950			0.12	0.013
960			0.11	0.012
970			0.11	0.011
980				0.014
990				0.011
1000				0.0075

Table D.4. Two-photon cross sections (GM) of the dyes at selected wavelengths (nm). The relative error of numbers shown here is  $\pm 15\%$  (Second four compounds)

Wavelength	<i>Coumarin 540A</i>	<i>Coumarin 485</i>	<i>Fluorescein</i>	<i>Lucifer Yellow</i>
550	7.4	6.6		
560	6.2	4.3		0.90
570	4.8	2.6		0.61
580	4.0	2.3		0.47
590	3.3	2.9		0.32
600	3.0	2.6		0.22
610	3.0	3.1	45	0.12
620	3.1	3.4	52	0.063
630	3.5	3.8	62	0.053
640	3.9	3.9	65	0.055
650	4.1	3.7	57	0.068
660	4.5	3.7	40	0.10
670	4.6	4.0	26	0.13
680	4.9	4.8	17	0.16
690	6.1	6.6	13	0.24
700	8.1	11	14	0.34
710	12	16	16	0.39
720	17	23	21	0.51
730	24	32	24	0.65
740	28	34	30	0.71
750	33	35	36	0.85
760	32	35	45	0.99
770	30	33	43	1.3
780	32	33	45	1.5
790	42	35	47	1.9
800	45	37	36	2.3
810	45	34	32	2.6
820	42	32	24	2.9
830	41	28	18	3.0
840	38	22	13	2.9
850	32	18	11	2.6
860	25	12	11	2.3
870	16	10	12	2.0
880	8.5	7.4	12	1.7
890	3.5	4.8	13	1.4
900	1.4	2.8	15	1.1
910	0.58	1.5	16	0.73
920	0.29	0.73	16	0.51
930	0.17	0.36	15	0.35
940	0.12	0.18	11	0.24
950	0.074	0.089	8.4	0.15
960	0.041	0.045	6.6	0.092
970	0.023	0.024	5.9	0.053
980	0.020	0.016	5.3	0.034
990	0.024	0.0097	4.6	0.022
1000	0.013	0.0065	3.1	0.013
1010	0.014		1.8	
1020			1.1	
1030			0.66	
1040			0.35	
1050			0.17	
1060			0.064	

1070			0.050	
1080			0.022	
1090			0.029	

Table D.5. Two-photon cross sections (GM) of the dyes at selected wavelengths (nm). The relative error of numbers shown here is  $\pm 15\%$  (Third four compounds)

Wavelength	<i>Rhodamine 6G</i>	<i>Rhodamine B</i>	<i>Tetraphenyl-porphyrin</i>	<i>Aluminium phthalocyanine</i>
630	5.7			
640	6.6			
650	10	53		
660	19	73		
670	32	96		
680	58	130		
690	100	180		
700	130	240		
710	99	180		
720	66	120		
730	53	86		
740	56	68		
750	58	67		
760	58	72		
770	62	83		
780	63	95		
790	69	120	12	
800	65	140	8.7	
810	70	160	8.0	130
820	64	190	5.8	96
830	51	200	3.8	92
840	42	180	2.9	100
850	23	160	1.5	88
860	12	110	0.81	93
870	6.4	74	0.66	98
880	4.4	54	0.51	100
890	3.8	27	0.39	100
900	4.2	13	0.43	100
910	4.9	7.3	0.53	81
920	5.7	6.0	0.28	53
930	6.6	6.4	0.30	29
940	8.3	7.7	0.27	14
950	9.2	9.3	0.25	6.3
960	11	11	0.24	2.9
970	12	12	0.28	1.6
980	13	14	0.25	1.0
990	12	18	0.35	0.69
1000	9.5	22	0.50	0.52
1010	7.6	28	0.74	0.46
1020	7.1	34	0.95	0.50
1030	7.6	39	0.97	0.56
1040	8.3	39	0.83	0.57
1050	9.5	38	0.65	0.58
1060	9.9	31	0.51	0.68
1070	9.2	27	0.55	0.71
1080	7.0	24	0.65	0.68
1090	4.8	25	0.92	1.0
1100		24	1.0	1.2
1110		21	1.1	1.3
1120		16	0.94	1.4
1130		8.9	1.3	1.4
1140		4.2	2.2	1.3

1150		2.6	2.8	1.2
1160		1.7	3.0	1.2
1170		0.77	4.0	1.0
1180		0.33	4.3	1.0
1190		0.26	3.8	1.0
1200		0.19	3.3	1.1
1210		0.12	2.4	1.2
1220		0.056	1.6	1.3
1230		0.056	1.1	1.4
1240		0.058	0.66	1.3
1250		0.052	0.51	1.1
1260			0.39	0.93
1270			0.37	0.73
1280			0.42	0.52
1290			0.41	0.40
1300			0.48	0.33
1310			0.35	0.31
1320			0.29	0.31
1330			0.17	0.30
1340			0.13	0.27
1350			0.061	0.23
1360			0.046	0.17
1370			0.033	0.12
1380			0.018	0.079
1390			0.024	0.047
1400			0.032	0.030
1410				0.018
1420				0.015
1430				0.0082
1440				0.0077
1450				0.0089
1460				0.0077
1470				0.010

Table D.6. Two-photon cross sections (GM) of the dyes at selected wavelengths (nm). The relative error of numbers shown here is  $\pm 15\%$  (Last four compounds)

Wavelength	<i>Zn-tetra-tert-butyl-phthalocyanine</i>	<i>Zn-tetrakis-(phenylthio)-phthalocyanine</i>	<i>Si-naphthalocyanine dioctyloxide</i>	<i>Styryl 9M</i>
820	110	300		
830	89	230		
840	79	210		
850	62	200		
860	61	150		
870	64	150		
880	65	130		
890	66	110		
900	57	100		510
910	39	75		450
920	21	55	1100	320
930	9.8	34	820	230
940	5.2	23	700	160
950	2.8	15	610	110
960	1.8	10	550	73
970	1.2	7.3	500	57
980	0.77	4.9	460	67
990	0.48	3.0	450	84
1000	0.33	1.7	450	82
1010	0.22	1.1	450	88
1020	0.24	0.76	470	120
1030	0.23	0.64	440	160
1040	0.29	0.55	380	200
1050	0.25	0.73	370	230
1060	0.30	0.96	420	290
1070	0.41	1.4	430	330
1080	0.56	3.1	320	370
1090	0.87	3.5	230	400
1100	0.92	5.0	210	480
1110	1.0	5.4	160	510
1120	1.2	6.3	110	550
1130	1.2	7.3	68	560
1140	1.2	8.1	48	590
1150	1.2	8.0	40	620
1160	1.1	8.7	37	650
1170	0.94	8.1	34	680
1180	0.86	7.7	33	730
1190	0.87	7.0	34	730
1200	0.93	6.7	36	740
1210	1.1	7.2	37	750
1220	1.2	7.6	39	740
1230	1.4	8.9	41	750
1240	1.6	10	45	780
1250	1.6	12	44	730
1260	1.4	13	46	720
1270	1.1	13	48	680
1280	0.80	12	48	650
1290	0.56	10	45	620
1300	0.41	8.5	40	580
1310	0.31	6.2	35	580
1320	0.26	4.5	32	570

1330	0.23	3.4	27	500
1340	0.21	2.9	26	450
1350	0.18	3.0	27	410
1360	0.14	2.9	28	360
1370	0.10	3.1	30	310
1380	0.070	2.9	31	270
1390	0.044	2.3	34	240
1400	0.028	1.5	35	220
1410	0.018	0.99	35	190
1420	0.014	0.64	33	180
1430	0.0099	0.45	30	170
1440	0.0094	0.21	27	140
1450	0.0063	0.16	23	130
1460	0.0051	0.25	21	110
1470	0.0062	0.30	15	83
1480			8.5	65
1490			6.8	49
1500			5.4	36
1510			5.4	27
1520			4.2	21
1530			5.5	17
1540			7.5	12
1550			7.4	8.4
1560			4.7	6.1
1570			5.9	5.2
1580				4.2
1590				4.7
1600				1.9



Table D.7. Measured spectroscopic parameters

Comp.	$r$	$\lambda_{em}$ , nm	$\tau_f$ , ns	$a$ , Å	$\frac{\Delta \bar{\nu}_s}{\Delta f(D)}$	$ \Delta \vec{\mu}_{01} $ , Debye	$\varepsilon$ , $10^4$ $M^{-1}cm^{-1}$	$\sigma_2^{ex}$ , GM (*)	$\sigma_2^{th(O)}$ , GM	$\sigma_2^{th(L)}$ , GM
<b>I</b>	0.022	416	1.71	5.3	4260	11.2	2.44	47	55	73
<b>2</b>	0.031	481	1.67	6.0	5330	14.9	3.09	136	136	182
<b>3</b>	0.030	419	1.57	5.8	2010	8.8	4.31	69	60	80
<b>4</b>	0.051	408	1.28	6.6	2990	12.9	4.20	49	79	93
<b>5</b>	0.053	414	1.46	7.0	3230	14.7	3.33	70	95	112
<b>6</b>	0.031	425	1.46	5.7	3080	10.7	3.26	40	26	30
<b>7</b>	0.055	666	2.73	8.3	210	4.5	2.20	20 (35)	17	19
<b>8</b>	0.071	631	1.72	8.2	490	7.1	0.825	16 (23)	16	18
<b>9</b>	0.029	662	3.11	7.1	3	0.4	2.49	0.07 (12)	0.11	0.13
<b>10</b>	0.031	663	2.99	7.2	89	2.6	1.668	2.1 (5.5)	3.7	4.5
<b>11</b>	0.036	386	N.A.	7.0 <sup>#</sup>	1870	11.2	3.20	78 (86)	68	80
<b>12</b>	0.065	453	1.45	7.5	520	6.6	4.60	51 (64)	40	47
<b>13</b>	0.069	469	1.88	7.7	800	8.6	5.30	103 (140)	83	97
<b>14</b>	0.036	429	1.15	5.6	890	5.5	5.24	39 (51)	31	36

$\lambda_{em}$ ,  $r$ ,  $\tau_f$  and  $a$  are measured in benzene.

$\varepsilon$  and  $\sigma_2^{ex}$  are measured as described in the text.

\* Value in the parentheses is the full  $\sigma_2$  from figure 5.1 at the transition wavelength.

<sup>#</sup> In case of **11**, we were unable to measure the fluorescence lifetime. Due to a close structural similarity, we use the same  $a$  as obtained for **5**.

Table D.8. Cross sections, transition dipole moments and angle between them, and line shape function of **TBTAC**:  $\sigma_2^{\text{exp}}$  and  $\sigma_2^{\text{theor}}$  refer to experimental and theoretical 2PA cross sections in the peak of the  $g$ - $g$  transition recalculated to remove resonance enhancement as  $\sigma_2(\nu) \frac{(\nu_{01} - \nu)^2}{\nu^2}$

$\sigma_2^{\text{exp}}$ , GM	$\sigma_2^{\text{theor}}$ , GM	$ \vec{\mu}_{01} $ , D	$ \vec{\mu}_{12} $ , D	$g(2\bar{\nu})$ , cm	$\alpha$ , °
28±6	34±10	5.8±0.5	3.0±0.3	0.0020±0.0004	0±10

Table D.9. Properties of photochromic materials suggested for two-photon absorption storage. The columns present 2PA cross section  $\sigma_2$  (form A at laser wavelength  $\lambda_{\text{ex}}$ ), quantum efficiency of fluorescence  $\phi^B$  (form B), quantum efficiency of photo-transformation  $\phi_{A \rightarrow B}$ , molecular figure of merit,  $FOM = \sqrt{\sigma_2^A \sigma_2^B \phi^B \phi_{A \rightarrow B}}$ , and working temperature

Compound (form A)	$\sigma_2, \text{GM} (\lambda_{\text{ex}}, \text{nm})$	$\phi^B$	$\phi_{A \rightarrow B}$	$FOM, \text{GM}$	working T, K
Fulgides					
E-form	$2.7^a (780) [150]$	0.033 [197]	0.12 [197]	$\sim 0.2^e$	300
C-form	–	0 [197]	0.018 [197]	0	300
Spiropyrans					
Spiro-form	$10^2^a (694) [149]$	0.05 [42]	0.5 [149]	$\sim 16^e$	220
Diarylethenes					
Open ring	$23^b (820) [151]$		0.12 [151]		300
Open ring	$43^b (770) [151]$		0.12 [151]		300
Open ring	$44^b (770) [151]$		0.17 [151]		300
Open ring	$181^c (800) [152]$		0.37 [152]		300
Open ring	$85^d (520) [56]$	$<0.02 [56]$	0.33 [56]	$<9.2$	300
Closed ring	$150^d (680) [56]$	0.02 [56]	0.33 [56]	9.2	300
Pc <sub>3</sub> Nc					
H2-tautomer T <sub>2</sub>	$5.8 \times 10^3^a (783)$	$0.32^g$	0.014	680	$<150$
H2-tautomer T <sub>1</sub>	$1.8 \times 10^4^a (783)$	$0.32^f$	0.0025	290	$<150$

<sup>a</sup>Measured from the kinetics of 2PA-induced photochromic reaction.

<sup>b</sup>Measured with femtosecond z-scan technique with 80MHz rep. rate.

<sup>c</sup>Measured with femtosecond z-scan technique with 1kHz rep. rate.

<sup>d</sup>Measured with picosecond z-scan.

<sup>e</sup>Assuming  $\sigma_2^A = \sigma_2^B$ .

<sup>f</sup>Measured in dichloromethane relatively to tetra-t-butyl-phthalocyanine (metal free) in chloroform [198].

<sup>g</sup>Assumed to be equal to that of T<sub>1</sub>.

Table D.10. Parameters used in model simulations of SNR and SBR

Parameter	Model compound (figure 6.2)	Pc <sub>3</sub> Nc (figure 6.6)	Parameter	Model compound (figure 6.2)	Pc <sub>3</sub> Nc (figure 6.6)
$\sigma_1(\nu_{01}), \text{cm}^2$	$4 \times 10^{-16}$	$4.8 \times 10^{-16} \text{ }^a$	$I, \text{photons} \cdot \text{cm}^{-2} \cdot \text{s}^{-1}$	$3 \times 10^{29}$	$(8-10) \times 10^{29}$
$\sigma_2(\nu_{01}), \text{GM}$	$7 \times 10^4$	$2.6 \times 10^4 \text{ }^b$	$\nu_\nu, \text{cm}^{-1}$	400	experim <sup>d</sup>
$N_0$	$10^9$	$10^8 \text{ }^c$	$S$	0.6	experim <sup>d</sup>
$\phi^B$	0.5	0.32	$\Gamma, \text{cm}^{-1}$	100	experim <sup>d</sup>
$\phi_{A \rightarrow B}$	0.5	0.014	$\Delta, \text{cm}^{-1}$	400	experim <sup>d</sup>
$T, \text{K}$	300	77	$\nu_{01}, \text{cm}^{-1}$	13330	13330

<sup>a</sup>Measured in methylene chloride at 295 K.

<sup>b</sup>Measured by approximating the 2PA spectrum, presented in figure 6.3. with the Voigt function with fixed central frequency,  $\nu_{01} = 13330 \text{ cm}^{-1}$ .

<sup>c</sup>Obtained by multiplying the model voxel volume  $d_v d_h^2 = 27 \text{ } \mu\text{m}^3$  by working concentration  $C = 10^{-2} \text{ M}$ .

<sup>d</sup>See text for explanations.

Table D.11. 1PA and 2PA cross sections of the studied phthalocyanines in CH<sub>2</sub>Cl<sub>2</sub>

Compound		$\epsilon^*$ , M <sup>-1</sup> cm <sup>-1</sup>	$\lambda_{Qx}$ , nm	$\lambda_{Qy}$ , nm	$\sigma_2^{(2\lambda_{Qx})}$ , GM	$\sigma_2^{(2\lambda_{Qy})}$ , GM	$\sigma_2^{(950)}$ , GM
1		111000	758	709	-	-	139
	a	132000	757	713	0.34	2.7	90
	b	114000	756	714	0.22	1.9	86
2		120000	729	686	0.16	1.8	64
3	Endo	141000	742	712	0.40	1.0	63
	Exo	116000	744	714	0.15	0.46	97
	Mixture	140000	742	714	0.12	0.30	70
4	Endo	113000	727**	-	0.52	-	106
	Exo	181000	729**	-	0.89	-	118
5	Endo	152000	739	711	0.51	1.2	118
	Exo	119000	738	710	0.34	0.90	74
	Mixture	143000	738	710	0.21	0.57	65
6	a) Endo	116000	757	715	0.55	3.4	126
	a) Exo	95000	748	717	0.41	2.6	85
	b) Endo	75000	758	714	0.31	2.1	76
	b) Exo	101000	748	717	0.29	1.8	91

\*The value of extinction coefficient is given for the lowest energy transition peak.

\*\*Two peaks overlap with each other and are not distinguishable in carbon tetrachloride at room temperature. One can distinguish these peaks in PE film at 77K.

Table D.12. Quantum yields and temperature stability of the non-centrosymmetrical phthalocyanines

Compound	$\varphi^B$	$\Phi_{T1 \rightarrow T2}$	$\Phi_{T2 \rightarrow T1}$	$T_{1/2}$ , K	$\Delta T$ , K
1	0.32	0.0018*	0.0067*	115	16
	0.19	0.0010**	0.0056**	150 <sup>+</sup>	16 <sup>+</sup>
	0.24				
3	0.22	0.0064*	0.0094*	127	39
	0.14	0.0073**	0.0086**		
	0.17				
4	0.38	0.0026*	0.0020*	134	32
	0.29	0.0022**	0.0017**		
5	0.20	0.0084*	0.0107*	118	28
	0.16	0.0194**	0.0127**		
	0.32				
6	0.21	-	-	-	-
	0.20				
	0.18				
	0.20				

\* In PVB

\*\* In PE

<sup>+</sup> Deuterated sample

Table D.13. Comparison of the efficiency of the molecules as photochromes for 3D optical memory

	Molecule 1	Molecule 2*,**	Molecule 3	Molecule 4	Molecule 5	Molecule 6*
$\frac{\sigma_2}{\epsilon}$	0.048	0.011	0.037	0.012	0.046	0.010
$\sqrt{\sigma_2^2 \phi_F \phi_{A \rightarrow B}}$	12.2	12.0	12.8	13.1	29.4	11.1

\* Tautomerization quantum yield was assumed as the average of the values for molecules 1, 3, 4

\*\* Fluorescence quantum yield was assumed as the average of the values for molecules 1, 3-6.

Table D.14. Linear properties of Styryl-9M

Solvent	$\bar{\nu}_s, \text{cm}^{-1}$	$\tau, \text{ps}$	$r$	$\bar{\nu}_{01}, \text{cm}^{-1}$	$F(n, \varepsilon)$
chloroform	3269	760	0.038	15950	0.227
2-chlorobutane	3290	-	-	15910	0.343
dichloromethane	2930	-	-	15500	0.344
pentanal	4340	-	-	16770	0.374
isopropanol	4570	410	0.095	16940	0.439
ethylene glycol	4870	470	0.184	17350	0.453
acetone	5150	-	-	17510	0.458
ethanol	4730	570	0.102	17290	0.467
70%Eth+30%Water	5170	-	-	17690	0.484
50%Eth+50%Water	5260	-	-	17790	0.495
acetonitrile	5260	-	-	17780	0.496
methanol	3201	410	0.065	17570	0.498
30%Eth+70%Water	6110	-	-	18660	0.506



Table D.15. Composition of some of the biological phantoms

Sample number	ml Collagen type I (2mg/ml) <sup>1</sup>	μl fatty acid mixture (3M Linoleic acid, 1.5M Oleic)	μl Liposin® <sup>2</sup>	μl Styryl-9M Dye in DMSO (mg/ml)	μl Collagen setting solution <sup>3</sup>	cells added in 200 μl complete medium	ml serum and phenol red-free medium layered on top of the gel
1	3	1	-	10 (5)	600	5 × 10 <sup>5</sup> mouse embryo fibroblasts	1
2	4	-	-	25 (1)	800	-	-
3	4	1	-	25 (1)	800	-	-
4	4	-	5, 1*	25 (1)	800	-	-
5**	4	-	-	25 (0)	800	-	-
6**	4	-	1	25 (0)	800	-	-
7***	3	1	-	10(5)	600	-	-
8****	4	-	50	25 (1)	800	-	-
9****	4	-	50	50 (1)	800	-	-

<sup>1</sup>Rat tail collagen type I, isolated as described in Robertson, et al. Cancer Res., 49:1816-1823, 1989

<sup>2</sup>Intravenous fat emulsion from Abbott Laboratories; each ml contains 200mg soybean oil, 12mg egg phosphatides and 25mg glycerin

<sup>3</sup>Modified collagen setting solution consisting of 2 parts (by volume) 10X DMEM medium to 1 part 0.15N NaOH, 10mM HEPES and 1mg/ml bovine hemoglobin

\* Two samples with different amount of Liposin® shows identical results within ~5% error

\*\* Samples 5-6 are used as a dye-free sample

\*\*\* Sample 7 is the cell-free control for the sample 1

\*\*\*\* Samples 8-9 are not used in imaging experiments due to high absorption/scattering at all available wavelengths

APPENDIX E

DETAILS ON THE MODELING OF THE SIGNAL-TO-NOISE  
AND SIGNAL-TO-BACKGROUND RATIOS FOR  
VOLUMETRIC OPTICAL MEMORY

Estimation of Minimum Two-Photon Cross Section  
Required for Fast Access Volumetric Optical Memory

Suppose first that 2PA takes place only inside the focus voxel, and that the contribution from 1PA, either inside or outside of the focus is negligibly small. Then an average number of molecules that switch from A to B as a result of one write pulse of peak intensity  $I_w$  is,

$$N_w = \frac{1}{2} \sigma_2^A I_w^2 t_L \varphi_{A \rightarrow B} N_0, \quad (\text{E.1})$$

where index  $w$  stands for writing,  $\sigma_2^A$  is the molecular 2PA cross section at the writing frequency,  $\varphi_{A \rightarrow B}$  is the quantum efficiency of the photochemical transformation from A to B, and  $N_0$  is the number of molecules in the voxel. For the readout a pulse of intensity  $I_r$  is applied, where index  $r$  stands for readout. The average number of photon counts of fluorescence photons emitted by form B is:

$$n_r = \frac{1}{2} \sigma_2^B \varphi^B I_r^2 t_L \frac{(NA)^2}{2} \eta N_w, \quad (\text{E.2})$$

where  $\varphi^B$  and  $\sigma_2^B$  are, respectively, the form's B quantum efficiency of the fluorescence emission and 2PA cross section at the readout frequency,  $\eta$  is the quantum efficiency of the detector.

In the limit of detector shot-noise, the signal-to-noise ratio is:

$$SNR = \sqrt{n_r} = \frac{1}{2\sqrt{2}} I_w I_r NA t_L \sqrt{\eta N_0} \sqrt{\varphi_{A \rightarrow B} \varphi^B} \sigma_2, \quad (\text{E.3})$$

where  $\sigma_2 = \sqrt{\sigma_2^A \sigma_2^B}$  is the geometric mean 2PA cross section of forms A and B.

Signal-to-Background and Signal-to-Noise Ratios

We define the probability that a molecule is excited by one laser pulse via 1PA as:

$$P_{1PA}(\nu) = \int_{\text{spectrum}} I(\nu', \nu) \sigma_1(\nu') d\nu', \quad (\text{E.4})$$

and via 2PA as:

$$P_{2PA}(\nu) = \frac{1}{2} \sigma_2(\nu) \int_{\text{pulse}} I^2(t') dt', \quad (\text{E.5})$$

where  $\sigma_1(\nu)$  and  $\sigma_2(\nu)$  are the one- and two-photon absorption cross sections,  $I(t)$  and  $I(\nu)$  are, respectively, the temporal- and spectral intensity of the laser pulse. Here and further on in this section, we consider the 2PA spectral width much larger than that of the laser. The overall probability that the molecule is excited by one pulse may be then expressed as:

$$P = P_{1PA} + P_{2PA}. \quad (\text{E.6})$$

Expressions (E.4) and (E.5) account for the actual spectral shapes of 1PA and 2PA and also for the temporal- and spectral profile of the pulse. In the following, we will assume that the pulse has a bandwidth-limited temporal Gaussian profile with  $FWHM = 100$  fs.

Under certain circumstances, the absorption may approach saturation. We account for the saturation by imposing the following additional condition: if  $P$ , calculated according to (E.4)–(E.6) is larger than 1, then instead of  $P_1$  and  $P_2$  we use  $P'_{1PA} = P_{1PA}/P$  and  $P'_{2PA} = P_{2PA}/P$ .

Suppose that the writing laser is focused to the  $i^{\text{th}}$  layer of the  $M$ -layer disk, at the depth  $D = (h_v + d_v)i$ . Also for simplicity assume that horizontal safeguard distance between the neighboring data tracks is zero,  $h_h = 0$ , such that voxels are placed immediately next to each other. Then the surface density within one layer is,  $R = (d_h)^{-2}$ . The number of writing pulses applied to address half of the voxels (which is approximately equal to the number of unit bits) within one layer is,

$$K_w = \frac{1}{2}SR, \quad (\text{E.7})$$

where  $S$  is the disk area. The focused laser beam has the shape of a double cone, with the waist located at the focus layer. Consider the effect of 1PA occurring in the cone. Some of the molecules, positioned in the illuminated layers above or below the focus, will be switched via 1PA. Even though each writing pulse may switch only a small number of out-of-focus molecules, because it takes a large number of pulses to write the whole disk, the total accumulated effect may be considerable. The average number of molecules that are switched in this way in an arbitrary voxel within the  $j^{\text{th}}$  out-of-focus layer is,

$$N_B^j = \sum_{i=1}^M K_w N_0 \varphi_{A \rightarrow B} \frac{S^{ij}}{S} P_{1PA}^{ij}, \quad (\text{E.8})$$

where  $S^{ij}$  and  $P_{1PA}^{ij}$  are, respectively, the beam cross-sectional area and the 1PA absorption probability in the  $j^{\text{th}}$  layer when the actual focus is in  $i^{\text{th}}$  layer, index  $B$  stands for background. Since 1PA is a linear function of the intensity, we can replace  $S^{ij} P_{1PA}^{ij}$  with  $P_{1PA}^w R^{-1}$  in the sum of (E.8), where  $P_{1PA}^w$  is the 1PA probability in the writing beam

waist. Therefore, the number  $N_B$  of unintentionally switched molecules in each voxel does not depend on the layer number. Taking this into account and substituting expression (E.7) into (E.8), we get

$$N_B = \frac{1}{2} M N_0 \varphi_{A \rightarrow B} P_{1PA}^w. \quad (E.9)$$

Now, the number of intentionally switched via 2PA molecules in the focus voxel is,

$$N_w = N_0 \varphi_{A \rightarrow B} P_{2PA}^w, \quad (E.10)$$

where  $P_{2PA}^w$  is the probability of 2PA in the focus.

During the readout the 2PA-induced fluorescence will be detected from the focus voxel independent of the way how the molecules were switched. We define SBR as the ratio between the fluorescence photon counts from the intentionally and unintentionally switched molecules:

$$SBR = \frac{N_w}{N_B} = \frac{2}{M} \frac{P_{2PA}^w}{P_{1PA}^w}. \quad (E.11)$$

This expression shows that, for a given value of SBR, to write more layers we need correspondingly larger ratio of probabilities of 2PA and 1PA, which can be achieved by increasing the peak power density  $I_w$  and/or by increasing the 2PA versus 1PA cross sections.

In the case of shot-noise only, the SNR, which is determined both by 2PA writing and 2PA-induced fluorescence readout processes, can be expressed as follows:

$$SNR = \sqrt{P_{2PA}^w P_{2PA}^r N_0 \varphi^B \varphi_{A \rightarrow B} \frac{(NA)^2}{2} \eta}, \quad (E.12)$$

where  $P_{2PA}^r$  is the probability of 2PA in the focus voxel upon readout. For simplicity, we assume here that the same wavelength is used for both writing and reading. In order to avoid data erasure during the readout, one needs to have a system where the backward reaction  $B \rightarrow A$  is much less efficient than the forward reaction. Some non-symmetrical tetrapyrroles do possess this feature. In our numerical simulations, presented in the chapter 6, we therefore consider the case of vanishing small efficiency of the backward reaction and set  $I_r = I_w$  for simplicity. In more general case of comparable quantum efficiencies, one would need to reduce the readout intensity.

Modeling of One- and Two-Photon Absorption  
Spectral Properties of Organic Molecules  
for Volumetric Optical Memory

At room temperature, 1PA in the frequency region  $500\text{--}3000\text{ cm}^{-1}$  below the lowest  $S_0 \rightarrow S_1$  electronic transition, is mostly due to transitions from thermally-excited vibrational levels of the electronic ground state. These so-called hot-band transitions are responsible for temperature-dependent low-frequency tail observed in the absorption spectrum of some solid impurity systems [199, 200]. In the first approximation, the cross sections of the hot-band absorption drops off exponentially with increasing frequency detuning from the band center [200]:

$$\sigma_1(\nu) = \sigma_1^{\max} \exp \left[ -(1 + \tilde{\beta}) \frac{h(\nu_{01} - \nu)}{kT} \right], \quad (\text{E.13})$$

where  $\sigma_1^{\max}$  is the maximum one-photon cross section at the peak of the band,  $\nu = \nu_{01}$ ,  $T$  is the temperature, and  $k$  is the Boltzmann factor. Parameter  $\tilde{\beta}$  is a function of molecular

normal vibration frequencies and Huang-Rhys factors and varies only slightly with frequency [200]. In a single vibrational mode approximation,

$$\tilde{\beta} = \frac{kT}{h\nu_v} \ln \left[ \frac{\nu_{01} - \nu}{\nu_v S e(1 - \exp(-h\nu_v / kT))} \right], \quad (\text{E.14})$$

where  $\nu_v$  is an effective vibrational frequency,  $S$  is an effective Huang-Rhys factor of this mode, and  $e$  is the base of natural logarithm.

The particular property of the hot-band absorption is that it vanishes in the low temperature limit,  $kT \ll h\nu_v$ . The vibrational spectrum of organic chromophores extends typically to about  $\nu_v \sim 2500 \text{ cm}^{-1}$ . At  $T < 100 \text{ K}$ , the probability of population of vibrational levels with frequencies above  $\nu_v > 500 \text{ cm}^{-1}$  is less than  $P \leq e^{-7.5}$ . Hot-band absorption cross sections are also smaller in the systems where the vibrations are only weakly coupled to the electronic transition.

Direct detection of the long-wavelength absorption tail in organic chromophores in solution is complicated by very low optical density and also by competing scattering and reflection losses. For this reason we have chosen to simulate the hot-band absorption by considering instead the measured fluorescence emission spectrum weighted with appropriate Boltzmann factor. Fluorescence signal is not obscured by scattering, it is background-free and also allows for better revealing of peculiar vibronic features. The modeling of the hot-band absorption based on the fluorescence spectrum is possible due to the mirror symmetry rule: in organic chromophores it is typical that the fluorescence spectrum represents a mirror image of the  $S_0 \rightarrow S_1$  absorption spectrum, because the



distribution of vibronic levels in the ground- and the first excited electronic states is usually the same.

In phthalocyanines in general and in  $\text{Pc}_3\text{Nc}$  in particular, the Stokes shift between  $S_0 \rightarrow S_1$  (Q(0-0)) transitions in absorption and fluorescence is very small. Most important, if the basic model [201] is involved, then we can assume that the Franck-Condon factors in the absorption and emission are the same. Therefore, the normalized absorption cross sections may be presented as:

$$\frac{\sigma_1(\nu)}{\sigma_1^{\max}} = F(\nu) \exp\left(-\frac{h(\nu_{1PA} - \nu)}{kT}\right), \quad (\text{E.15})$$

where  $F(\nu)$  is the normalized fluorescence spectrum.

Figure E.1 shows the normalized 1PA spectrum of  $\text{Pc}_3\text{Nc}$  in methylene chloride at 300 K measured (black bold solid line) and calculated based on the expression (E.13) (blue dashed line) and based on the expression (E.15) (color dash-dotted lines) at the temperatures  $T = 300, 200, 120$ , and  $77$  K. Figure E.1 presents also the fluorescence spectrum of  $\text{Pc}_3\text{Nc}$  in polyethylene film at 77K (green line). The absorption decreases rapidly with the detuning from the band maximum, and at  $\nu_{01} - \nu > 2000 \text{ cm}^{-1}$  it already falls by more than 4 orders of magnitude. Expression (E.13) provides a reasonably good fit to the room temperature data with  $\nu_v = 320 \text{ cm}^{-1}$  and  $S = 1.0$  (dash-dotted line).

Expression (2.8) describing 2PA spectrum was derived with the assumption that the line width of the intermediate state  $I$  is dominated by homogeneous broadening. The homogeneous line width decreases at low temperature [199], and inhomogeneous

broadening becomes more important. If we take Gaussian inhomogeneous broadening line width into account, then the 2PA cross section spectrum may be expressed as:

$$\sigma_2(\nu) = \sigma_2(\nu_{01}) \left( \frac{\nu}{\nu_{01}} \right)^2 \frac{H(a, \nu)}{H(a, 0)} \frac{g_{2PA}(2\nu)}{g_{2PA}(2\nu_{01})}, \quad (\text{E.16})$$

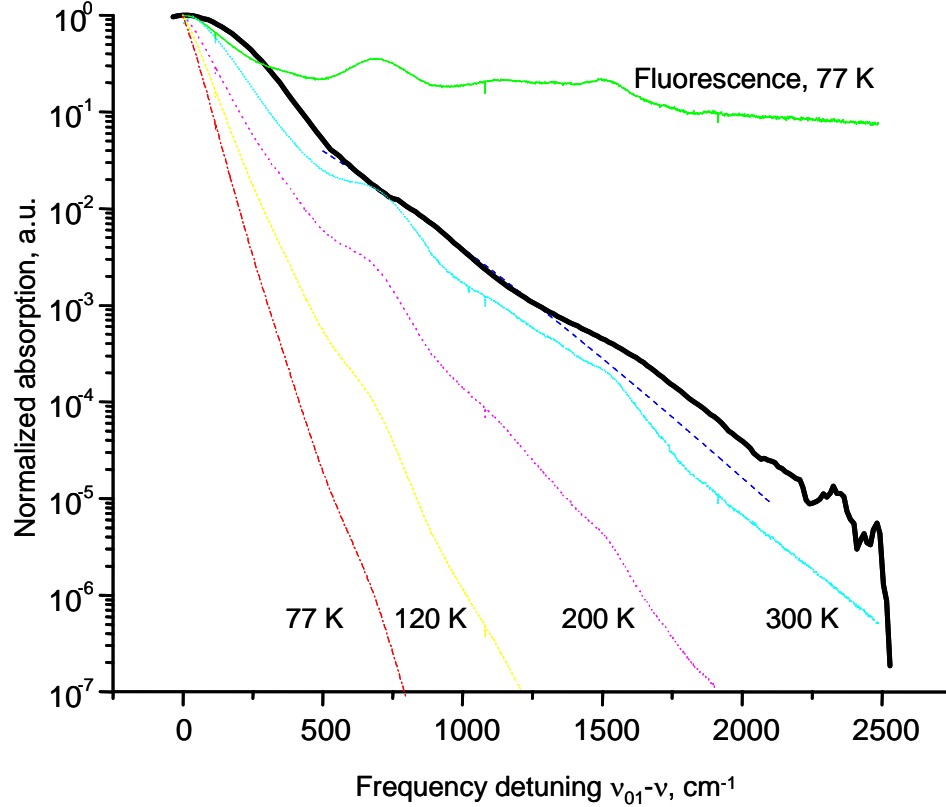


Figure E.1. Long-wavelength absorption of Pc<sub>3</sub>Nc in semi-logarithmic scale. Absorption spectrum in methylene chloride at room temperature is shown by bold solid black line and its best fit to expression (E.13) by dashed blue line. Green line shows normalized and corrected fluorescence spectrum, measured at 77 K. Dash-dotted color lines show fluorescence spectra weighted with Boltzmann factor, according to (E.15) at different temperatures

where

$$H(a, u) = \frac{a}{\pi} \int_{-\infty}^{\infty} \frac{e^{-y^2} dy}{a^2 + (u - y)^2} \quad (\text{E.17})$$

is the Voigt function [202],  $a = \sqrt{\ln 2} \Gamma / \Delta$  is the Voigt parameter,  $u = (\nu - \nu_{01}) \sqrt{\ln 2} / \Delta$  is the frequency in the units of inhomogeneous width,  $\Delta$  (HWHM). For simplicity, we assume that the maximum value  $\sigma_2(\nu_{01})$  corresponds to  $\nu = 2\nu_{01}$ .

The line shape function,  $g_{2PA}(2\nu)$ , depends on the density and energy distribution of 2PA-allowed states, and above certain transition frequency may become rather broad. This behavior has been observed for a number of tetrapyrroles, including phthalocyanines [203-206]. In our spectral region of interest we may assume that  $g_{2PA}(2\nu) \equiv \text{const}$ , and we finally obtain,

$$\sigma_2(\nu) = \sigma_2(\nu_{01}) \left( \frac{\nu}{\nu_{01}} \right)^2 \frac{H(a, \nu)}{H(a, 0)}. \quad (\text{E.18})$$

### Two-Photon-Induced Photo-Tautomerization of Pc<sub>3</sub>Nc

Figure E.2 shows 2PA-induced switching of Pc<sub>3</sub>Nc at 77K. Initially, the molecules are present as form T<sub>1</sub>. The lowest frequency band corresponds to S<sub>0</sub>→S<sub>1</sub> pure electronic Q<sub>x</sub>(0-0) transition. Such strongly-allowed absorption band in near-infrared range of the wavelengths is characteristic for phthalocyanines [207]. In polyethylene host, tautomer T<sub>1</sub> has this transition at 13330 cm<sup>-1</sup> (750 nm). In tautomer T<sub>2</sub>, this transition is shifted to 13700 cm<sup>-1</sup> (730 nm), and it overlaps in part with the next, Q<sub>y</sub>(0-0) electronic band.

For 2PA-induced switching we use a regenerative Ti:Sapphire amplifier (CPA-1000 Clark MXR) operating at 1 kHz repetition rate and pulse duration 200 fs. The width of the Q<sub>x</sub>(0-0) band is less than 300 cm<sup>-1</sup>, which allows us to use very close-to-resonance excitation at 783 nm. The peak intensity at the sample was  $\sim 4-8 \times 10^{27}$  photons·cm<sup>-2</sup>·s<sup>-1</sup>,

and the beam diameter was  $\sim 1$  cm. Upon illumination, the absorption of  $T_1$  decreases (see transformation of the peak at  $13330\text{ cm}^{-1}$  from the black curve to blue curve, shown by arrow down), while the absorption of  $T_2$  increases (shown by arrow up).

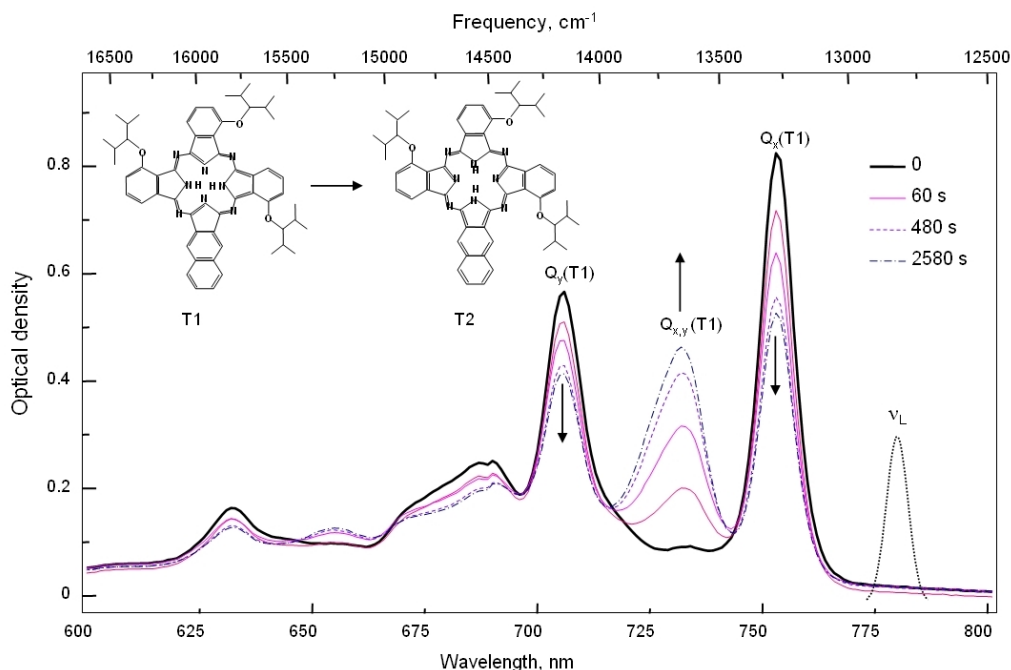


Figure E.2. Spectral changes observed upon 2PA-induced transformation of tautomer form  $T_1$  into form  $T_2$  in  $Pc_3Nc$  in polyethylene film at 77K. The sample was irradiated with 783-nm femtosecond laser pulses of constant intensity and different exposure times. Laser spectrum is indicated with dotted line. Laser intensity was  $4 \times 10^{27}$  photons $\cdot$ s $^{-1}$  $\cdot$ cm $^{-2}$ . Vertical arrows show the spectral changes during irradiation. Insert shows the structure of the two tautomers

Figure E.3 presents the kinetics of the absorption of  $T_2$  at two different intensities,  $I_1 = 4 \times 10^{27}$  and  $I_1 = 8 \times 10^{27}$  photons $\cdot$ cm $^{-2}$  $\cdot$ s $^{-1}$ . Fitting of experimental data with exponential function yields the transformation rate constants  $k = 1.8 \times 10^{-3}$  s $^{-1}$  and  $k = 7.3 \times 10^{-3}$  s $^{-1}$ , which demonstrates that the reaction rate increases four-fold when the intensity increases by a factor of two. This quadratic correspondence of the four-fold

difference in kinetics to the two-fold difference in the laser intensities confirms that the excitation process is indeed due to the intrinsic 2PA and not due to e.g. residual 1PA.

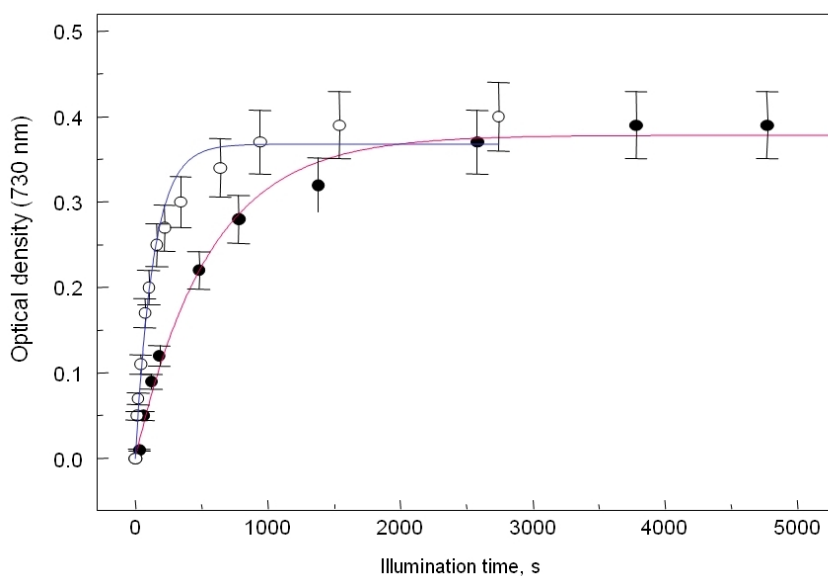


Figure E.3. Kinetics of 2PA-induced  $T_1 \rightarrow T_2$  phototransformation at two different laser intensities. Filled circles correspond to peak intensity of  $4 \times 10^{27}$  photons.s<sup>-1</sup>.cm<sup>-2</sup> and open circles – to  $8 \times 10^{27}$  photons.s<sup>-1</sup>.cm<sup>-2</sup>. The continuous lines represent the best fits with exponential function

APPENDIX F

SPECTROSCOPIC CHARACTERIZATION OF STYRYL-9M

### One- and Two-Photon Spectroscopy of Styryl-9M

Figure F.1 (see also figure C.18) shows absolute 2PA spectrum of Styryl-9M dissolved in chloroform (symbols, left vertical axis) [165]. The graph also shows the 1PA extinction coefficients (solid line, right vertical axis), and the fluorescence spectrum (relative units, dashed line). The bottom x-axis represents the 1PA or transition wavelength, which is equal to one half of the excitation laser wavelength. The top x-axis represents the transition wavelength in frequency units ( $\text{cm}^{-1}$ ).

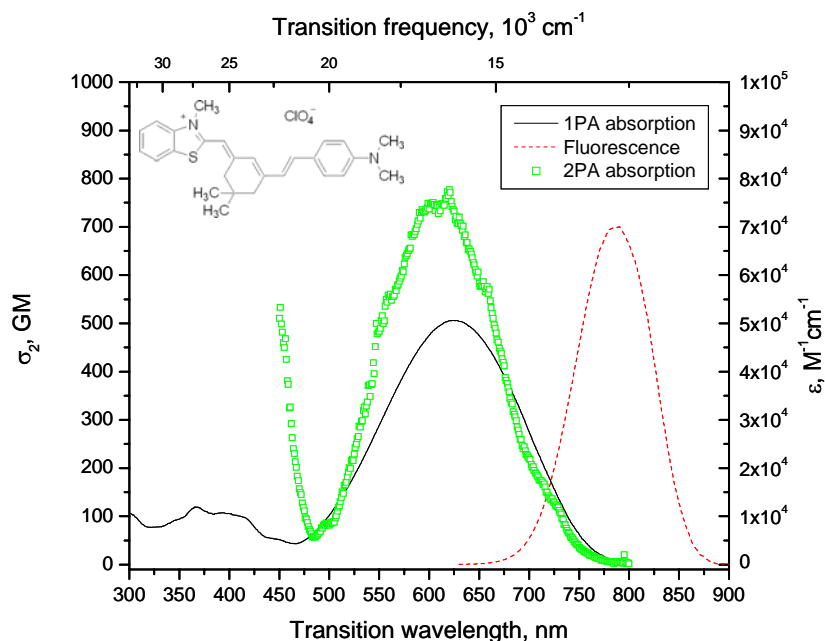


Figure F.1. Two-photon absorption (symbols), one-photon absorption (solid line), and fluorescence (dashed line) of Styryl-9M in chloroform

The lowest-energy 1PA absorption consists of a very broad peak ( $\lambda_{1PA} \approx 470 - 770$  nm) with the maximum at  $\lambda = 625$  nm. The 1PA and 2PA peaks overlap, almost within the

accuracy of the measurement. Although the spectral bands closely overlap within the lowest energy transition, the small ( $\sim 100 \text{ cm}^{-1}$ ) shift is present between the 1PA and 2PA peaks. The shift can be due to redistribution of the permanent dipole moment difference within the absorption band due to possibly strong charge transfer. The width of the peaks in both 1PA and 2PA is about  $4500 \text{ cm}^{-1}$  and both line shapes are closer to Gaussian. The fluorescence occurs at  $\lambda \approx 790 \text{ nm}$ , and the width of the fluorescence peak is about  $1570 \text{ cm}^{-1}$ . Since the fluorescence occurs in the same spectral region as the 1PA peak, we suppose that the whole or the part of the observed 1PA peak represents the  $S_0 \rightarrow S_1$  transition, similarly to the molecules in group (i), chapter 4. A significant difference between the 1PA and 2PA spectra is observed only at shorter wavelengths,  $\lambda < 480 \text{ nm}$ , where the 2PA cross sections increase sharply, whereas the 1PA shows only some weak structure. The increase of 2PA may be attributed to resonance enhancement effect, as the laser excitation wavelength comes closer to the  $S_0 \rightarrow S_1$  transition. It also could be due to a higher energy transition, which is not accessible for our 2PA measurements due to competing 1PA. The maximum 2PA cross sections in both sections of the spectrum are rather high,  $\sigma_2(900\text{nm}) \approx 550 \text{ GM}$ , and  $\sigma_2(1200\text{nm}) \approx 750 \text{ GM}$ , which is significantly higher, compared to most other commercial laser dyes (see chapter 4) [165]. The 2PA spectrum shows a distinct minimum at  $\lambda_{2PA} \approx 960 \text{ nm}$  with  $\sigma_2 \approx 50 \text{ GM}$ .

In chapter 5, we showed that if the 1PA and 2PA of the lowest energy  $S_0 \rightarrow S_1$  transition overlap, then the maximum 2PA cross section can be described in terms of a two-level model [85]. In this case, the maximum 2PA cross section in the  $S_0 \rightarrow S_1$



transition peak can be calculated from the 1PA parameters using expression (2.6). The linear shape of Styryl-9M suggests that the angle  $\beta$  is close to  $0^\circ$ .

Figure F.2 shows the solvatochromic shifts of Styryl-9M measured in a series of solvents versus a polarity function, which are in agreement with the values measured previously [169]. As shown in Ref. [208], generalized polarity function should be used to establish correlation between the solvatochromic shifts and the permanent dipole moment difference for charged ionic molecules:

$$F(n, \varepsilon) = \frac{1}{\varepsilon_i} \left( \frac{\varepsilon_i - n^2}{\varepsilon_i + 2n^2} - \frac{\varepsilon_i - \varepsilon}{\varepsilon_i + 2\varepsilon} \right), \quad (\text{F.1})$$

where  $\varepsilon_i = 2$  is the intramolecular dielectric constant, and  $\varepsilon$  is the dielectric constant of the solvent. The choice of the intramolecular dielectric constant implies that the negatively charged moiety of the dye does not contribute to the solvatochromism.

Table D.14 summarizes the measured fluorescence anisotropy and lifetimes in ethanol, methanol and chloroform solutions, which are then used to find the effective radius of Styryl-9M from expression (B.4),  $a = 5.1 \pm 0.5$  Å.

From the expression (B.3) and data, presented in table D.14 and on figure F.2, we estimate,  $|\Delta\vec{\mu}_{01}| = 24.5 \pm 2.5$  D. If we use this value to calculate peak 2PA cross section of Styryl-9M in chloroform according to expression (2.6), then we get  $\sigma_2 = 600 \pm 180$  GM, which agrees well with the experimentally measured value  $\sigma_2 = 740 \pm 150$  GM. We conclude that the 2PA can be well described by the two-level model.

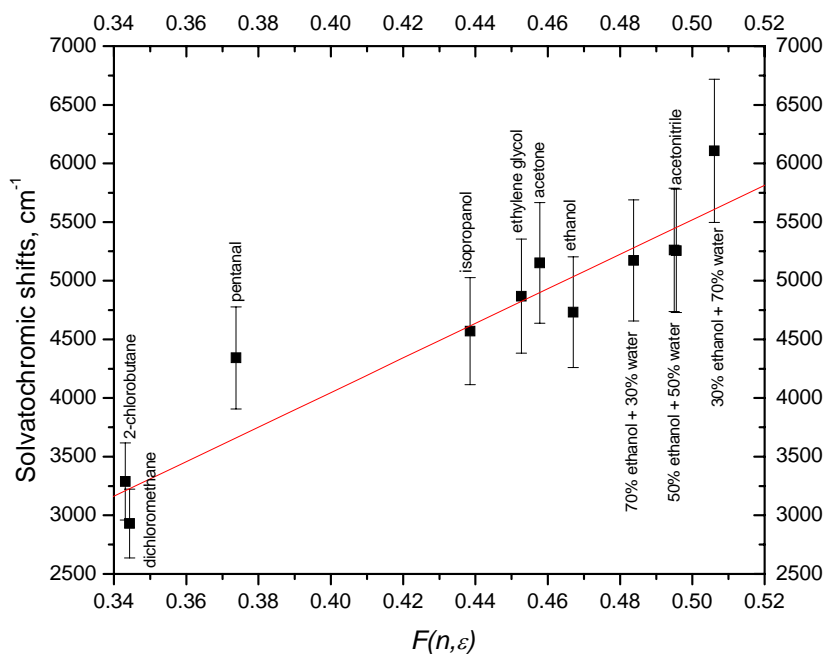


Figure F.2. Solvatochromic shifts of Styryl-9M in a series of solvents

### pH sensitivity of the Absorption and Fluorescence of Styryl-9M

One can note that the position of the 1PA maximum ( $\bar{\nu}_{01}$  in table D.14) changes significantly with the solvent. The  $\sim 2.2$  fold change in the polarity function for the most polar and the least polar solvents used in our measurements corresponds to the change in solvatochromic shifts  $\sim 2850 \text{ cm}^{-1}$ .

Similar changes are observed by changing pH of the solution. Figure F.3 shows the absorption spectrum of Styryl-9M as a function of pH of DI water. With the increase of pH-level, the  $S_0 \rightarrow S_1$  absorption (450–650 nm) shows a strong decrease of the intensity, and simultaneously absorption in a blue peak (350–450 nm) increases in intensity. The sensitivity is quite remarkable: the ratio of the peak red/blue optical density varies from

6.8 to 0.04 with the change of pH from 8.0 to 10.4, which gives 170 fold difference between pH8.0 and pH10.4.

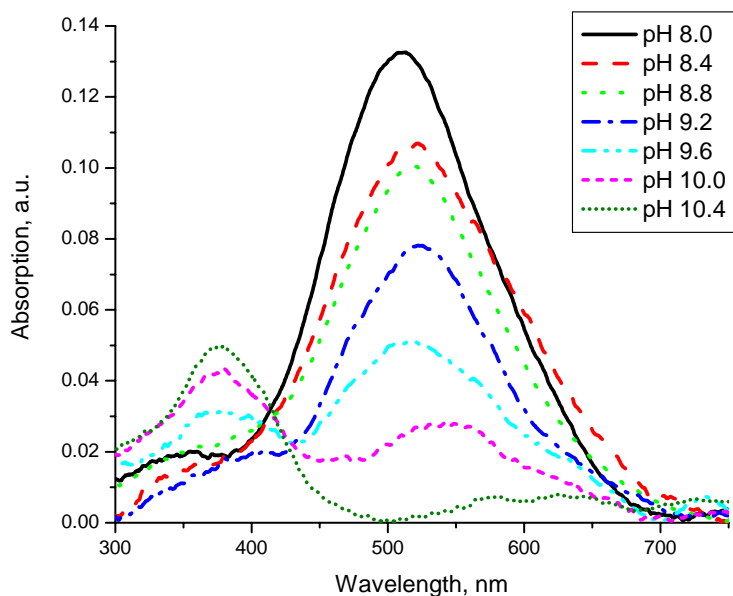


Figure F.3. Dependence of the absorption of Styryl-9M on the pH-level of the solvent

Figure F.4 shows the fluorescence spectrum of Styryl-9M as a function of pH of DI water. The fluorescence, excited at 395 nm, shows also two peaks, at 650 nm and 795 nm, where the relative intensity depends strongly on the pH.

Fluorescence variations with the pH-level are easier to detect in biological applications. Figure F.5 shows the dependence of the intensity ratio of the two fluorescence peaks on the pH-level of the DI water. The dependence can be well fitted by a third order polynomial. The change of pH from 8.0 to 10.4 changes the fluorescence intensity ratio by factor of 50.

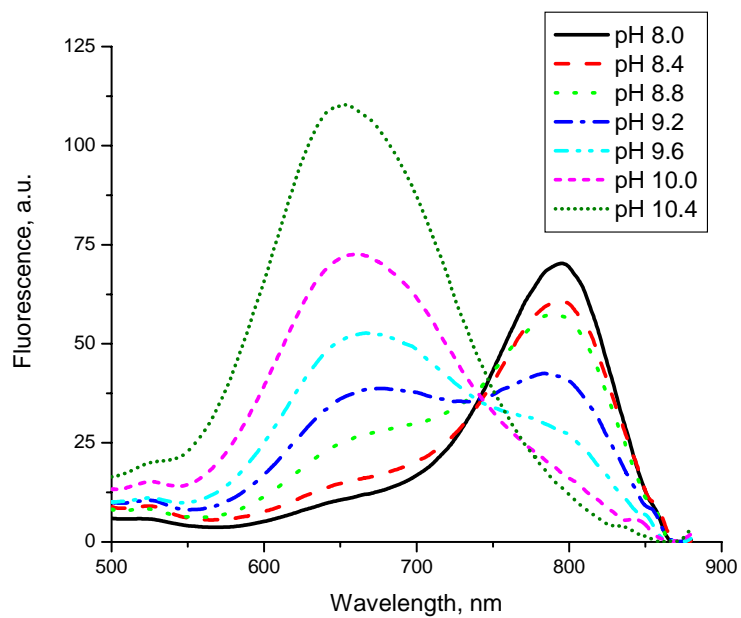


Figure F.4. Dependence of the fluorescence of Styryl-9M on the pH-level of the solvent

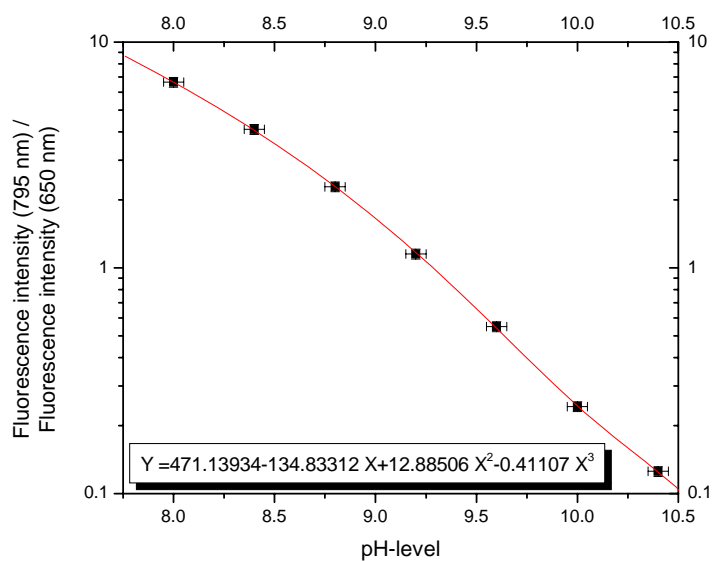


Figure F.5. Dependence of the ratio of the intensity of the fluorescence peaks of Styryl-9M on pH of DI water

Even though this is less than the corresponding changes of the absorption, this variation is still larger than that reported for other pH sensors [209, 210]. For example, biological pH sensor reported in Ref. [209] shows intensity ratio change from  $\sim 0.65$  to  $\sim 1.05$  with the change of pH from 3.0 to 8.0. Unfortunately this change occurs at high pH values,  $\text{pH} > 8.0$ , which is out of typical range of interest for biological studies.

### Two-Photon Sensitivity of Styryl-9M on the Solvent Polarity

Figure F.6 shows changes in the 2PA spectra (symbols) and 1PA spectra (lines) of the dye in a series of solvents with different polarity. The 2PA spectra and cross sections are measured relative to Styryl-9M in chloroform according to the procedure described in appendix C.

The general shape of 1PA and 2PA spectra is the same as in chloroform and the changes that occur do not compare to the large variations due to pH in water. Nevertheless, the relative strengths of the blue and the red peaks in the 1PA spectra vary several times with the change of the solvent. The position of the red peak shifts from 2-chlorobutane to acetonitrile  $\sim 75$  nm. The wavelength of the 2PA maximum and minimum, and the maximum 2PA cross section also vary depending on the solvent polarity. We may use the fact that both the position and the value of the 2PA minimum are sensitive to the solvent polarity, to calculate the ratio between 2PA cross sections on both sides of the minimum and use this value to distinguish between different solvents. Below, we use this approach for efficient local polarity determination using 2PA-excitation.

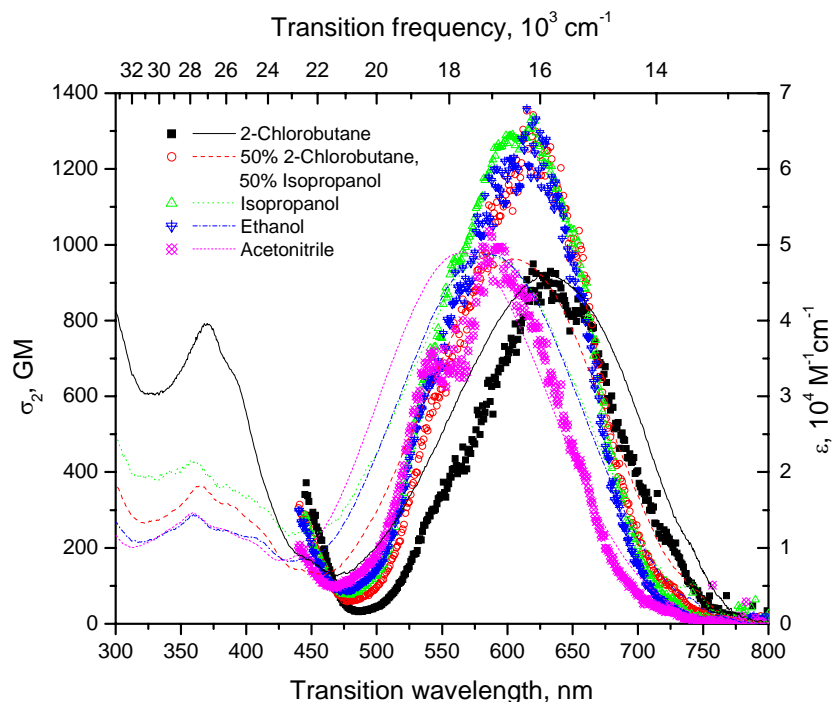


Figure F.6. Two-photon absorption (symbols), and one-photon absorption (lines) of Styryl-9M in a series of solvents with different polarity

It is interesting to note that the fluorescence spectrum is almost unaffected by the solvent polarity. The shift of the fluorescence with the solvent polarity is proportional to the permanent dipole moment in the first excited state. Therefore, such behavior of the fluorescence implies that the permanent dipole moment in the first excited state is approximately zero. This also implies that the large permanent dipole moment difference is predominantly due to large permanent dipole moment in the ground state.

One-Photon Detection of the  
Solvent Polarity Using Styryl-9M

As a proof of concept we apply imaging technique described in chapter 7 to check how the absorption of Styryl-9M changes depending on the solvent polarity under 1PA and 2PA excitation, as well as an ability to distinguish between several types of biological phantoms and cells.

In order to determine the position of the 1PA maximum, we collect CCD images of the fluorescence, excited in the sample at 8 different wavelengths in the interval, 550–725 nm, with 25 nm steps. The VariSpec filter is set at 785 nm to transmit the fluorescence and reject the scattered laser light. The intensity of the images is integrated and normalized by dividing by the average power of the excitation beam. Figure F.7a shows images of the fluorescence of the dye excited in a series of solvents (2-chlorobutane, isopropanol, acetone, and acetonitrile) and mixtures of solvents (50% 2-chlorobutane + 50% isopropanol, and 70% ethanol + 30% DI water). A distinct shift of the absorption maximum to the blue with the increase of the solvent polarity is clearly visible.

To better quantify this dependence and to determine the peak absorption wavelength we fit the integrated fluorescence for each solvent as a function of the excitation wavelength with a Gaussian. In figure F.7b the peak absorption wavelength is plotted versus solvent polarity. Two “unknown” samples are studied blind based on the best linear fit: mixture of 50% 2-chlorobutane + 50% isopropanol (**1**) and mixture of 40% ethanol + 60% DI water (**2**). The determined polarity function is 0.386 for (**1**) and 0.497 for (**2**) which is less than 2% off the “true” values.

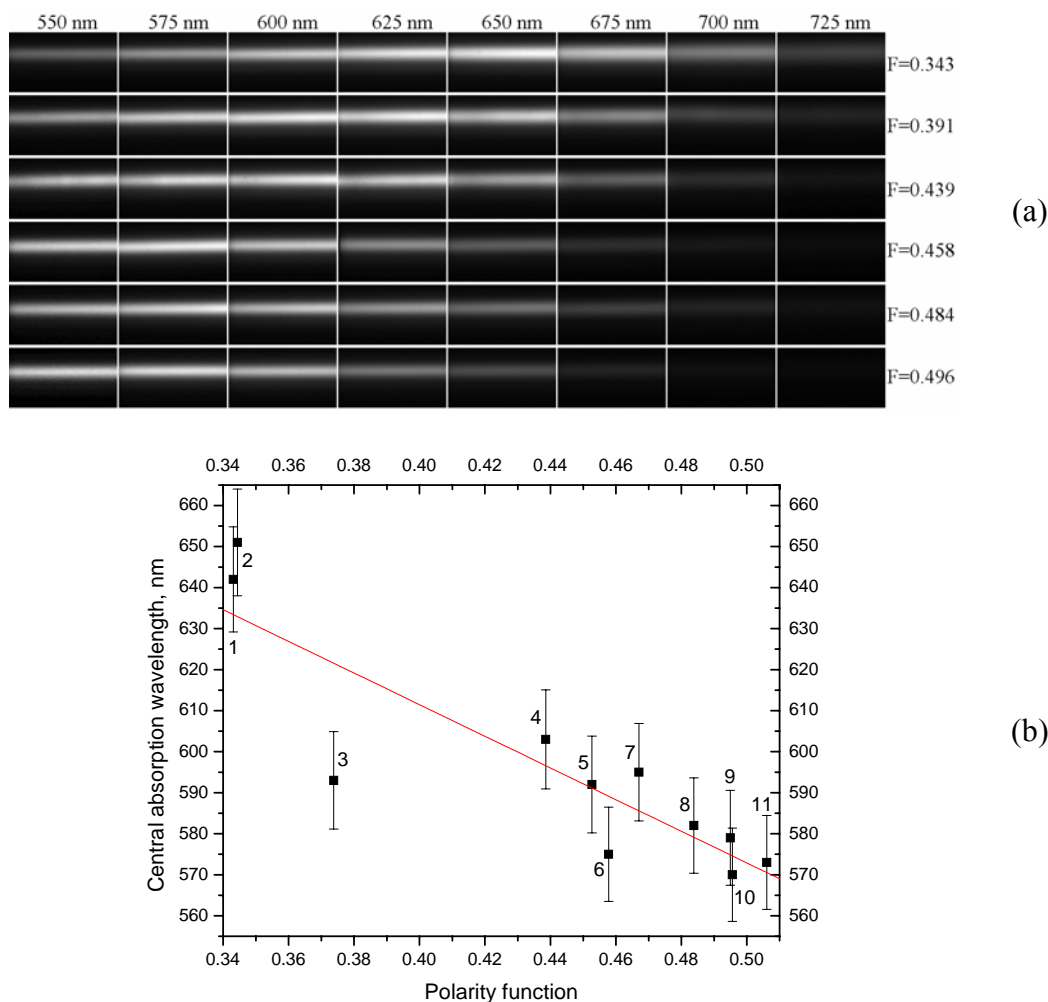


Figure F.7. (a) 1PA-induced fluorescence of Styryl-9M excited at several visible wavelengths in a set of solvents with different polarity (b) Position of the absorption maximum of Styryl-9M versus solvent polarity function. Linear fit is shown. The solvents used are: 1 – 2-chlorobutane; 2 – dichloromethane; 3 – pentanal; 4 – isopropanol; 5 – ethylene glycol; 6 – acetone; 7 – ethanol; 8 – mixture of 70% ethanol + 30% DI water; 9 – mixture of 50% ethanol + 50% DI water; 10 – acetonitrile; 11 – mixture of 30% ethanol + 70% DI water

### Sensing of the Solvent Polarity by Imaging Two-Photon-Excited Fluorescence

As shown on figure F.8, the position and the cross section of the minimum of the 2PA spectrum of Styryl-9M is sensitive to the solvent polarity. As shown above, the ratio



of the 2PA cross sections taken on both sides of the minimum can be used as a sensitive way of determining solvent polarity. Based on this observation, we propose a new method of sensing the local environment in solutions and biological systems using 2PA excitation of Styryl-9M. As a proof of principle we carry out experiments with the dye in solution. We excite the fluorescence of Styryl-9M using two wavelengths, located on the both sides of the minimum of the 2PA spectrum, 900 nm and 1000 nm, and determine the ratio of the integrated fluorescence intensities measured at these two wavelengths.

Figure F.8a shows the 2PA-excited fluorescence in a series of solvents (2-chlorobutane, isopropanol, ethanol, and acetonitrile) and mixture of solvents (50% 2-chlorobutane + 50% isopropanol). The fluorescence intensity is normalized by the squared average power of the excitation beam. The VariSpec transmission is set at 785 nm. The change of fluorescence ratio at 900 nm and 1000 nm with the change of the solvent polarity is clearly visible. Figure F.8b shows that the change in the fluorescence intensity ratio versus solvent polarity function is well described by exponential function,  $F(900)/F(1000) = 0.2 + 1520e^{-0.06F(D,n)}$ .

The experiment shows the advantage of 2PA excitation as compared to the 1PA excitation: In case of 2PA we need only two distinct excitation wavelengths, and the fluorescence can be measured at one fixed wavelength. In addition, in contrast with the linear dependence upon 1PA excitation, the polarity dependence of 2PA detection is exponential, which further increases sensitivity of the 2PA excitation. For example, the difference between the observed 2PA-excited intensity ratio (figure F.8b) for the most polar and the least polar solvents is about 9 fold, while the same difference for the

absorption peak position, determined based on 1PA-excitation (figure F.7b) is only 15% or less. Longer wavelengths used in the 2PA excitation also offer less scattering, which is important for imaging of the tissues described in the next sections.

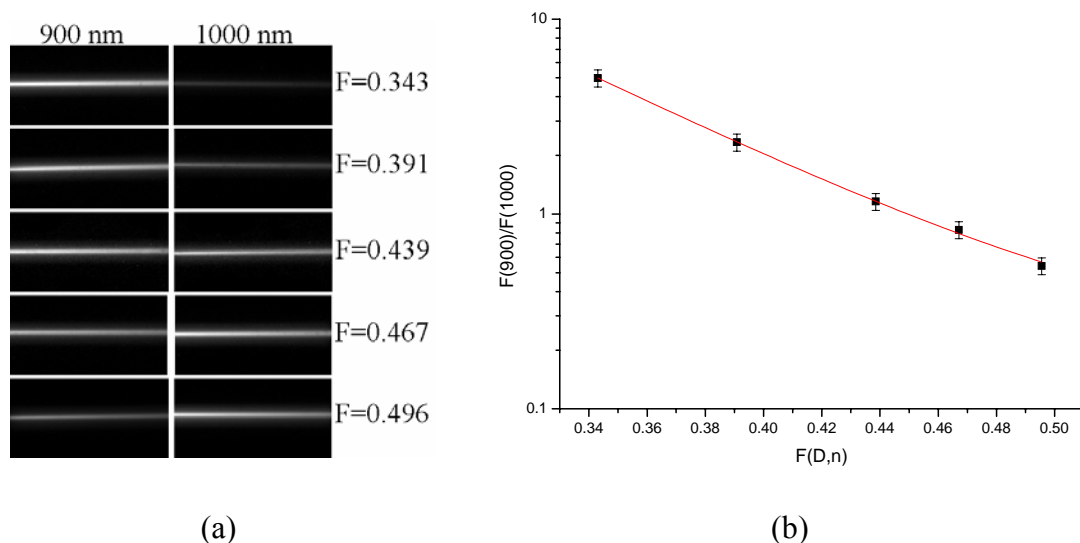


Figure F.8. (a) 2PA-induced fluorescence of Styryl-9M excited at two infrared wavelengths in a set of solvents with different polarity. (b) Ratio of the fluorescence intensity of Styryl-9M excited via 2PA at 900 nm and 1000 nm as a function of solvent polarity function

### Phantom Preparation

Our next experiments are made using collagen-based biological tissue phantoms. Here we explain how the phantoms are made.

Collagen type I was isolated from rat tail tendons as described in Ref. [211], and was used at a concentration of 1 mg/ml. To set up the phantoms, 0.3 ml of setting solution was quickly mixed with 1.5 ml collagen solution, then  $10^5$  cells were added to the mixture which was poured into a sterile disposable plastic fluorescence cuvette. The setting solution was prepared as described in Ref. [211] except that it was phenol red free

and contained 1 mg horse hemoglobin (Sigma) per ml. After the collagen had gelled, 1.5 ml of tissue culture medium was carefully layered over the gel, and a tissue culture flask filtered cap was applied. The preparation was allowed to stand at room temperature and atmosphere for 30 minutes for dissipation of pH gradients, before being placed in a regular 37°C 6%CO<sub>2</sub> gassed incubator. Stylyl-9M dye was added (7 µl of a 10 mg/ml DMSO solution per phantom) 16 hours before imaging was attempted.

The following tumor cell lines were used in this study: NIHOVCAR3, human ovarian cancer obtained from ATCC; MDA-MB-231, human mammary carcinoma, obtained from ATCC; 4T1, mouse mammary carcinoma, obtained from ATCC; +SA mammary carcinoma [212], kindly provided by Dr Howard Hosick, Washington State University. When the cancer cells were added to phantoms already containing dispersed normal mouse mammary cells [213], then an extended micropipettor tip was used to dispense 1 µl of tissue culture medium. To assist in the subsequent imaging, a template was used to guide the tip to the same relative position in each gel.

#### Dye Sensitivity to Biological Phantoms

The same procedure as described above for various solutions is used here to distinguish between several biological phantoms. We observe that short excitation wavelengths,  $\lambda < 940$  nm, result in autofluorescence and/or scattering in the phantoms. For this reason we use the longer laser excitation wavelengths, 950 nm and 1100 nm, to excite 2PA fluorescence from the dye. We also find that the biological environment shifts the fluorescence maximum of the dye towards blue compared to the solutions, which might be due to formation of hydrogen bonds between the dye and its surrounding in

aqueous solutions. To accommodate this shift, the variable wavelength filter transmission is set at 730 nm in this experiment. As before, the fluorescence intensity is normalized by the squared average power of the excitation beam.

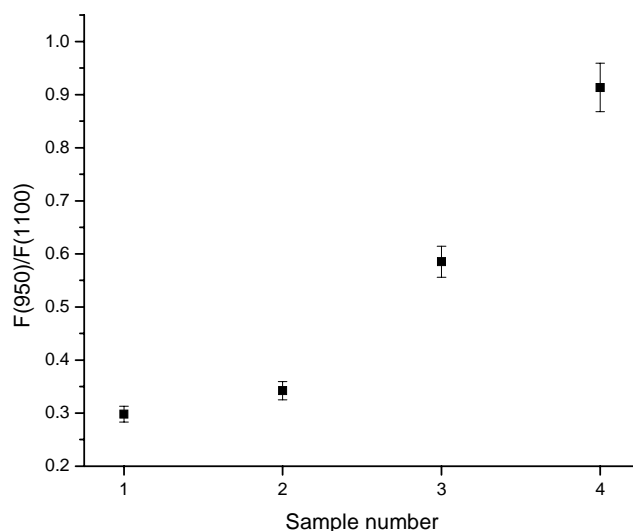


Figure F.9. Dependence of the ratio of the fluorescence intensity of Styryl-9M excited via 2PA at 950 nm and 1100 nm on the content of biological phantom

Figure F.9 shows the ratio of the fluorescence intensity excited at the two wavelengths in a series of tissue phantoms. The phantoms are: 1) 10  $\mu$ l of 5mg/ml Styryl-9M dissolved in DMSO,  $5 \times 10^5$  Mouse embryo fibroblast cells, 0.6 ml setting solution, 3 ml rat tail collagen, 1  $\mu$ l linoleic/oleic acid mixture, 1 ml serum and phenol red –free medium overlay; 2) 25  $\mu$ l of 1mg/ml Styryl-9M dissolved in DMSO, 0.8 ml setting solution, 4 ml rat tail collagen; 3) 25  $\mu$ l of 1mg/ml Styryl-9M dissolved in DMSO, 0.8 ml setting solution, 4 ml rat tail collagen, 1  $\mu$ l linoleic/oleic acid mixture; 4) 25  $\mu$ l of 1mg/ml

Styryl-9M dissolved in DMSO, 0.8 ml setting solution, 4 ml rat tail collagen, 1  $\mu$ l liposin.

Further data on the sample composition is shown in table D.15.

The fluorescence intensity ratio varies considerably depending on the composition of the phantom: addition of the 1  $\mu$ l of the linoleic/oleic fatty acid mixture to the 830  $\mu$ l of the phantom (sample 3 vs. sample 2) increases the ratio by 70%. Using 1  $\mu$ l of liposin (sample 4 vs. sample 2), increases the ratio by as much as 270%. The value for the cell-containing phantom (sample 1 vs. sample 2) differs from the value for the cell-free phantom by 15%. Comparing the results with the previous section, we can conclude that the cell-containing phantom represents the most polar environment. Phantoms without cells show lower polarity, while the addition of linoleic acids, and especially of liposin, further decreases polarity of the surrounding. All four samples represent surrounding polarity with values of the polarity function (F.1) higher than 0.5.

#### Differentiation between Cancer and Normal Cells in Biological Phantoms

We apply the two-photon method described above (see chapter 7) for selective diagnostics of cancer cells in tissue phantoms. According to our observations, the ratio of fluorescence signals excited at 1100 and 1200 nm,  $F(1100)/F(1200)$ , is smaller in the presence of cancer cells, as compared to the reference samples with normal cells or without any cells. To prove the principle, we measure the fluorescence signal integrated over the entire 1-cm excitation laser beam path length in the phantom upon excitation first at 1100 nm and then at 1200 nm. The ratio  $F(1100)/F(1200)$  is presented in figure F.10 for the phantoms without cells, with normal mouse mammary cells, with MBA-MD-

231 human breast carcinoma cells, with +SA mouse mammary carcinoma cells, and with 4T1 mouse mammary carcinoma cells.

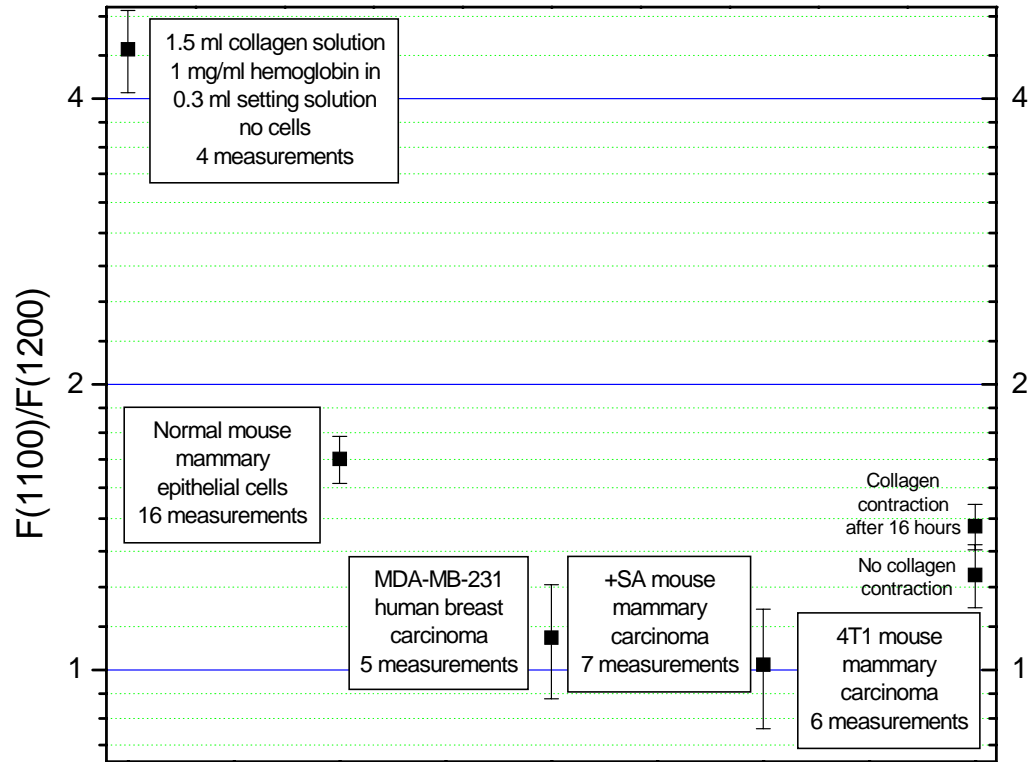


Figure F.10. Cancer cells detection using the ratio of fluorescence of Styryl-9M excited at 1100 and 1200 nm. Phantoms with cancer cells can be differentiated from the phantoms with normal cells and phantoms without any cells. Aggressive cancer cell line 4T1 shows an artifact due to collagen gel contraction several hours after sample preparation

The fluorescence ratio in the sample without cells is 2.7-fold higher than that in the sample with normal cells. This ratio in the sample with normal cells is 1.6-1.3-fold higher than that in the sample with cancer cells. The samples with MBA-MD-231 and +SA cancer cells show comparable fluorescence ratios, with the differences between them less than the experimental error. The sample with 4T1 cancer cells shows higher ratio of

fluorescence signals. This particular cancer cell line causes collagen gel contraction few hours after the sample was prepared. The fluorescence ratio is sensitive to the effect of gel contraction, and increases with time. The measured fluorescence ratio for the 4T1 containing fresh sample may be already affected by the collagen gel contraction effect, and therefore the measured value may be higher compared to other cancer cells.

These results show that the ratio,  $F(1100)/F(1200)$ , can be used to distinguish between the tissue phantoms containing no cells, normal cells and cancer cells. This also shows that Styryl-9M is not specific to any particular cancer cell line, i.e. the same dye can be used for various cancer lines, and that the technique can be applied to cancer cells in general. These results stimulate our study in chapter 7 of the ability of Styryl-9M to localize small cancer cell colonies and the mechanism responsible for observed cancer sensitivity of the 2PA spectrum of Styryl-9M.

To conclude, in this spectroscopic study we found that a commercially available laser dye, Styryl-9M, possesses unique properties for biological imaging and microscopy. The dye molecule shows one of the largest peak two-photon cross section, 740 GM, among commercially available chromophores. The maximum 2PA cross section in the lowest energy absorption band of Styryl-9M can be described by the two-level model. Both absorption and fluorescence spectra of the dye are highly sensitive to the pH in the interval pH=8–11. Chemical modifications of the dye are still required to bring this sensitivity into the biologically useful range, pH<8. The one- and two-photon absorption peaks of the dye are sensitive to a change of solvent, and thus to the environment of the dye. We demonstrate the use of this dependence in two-photon biological imaging for

sensing of the local polarity. We conclude that Styryl-9M could be a useful sensor for the polarity of solvents. Combining fluorescence sensitivity of Styryl-9M to local pH-level and its absorption sensitivity to local polarity, one can achieve an efficient local environment sensor. The experiment shows that Styryl-9M can be used for imaging of biological phantoms. The analysis of the fluorescence intensity can be used to distinguish between different local environments. It also can be used to distinguish between cancer and normal cells in the phantoms.



APPENDIX G

SOME DOCUMENTATION ON THE PUMP-PROBE EXPERIMENTAL SETUP

This appendix contains some of the documentation on the pump-probe setup designed and implemented for the measurements of transient absorption spectra (see chapter 3).

Figure G.1 shows schematic of the amplifier for Si/InGaAs sandwich detector. The amplifier features adjustable gain and current flow from the diode to the operational amplifier.

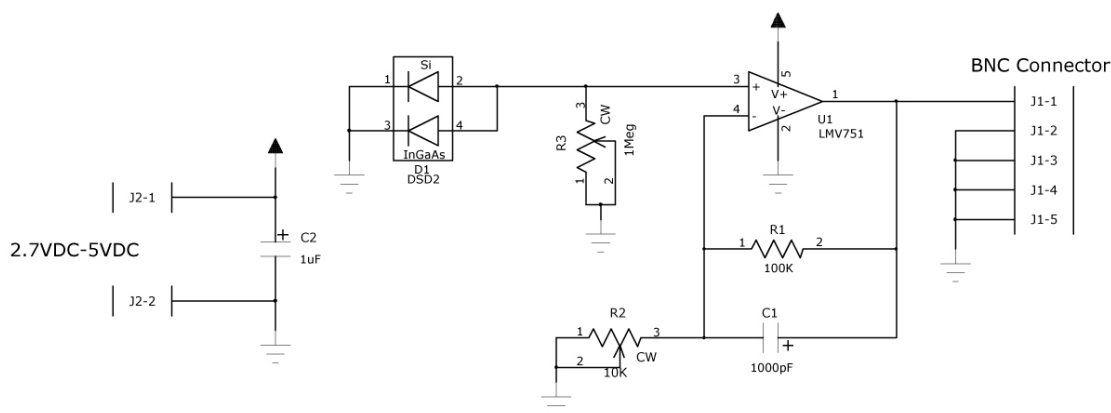


Figure G.1. Schematic of the amplifier for Si/InGaAs sandwich detector (ThorLabs DSD2)

Figure G.2 shows schematic of the variable voltage power supply used to power magnetic stirrer of the sample and to control stirring intensity (motor rpm).

Figure G.3 shows schematic of the controller used to address and computer-control 16 stepper motors. Each motor is connected to the controller using 9-pin serial connector. The controller is connected to a computer through a USB digital I/O board (Measurement Computing USB-1024HLS), such that the computer can address and control each individual motor, one at a time. The figure is divided into three parts for clarity purposes.

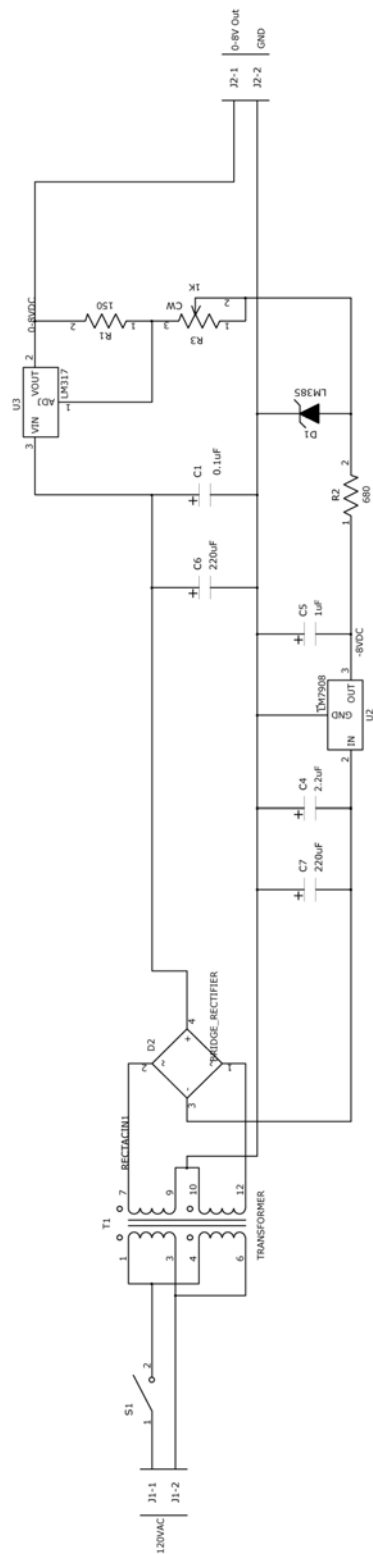


Figure G.2. Schematic of the variable voltage power supply for magnetic stirring of the sample

Figure G.4 shows front panel of the LabView VI designed for manual pre-alignment of the computer-controlled mirrors. The pre-alignment is required to fill the quad detectors controlling overlap of the pump and the probe beams.

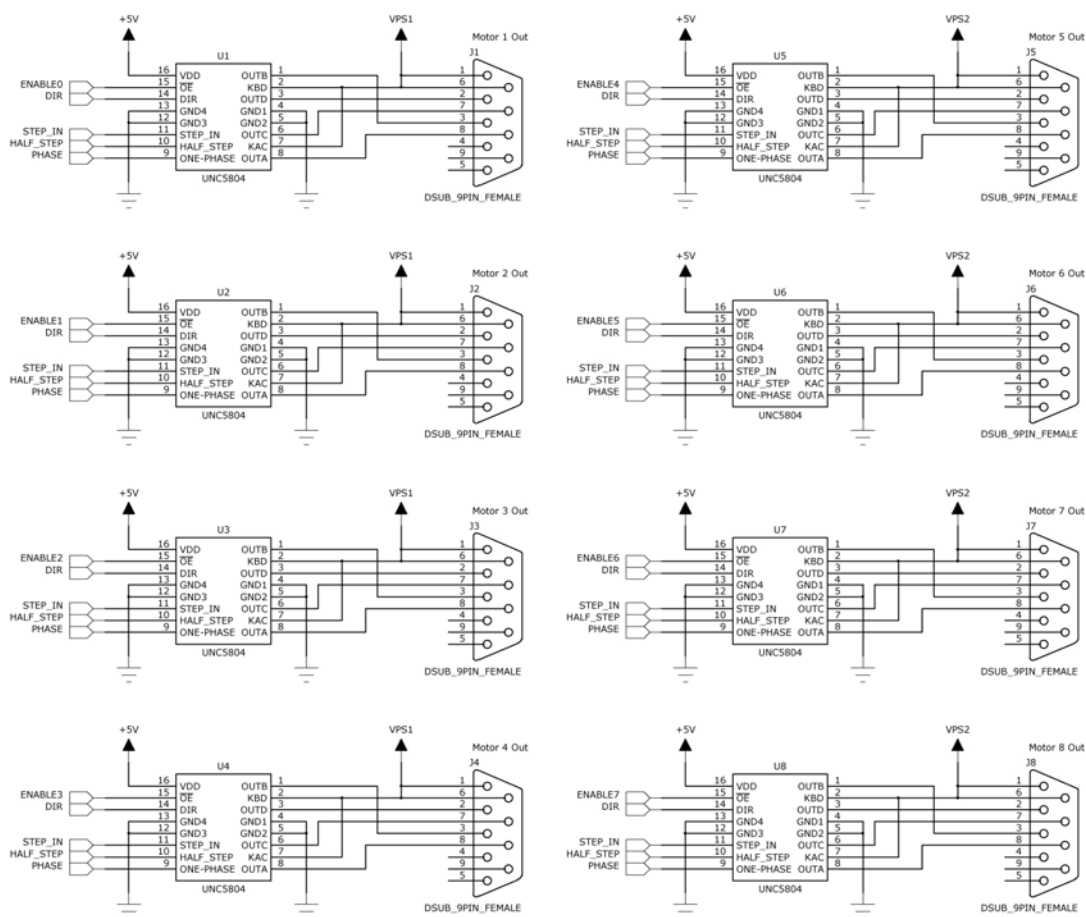


Figure G.3a. First 8 outputs of the 16-motor controller

Figure G.5 shows block diagram of the pre-alignment LabView VI. The VI is running continuously. Eight switches allow sequential control over the mirrors. If the switch is pressed, then the VI runs one of the sub-VIs to perform an action, and after it is finished, VI returns into the main loop, such that the next switch can be pressed and the next action can be performed.

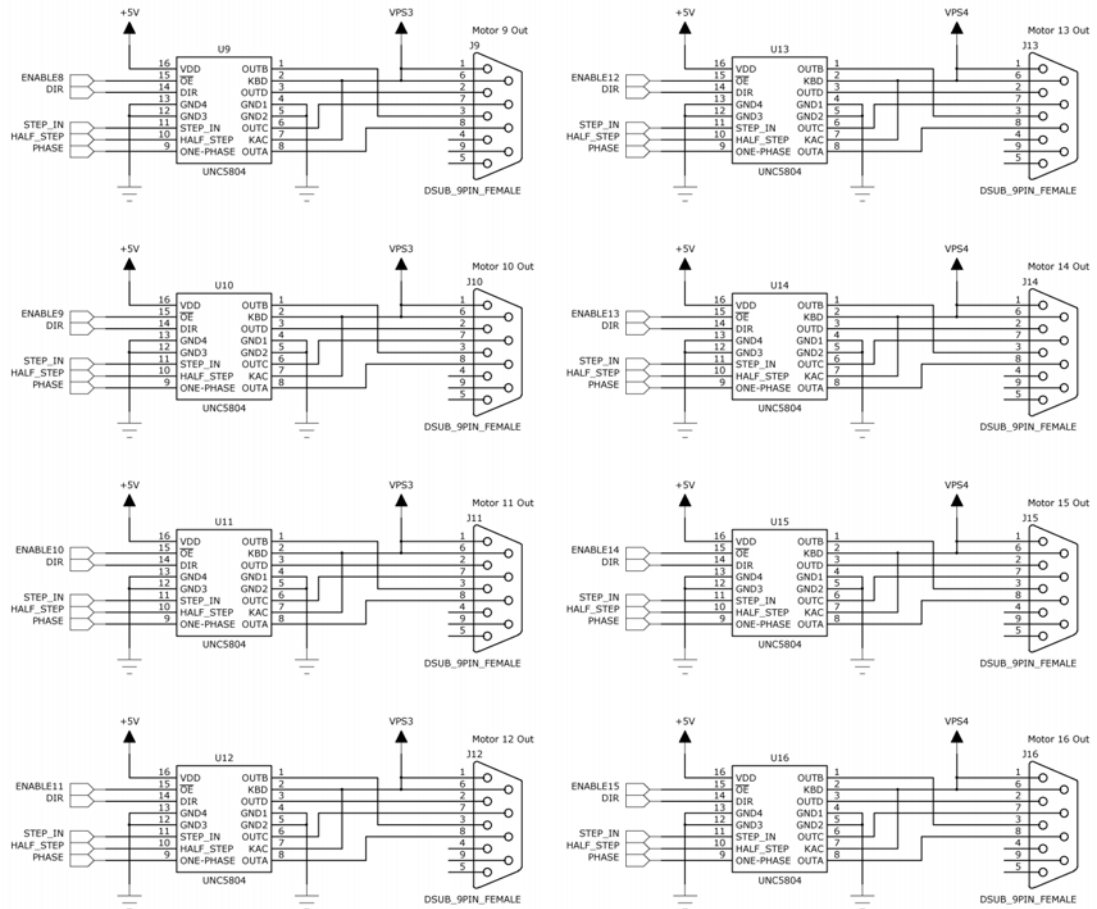


Figure G.3b. Last 8 outputs of the 16-motor controller

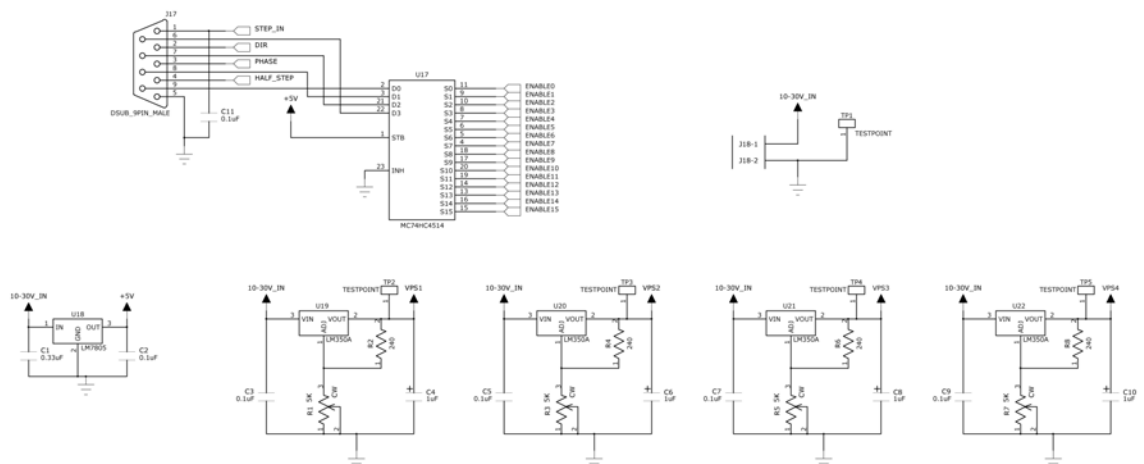


Figure G.3c. Power control and address demultiplexing of the 16-motor controller



Figure G.4. Front panel of the VI for manual alignment of the computer-controlled mirrors

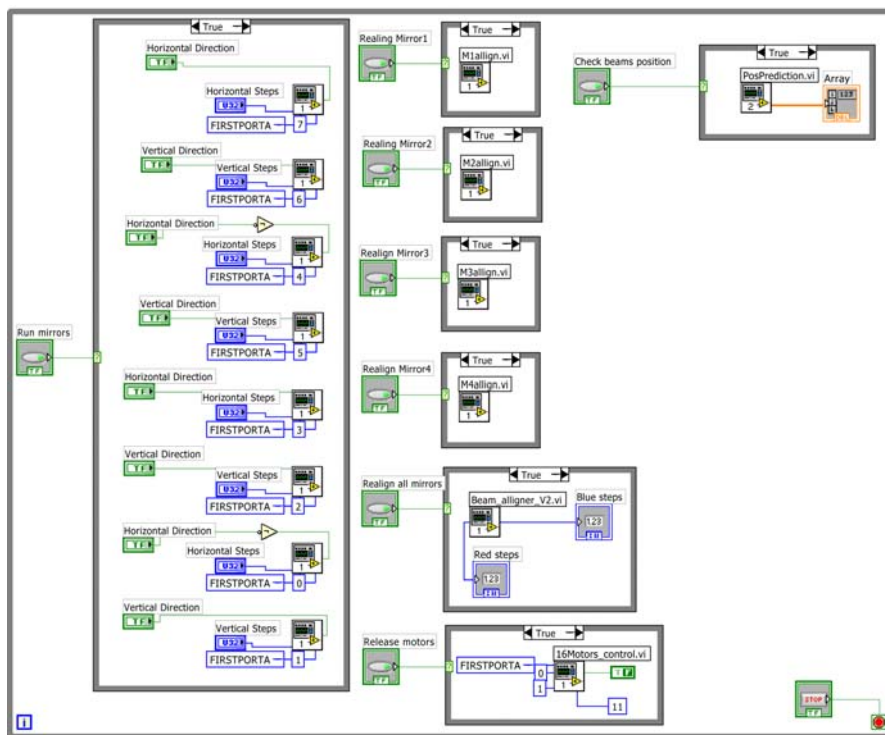


Figure G.5. Block diagram of the VI for manual alignment of the computer-controlled mirrors

The VI can: 1) move any of the computer-controlled mirrors into a given direction on a given number of steps, 2) auto-align individually any of the four computer-controlled mirrors provided that the laser beams fill the quad detectors, 3) auto-align all of the computer-controlled mirrors, and 4) check if the laser beams fill the quad detectors.

Figure G.6 shows front panel of the main VI designed to run the pump-probe experiments. The VI controls acquisition of the transient absorption spectra, wavelength steps of the OPA, delay line, and dynamic realignment of the mirrors during the experiments. Left half of the front panel allows control over each individual parameter of the experiment. Right half displays the measured spectrum. Top row of the controls is used to setup 14-bit acquisition board (GaGe CS8420-128MS). Middle row of the controls is used to choose the range for analysis of the sandwich detector outputs and calculation of the  $\Delta OD(\lambda)$ . The bottom row allows controlling wavelength and delay steps, and also automated mirror realignment.

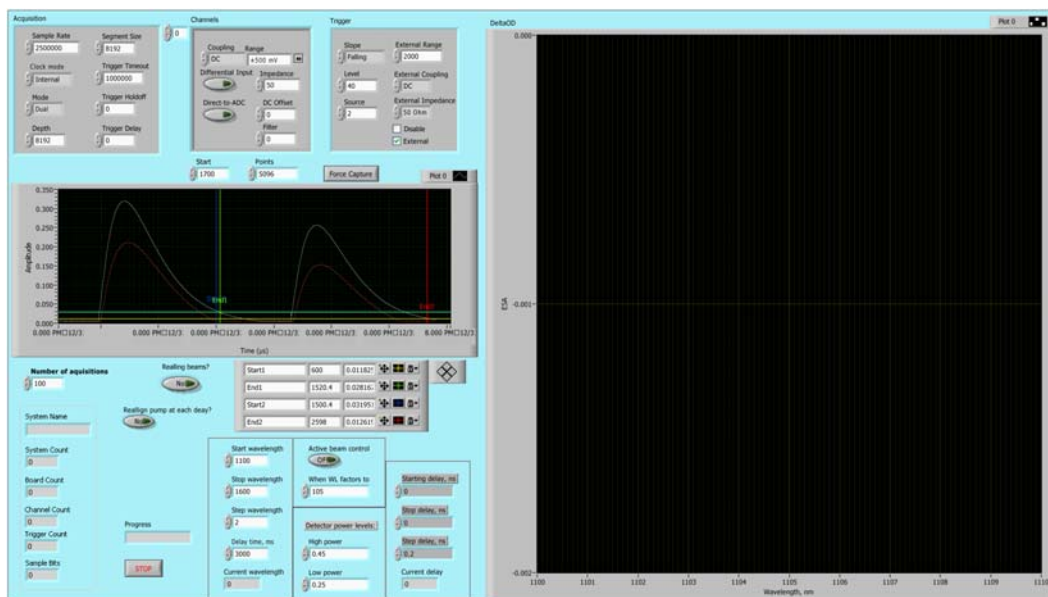


Figure G.6. Front panel of the VI for the acquisition of the ESA spectra

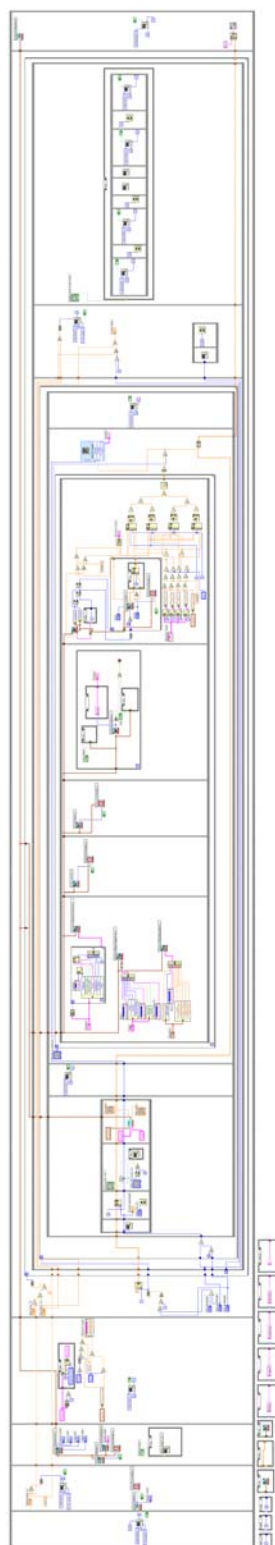


Figure G.7. Block diagram of the VI for the acquisition of the ESA spectra



Figure G.7 shows block diagram of the main VI controlling pump-probe experiments. The VI runs in three nesting loops: the outer loop steps over selected delays, the middle loop steps over selected wavelengths, and the inner loop averages over the given number of data acquisitions. Each data acquisition compares single probe laser pulses with blocked and unblocked pump to measure the value of  $\Delta OD(\lambda)$ .